

FINAL REPORT

Contract **Number:** NA81-RAC00046
Research Unit Number: 265/250
Number of Pages: 260

MECHANICAL PROPERTIES OF SEA ICE
AND
SEA ICE DEFORMATION IN THE NEAR-SHORE ZONE

by

Lewis H. Shapiro

Geophysical Institute
University of Alaska-Fairbanks
Fairbanks, Alaska 99775-0800

Contributing Scientists

Peter W. Barnes
Arnold Hanson
Earl R. **Hoskins**
Jerome B. Johnson
Ronald C. Metier

December, 1987

✓

FINAL REPORT

Contract Number: **NA81-RAC00046**

Research Unit Number: 265/250

Number of Pages 260

MECHANICAL PROPERTIES **OF** SEA ICE AND SEA ICE DEFORMATION IN THE NEAR-SHORE ZONE

by

Lewis H. Shapiro

Geophysical Institute
University **of** Alaska-Fairbanks
Fairbanks, **Alaska** 99775-0800

Contributing Scientists

Peter W. Barnes
Arnold Hanson
Earl R. **Hoskins**
Jerome B. Johnson
Ronald C. **Metzner**

December, 1987

TABLE OF CONTENTS

| | <u>Page</u> |
|---|-------------|
| List of Figures | 7 |
| List of Tables | 11 |
| Abstract | 13 |
| Acknowledgements. | 14 |
| 1. EXECUTIVE SUMMARY | 15 |
| 2. MECHANICAL PROPERTIES OF SEA ICE | 20 |
| 2.1 INTRODUCTION | 20 |
| 2.2 FIELD EXPERIMENTS ON THE MECHANICAL PROPERTIES OF SEA ICE | 23 |
| Abstract | 23 |
| 2.21 Introduction | 25 |
| 2.22 Loading System | 26 |
| 2.22.1 Flatjacks | 26 |
| 2.22.2 Load Transmission and Efficiency | 26 |
| 2.22.3 Load Control | 33 |
| 2.23 Deformation Measurements | 34 |
| 2.24 Uniaxial Compression Tests | 37 |
| 2.24.1 Sample Preparation | 39 |
| 2.24.2 Test Procedures.. | 41 |
| 2.24.3 Temperature and Salinity | 44 |
| 2.24.4 Acoustic Emmissions. | 44 |
| 2.24.5 Results of Experiments in Uniaxial Compression | 45 |
| 2.24.6 Discussion of Uniaxial Test Results | 48 |
| 2.25.61 Introduction | 49 |
| 2.25.62 Strength vs. Stress Rate | 49 |
| 2.25.63 Long-term Strength | 51 |
| 2.25.64 Grain Size and Orientation | 55 |

| | | |
|---|------------|---|
| 2.25.65 Comparison of the Strength of First Year and Multiyear Ice | 61 | |
| 2.25 Direct Shear Tests | 63 | |
| 2.26 Indirect Tension (Brazil) Test | 67 | |
| 2.27 Biaxial Compression Tests | 68 | |
| 2.28 Summary and Discussion | 69 | |
| References Cited | 73 | |
| 2.3 A STRESS-STRAIN LAW AND FAILURE CRITERION FOR SEA ICE | 75 | |
| Abstract | 75 | |
| 2.31 Introduction | 76 | |
| 2.32 Description of the 4-Parameter Fluid Model (4-PF). | 78 | |
| 2.33 Description of the Distortional Strain Energy Yield Criterion (DSEC) | 83 | |
| 2.34 Application of the DSEC to the 4-PF Model | 87 | |
| 2.34.1 Upper and Lower Strength Limits | 8 | 7 |
| 2.34.2 Relationships at Failure | 92 | |
| 2.34.21 Introduction | 92 | |
| 2.34.22 Strain at Failure | 94 | |
| 2.34.23 Strain Rate at Failure | 97 | |
| 2.34.24 Time-to-Failure | 102 | |
| 2.34.3 Summary of Model | 102 | |
| 2.35 Comparison with Data | 106 | |
| 2.35.1 Introduction | 106 | |
| 2.35.2 Lower Limit of Strength | 106 | |
| 2.35.3 Upper Limit of Strength | 109 | |
| 2.36 Discussion and Conclusions | 109 | |
| Appendix. | 112 | |

| | |
|--|------------|
| References Cited | 126 |
| 2.4 FRACTURE TOUGHNESS OF SEA ICE | 129 |
| 2.41 Introduction | 129 |
| 2.42 Sample Description and Methods | 129 |
| 2.43 Results and Conclusions | 132 |
| References Cited | 136 |
| 2.5 STRAIN TRANSDUCER FOR LABORATORY MEASUREMENTS | 137 |
| 2.51 Introduction | 137 |
| 2.52 Clip-Type Strain Gages | 137 |
| 2.53 Calculation of Arch-Gage Properties | 139 |
| 2.54 Measurement of Gage Response | 142 |
| 2.55 Discussion and Conclusions | 144 |
| References Cited | 147 |
| 3. DEFORMATION OF ICE IN THE NEAR-SHORE ZONE | 148 |
| 3.1 FAST ICE SHEET DEFORMATION DURING ICE-PUSH AND SHORE ICE RIDE-UP | 148 |
| 3.11 Introduction | 148 |
| 3.12 Summary of Data and Observations | 149 |
| 3.13 Discussion | 151 |
| 3.14 Proposed Model | 155 |
| 3.15 Conclusions | 158 |
| References Cited | 160 |
| 3.2 HISTORICAL REFERENCES TO ICE CONDITIONS ALONG THE BEAUFORT SEA COAST OF ALASKA | 161 |
| 3.21 Introduction | 161 |
| 3.22 Procedures | 161 |
| 3.23 Summary and Discussion | 162 |

| | |
|--|------------|
| References Cited | 164 |
| 3.3 VIBRATION OF SEA ICE SHEETS | 165 |
| 3.31 Introduction | 165 |
| 3.32 Background | 165 |
| 3.33 Wave Propagation in an Ice-Covered Sea | 167 |
| 3.34 Summary | 169 |
| References Cited | 170 |
| 3.4 COEFFICIENTS OF FRICTION OF SEA ICE ON BEACH GRAVEL | 171 |
| Abstract | 171 |
| 3.41 Introduction | 171 |
| 3.42 Procedure | 172 |
| 3.43 Results and Discussion | 176 |
| 3.5 NEARSHORE ICE CONDITIONS FROM RADAR DATA, POINT BARROW AREA, ALASKA | 181 |
| Abstract | 181 |
| 3.51 Introduction | 182 |
| 3.52 Equipment and Methods | 182 |
| 3.52.1 Radar System and Data Recording | 182 |
| 3.52.2 Data Analysis | 186 |
| 3.52.3 Reflectors | 188 |
| 3.52.4 Measurement of Ice Motion | 190 |
| 3.53 Characteristic Ice Motion Patterns | 192 |
| 3.53.1 Introduction. | 192 |
| 3.53.2 Generalized Drift Patterns | 192 |
| 3.53.3 Flickering of Reflectors | 195 |
| 3.54 Annual Cycle | 196 |

| | |
|--|------------|
| 3.54.2 Open Water Season | 196 |
| 3.54.3 Freeze Up | 197 |
| 3.54.4 Winter | 202 |
| • 3.54.5 Breakup | 208 |
| 3.54.6 Relationship of the Annual Cycle to Climate Data | 213 |
| 3.55 Summary and Conclusions. | 216 |
| References Cited | 220 |
| 3.6 CORRELATION OF NEARSHORE ICE MOVEMENT WITH SEA-BED ICE GOUGES | 221 |
| Abstract | 221 |
| 3.61 Introduction | 221 |
| 3.62 Methods and Equipment | 224 |
| 3.63 Observations | 227 |
| 3.64 Discussion | 236 |
| 3.64.1 Ice Gouge Orientation and Ice Motion | 236 |
| 3.64.2 Ice Gouge Density and Depth | 240 |
| 3.65 Conclusions. | 241 |
| References Cited | 243 |

LIST OF FIGURES

FIGURES IN SECTION 2.2

| | | |
|--------|--|----|
| 2.2-1 | Plan view and cross-section of flatjack calibration experiment using copper flatjack . | 28 |
| 2.2-2 | Results of calibration experiment in Figure 2.2-1 . | 29 |
| 2.2-3 | Cross section of set-up for second calibration experiment | 31 |
| 2.2-4 | Set-up for uniaxial compression test illustrating the placement of linear potentiometers in the sample. | 36 |
| 2.2-5 | Geometric relationships between the pegs and linear potentiometers used for strain relationships. | 38 |
| 2.2-6 | Plan and end views of uniaxial compression test set-up using triangular flatjacks . | 40 |
| 2.2-7 | Set-up for uniaxial compression tests using 30 x 30 x 60 cm test sample (same as Figure 2.2-4). | 42 |
| 2.2-8 | Plots of uniaxial compressive strength vs. stress rate for three temperature ranges. | 50 |
| 2.2-9 | Uniaxial compressive strength vs. time-to-failure and time to minimum strain rate for the temperature range -16 to -19 °C. | 53 |
| 2.2-10 | Uniaxial compressive strength vs. time-to-failure and time to minimum strain rate for the temperature range -5.5 to -7.5 °C. | 54 |
| 2.2-11 | Arrangement of samples collected for evaluation of uniaxial compressive strength vs. grain size and c-axis orientation. | 56 |
| 2.2-12 | Results of the 1979 series of tests of uniaxial compressive strength vs. grain size and c-axis orientation. | 57 |
| 2.2-13 | Results of the 1980 series of tests of uniaxial compressive strength vs. grain size and c-axis orientation. | 60 |
| 2.2-14 | Uniaxial compressive strength of first year and multiyear ice vs. stress rate. | 62 |
| 2.2-15 | Set-up for direct shear test. | 64 |
| 2.2-16 | Results of finite element analysis of a punch test and a direct shear test. | 65 |

FIGURES IN SECTION 2.3

| | |
|--|-----|
| 2.3-1 Spring-dashpot model of a 4-parameter linear viscoelastic fluid. | 80 |
| 2.3-2 Yield envelope in terms of the applied stress and the stress across the spring of the Voigt model | 90 |
| 2.3-3 Chart showing the relationships between the stress, strain and strain rate in each element of the 4-PF model at yield. | 95 |
| 2.3-4 Strain ratio vs. stress ratio at yield for the linear model | 96 |
| 2.3-5 Stress vs. strain at yield for the non-linear 4-PF model described in the text. | 98 |
| 2.3-6 Stress ratio vs. strain rate at yield for the linear model. | 100 |
| 2.3-7 Stress ratio vs. strain rate at yield for the non-linear 4-PF model | 101 |
| 2.3-8 Stress ratio vs. time ratio at yield for the linear model | 103 |
| 2.3-9 Strength vs. time-to-yield for the non-linear model. | 104 |
| 2.3-10 Unaxial compressive strength vs. time to minimum strain rate for CS tests and time to peak stress for CDR tests. | 107 |
| 2.3-A1 Strain ratio vs. time ratio for CS tests at various stress ratios for the linear 4-PF model. | 114 |
| 2.3-A2 Stress ratio vs. strain ratio for CSR tests at various stress rates for the linear 4-PF model. | 117 |
| 2.3-A3 Stress ratio vs. strain ratio for CDR tests at various strain rates for the linear 4-PF model . | 122 |

FIGURES IN SECTION 2.4

| | |
|---|-----|
| 2.4-1 Schematic diagram of 4-point bending apparatus. | 130 |
| 2.4-2 Fracture toughness vs. square root of brine volume. | 133 |

FIGURES IN SECTION 2.5

| | |
|--|-----|
| 2.5-1 Schematic diagram of a clip gage in the form of a semi-circular arch. | 138 |
| 2.5-2 Schematic diagram of a typical channel-type clip gage. | 140 |

| | |
|---|-----|
| 2.5-3 Bending of an arch clip gage as a result of sample shortening. | 143 |
| 2.5-4 Voltage output per unit strain vs. thickness to diameter ratio for six arch gages. | 145 |
| 2.5-5 Plot of arch clip gage output vs. resistance gage output for the bending beam experiment. | 146 |

FIGURES IN SECTION 3.1

| | |
|--|-----|
| 3.1-1 Relationships between shear lines and a rigid boundary from Prandtl's solution. | 152 |
| 3.1-2 Proposed model for the fracture and displacement of a fast ice sheet during an ice-push event. | 156 |

FIGURES IN SECTION 3.4

| | |
|--|------------|
| 3.4-1 Geometry and weights of test blocks. | 173 |
| 3.4-2 Schematic diagram of the experimental set-up. | 174 |
| 3.4-3 Plots of coefficients of friction vs. test number for the three test series. | 177 |

FIGURES IN SECTION 3.5

| | |
|---|-----|
| 3.5-1 Map of the Point Barrow area showing the location of the radar site. | 184 |
| 3.5-2 Typical frame of radar data at 5.5 km (3 NM) range. | 185 |
| 3.5-3 Schematic diagram illustrating the possible senses of ice motion within the field-of-view of the radar. | 193 |
| 3.5-4 Pattern of shear ridges in fast ice which formed during a storm on January 1, 1974. | 199 |
| 3.5-5 Percent of films of radar data showing drifting pack ice, plotted by month. | 201 |
| 3.5-6 Displacement path of a hypothetical point on the pack ice surface during the movement episode of March, 1974. | 205 |
| 3.5-7 Displacement path of a hypothetical point on the pack ice surface during the movement episode of June, 1974. | 210 |

| | |
|---|-----|
| 3.5-8 Schematic diagram of an unusual ice movement pattern during break up. | 212 |
|---|-----|

FIGURES IN SECTION 3.6

| | |
|---|-----|
| 3.6-1 Location of study area in the field-of-view of the radar system | 223 |
| 3.6-2 Tracklines of the 1977 side-scan sonar survey. | 225 |
| 3.6-3 Tracklines of the 1978 side-scan sonar survey. | 226 |
| 3.6-4 Density of ice gouges in 1977. | 229 |
| 3.6-5 Density of ice gouges in 1978. | 230 |
| 3.6-6 Locations of prominent ice ridges in the field-of-view of the radar system. | 231 |
| 3.6-7 Maximum ice gouge incision depth, 1977. | 232 |
| 3.6-8 Maximum ice gouge incision depth, 1978. | 233 |
| 3.6-9 Principal orientation of ice gouges, 1977. | 235 |
| 3.6-10 Principal orientation of ice gouges, 1978. | 235 |
| 3.6-11 Displacement vectors from the 1975 ice-push event superimposed on principal ice gouge orientations mapped in the 1977 survey. | 239 |

LIST OF TABLES

TABLES IN SECTION 2.2

| | |
|--|------|
| 2.2-1 Results of constant load rate tests -1978. | 47a |
| 2.2-2 Results of creep-rupture tests -1978. | 47e |
| 2.2-3 Results of creep tests -1978. | 47g |
| 2.2-4 Results of constant stress rate tests -1979. | 47h |
| 2.2-5 Results of constant stress rate tests on multiyear ice in uniaxial compression -1979. | 47j |
| 2.2-6 Results of creep-rupture tests -1979. | 47k |
| 2.2-7 Results of creep tests -1979. | 47l |
| 2.2-8 Results of constant stress rate tests to evaluate the effect of grain size and c-axis orientation-1979. | 47rn |
| 2.2-9 Results of constant stress rate tests -1980. | 47n |
| 2.2-10 Results of constant stress rate tests to evaluate the effect of grain size and c-axis orientation-1980. | 47p |

TABLE IN SECTION 2.3

| | |
|--|-----|
| 2.3-A1 Values of constants used in calculations of the response to load of the non-linear 4-PF model. | 125 |
|--|-----|

TABLE IN SECTION 2.4

| | |
|--|-----|
| 2.4-1 Results of fracture toughness tests. | 135 |
|--|-----|

TABLE IN SECTION 2.5

| | |
|---|-----|
| 2.5-1 Characteristics of fabricated arch-type clip gages . | 141 |
|---|-----|

TABLE IN SECTION 3.1

| | |
|---|-----|
| 3.1-1 Ice pile-up and ride-up events in the Point Barrow area, 1975-1978. | 150 |
|---|-----|

TABLE IN SECTION 3.4

| | |
|---|-----|
| 3.4-1 Values of coefficients of friction and standard deviations. | 180 |
|---|-----|

TABLES IN SECTION 3.5

| | |
|---|-----|
| 3.5-1 Total days of radar coverage by month and year. | 187 |
| 3.5-2 Ice drift directions by month. | 189 |
| 3.5-3 Climate data by month (1966-1974). | 215 |

ABSTRACT

The primary objectives of this program were to (1) develop and test procedures and hardware required for in-situ measurement of the strength and other mechanical properties of sea ice, (2) use the appropriate procedures to determine the reformational behavior of ice and (3) combine the experimental results with existing data for use as background in a search for an appropriate stress-strain law and failure criterion for sea ice. In addition, ~~to~~ take advantage of the extended field season required for the objectives above and the presence of a radar system in the field area, a series of studies of fast ice deformation in the near shore area was conducted. The subjects under this part of the program included ice-push, ice sheet vibration as an indicator of rising stress levels, ice gouges and other topics. The program results are described in the ten technical sub-sections of this report.

ACKNOWLEDGEMENTS

This program was funded primarily by the Minerals Management Service, Department of the Interior, through an Interagency Agreement with the National Oceanic and **Atmospheric** Administration, Department of Commerce, as part of the Alaska Outer Continental Shelf Environmental Assessment Program. **Additonal** funding support for the study **titled "Vibration** of Sea Ice Sheets" came from the National Science Foundation. The Alaska Sea Grant Program contributed funds for analysis of the radar data which was used in several studies. Timely support from several industry groups was important for the conduct of the experimental program on the mechanical properties of sea ice. Finally, additional funds from the State of Alaska were used for preparation of reports.

1.0 EXECUTIVE SUMMARY

This report describes the results of studies in two general subject areas; (1) strength and mechanical properties of sea ice and (2) ice deformation in the nearshore area. During the course of the program, numerous studies were done consistent with the two basic themes. The number of these studies is large enough that it is not feasible to include complete reports on all of them here; in fact, most have been described in reports or publications in the open literature. However, **all** are summarized (or noted in passing) and references are provided to the earlier work. Material which was not covered completely in previous reports and publications is, of course, treated fully here. Thus, this report provides a complete record of the program.

The primary objectives of this program were to **(1)** develop and test procedures and hardware required for in situ measurement of the strength and other mechanical properties of sea ice, (2) use the appropriate procedures to determine some aspects of the reformational behavior of ice and, (3) combine the experimental results with existing data for use in a search for an appropriate stress-strain law and failure criterion for sea ice. In addition, in order to take advantage of the extended field season required for the objectives above and the presence of a radar system in the field area near Barrow, Alaska, several aspects of fast ice deformation in the nearshore area were studied while the the work of the first project was in progress. Projects under this part of the program included studies of ice-push and ice-override, ice sheet vibration as an indicator of rising stress levels, nearshore ice motion patterns, correlation of **ice** movement with sea-bed ice gouges and other subjects. The results of all aspects of the program are described in the ten technical sub-sections of this report.

Numerous individuals contributed to different studies in the program and are acknowledged as co-authors in the relevant sections of the report.

The rationale for the study and its relevance to problems of offshore development follow from the premise that any permanent or semi-permanent offshore structure off the **Chukchi**, Beaufort or (most of) the Bering Sea coast of Alaska must contend with problems related to the presence of sea ice. A broad range of potential problem areas were examined in this project. The purpose was to help define some of the properties and processes in the ice cover which needed to be considered in both the design and the evaluation of structures for offshore exploration and development.

The major results of the program are:

(1) Procedures and hardware for tests in **uniaxial** and biaxial compression, direct shear and indirect tension were developed and tested. In all cases, **flatjacks** were used to apply loads to samples in situ in the ice sheet. The samples were intermediate in size between small-scale laboratory samples and the full thickness of the ice sheet.

(2) An extensive series of **uniaxial** compression tests was conducted which yielded data on strength vs. stress rate and stress vs. time-to-minimum strain rate in constant stress tests. The data provide useful values and, in addition, they define strength ranges which are important elements in the stress-strain law and failure criterion developed to interpret the data.

(3) The stress-strain law under study is based on the model of a 4-parameter **viscoelastic** fluid constrained by the distortional strain energy yield criterion. Both linear and non-linear **viscoelastic** models have been considered, and the similarity of the trends predicted by the theory are evident in the data. However, further refinements are required in order for the results to agree **quantitatively**.

(4) Two series of tests were conducted to examine the effect of grain size and c-axis orientation on the **uniaxial** compressive strength of sea ice. In the first series, the results were in general agreement with the results of small-scale laboratory

tests; the strength varied with loading direction relative to the dominant c-axis orientation direction. However, the second series, which was done on ice which clearly had a well-developed c-axis fabric, showed no variation of strength with direction. We interpret this to indicate that there maybe a sharp limit to the intensity **of** c-axis orientation required for the ice to become mechanically **anisotropic** for loading in the **plane** of the ice sheet.

(5) A short series of tests were done to compare the **uniaxial** compressive strength of first year and **multiyear** ice over a range of loading rates. The results showed no significant differences over the range of loading rates used.

(6) There were opportunities to study several ice-push and ice-override events in the field, including the first documented case of complete override of a barrier island during an ice-push event. A model of the deformation pattern in the plane of the fast ice sheet during an ice-push event was developed, based upon observations made during the project. In the winter, when the fast ice is firmly in contact with (and possibly frozen to) the beach, ice-push events originate with fracture of the ice sheet in a pattern which resembles the shear lines in a plastic medium compressed between rough plates. This pattern apparently serves to concentrate the distributed stress from the pack ice-fast ice boundary to a smaller reach along the beach. Subsequently, the fast ice sheet can advance as series of segments bounded by fractures at high angles to the beach, which appear to originate at the shoreline and extend offshore in response to the motion. Ice-push events during breakup, when the ice is not frozen to the beach, do not display the initial pattern of shear fracturing. Instead, the ice sheet simply advances by the mechanism of segmenting along fractures at high angles to the beach.

(7) Several instances of "long" period vibration **of the** fast ice sheet as **an** indicator (leading by periods of hours) of rising stress level were observed during the project. Based upon these, a theoretical study was conducted of wave propagation in

an ice covered sea. The purpose of the study was to evaluate a model of the relationship between the vibrations and the rising stress level, in order to determine whether the association could be useful as a warning of impending stress increase or motion of the ice sheet. The study suggests that the model is reasonable. In addition, some results were obtained which suggest guidelines for the safe transit of vehicles over ice or, conversely, for ~~the~~ use of over-ice vehicles in ice breaking.

(8) Side-scan sonar surveys of the sea floor were done in two consecutive summers within the field-of-view of the radar system near Barrow. The purpose was to attempt to correlate the pattern of gouges in the sea floor with movement of the ice as monitored by the radar. The results showed that the dominant ice gouge direction was at a high angle to the **isobaths** (and the shoreline) in the area. This is different from the pattern along the Beaufort Sea coast where the gouges tend to be parallel to the **isobaths** (and the shore). The history of the ice cover in the area was determined from the radar data for the years prior to and between the side-scan sonar surveys and was used to interpret the gouge pattern. The results suggest that the prominent gouge orientations in the area normally occupied by fast ice were formed by the drag of keels during ice-push events, while the majority of the gouges reflect incision during ridging.

(9) The imagery from the sea ice radar system was evaluated and used to describe some of the processes and patterns of sea ice drift in the nearshore area. In addition, ice conditions through a "typical" ice year in the Barrow area were defined. The results of this work, while specific to the area, are used to point out the potential utility of data of this type for any area where development in the nearshore zone is anticipated.

(10) A short series of experiments were done to determine the coefficients of static and kinetic friction between sea ice and unfrozen beach gravel. The experiments involved dragging large blocks of ice (i.e., 10,000 to 12,000 kg) up the

beach slope with a bulldozer and monitoring the forces required. The results of 36 separate movements of the blocks gave values for the **coefficients** of static and kinetic friction of 0.50 and 0.39, respectively. These values should be applicable to calculations of the forces required to drive an ice sheet on shore during an ice push event.

Other completed work summarized in the report includes (1) the results of preliminary measurements of the fracture toughness of sea ice, (2) the design of a new strain transducer for laboratory studies of ice strength, and (3) the description of a series of interviews with older residents of the Arctic Alaska regarding historical occurrences of unusual or extreme events in the fast ice cover along the Beaufort Sea coast.

2.0 MECHANICAL Properties OF SEA ICE

2.1 INTRODUCTION

The problem of translating the results of laboratory tests of the mechanical properties of natural materials into field application is well-known in both soil and rock mechanics, and is no less acute for the case of sea ice. In its natural state, sea ice occurs as an ice sheet which, in the offshore areas of Alaska, may freeze to a thickness of about 2 m through a winter. Within this vertical distance grain sizes range from dimensions of a few millimeters at the surface **to** several centimeters at the base. Often there is a tendency for strong preferred orientation of the grains by **alignmnet** of c-axes **in** the horizontal plane (Weeks and **Gow**, 1978; Weeks and Assur, 1967). Superimposed over this fabric are both horizontal and vertical variations in salinity of the ice, and a temperature gradient reflecting temperature differences which may be in excess of 40 °C between the top and bottom of an ice sheet at various times during the winter.

Prior to the start of this project, the determination of the mechanical properties of sea ice sheets under in-plane loading (as opposed to bending under vertical loads) was approached from two directions. The first was through small-scale laboratory or field tests involving large numbers of samples. The best example is the work of Peyton (1966) in which the properties of an ice sheet were deduced by integrating the results of tests on samples collected at different depths in an ice sheet. The second approach was to test the full thickness of an ice sheet in crushing (**Croasdale, 1974; Croasdale et al., 1977**). Obviously, the number of tests of this type which could be done is limited, and not all properties or ice types of interest could be tested. The objective of this project was to develop a series of tests through which the strength and other mechanical properties of sea ice could be determined for samples which were large relative to those normally used in **laboratory** testing programs. The samples were to be loaded parallel to the surface of the ice sheet (as opposed to

vertical loading as in tests of bearing strength), and the tests were to be done **in** the field under ambient conditions in a manner which minimized the disturbance to the samples. Thus, the tests were required to be relatively easy to set-up and run. Once the test procedures were developed, a program of measurements was to be conducted to determine the strength and **viscoelastic** properties of the ice.

During **the** course of the program we developed procedures for doing **uniaxial** and biaxial compression tests, direct shear tests and indirect tension (Brazil) tests. This involved experiments to evaluate (1) the loading system, (2) strain measuring devices, (3) the accuracy of temperature and salinity measurements, and (4) the extent **to** which the samples represented the ambient conditions in the ice sheet. The nature of the tests required that these experiments all be done as part of the field **program**. Then, an extensive series of **uniaxial** compression tests was done in the field to attempt to define the strength and reformational properties of sea ice in this loading mode. Some experiments were also done in biaxial compression over a small range of confining pressures. Late in the program a series of fracture toughness measurements on small beams of sea ice were made in the laboratory, and development work was done on an inexpensive strain gauge for use in testing **small-scale** samples of sea ice in **uniaxial** compression. It was anticipated that this gauge would **be** used in a series of tests to be done in the field using small samples collected from the site at which the tests on the large samples were being conducted. Unfortunately, the experimental phase of the project was terminated before this could be done.

Along with the testing program, we undertook a review of previous work on the strength and mechanical properties of sea ice [most notably, the extensive series of tests done **by Peyton** (1969)]. The objective was to combine these results with those of the field testing program to develop a stress-strain law and failure criterion for sea ice.

All of the experimental work done in the field is described in Section 2.2 including the equipment and procedures for the different types of field tests and the results of experimental measurements of the strength of sea ice in **uniaxial** compression at constant stress and constant stress rates. A discussion of the progress made toward the development of a stress-strain law and failure criterion for sea ice is then given in Section 2.3. Finally, the results of the laboratory measurements of the fracture toughness of sea ice and the work the strain transducer are described in Sections 2.3 and 2.4, respectively.

2.2 FIELD EXPERIMENTS ON THE MECHANICAL PROPERTIES OF SEA ICE

by

Lewis H. Shapiro, Ronald C. Metzner and Earl R. Hoskins*

ABSTRACT

The purpose of this project was to develop procedures for conducting field tests of the mechanical properties of sea ice. Stresses were **to** be applied in the plane of the ice sheet and the samples were to be large in comparison to those normally used in laboratory tests. Following this, tests were to be done to determine aspects of the reformational behavior of sea ice for comparison with the results of laboratory tests and for use in the development of a stress-strain law and failure criterion for sea ice in **uniaxial** compression.

Procedures for tests in **uniaxial** compression, direct shear and indirect tension were devised and a procedure for testing in biaxial compression was under development when field work for the project was terminated. **In** all the tests, the stresses were provided by **flatjacks** loaded by high-pressure gas through a pressure regulator. The system permits tests in both constant stress rate and constant stress to be conducted. Deformation was monitored by linear potentiometers mounted on pegs frozen into the surface of the samples.

Uniaxial compression tests were conducted on samples with dimensions of 30 x 30x 60 cm at constant stress rates from about 0.4 to 4×10^4 **kPa/sec** and in several temperature ranges. The results follow the same trend of increasing strength with loading rate as is found in constant strain rate tests. Based upon the peak strengths reached in tests of both types, the results suggest that there is no marked difference in strength between the samples tested in this program and the smaller samples usually used in laboratory testing programs.

The results of **uniaxial** compression tests at constant stress define a "transition" stress, below which there is a rapid increase in the time which a sample can sustain the applied stress without failure.

The trends in the results of tests to evaluate the effects of grain size and c-axis orientation on the **uniaxial** compressive strength of sea ice generally **agree** with the results of small-scale laboratory tests. However, the data acquired in this program suggest that it is possible for ice which shows an apparently strong c-axis orientation in thin section to be mechanically isotropic. This implies that there is a sharp limit to the intensity of c-axis orientation that is required in order for the ice to be mechanically **anisotropic**.

A short series of **uniaxial** compression tests was done to compare the strengths of first year and **multiyear** sea ice. The results indicate that there is little difference in strength over the range of temperatures and stress rates used in the experiments.

2.21..INTRODUCTION

The same basic approach was used in all of the tests done in the field for this program. The loading devices were **flatjacks** which were expanded under internal pressure to provide a known force. In some tests, the geometry of the resulting stress field was controlled by creating internal boundaries in the ice sheet using chain saw cuts as free surfaces; these cuts defined the geometry of the samples. In other tests, samples were removed from the ice sheet, shaped according to the type of test, replaced and then loaded. In either case, the ice sheet served as the loading frame.

The tests were done by controlling the load or loading rate on the sample, rather than the rate of deformation. This was a necessary choice, because the equipment required to load large samples under controlled rates of deformation (**large** hydraulic rams, pumps, an elaborate strain measuring system, automatic controls, etc.), and the personnel to operate that equipment, were too costly. Various loading paths were used in experiments to develop the test procedures. Constant loading rates or constant loads were used in the experiments to provide data to determine the strength and mechanical properties of the ice.

Sensors of various types were used to monitor displacements from which strains were calculated. Temperature and salinity measurements were made by conventional methods, although some preliminary work was required to determine the effect of the process of setting up the experiments on these parameters.

This section is devoted primarily to descriptions of the loading system and strain measurement procedures. The reader is referred to Shapiro et al. (1979) for a more complete discussion.

2.22 LOADING SYSTEM

2.22.1 FLATJACKS

In all the experiments, the loads were introduced into the ice sheet by **flatjacks**. These are simple devices which are inexpensive to construct, consisting only of an envelope of thin, sheet metal (or other suitable material) welded together along the edges. One or two nipples are installed along the edges of the envelopes. A fluid under pressure is introduced through one nipple to expand the **flatjack** and transmit a force to the surrounding ice. A pressure transducer can be attached to the other nipple to monitor the pressure in the **flatjack**. The envelope can be constructed in any suitable size and shape, depending upon the experiment to be done. During this program, experiments were done using square, rectangular and triangular **flatjacks** of various sizes. In addition, for the indirect tension test, the **flatjacks** were curved to provide a **load** over part of a cylindrical surface. In all cases, the **flatjacks** were thin enough to be inserted into a chain saw cut in the ice.

Loading is done by introducing a fluid under pressure into the envelope. The properties of the fluid are not important, although, of course, it must not freeze. The bulk of the experiments done on this program were loaded by high pressure nitrogen gas through a **pressure** regulator, although a few tests were done with hydraulic oil loaded through a hand-operated hydraulic pump.

2.22.2 LOAD TRANSMISSION AND FLATJACK EFFICIENCY

When under internal pressure, the **flatjacks** tend to expand, transmitting a force to the surrounding ice. If the expansion were uniform, and if the contact area between the **flatjack** and the ice remained constant, then the total force transmitted would simply be the product of the internal pressure and the **flatjack** area. However, the expansion of the **flatjacks** is not uniform because the edge welds prevent expansion near the margins of the envelope. Thus, the force transmitted is not the

simple product described above. Instead, it depends upon the ratio of the **flatjack** area to the edge length (**Deklotz** and **Boison**, 1970; Pratt et al., 1974), so that it is necessary to calibrate **flatjacks** of different sizes and shapes.

Calibration experiments were done only for the 30x 30 cm **flatjacks** used in the **uniaxial** compression testing program (Section 2.24) for which a knowledge of the stress magnitudes was required. No calibrations were done for **flatjacks** used in the experiments for developing techniques only.

Two separate calibration experiments were done. The first was described in Shapiro et al. (1979) and is illustrated in Figure 2.22-1. A block of ice 30 x 32 x 60 cm was prepared as if for a **uniaxial** test (as described in Section 2.24.1) with a double layer of polyethylene sheeting at its base and a 30 x 30 cm steel **flatjack** at each end. A 35 x 35 cm **flatjack** made of thin, sheet copper was installed in a chain saw cut parallel to, and midway between, the steel **flatjacks**, with its top edge at the surface of the ice. Chain saw cuts were then made to define the sides of the block as shown in the figure, forming two blocks, 30x 30x 32 cm which separated the copper **flatjack** from the steel **flatjacks**. The copper **flatjack** was then expanded slightly with hydraulic oil, sealed, and the pressure allowed to relax back to near zero. In this configuration, the full surface area of the steel **flatjacks**, and most of the surface area of the copper **flatjack**, were in contact with the test block, while most of the edge of the copper **flatjack** (with the exception of the edge at the surface) was outside the test block, but confined in the surrounding ice. In its expanded condition, the copper **flatjack** then acted as a pressure sensor to the load transmitted through the ice from the steel **flatjacks**.

The steel **flatjacks** were loaded at rates of about 14 **kPa/sec** (2 psi/sec) and the internal pressure of the copper **flatjack** was recorded. The results are shown in Figure 2.2-2; the data points were acquired at 10 second intervals.

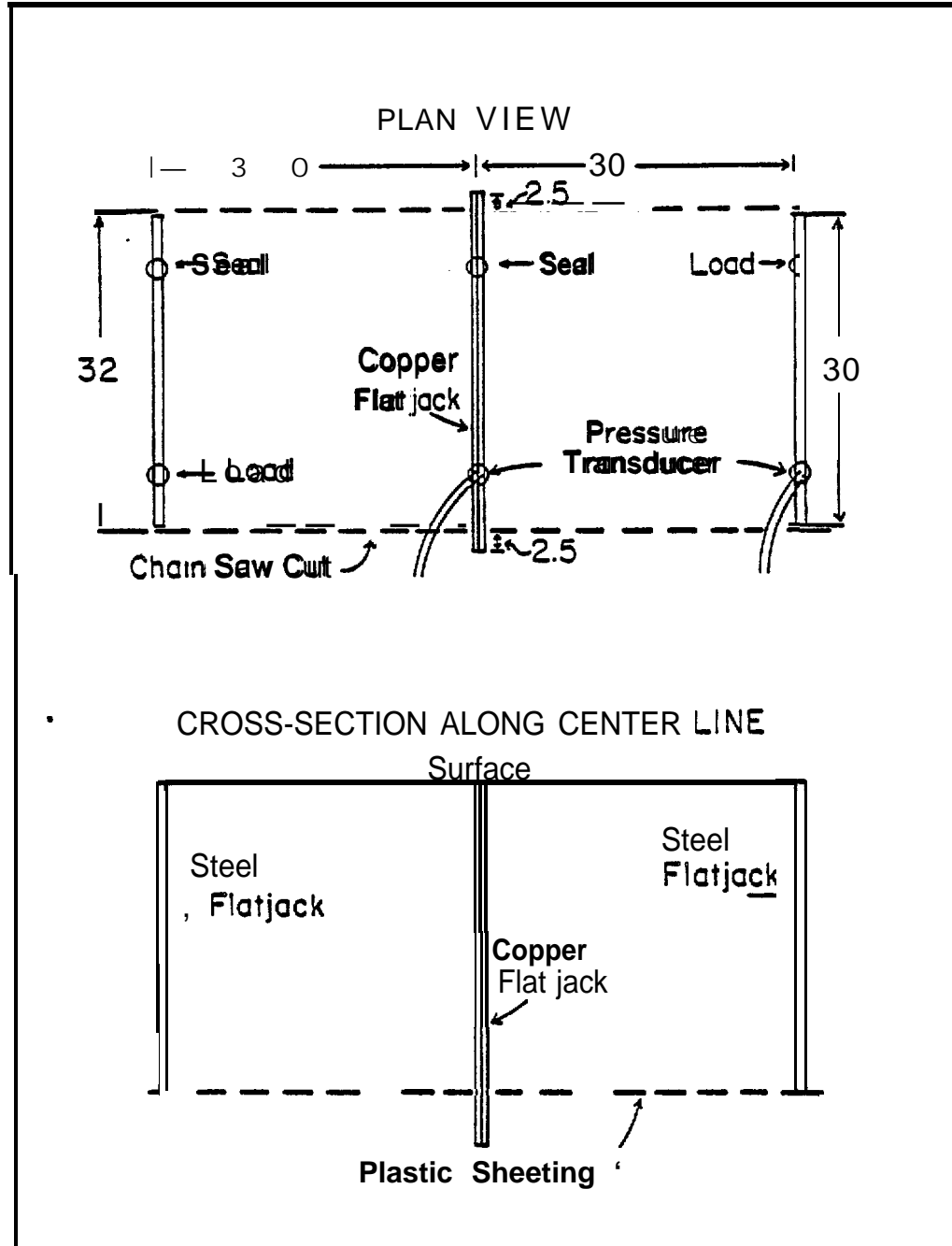


Figure 2.2-1 Plan view and cross-section of set-up for **flatjack** calibration experiment using copper **flatjack**. The dimensions are in cm.

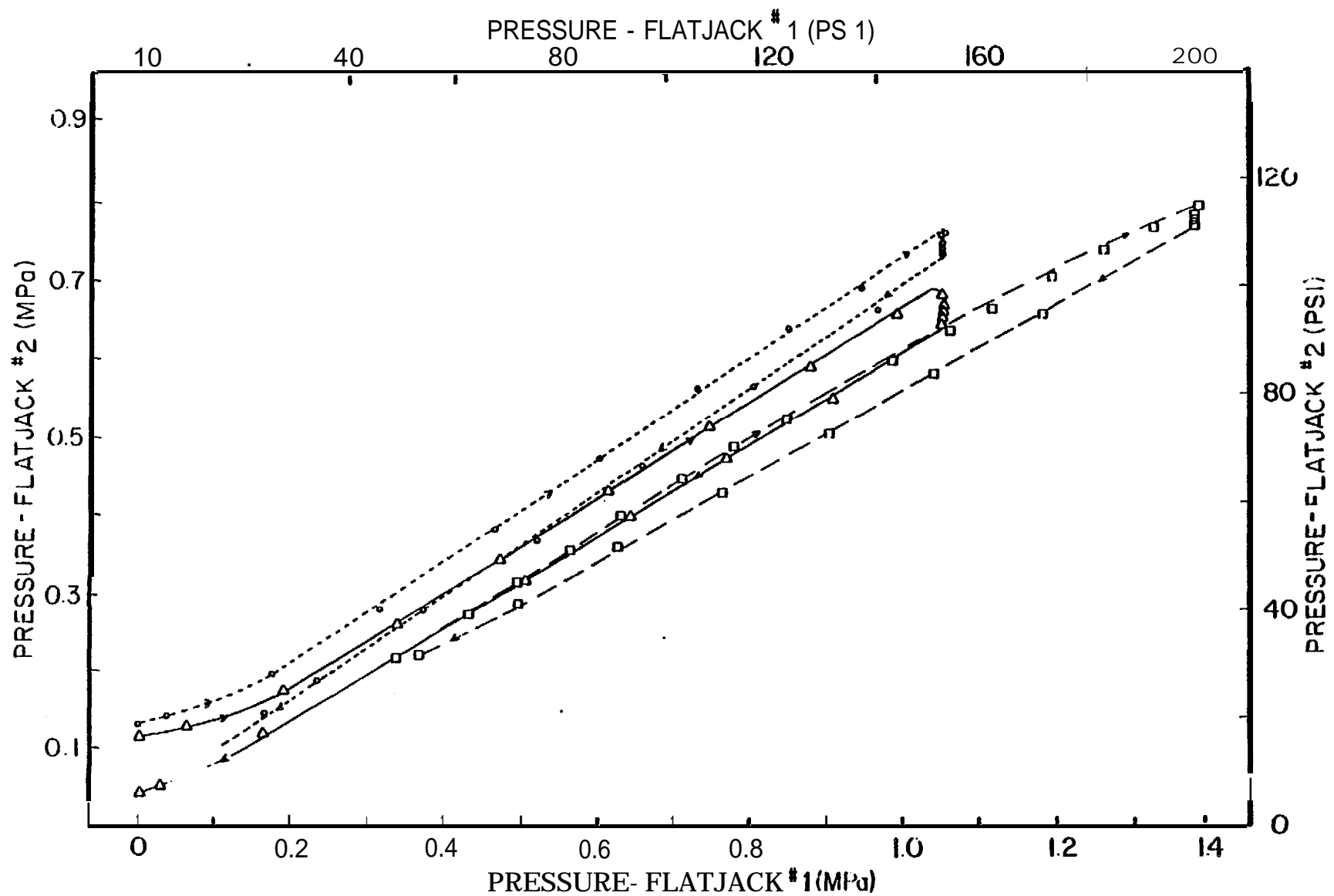


Figure 2,2-2 Results of calibration experiment. Flatjack #1 is the steel flatjack pair and flatjack #2 is the copper flatjack.

At the peak **load** the pressure in the steel **flatjacks** was held constant for about 1 minute, during which time the pressure in the copper **flatjack** drifted down. The drift may have been in response to the gradual closure of the copper **flatjack** as the fluid was squeezed toward the margins outside of the loaded surface. This was indicated by the formation of tension fractures at the tips of the copper **flatjack**.

The **efficiency** “e” of the steel **flatjacks** can be calculated from the equation

$$eP_s A_s = P_c A_c$$

where P_s and P_c are the internal pressures of the steel and copper **flatjacks**, A_s is the area of the steel **flatjacks** (30 x 30 cm) and A_c is the area of the copper **flatjack** which is in contact with the test block (30x 32 cm). Over the linear portions of the loading segments of the curves in Figure 2.2-2 the slopes average 0.63. Thus, using $P_c = 0.63P_s$, the efficiency “e” is found to be 67% for the range of pressures from about 0.2 MPa (30 psi) to 1.38 MPa (200 psi). This is in agreement with the efficiency determined by Deklotz and Boisen (1970) for **flatjacks** of this size.

The nature of the experimental set-up required that the calibration be done at relatively low stresses. This was necessary to assure that the fluid was not squeezed entirely out of the part of the copper **flatjack** which was in contact with the test block. If this occurred, the copper **flatjack** would no longer serve as a pressure sensor.

In order to extend the calibration to the higher loads reached in tests taken to failure of the ice, a second experiment was done using different equipment. The arrangement is shown in Figure 2.2-3. A load cell with a capacity of 1.03 GN (150,000 lbs) was placed in contact with the **flatjack** at one end of a **uniaxial** compression sample, through a spherical seat and a rigid plate with dimensions of 30 x 30 cm. The other end of the load cell was fixed to a reaction plate. The entire apparatus was enclosed in an aluminum box for ease of handling and emplacement.

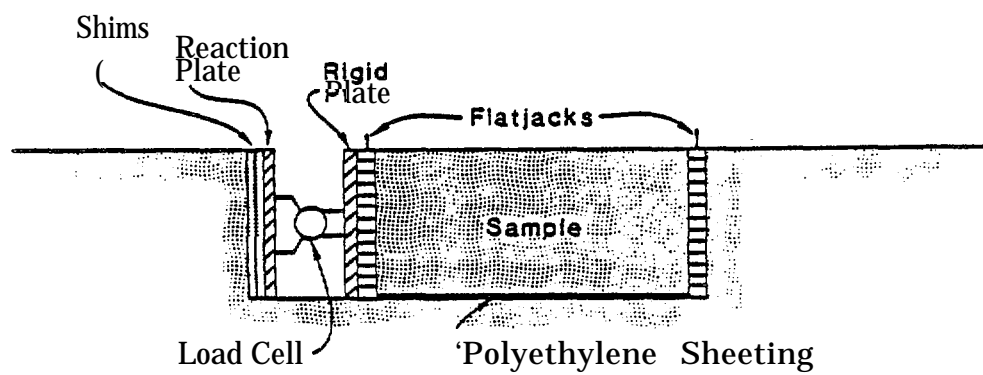


Figure 2.2-3 Cross-sectional view of the set-up for **the second flatjack** calibration experiment.

Once in position, the box was pressed **close** against the **flatjack** by shims driven between the reaction plate and the ice, so that the pressure exerted by the **flatjack** could be sensed by the load cell. The output from the load cell and the pressure transducer on the **flatjacks** was recorded on an X-Y recorder. The ratio between these values was the required measure of **flatjack efficiency**.

Experiments were done at several loading rates and the curves were generally repeatable. For **flatjack** pressures above about **1.38 MPa** (200 psi), the output stress of the **flatjacks** was found to be represented by the equations

$$\text{Output stress} = 0.875 (\text{flatjack pressure}) - 0.24$$

in units of MPa, or

$$\text{Output stress} = 0.875 (\text{flatjack pressure}) - 35$$

in psi. For lower **flatjack** pressures the curves were similar to those determined in the first experiment. The slopes of the curves between **0.35 MPa (50psi)** and **1.38 MPa** (200 psi) give an efficiency of approximately 70%, compared to the 67% determined for this range of **flatjack** pressures in the first experiment.

The **uniaxial** compression test set-up requires that a double **layer** of polyethylene sheeting be installed at the base of the sample to reduce the shear stress between the sample and the ice sheet. This stress component was measured during the second calibration experiment by loading the **flatjacks** separately and attributing the difference in efficiency between the two **flatjacks** to the shear stress transmitted across the base of the **sample**. The result was about 2% of the **flatjack** pressure, so that the shear stress can be considered to be negligible.

2.22.3 LOAD CONTROL

In all the experiments to determine **ice** properties, loading was done with **high-pressure** nitrogen gas from a pressurized gas bottle (initial pressure about **14 MPa** or **2000 psi**) controlled by a pressure regulator. **Flatjacks** at both ends of a test sample were loaded simultaneously and at the same rate. The load was controlled by

monitoring the pressure at the gas bottle while the pressure in the **flatjacks**, which was used for stress calculation, was monitored by a pressure transducer mounted on the **flatjacks**. Comparison of the pressures measured at both sites indicated that the pressure drop in the line between them was always less than 1%.

In creep tests (which are run at relatively low constant loads), the pressure regulators proved capable of maintaining the desired pressures to within about **5%** of the selected value for up to 12 hours. Thus, long-term tests could be run without the continuous presence of the experimenter

Creep-rupture tests (which require that a constant load be held until failure of the sample) were run using two different methods of load control depending upon the anticipated time to the inflection point in the strain-time curve. In creep-rupture tests at low loads, the time required to apply the load is negligible compared to the time to the minimum strain rate, so that the load was applied **by** a hand-operated pressure regulator. At higher loads, **the** loading time can be significant with respect to the time to the minimum strain rate, so that it must be applied rapidly. For tests at high loads, a gas bottle was used as an accumulator and loaded to the desired test pressure. Then, the gas was released rapidly through a ball valve, so that the only limitation on the rate of loading was the rate at which the gas could flow into the **flatjacks** under the bottle pressure. A valving system was used to maintain the load through the pressure regulator after the desired test pressure was reached.

Most of the constant loading rate tests were also controlled by a pressure regulator. In this case it was operated by hand to control the rate of application of the load; the operator simply watched the time and pressure indicators and adjusted the pressure regulator so that the pressure followed a selected path with time. Loading rates that were accurate and repeatable to within a few percent were easily achieved in this manner, although the actual stress rates varied because of variations in sample size. The problem is discussed in Section 2.24.2.

Constant loading rate tests at rates greater than 20 **MPA/sec** (about 3000 psi/sec) were also run by using a ball valve to release the gas directly from a bottle at high pressure into the **flatjacks**

Flatjacks provide a relatively inexpensive and efficient tool for introducing controlled stresses into an ice sheet. The details of their installation for specific tests are given in the appropriate sections below.

2.23 DEFORMATION MEASUREMENTS

Strain measurements presented particular problems in this program because only the surface of the ice sheet was exposed for the installation of strain measuring equipment. Restricting measurements to only one surface does not permit corrections to be made for bending of the sample due to misalignment of the loading surfaces. In the early stages of the field program, we attempted to overcome this problem by measuring strain using wire strain gages embedded in cylinders of ice to form "strain cells." The gages (either 2.5 cm or 1.25 cm **long**) were waterproofed and sealed with epoxy. They were then frozen into the centers of small cylinders prepared from fine chips of sea ice frozen together with water with a salinity of 6 parts per thousand. The cylinders (diameter 5 cm and length 10 cm) were then frozen into **holes** drilled in the ice samples with the strain gages oriented **parallel** to the sample axes to measure axial strain, or normal to the axis for measurement of lateral or vertical strain. The cylinders acted as inclusions of a relatively homogeneous material with properties similar to those of the surrounding normal sea ice. They deformed along with the sample when the load was applied. However, strain gages in the cylinders were in contact with many small, randomly oriented grains, so that the measured strain was not dominated by the deformation of a few **large** grains.

The strain gages prepared in this manner responded instantly to changes in load and generally provided repeatable results for small strains. However, the time required for preparation and installation of the gages made them impractical for use in a program involving a large number of tests. The technique could be useful in programs in which only a limited number of measurements are to be made, or when it is necessary to monitor the strain variation through the entire thickness of a sample or an ice sheet

An alternative method of monitoring strain was developed for use in the **uniaxial** compression testing program, because the data were needed for identifying the inflection point in creep-rupture tests. The method involved the use of linear potentiometers (**LP's**) attached to pegs frozen into the surface of the sample, so that, as explained above, the measurements could not be corrected for bending.

The depth to which the pegs can be sunk varies with the sample size because, if sunk too deeply, the pegs tend to reinforce the strength of the ice by restricting vertical expansion of the sample during loading. For the 30 cm thick samples used in the **uniaxial** testing program, experiments showed that the pegs had no effect on the strength if they were sunk to depths of 12 cm or less. Observations of samples during and after testing showed that no identifiable patterns of fractures were associated with the pegs.

The arrangement of the **LP's** for **uniaxial** tests (described in Section 2.24.1) is shown in Figure 2.2-4. The slide bars of the **LP's** were held **firmly** to a flat plate by springs, which left them free to rotate if the pegs rotated outward as the sample surface expanded vertically. The LP's were calibrated for displacements of 1 part in **10⁻⁵**, so that over the gauge length of 20 cm, strains on the order of **10⁻⁶** could be measured.

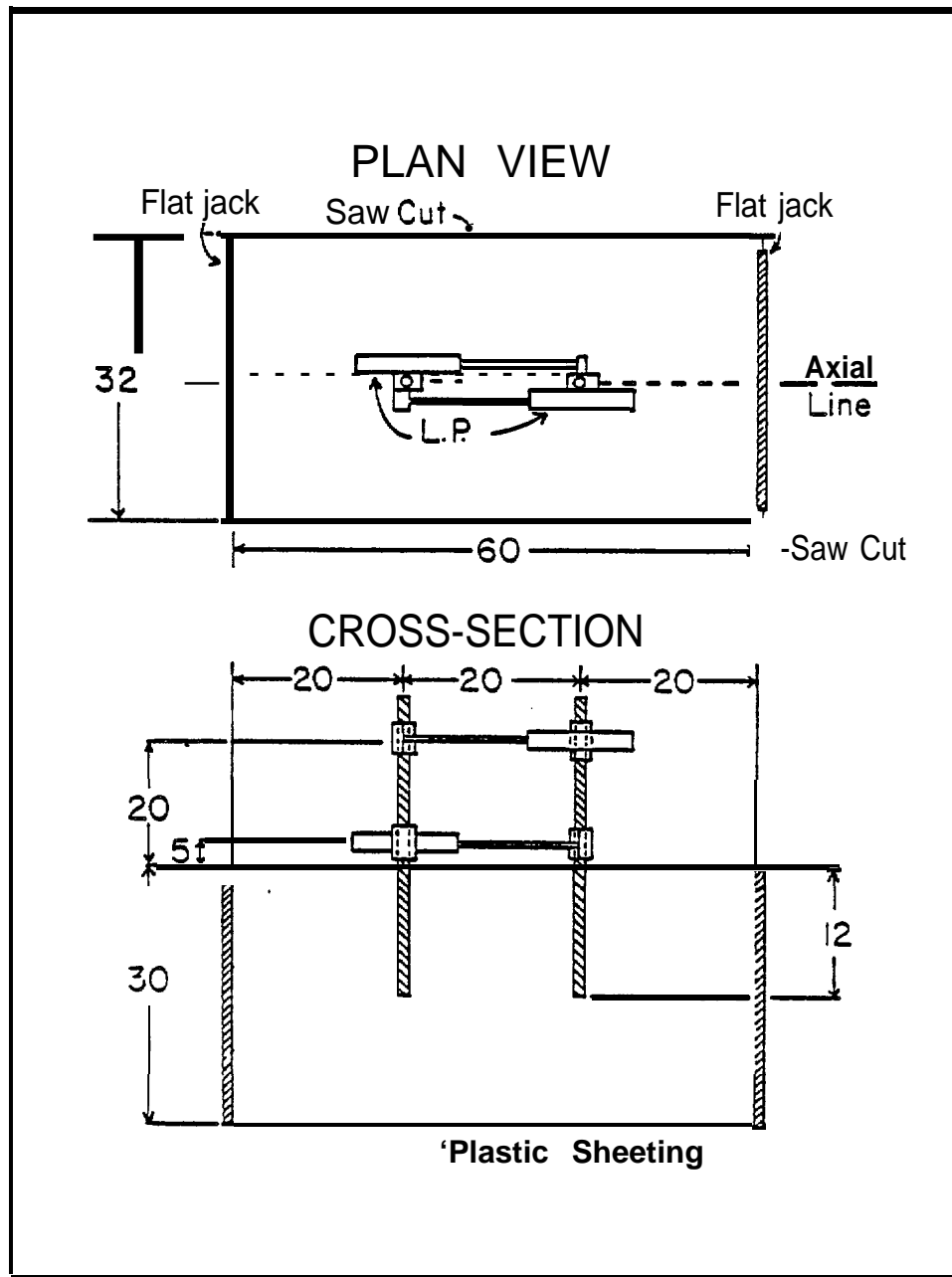


Figure 2.2-4 Set-up for a **uniaxial** compression test illustrating the placement of linear potentiometers on pegs frozen into the sample. Dimensions are in cm.

The geometric relations used in calculating the strain from displacement measurements are shown in Figure 2.2-5. The strain δ_d is calculated from the equation

$$\delta_d = \delta_l - [(a-d)/(b-a)](\delta_u - \delta_l)$$

where a and b are the heights from the ice surface of the **lower** and upper LP's respectively (5 and 20 cm in Figure 2.2-4), d is the depth at which the strain is calculated and δ_l and δ_u are the displacements of the lower and upper **LP's**. Note that this equation is derived on the assumption that the LP's remain horizontal during deformation. However, it can be shown that for small strains, only a minor correction is required to correct for peg rotation out of vertical as the surface of the sample bends upward. For simplicity, the correction was neglected.

The strain measuring system shown in Figure 2.2-4 proved to be easy to set-up in the field, and the instrumentation was **sufficiently** rugged to withstand repeated use.

2.24 UNIAXIAL COMPRESSION TESTS

2.24.1 SAMPLE PREPARATION

Uniaxial compression test procedures were developed using specimens in two geometries; triangular prisms and rectangular prisms. In the former, triangular **flatjacks** are installed in the ice as shown in Figure 2.25-6. After freezing, chain saw cuts are made connecting the ends of the **flatjacks** and dipping into the ice sheet parallel to the edges of the jacks. This isolates a triangular prism of ice which is attached to the ice sheet only through the **flatjacks** at the ends of the sample. The test is relatively easy to set up using flat-jacks of any size. However, it can be **difficult** to control the angle of the chain saw cuts to assure that the test specimen has smooth, straight sides. In addition, there are uncertainties in

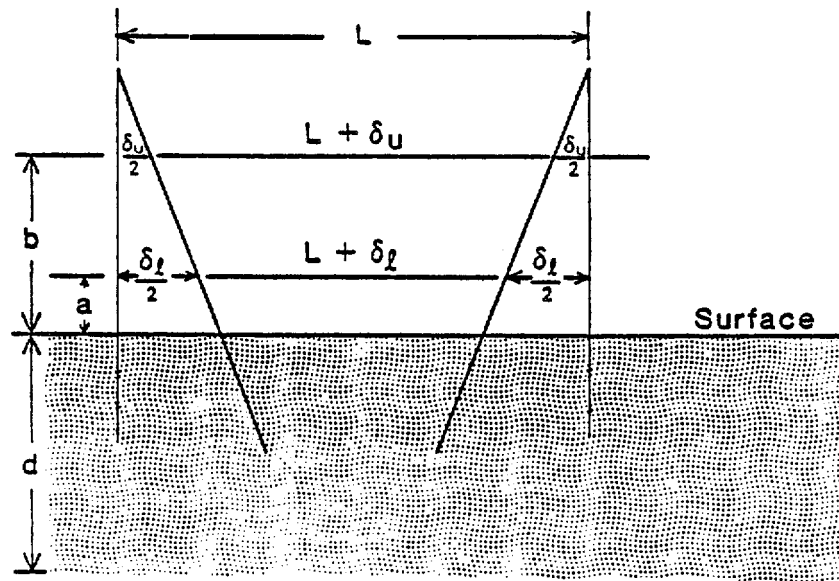


Figure 2.2-5 Geometric relationships between the pegs and linear potentiometers used for strain calculations. a and b are the heights of the **lower** and upper **LP's** respectively in Figure 2.2-4, and d is the depth at which the strain is calculated.

interpreting the results of the tests, because of the unusual geometry of the samples in relation to the ice fabric.

All of the data reported in the next section were done using test specimens in the form of rectangular prisms with dimensions of 30 x 32 x 60 cm. Most were collected from the surface of the ice sheet. Therefore, they included the slush layer, with a maximum thickness of **10-15** cm, consisting of **fine-grained** ice with random c-axis orientation. Most of the remainder of the samples was ice of the transition zone between the slush **layer** and the columnar ice zone below. In general, the ice in the transition zone shows a tendency to increase in grain size with depth and to take on the preferred orientation (if present) of the c-axes of the crystals of the columnar zone. In a few cases, the ice at the base of the samples (30 cm depth) might properly have been classified as part of the columnar zone, but the bulk of any particular sample was always in the slush layer and transition zone. For consistency, samples were always oriented along the dominant direction of c-axis orientation in the columnar zone.

The completed test set up is shown in Figure 2.2-7. To prepare it, samples about 40 cm wide were cut from the surface of the ice sheet and trimmed to a thickness of 30 cm and a length of 60 cm. Cutting was done with a chain saw and various methods were used to assure that the sample ends were parallel and at a right-angle to the base of the sample. This could not be done to the degree that would be expected in Laboratory tests. However, the results of experiments done under **similar** conditions were generally repeatable, indicating that variations between samples were relatively minor.

After a sample was removed from the ice sheet, the bottom of the hole from which it was taken was filled with fresh water leaving a depth of 30 cm. When the water was frozen, a double layer of plastic sheeting was placed at the bottom of the hole and the test block was replaced. The plastic sheeting provided a low friction

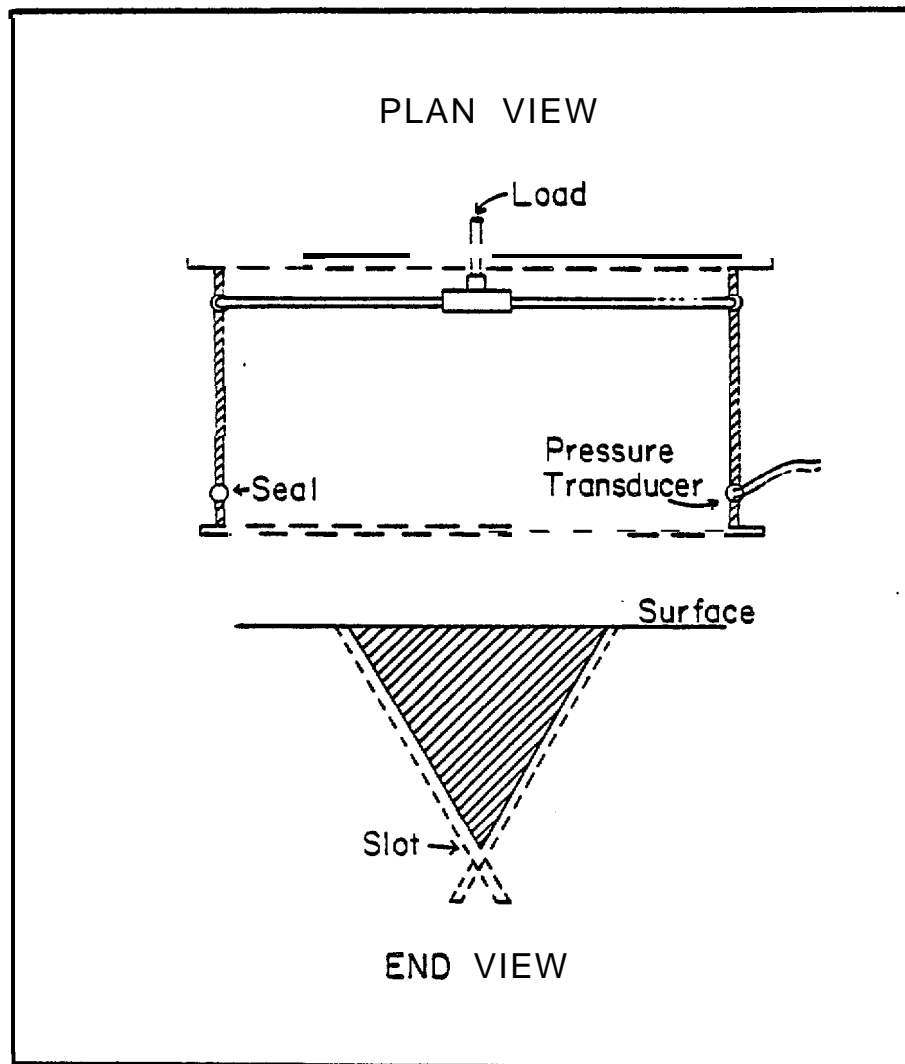


Figure 2.2-6 Plan and end views of uniaxial compression test set-up using triangular flatjacks.

boundary at the base of the test block, across which only minimal shear stress could be transmitted (see discussion of calibration in Section **2.22.2 above**). 30x30cm **flatjacks** were placed at the ends of the sample and fresh water was added to fill the void spaces around the test block and **flatjacks**. Pegs for attachment of LP's for strain measurement were then installed. The samples were then left for a minimum of several days to come to temperature equilibrium with the ice sheet (Shapiro and Hoskins, 1975) so that testing was done at the ambient temperature gradient.

2.24.2 TEST PROCEDURES

In order to conduct a test, the sides of the sample were cut loose from the surrounding ice sheet by removing thin slabs of ice with a chain saw. An allowance of about 1 cm was made on each side of the sample to provide clearance so that the **flatjacks** were not damaged by the chain saw during cutting. Thus, the final sample width was approximately 32 cm (the actual width of each sample was measured so that the cross-sectional area could be used for calculating the stress). Prepared in this manner, the sample was isolated from the ice sheet along the sides, free at the upper surface, and rested on a base across which friction was low. In most tests the **flatjacks** were also wrapped with double layers of plastic sheeting to reduce friction on the sample ends. On loading, the degree to which **uniaxial** compression was approximated depended upon the ease with which the sample could expand upward, particularly at the sample ends. Vertical expansion always occurred (except in tests at high rates of loading), but we were not able to measure it.

As noted in Section 2.22.3, the loading system was capable of controlling the rate of increase of internal **flatjack** pressure so that the curves of **flatjack** pressure vs. time were virtually identical for different tests at the same rates. However, the actual stress rates varied, because of the need to account for variations in width between samples for stress calculations. As an example, tests at a loading rate of 6.9

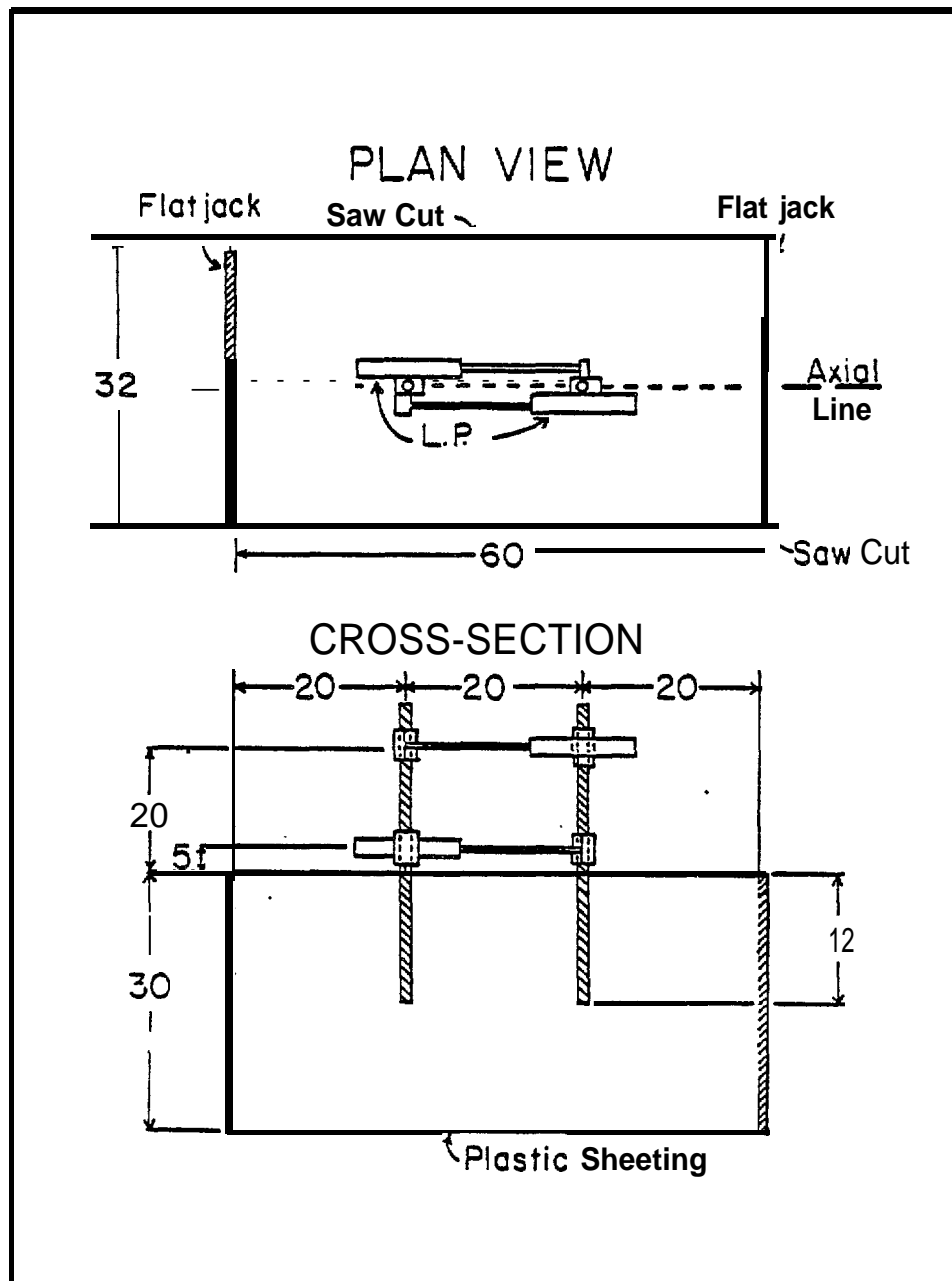


Figure 2.2-7 Set-up for a **uniaxial** compression test using a 30 x 30 x 60 cm test sample (same as Figure 2.2-4).

kPa/sec (1 psi/sec) for flat-jack pressure gave actual stress rates from about 4.9 to 5.3 **kPa/sec**.

The combined use of **flatjacks** to apply load and the ice sheet as a loading frame gives the effect of a "soft" testing machine, so that samples tend to fail explosively. However, it is not the release of strain energy stored in the ice sheet or the samples which causes failure in this manner. Instead, it results from the fact that as failure is approached the sample weakens and loses the capability to resist load. The deformation rate then increases rapidly, reducing the constraint on the **flatjacks**. This permits the **flatjacks** to expand rapidly with an accompanying stress drop. The operator must then increase the rate of gas flow in order to keep the stress-rate constant up to the point of failure. It was usual for the operator to have no more than one or two seconds of warning that the **sample** was about to fail. **If** it was not possible to stop the flow of gas and release the internal **flatjack** pressure within that time, the **flatjacks** would expand rapidly and fail explosively, shattering the sample. Thus, examination of samples for indications of the failure mechanisms was generally not possible, other than in a few cases in which pressure was released quickly enough to save the sample. However, in tests at very high loading rates the samples generally failed along a few (or one) long cracks which traversed the sample, with only minor shattering at the sample ends. Observations of failure mechanisms are given in Section 2.24.62.

2.24.3 TEMPERATURE AND SALINITY MEASUREMENTS

The large number of tests run made it impractical to measure the temperature profile of each sample at the time it was tested. Instead, a **thermister** string (with thermistors at the surface and at depths of 10,20 and 30 cm) was installed at a central location within the test area. The ice surface at its location was regularly

cleared of snow to simulate test conditions. The readings from these thermistors at the time a test was run were averaged to give the test temperature.

Salinities were determined by collecting a column of ice 5 x 5 x 30 cm deep adjacent to each sample at the completion of a test. Each column was cut into 5 cm cubes and the salinity was determined for each cube. The results were then averaged to give an average salinity for the sample. The validity of the method was checked by dividing one sample block into columns as described above, and determining the range of salinities of these. The result showed that the salinity variation between the columns within the single test sample was greater than that between the representative columns for the individual test blocks through the entire field season, indicating that the method was appropriate.

2.24.4 ACOUSTIC EMISSIONS

We conducted a short pilot program of monitoring rates of acoustic emissions indicating sample cracking. The intent was to use simple, available equipment for a feasibility study to determine whether usable data on fracture rates could be obtained during field testing. If so, the tests were to regularly include such measurements to provide additional data for interpretation of failure mechanisms. The results were promising, but the project was terminated before the equipment could be upgraded to provide data of the required quality.

For the pilot program, no attempt was made to determine the sensitivity of the equipment to small cracking events. However, the system certainly recorded events which were inaudible to an observer standing near the test samples.

The data were taken by freezing a piezoelectric crystal to the surface of a test sample, and recording its output on a strip chart recorder. An event counter would have been more desirable for the purpose, but we were unable to acquire one because of budget limitations. The strip chart recorder was adequate for discriminating

individual events at low rates of cracking. Each event was recorded as a peak on the output chart. However, the rate at which the pen recovered toward zero after each event was slow compared to the time between events, so that it seldom reached the zero line before the next event occurred. As a result, the pen migrated across the chart and eventually became pinned (usually at 50 to 60% of peak load) so that individual events could **no** longer be discriminated.

The results suggest that, given proper recording equipment, measuring acoustic emission rates on samples in the field is no more difficult than doing so in the laboratory (as described, for example, by St. Lawrence and Cole, 1982).

2.24.5 RESULTS OF EXPERIMENTS IN UNIAxIAL COMPRESSION

The results of all experiments in **uniaxial** compression **on** rectangular prisms are presented in Tables 2.2-1 to 10. Samples were first year ice, except for those listed in Table 2.2-5. The reported values of strength or applied stress were calculated from the measured **flatjack** pressures using the equation

$$\sigma_c = (P \times A_f)/(A_s)$$

where P is the output stress of the **flatjack** as determined from the calibration equation (Section 2.22.1), **A_f** is the area of the **flatjack** and **A_s** is the cross-sectional area of the sample. Stress rates were calculated as the strength divided by the **time-** to failure. The **values** should be close to the true loading rates because, as noted in Section 2.22.4, loading curves were generally **linear** and repeatable. The methods of measuring the average temperature and salinity for each sample were given in Section 2.24.3. The average brine volume (**v_{ave}**) was calculated from the equation

$$v_{ave} = S_{ave} (0.532 - 49.15/T_{ave})$$

where S_{ave} and T_{ave} are the average salinity and temperature.

Note that the time measurements in the tables are given in different degrees of precision for different tests. The variation reflects the fact that different methods were used, depending upon the expected duration of a particular test.

Procedures used in setting up individual tests varied through the first year of the program as new materials or methods were introduced. These are described in the keys to the column labeled "Set-up" in Tables 2.2-1 to 3; the key is given at the end of Table 2.2-3. In subsequent field seasons all tests were done with the set-ups described in either note 4 or 6 of the key.

The comments in the tables record particular features of some of the tests. As an example, after some creep tests, the sample was allowed to relax for some time, and then loaded as a constant loading rate test. The purpose was to attempt to evaluate the effect of possible strain softening (or hardening) during creep. However, the results were inconsistent. Similarly, if one **flatjack** on a sample failed (**by** splitting along one edge) before the sample failed, the test was usually completed with the one remaining **flatjack**. The results of these tests are presented here for the sake of completeness; none are used in the discussion of the results (Section 2.25.6).

The presence of thin silt layers (which were of various thicknesses, depths and lateral extent) in the samples is also noted in the comments. These were always associated with layers of **fine-grained** ice which served to break the smooth downward transition from slush ice to columnar ice. The presence of silt layers had the apparent effect of increasing the strength of the samples by up to (about) 20% over silt-free samples tested under the same conditions. There are not enough examples to permit any relationships to be established between the distribution and thickness of the silt layers and the specific increase in strength. Hence, the data are not included in the discussion in Section 2.25.6.

TABLE 2.2-1
RESULTS OF CONSTANT LOADING-RATE TESTS IN
UNIAXIAL COMPRESSION - 1978

| Sample Number | Peak Stress (MPa) | Time to Peak Stress (sec.) | Stress Rate (kPa/sec.) | Average Temp. (°C) | Average Brine Volume \bar{V}_v (ppt) | Set-up (see key after Table 2.2-3) | Comments |
|---------------|-------------------|----------------------------|------------------------|--------------------|--|------------------------------------|--|
| 1 | 3.90 | 25.0 | 156 | 14.9 | 5.13 | 1 | |
| 2 | 2.17 | 1.4 | 1550 | 6.5 | 7.50 | 1 | |
| 8 | 2.22 | 420 | 5.29 | 9.8 | 6.37 | 1 | Silt 8-12 cm |
| 10 | 3.56 | 65.0 | 54.8 | 9.6 | 6.26 | 1 | |
| 15 | 2.07 | 390 | 5.31 | 11.5 | 5.74 | 1 | |
| 16 | 3.95 | 2.5 | 1580 | | | 1 | |
| 17 | 3.68 | 3.0 | 1230 | | | 1 | |
| 18 | 2.95 | 575 | 5.13 | 11.5 | 5.92 | 1 | Break in loading curve at 2.46 MPa, 480 sec. |
| 20 | 3.56 | 2.6 | 1370 | 10.3 | 5.92 | 1 | |
| 21 | 3.68 | 6.8 | 540 | 10.3 | 6.02 | 1 | |
| 22 | 3.68 | 82.5 | 44.5 | 10.0 | 5.73 | 1 | |
| 23 | 3.04 | 116 | 26.2 | 10.3 | 6.05 | 1 | |
| 24 | 3.40 | 21.8 | 156 | 10.3 | 6.01 | 1 | |
| 25 | 1.70 | 4200 | 0.41 | | | 1 | |
| 26 | 3.65 | 6.4 | 570 | 11.5 | 5.71 | 1 | |
| 27 | 3.40 | 24.8 | 137 | 10.3 | 5.94 | 1 | |
| 28 | 3.95 | 1.0 | 3950 | | | 1 | |
| 29 | 3.00 | 0.072 | 4.17 x 10 ⁴ | 13.2 | 5.26 | 1 | |
| 30 | 3.10 | 0.4 | 7760 | 12.4 | 5.68 | 1 | |
| 31 | 4.21 | 7.5 | 562 | 11.5 | 5.66 | 1 | |
| 32 | 4.29 | 0.48 | 8930 | 13.2 | 5.29 | 1 | |
| 33 | 3.79 | 0.11 | 3.45 x 10 ⁴ | 13.1 | 5.46 | 1 | |
| 34 | 3.45 | 0.15 | 2.30 x 10 ⁴ | 14.0 | 5.29 | 1 | |

TABLE 2.2-1 (Cont'd)

| Sample Number | Peak Stress (MPa) | Time to Peak Stress (sec.) | Stress Rate (kPa/sec.) | Average Temp. (°C) | Average Brine Volume \sqrt{V} (ppt) | Set-up (see key after Table 2.2-3) | Comments |
|---------------|-------------------|----------------------------|------------------------|--------------------|---------------------------------------|------------------------------------|---|
| 36 | 4.01 | 20 | 201 | 19.8 | 4.49 | 2 | 2nd loading after rupture of one flatjack at low stress |
| 37 | 3.00 | 578 | 5.19 | 19.8 | 4.51 | 2 | |
| 39 | 5.07 | 0.18 | 2.82 x 10 ⁴ | 19.4 | 4.44 | 2 | |
| 40 | 3.95 | 0.14 | 2.82 x 10 ⁴ | 19.4 | 4.42 | 2 | |
| 43 | 4.62 | 0.16 | 2.89 x 10 ⁴ | 12.7 | 5.30 | 6 | |
| 47 | 3.58 | 677 | 5.29 | 14.3 | 5.39 | 6 | Previous creep test at 0.61 MPa for 24 hrs. |
| 48 | 2.33 | 5476 | 0.43 | | | 6 | Previous creep test at 0.62 MPa for 18 hrs. |
| 50 | 4.66 | 1.50 | 31.1 | 18.8 | 4.71 | 6 | Previous creep test at 0.81 MPa for 20 hrs. |
| 55 | 1.92 | 387 | 4.97 | 7.4 | 6.96 | 6 | |
| 61 | 2.59 | 514 | 5.04 | 18.4 | 4.55 | 6 | |
| 62 | 1.72 | 360 | 4.91 | 6.5 | 7.31 | 4 | 1Rotated 90° |
| 63 | 1.83 | 374 | 4.89 | 7.1 | 7.17 | 4 | |
| 64 | 2.59 | 102 | 25.4 | 6.5 | 7.31 | 4 | 1Rotated 90° |
| 65 | 1.87 | 385 | 4.85 | 7.0 | 7.13 | 4 | |
| 68 | 1.94 | 405 | 4.78 | 10.5 | 6.15 | 6 | 2Composite block, lower halves |
| 69 | 2.24 | 463 | 4.84 | 9.9 | 6.24 | 6 | 2Composite block, upper halves |

TABLE 2.2-1 (Cent'd)

| Sample Number | Peak Stress (MPa) | Time to Peak Stress (sec.) | Stress Rate (kPa/sec.) | Average Temp. (-°C) | Average Brine Volume \sqrt{v} (ppt) | Set-up (see key after Table 2.2-3) | Comments |
|---------------|-------------------|----------------------------|------------------------|---------------------|---------------------------------------|------------------------------------|--|
| 70 | 2.45 | 489 | 5.01 | 9.8 | 6.20 | 6 | 2Composite block, upper halves |
| 71 | 1.87 | 385 | 4.85 | 9.9 | 6.24 | 6 | 2Composite block, lower halves |
| 77 | 1.41 | 3333 | 0.422 | 9.5 | 6.20 | | |
| 79 | 1.90 | 390 | 4.86 | 8.8 | 6.38 | | |
| 86 | 2.32 | 463 | 5.00 | 8.4 | 6.58 | 6 | Silt zone 7.5-23 cm |
| 87 | 1.87 | 376 | 4.97 | 8.3 | 6.55 | 6 | |
| 88 | 1.85 | 373 | 4.97 | 8.1 | 6.48 | | |
| 90 | 1.88 | 385 | 4.89 | 8.3 | 6.58 | | |
| 91 | 2.54 | 48.8 | 52.0 | 7.9 | 6.77 | | |
| 93 | 2.07 | 418 | 4.95 | 8.1 | 6.95 | | |
| 94 | 2.11 | 424 | 4.98 | 8.3 | 6.76 | 6 | Silt zone 5-20 cm |
| 95 | 1.90 | 384 | 4.96 | 8.1 | 6.41 | 6 | |
| 98 | 1.81 | 372 | 4.86 | 7.0 | 7.23 | 6 | Tested 3 min. after unloading constant load test at 0.33 MPa for 55,800 sec.; minimum strain rate at 39,900 sec. |

TABLE 2.2-1 (Cent'd)

| Sample Number | Peak Stress (MPa) | Time to Peak Stress (sec.) | Stress Rate (kPa/sec.) | Average Temp. (-°C) | Average Brine Volume \bar{V}_v (ppt) | Set-up (see key after Table 2.2-3) | Comments |
|---------------|-------------------|----------------------------|------------------------|---------------------|--|------------------------------------|--|
| 103 | 2.36 | 48.0 | 49.1 | 5.9 | 7.43 | 6 | |
| 104 | 2.12 | 15.3 | 138 | 6.9 | 7.74 | 6 | |
| 108 | 1.86 | 378 | 4.93 | 5.6 | 7.72 | 6 | Previous tree-rupture test at 0.33 MPa for 58,800 sec.; minimum strain-rate at 40,200 sec. |
| 109 | 2.47 | 15.0 | 165 | 6.0 | 7.69 | 6 | |
| 110 | 2.90 | 5.0 | 579 | 7.7 | 6.42 | 6 | Thin silt band at 15 cm |
| 111 | 2.56 | 3.5 | 733 | 7.0 | 6.90 | 6 | |
| 112 | 2.27 | 85.0 | 26.7 | 7.0 | 7.05 | 6 | |
| 113 | 2.32 | 1.5 | 1540 | 6.9 | 7.15 | 6 | |
| 114 | 2.01 | 1.5 | 1340 | | | 6 | |
| 115 | 2.73 | 1.4 | 1950 | | | 6 | |
| 116 | 2.34 | 1.4 | 1670 | | | 6 | Silt band 10-20 cm |
| 117 | 2.23 | 4.5 | 495 | 7.2 | 6.93 | 6 | |
| 118-1 | 2.52 | 500 | 5.03 | | | 6 | 1st loading, one flatjack failed |
| 118-2 | 3.89 | 85.0 | 45.8 | | | 6 | 2nd loading, with one remaining flatjack |
| 119 | 4.54 | 109 | 41.7 | | | 6 | |

1. Sample rotated 90° about long axis.

2. Composite samples prepared by freezing together the top 15 cm (slush ice zone) and the bottom 15 cm (transition zone) of two samples to form composite samples of both zones.

TABLE 2.2-2

RESULTS OF CREEP-RUPTURE TESTS IN
UNIAXIAL COMPRESSION -1978.

| Sample Number | Stress (MPa) | Time to Min. Strain rate (sec) | Time to Rupture (sec) | Strain at Minimum Strain rate | Minimum Strain rate | Average Temp (-°C) | Average Brine Vol. \sqrt{v} (ppt) | Set-up (see key after Table 2.2-3) | Comments |
|---------------|--------------|--------------------------------|-----------------------|-------------------------------|----------------------|--------------------|-------------------------------------|------------------------------------|--|
| 5 | 1.11 | | 590 | | | 10.4 | 6.76 | 1 | |
| 9 | 1.66 | | 40 | | | 9.8 | 6.34 | 1 | |
| 11 | 3.34 | | 3.8 | | | 9.6 | 6.32 | 1 | Silt 5-15 cm |
| 14 | 3.01 | | 10 | | | 11.5 | 6.72 | 1 | |
| 19 | 1.90 | | 70 | | | 11.5 | 6.85 | 1 | |
| 35 | 1.45 | | 900 | | | 10.0 | | 2 | |
| 38 | 1.45 | | 820 | | | 17.3 | 4.79 | 2 | |
| 42 | 2.34 | 20 | 230 | 1.6×10^{-3} | 3.2×10^{-5} | 18.4 | | 6 | |
| 44 | 2.94 | | 55 | | | 18.6 | | 6 | |
| 46 | 0.89 | 9070 | >18,000 | 3.9×10^{-3} | 8.4×10^{-7} | 16.0 | 4.96 | 6 | |
| 49 | 2.34 | | 1080 | | | 18.4 | 4.60 | 6 | |
| | | 20 | 170 | 1.4×10^{-3} | 1.6×10^{-5} | 20.5 | 4.43 | 6 | Silt 10-22 cm, previous creep test, 0.2 MPa for 58,900 sec. |
| 52 | 1.23 | 410 | 1085 | 2.0×10^{-3} | 3.7×10^{-6} | 20.0 | 4.49 | 6 | |
| 53 | 1.17 | | 6960 | | | 20.0 | 4.52 | 9 | |
| 58 | 1.55 | 264 | 735 | 3.4×10^{-3} | 1.3×10^{-5} | 16.0 | 4.92 | 6 | |
| | | 50 | 400 | 2.2×10^{-3} | 1.6×10^{-5} | 18.9 | 4.41 | 6 | Silt 10-22 cm, previous creep test, 0.66 MPa for 27,000 sec. |

TABLE 2.2-2 (Cont'd)

| Sample Number | Stress (MPa) | Time to Min. Strain rate (sec) | Time to Rupture (sec) | Strain at Minimum Strain rate | Minimum Strain rate | Average Temp (-°C) | Average Brine Vol. Vv (ppt) | Set-up (see key after Tab 2.2-3) | Comments |
|---------------|--------------|--------------------------------|-----------------------|-------------------------------|------------------------|--------------------|-----------------------------|----------------------------------|----------------|
| 60 | 2.62 | 10 | 100 | 1.1 x 10 ⁻³ | 4.1 x 10 ⁻⁵ | 18.0 | 4.73 | 6 | |
| 66 | 1.72 | | 86 | | | 7.6 | 6.76 | 6 | |
| 67 | 1.72 | 13 | 53 | 1.8 x 10 ⁻³ | 1.1 x 10 ⁻⁴ | 7.3 | 6.73 | 6 | |
| 72 " | 1.45 | 20 | 140 | 1.8 x 10 ⁻³ | 3.1 x 10 ⁻⁵ | 7.1 | 7.26 | 6 | |
| 73 | 1.45 | 10 | 130 | 9.2 X 10 ⁻⁴ | 4.3 x 10 ⁻⁵ | 7.2 | 6.95 | 6 | |
| 76 | 1.40 | 30 | 245 | 1.5 x 10 ⁻³ | 7.4 x 10 ⁻⁶ | 9.1 | 6.47 | 6 | |
| 78 | 1.61 | 50 | 175 | 2.1 x 10 ⁻³ | 2.6 x 10 ⁻⁵ | 8.8 | 6.35 | 6 | |
| 81 | 1.17 | 440 | 1240 | 5.5 x 10 ⁻³ | 1.7 x 10 ⁻⁵ | 11.1 | 6.00 | 6 | |
| 82 | 1.19 | | 683 | | | 10.8 | 6.18 | 6 | |
| 83 | 1.33 | 130 | >305 | 4.2 X 10 ⁻³ | 4.2 x 10 ⁻⁵ | 7.5 | 6.90 | 6 | |
| 92 | 1.04 | 260 | 716 | 4.5 x 10 ⁻³ | 1.7X 10 ⁻⁵ | 7.3 | 7.16 | 6 | Silt, 10-20 cm |
| 96 | 2.01 | 10 | 37 | 1.2103 | 5.0 x 10 ⁻⁵ | 5.5 | 7.78 | 6 | Silt, 5-17 cm |
| 97 | 1.62 | 46 | 174 | 1.8 X 10 ⁻³ | 2.8 x 10 ⁻⁶ | 7.0 | 7.37 | 6 | |
| 98 | 0.33 | 34900 | >55600 | 8.5 x 10 ⁻⁴ | 8.1 x 10 ⁻⁹ | 7.0 | 7.25 | 6 | |
| 99 | 0.85 | 480 | 3127 | 2.7 x 10 ⁻³ | 3.3 x 10 ⁻⁷ | 6.9 | 7.14 | 6 | |
| 100 | 1.87 | 15 | 49 | 1.4 x 10 ⁻³ | 9.6 x 10 ⁻⁵ | 6.5 | 7.36 | | |
| 108 | 0.33 | 40200 | >58800 | 4.1 x 10 ⁻⁴ | 1.7 x 10 ⁻⁸ | 6.5 | 7.74 | 6 | |

TABLE 2.2-3
RESULTS OF CREEP TESTS IN UNIAXIAL
COMPRESSION -1978.

| Sample Number | Stress (MPa) | Strain rate (sec ⁻¹) | Test Duration (see) | Average Temp (-°C) | Average Brine Volume \sqrt{V} (ppt) | Set-up (see key below) | Comments |
|---------------|--------------|----------------------------------|---------------------|--------------------|---------------------------------------|------------------------|--------------------|
| 3 | 0.41 | | 66,600 | 13.6 | 5.5 | 1 | |
| 41 | 0.67 | 9.06×10^{-8} | 63,000 | 10.0 | | 6 | |
| 47 | 0.48 | 9.69×10^{-9} | 81,900 | 14.3 | 5.39 | 6 | |
| 48 | 0.49 | 1.11×10^{-8} | 60,320 | 18.5 | | 6 | |
| 50 | 0.67 | 1.64×10^{-8} | 64,800 | 18.1 | 4.71 | 6 | |
| 51 | 0.22 | 5.99×10^{-9} | 58,900 | 19.0 | 4.43 | 6 | Silt zone 10-18 cm |
| 53 | 0.12 | | 40,000 | 19.9 | 4.50 | | |
| 54 | 0.33 | | 36,000 | 18.0 | | 6 | |
| 57 | 0.43 | 5.25×10^{-8} | 90,600 | 13.0 | 5.30 | 6 | |
| 59 | 0.66 | | 27,000 | 18.9 | 4.40 | 6 | |
| 74 | 0.10 | 6.56×10^{-9} | 127,800 | 10.9 | 6.17 | 6 | |
| 75 | 0.28 | 1.42×10^{-8} | 91,100 | 9.2 | 6.38 | 6 | |
| 80 | 0.67 | 2.35×10^{-7} | 37,000 | 10.7 | 6.12 | 6 | |

Set-up Key:

1. No plastic sheeting on flatjacks; wooden pegs, 1.3 cm diameter, 20 cm deep.
2. Plastic sheeting on flatjacks; wooden pegs 10 cm deep.
3. Plastic sheeting on flatjacks; aluminum pegs 1.3 cm diameter, 20 cm deep.
4. Plastic sheeting on flatjacks; no pegs.
5. No plastic sheeting on flatjacks; aluminum pegs 12 cm deep.
6. Plastic sheeting on flatjacks; aluminum pegs 12 cm deep.

TABLE 2.2-4
RESULTS OF CONSTANT LOADING-RATE TESTS
IN UNIAxIAL COMPRESSION -1979.

| Sample Number | Peak stress (MPa) | Time to peak stress (sec) | Average stress rate (kPa/sec) | Average temp. (°C) | Average Bragg Volume \sqrt{V} (ppt) | Comments |
|---------------|-------------------|---------------------------|-------------------------------|--------------------|---------------------------------------|---|
| 1 | 3.28 | 645 | 5.08 | 23.9 | 3.69 | |
| 2 | 3.72 | 711 | 5.24 | 23.8 | 3.86 | |
| 3 | 5.45 | 0.9 | 6060 | 20.8 | 3.96 | 1 Flatjack |
| 5 | 5.69 | 1.3 | 4380 | 20.4 | 3.78 | |
| 6 | 3.34 | 671 | 4.98 | 18.0 | 4.21 | Previous creep-rupture test at 0.90 MPa, minimum strain-rate at 14,640 sec. |
| 7 | 5.40 | 22.8 | 237 | 19.3 | 3.86 | |
| 8 | 6.05 | 24.0 | 252 | 18.9 | 3.97 | Previous creep test at 0.96 MPa for 75,300 sec. |
| 9 | 5.89 | 0.33 | 17800 | 18.5 | 4.12 | |
| 10 | 6.26 | 1.73 | 3620 | 19.0 | | |
| 11 | 4.67 | 99 | 47.2 | 17.9 | 4.32 | |
| 12 | 4.56 | 96 | 47.5 | 18.5 | 4.18 | |
| 15 | 6.18 | 25 | 251.0 | 18.3 | 4.22 | Previous creep test at 0.62 MPa for 47,800 sec. |
| 16 | 3.24 | 600 | 5.4 | 17.9 | 4.30 | Previous creep test at 0.68 MPa for 51,300 sec. |
| 28 | 6.68 | 0.48 | 13900 | 16.1 | 4.38 | |
| 30 | 4.63 | 84 | 55.2 | 15.9 | 4.56 | |
| 35 | 6.21 | 24 | 259 | 18.4 | 3.98 | |
| 36 | 3.51 | 664 | 5.29 | 18.4 | 3.98 | |
| 42 | 4.46 | 19 | 235 | 12.3 | 4.77 | |

TABLE 2.2.4 (Cont'd)

| Sample Number | Peak stress (MPa) | Time to peak stress (sec) | Average stress rate (kPa/sec) | Average temp. (-°C) | Average Brine Volume \sqrt{v} (ppt) | Comments |
|---------------|-------------------|---------------------------|-------------------------------|---------------------|---------------------------------------|--|
| 43 | 2.87 | 550 | 5.22 | 11.8 | 4.82 | |
| 44 | 4.21 | 15 | 274 | 12.5 | 4.78 | |
| 46 | 2.61 | 495 | 5.28 | 6.0 | 6.82 | |
| 47 | 3.16 | 61 | 51.9 | 5.5 | 6.99 | |
| 48 | 2.11 | 420 | 5.02 | 4.8 | 7.40 | |
| 50 | 1.74 | 4350 | 0.40 | 6.0 | 6.74 | Previous creep test at .36 MPa for 28,000 sec. |
| 60 | 3.92 | 72 | 54.4 | 5.9 | 6.76 | Low (?); -gas ran out during test |
| 61 | 4.20 | 16 | 262 | 3.8 | 8.76 | |
| 62 | 4.27 | 17 | 251 | 3.3 | 9.31 | |
| 63 | 2.25 | 0.15 | 15000 | 2.7 | 10.02 | Low; peak stress not recorded |
| 64 | 3.98 | 0.40 | 9950 | 3.0 | 9.50 | |
| 65 | 4.37 | 0.40 | 10900 | 2.5 | 10.15 | |
| 68 | 1.76 | 3960 | 0.44 | 3.6 | 8.62 | |

TABLE 2.2-5
RESULTS OF CONSTANT LOADING-RATE TESTS IN
COMPRESSION -1979, MULTI-YEAR* ICE.

| Sample Number MY. | Peak stress (MPa) | Time to peak stress (sec) | Average stress rate (kPa/sec) | Average Temp. (-°C) | Comments |
|----------------------|----------------------|------------------------------|-------------------------------------|------------------------|----------|
| 1 | 4.76 | 95 | 50.1 | 20.0 | |
| 2 | 2.72 | 518 | 5.24 | 14.0 | |
| 3 | 1.94 | 4518 | 0.43 | 11.2 | |
| 4 | 2.68 | 503 | 5.32 | 13.8 | |
| 5 | 4.26 | 15 | 284 | 3.3 | |
| 7 | 5.65 | 0.75 | 7540 | 2.0 | |
| 8 | 3.63 | 69 | 52.6 | 5.7 | |
| 9 | 2.41 | 47a | 5.03 | 5.9 | |
| 10 | 2.28 | 456 | 5.00, | 5.5 | |
| 11 | 3.69 | 66 | 65.9 | 5.3 | |
| 12 | 4.87 | 0.59 | 8250 | 3.0 | |
| 13 | 1.50 | 3510 | 0.43 | 3.0 | |
| 14 | 4.37 | 16 | 273 | 3.0 | |
| 15 | 1.67 | 3990 | 0.42 | 3.4 | |

*Salinity <0.2 ppt for all samples.

TABLE 2.2-6
RESULTS OF CREEP RUPTURE TESTS IN UNIAXIAL
COMPRESSION -1979

| Sample Number | Stress (MPa) | Time to min. strain rate (sec.) | Time to rupture (sec.) | Strain at min. strain rate | Minimum strain rate (sec ⁻¹) | Average Temp. (°C) | Average Brine Volume \sqrt{v} (ppt) | Comments |
|---------------|--------------|---------------------------------|------------------------|----------------------------|--|--------------------|---------------------------------------|----------|
| 4 | 1.19 | 5770 | >14460 | 5.7×10^{-3} | 6.23×10^{-7} | 16.2 | 4.96 | |
| 6 | 0.90 | 14640 | | 2.2×10^{-3} | 9.11×10^{-8} | 16.8 | 4.06 | |
| 37 | 1.48 | 840 | >5007 | 2.4×10^{-3} | 2.18×10^{-6} | 16.8 | 4.42 | |
| 38 | 2.04 | 220 | 878 | 2.9×10^{-5} | 1.18×10^{-5} | 16.6 | 4.28 | |
| 39 | 2.69 | 136 | 340 | 2.6×10^{-3} | 1.35×10^{-5} | 19.0 | 4.1 | |
| 41 | 1.79 | | 2384 | | | 14.3 | 4.67 | |

TABLE 2.2-7
RESULTS OF CREEP TESTS IN UNIAXIAL
COMPRESSION -1979

| Sample Number | Stress (MPa) | Strain rate (sec ⁻¹) | Test Duration (sec.) | Average Temp. (-°C) | Average Brine Volume \sqrt{v} (ppt) |
|---------------|--------------|----------------------------------|----------------------|---------------------|---------------------------------------|
| 8 | 0.96 | 4.12 x 10 ⁻⁸ | 76,300 | 17.6 | 4.09 |
| 1 - 14 | 0.86 | 1.67X 10 ⁻⁸ | 202,200 | 17.6 | 4.04 |
| 15 | 0.62 | 2.41X 10 ⁻⁸ | 47,800 | 17.8 | 4.22 |
| 16 | 0.68 | 2.12 X 10 ⁻⁸ | 61,300 | 18.0 | 4.30 |
| 45 | 0.53 | 6.78 x 10 ⁻⁹ | 147,100 | 13.9 | 4.72 |

TABLE 2.2-8
RESULTS OF CONSTANT LOADING RATE TESTS IN UNIAxIAL COMPRESSION - 1979;
VARIATION WITH DEPTH AND ORIENTATION

| ¹ Loading Direction (deg) | ² Column Number | Depth range (cm) | Peak stress (MPa) | Time to peak stress (sec) | Average stress rate (kPa/sec) | ³ Average Brine Volume \sqrt{v} (ppt) |
|--------------------------------------|----------------------------|------------------|-------------------|---------------------------|-------------------------------|--|
| 0° | 1 | 0-30 | 3.45 | 65 | 53.0 | 9.36 |
| | | 30-60 | 3.97 | 76 | 52.3 | 9.26 |
| | | 60-90 | 4.05 | 76 | 53.3 | 9.16 |
| 0° | 2 | 0-30 | 3.54 | 67 | 52.8 | 9.36 |
| | | 30-60 | 4.06 | 81 | 50.1 | 9.26 |
| | | 60-90 | 4.46 | 83 | 53.7 | 9.16 |
| 0° | 3 | 15-45 | 3.36 | 65 | 51.7 | 9.19 |
| | | 45-75 | 4.49 | 86 | 52.2 | 9.20 |
| | | 75-105 | | | | |
| 0° | 4 | 15-45 | 3.41 | 63 | 54.2 | 9.19 |
| | | 45-75 | 4.07 | 78 | 52.2 | 9.20 |
| | | 75-105 | 4.40 | 83 | 53.0 | 9.32 |
| 45° | 1 | 0-30 | 2.66 | 49 | 54.3 | 9.36 |
| | | 30-60 | 1.81 | 37 | 49.0 | 9.26 |
| | | 60-90 | 2.08 | 41 | 50.8 | 9.16 |
| 45° | 2 | 0-30 | 2.29 | 45 | 50.9 | 9.36 |
| | | 30-60 | 2.34 | 47 | 49.9 | 9.26 |
| | | 60-90 | 2.09 | 42 | 49.7 | 9.16 |
| 45° | 3 | 15-45 | 1.99 | 40 | 49.6 | 9.19 |
| | | 45-75 | 1.97 | 40 | 49.1 | 9.20 |
| | | 75-105 | 2.00 | 40 | 50.0 | 9.32 |
| 45° | 4 | 15-45 | 1.99 | 41 | 48.6 | 9.19 |
| | | 45-75 | 2.10 | 45 | 46.7 | 9.20 |
| | | 75-105 | 2.22 | 44 | 50.5 | 9.32 |
| 90° | 1 | 0-30 | 2.91 | 56 | 52.0 | 9.36 |
| | | 30-60 | 3.90 | 75 | 51.9 | 9.26 |
| | | 60-90 | 4.39 | 81 | 54.1 | 9.16 |
| 90° | 2 | 0-30 | 3.42 | 64 | 53.4 | 9.26 |
| | | 30-60 | 3.57 | 72 | 49.6 | 9.26 |
| | | 60-90 | 4.36 | 76 | 57.4 | 9.16 |
| 90° | 3 | 15-45 | 3.84 | 70 | 54.9 | 9.19 |
| | | 45-75 | 3.78 | 77 | 49.1 | 9.20 |
| | | 75-105 | 4.35 | 81 | 53.7 | 9.32 |
| 90° | 4 | 15-45 | 4.00 | 73 | 54.8 | 9.19 |
| | | 45-75 | 4.12 | 74 | 55.6 | 9.20 |
| | | 75-105 | 4.48 | 81 | 55.3 | 9.32 |

¹ Angle between average c-axis orientation and direction of load application.

² See Figure for sampling scheme.

³ Average temperature -3°C for all tests.

TABLE 2.2-9
RESULTS OF CONSTANT LOADING RATE TESTS IN
UNIAXIAL COMPRESSION- 1980

| Sample Number | Peak stress (MPa) | Time to peak stress (sec.) | Average stress rate (kPa/sec.) | Average Temp (°C) | Average. Volume Brine \sqrt{v} (ppt) | Sample type (see note below) | Comments |
|---------------|-------------------|----------------------------|--------------------------------|-------------------|--|------------------------------|--|
| 1 | 2.23 | 479 | 4.66 | 12.3 | 4.8 | 1 | |
| 2 | 2.52 | 505 | 4.99 | 12.4 | 4.8 | 1 | |
| 3 | 3.12 | 12.4 | 251 | 4.8 | 8.6 | 2 | 1 flatjack |
| 4 | 2.31 | 476 | 4.86 | 8.8 | 5.6 | 1 | |
| 5 | 2.06 | 9.0 | 229 | 4.7 | 8.6 | 2 | Peak stress low, sample cracked across one corner. |
| 6 | 1.87 | 3.3 | 568 | 4.7 | 8.6 | 2 | |
| 7 | 2.47 | 5.2 | 476 | 4.7 | 8.6 | 2 | 1 flatjack |
| 9 | 2.15 | 427 | 5.02 | 13.1 | 4.6 | 3 | |
| 10 | 2.13 | 415 | 5.14 | 13.1 | 4.6 | 3 | |
| 11 | 2.63 | 54.2 | 48.5 | 8.4 | 5.6 | 3 | |
| 12 | 2.51 | 56.8 | 44.3 | 8.4 | 5.6 | 3 | |
| 13 | 1.73 | 380 | 4.56 | 8.7 | 5.5 | 3 | |
| 15 | 1.84 | 3.75 | 4.90 | 8.7 | 5.5 | 3 | |
| 16 | 12.9 | 3480 | 0.37 | 3.7 | 9.7 | 2 | 1 flatjack |
| 17 | 1.22 | 3387 | 0.36 | 3.7 | 9.7 | 2 | |
| 18 | 2.38 | 48 | 49.5 | 4.9 | 8.5 | 2 | |
| 19 | 2.31 | 46 | 50.2 | 4.9 | 8.5 | 2 | |
| 20 | 3.07 | 9.8 | 314 | 5.2 | 7.0 | 4 | Load cell operated during test |
| | | | | | | | |
| 22 | 1.84 | 370 | 4.97 | 5.0 | 8.4 | 2 | |
| 23 | 2.17 | 425 | 5.11 | 4.9 | 8.5 | 2 | |

TABLE 2.2-9 (Cent'd)

| Sample Number | Peak stress (MPa) | Time to peak stress (sec.) | Average stress rate (kPa/sec) | Average Temp. (-°C) | Average Volume Brine \sqrt{v} (ppt) | Sample type (see note below) | Comments |
|---------------|-------------------|----------------------------|-------------------------------|---------------------|---------------------------------------|------------------------------|----------|
| 24 | 2.58 | 50.4 | 51.2 | 5.2 | 8.2 | 2 | |
| 25 | 1.85 | 38.5 | 48.0 | 4.9 | 8.5 | 2 | |
| 28 | 1.04 | 3043 | 0.34 | 9.0 | 5.4 | 4 | |
| 29 | 1.45 | 3460 | 0.42 | 9.0 | 5.4 | 4 | |
| 30 | 2.16 | 410 | 5.26 | 8.8 | 5.5 | 4 | |
| 31 | 2.14 | 414 | 6.18 | 8.6 | 5.5 | 4 | |
| 32 | 3.19 | 59.4 | 53.7 | 8.4 | 5.6 | 4 | |
| 33 | 3.04 | 56.8 | 53.6 | 8.4 | 5.6 | 4 | |
| 34 | 1.66 | 330 | 5.02 | 5.3 | 6.9 | 4 | |
| 35 | 1.90 | 356 | 5.34 | 5.0 | 7.1 | 4 | |

Sample types

1. Silty, fine-grained, 0-30 cm depth, random c-axis orientation.
2. Clean, fine-grained, 0-30 cm depth, random c-axis orientation.
3. Columnar ice from 25-55 cm depth, weak orientation (see Table 3B).
4. Same as 3, with flatjacks backed by aluminum plates 30 cm deep by 60 cm wide.

TABLE 2.2-10
RESULTS OF CONSTANT LOADING RATE TESTS
IN UNIAXIAL COMPRESSION - 1980;
VARIATION WITH DEPTH AND ORIENTATION

| 1>Loading Direction | Depth range (cm) | Sample Number | Peak stress (MPa) | Time to Peak stress (sec.) | Average stress [kPa/sec.) | Average Temp. (-°C) | Average Brine Vol. (v ppt) |
|-------------------------------|-------------------------|----------------------|--------------------------|-----------------------------------|----------------------------------|----------------------------|-----------------------------------|
| 0° | 25-55 | 26 | 2.46 | 58.2 | 42.3 | 7.8 | 5.8 |
| | | 27 | 2.84 | 61.0 | 46.6 | 7.8 | 5.8 |
| 0° | 40-70 | 38 | 2.67 | 56.3 | 47.5 | 9.3 | 5.3 |
| | | 39 | 2.78 | 58.0 | 48.0 | 9.3 | 5.3 |
| 0° | 55-85 | 36 | 2.63 | 56.8 | 46.3 | 9.1 | 5.2 |
| | | 37 | 2.79 | 60.0 | 46.5 | 9.1 | 5.2 |
| 0° | 70-100 | 14 | 2.50 | 52.2 | 48.0 | 9.4 | 4.9 |
| | | 40 | 2.62 | 55.8 | 45.2 | 9.3 | 4.9 |
| 0° | 85-115 | 43 | 2.84 | 60.0 | 47.4 | 8.8 | 4.8 |
| | | 44 | 2.48 | 57.4 | 43.2 | 9.0 | 4.8 |
| | | | | | | | |
| 45° | 25-55 | 41 | 2.95 | 61.0 | 48.4 | 8.9 | 5.4 |
| | | 42 | 2.65 | 63.0 | 42.0 | 8.7 | 5.5 |
| 45° | 40-70 | 65 | 2.75 | 59.0 | 46.4 | 9.3 | 5.3 |
| | | 66 | 2.56 | 52.6 | 48.7 | 9.3 | 5.3 |
| | | 75 | 2.16 | 44.0 | 49.1 | 3.7 | 8.1 |
| | | 76 | 1.97 | 41.4 | 47.5 | 3.7 | 8.1 |
| 45° | 55-85 | 67 | 2.73 | 56.8 | 48.1 | 8.9 | 5.3 |
| | | 68 | 2.47 | 52.8 | 46.7 | 8.9 | 5.3 |
| 45° | 70-100 | 63 | 3.12 | 63.6 | 49.0 | 8.9 | 5.0 |
| | | 64 | 2.66 | 59.0 | 45.1 | 8.9 | 5.0 |

TABLE 2.2-10 (Cent'd)

| Loading Direction | Depth range (cm) | Sample Number | Peak stress (MPa) | Time to Peak stress (sec.) | Average stress rate (kPa/sec.) | Average Temp. (-°C) | Average Brine Vol. (√v ppt) |
|-------------------|------------------|---------------|-------------------|----------------------------|--------------------------------|---------------------|-----------------------------|
| 45° | 85-115 | 45 | 2.48 | 53.8 | 46.0 | 8.7 | 4.8 |
| | | 46 | 2.49 | 54.5 | 45.6 | 8.6 | 4.9 |
| 90° | 25-55 | 59 | 2.39 | 52.0 | 45.9 | 7.7 | 5.8 |
| | | 60 | 2.47 | 52.5 | 47.0 | 7.7 | 5.8 |
| 90° | 40-70 | 56 | 2.63 | 56.4 | 46.6 | 9.3 | 5.3 |
| | | 58 | 2.63 | 57.2 | 45.9 | 9.3 | 5.3 |
| | | 77 | 2.02 | 43.6 | 46.2 | 3.6 | 8.3 |
| | | 78 | 2.16 | 46.8 | 46.2 | 3.7 | 8.1 |
| 90° | 55-85 | 61 | 2.68 | 58.6 | 45.8 | 8.9 | 5.3 |
| | | 62 | 2.81 | 60.8 | 46.2 | 8.9 | 5.3 |
| 90° | 70-100 | 55 | 2.84 | 59.0 | 48.2 | 9.3 | 4.9 |
| | | 57 | 2.74 | 58.6 | 46.7 | 8.4 | 5.1 |
| 90° | 85-115 | 69 | 2.79 | 61.0 | 45.8 | 8.6 | 4.9 |
| | | 74 | 2.54 | 56.8 | 44.7 | 8.5 | 4.9 |

2.24.6 DISCUSSION OF RESULTS OF **UNIAXIAL** COMPRESSION TESTS

2.24.61 INTRODUCTION

The purpose of this section is to present and describe the results of the experiments listed in the tables in the last section. The interpretations are given strictly in terms of the data and the relevant back- ground material. More general interpretations in terms **of** the results of the theoretical study are given in the appropriate sections of Section 2.3.

Because the program was done entirely in the field under ambient conditions, it was obviously not possible to control the temperature or the sample properties. This leads to some difficulty in organizing the data because the range of variables examined is limited to some extent. This is because it was generally not possible to run large numbers of tests at the same temperatures. In general, tests were selected depending upon the ice temperature on a particular day and the number and types of tests already done at that temperature. The intent was to assemble the most complete data set possible within a given temperature range. However, there was no certainty that temperatures in a particular range would occur often enough to permit an acceptable data set to be obtained. In addition, it was necessary to duplicate (or triplicate) some tests in order to establish repeatability so that variations in sample properties and set-up could be accounted for. This further reduced the range of variables which **could** be covered with the available samples. For these reasons, the results have been grouped into temperature ranges, which are kept as small as possible while providing a reasonable sample size. This introduces some scatter into the data, but the trends are still apparent.

In the following sections data bearing **on** four aspects of sea ice properties in **uniaxial** compression are described. These are (1) the relationship between strength and stress rate in different temperature ranges, (2) the "long" term strength of sea

ice, (3) the effect of **grain size** and c-axis **orientation** on **sea ice strength** and (4) comparison of the strength of first year and **multiyear** ice in **uniaxial** compression.

2.24.62 STRENGTH VS. STRESS RATE

The results of measurements of strength vs. stress rate in three temperature ranges are shown in Figure 2.2-8. The data show the anticipated increase of strength with stress rate (although the scatter is large) as well as the increase in strength with decreasing temperature. Peak strengths varied from 2.7 **MPa** for the temperature range from -5.5° to -7.5°C, to about 4.5 **MPa** for -10° to -14°C to about 6.2 **MPa** for temperatures between -17° and -22°C.

The strength of 4.5 **MPa** for the temperature range of -10° to -14°C can be compared to the peak strengths reached in Wang's (1979) laboratory tests of the **uniaxial** compressive strength of small-scale cylindrical (7.5 x 15 cm) samples of natural sea ice at constant strain rates and a temperature of -10°C. For **fine-grained** (<2 mm) ice, the peak strength was about 7.2 **MPa**, while for slightly larger grain sizes (2-3 mm) the peak decreased to about 5.9 **MPa**. However, for unoriented columnar ice, Wang found peak strengths of 4.8 and 3.8 **MPa** for grain sizes of 10 and 15 mm, respectively, which are similar to the value of 4.5 **MPa** reported above. It is difficult to draw a conclusion from this, other than to speculate on the possibility that the strengths reported here may reflect the strength of the ice in the transition zone of the samples rather than the **fine-grained** slush ice near the surface.

In experimental programs in which samples are failed at high rates of deformation, the strength of the ice often appears to decrease at strain rates in excess of (about) **10⁻³/sec** (the question is discussed more fully in Section 2.36). No such decrease in strength is evident in the data in Figure 2.2-8, which raises the question of whether the stress rates were high enough to reach the peak if, in fact, it is real. There is no stress-strain law with which to accurately calculate the strain rate.

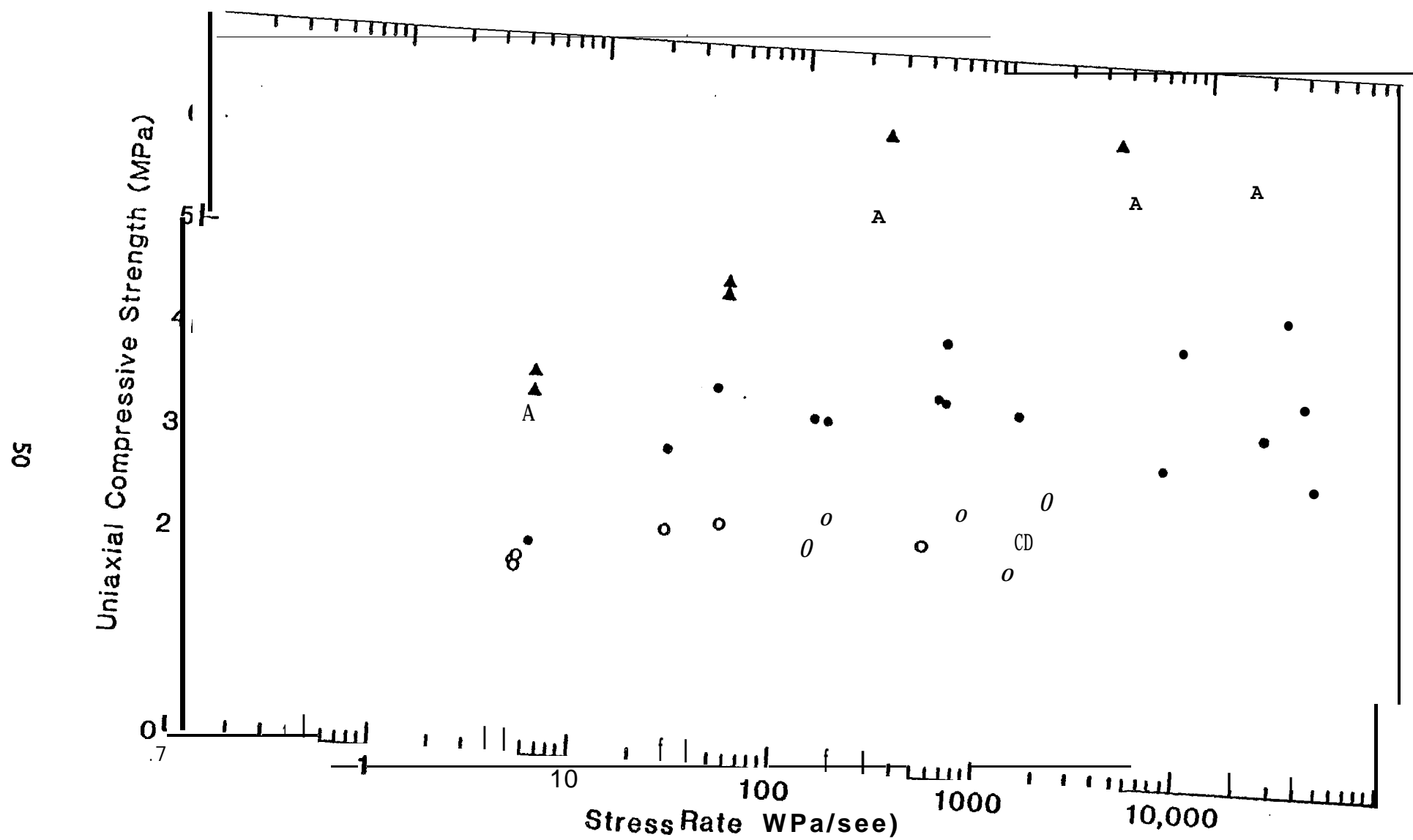


Figure 2.2-8 Plots of uniaxial compressive strength vs. stress rate for three temperature ranges (-17° to -22°C - solid triangles; -10° to -14°C - solid circles; -5.5° to -7.5°C - open circles).

However, a lower limit to the strain rate can be calculated if it is assumed that the ice deformed as a linear elastic solid at the higher stress rates. In that case, the strain rate is related to the stress rate through the derivative of the one-dimensional Hooke's law,

$$\dot{\epsilon}(t) = \dot{\sigma}(t)/E$$

where E is Young's modulus. At the higher rates used in this project (say, $\dot{\sigma} = 104$ kPa/sec), for a modulus of 9 GPa, the strain rate would have been on the order of 10^{-3} /sec. This suggests that the data at the highest rates are probably close to the peak and do not contribute to the resolution of the problem.

The variation in failure mechanism over the range of stress rates shown followed the same pattern for all three data sets. At the lower rates, the ice failed by the pervasive formation of small, stable cracks which progressively weakened the sample until it could no longer sustain the load. Samples that were unloaded before they failed explosively were milky-white, due to the distribution of small cracks. At the higher rates, the failure always occurred by brittle fracture. In some cases the fractures were through-going extension cracks aligned parallel to the sample axes. In others, a single vertical shear crack extended across the sample at about 30° to the axis. In either case, the ice between the main fractures was still clear, with no small fractures such as were present in samples which were tested at lower rates.

2.24.63 LONG-TERM STRENGTH

Gold (1979) presented data for the time-to-failure of fresh water polycrystalline ice in constant stress in which, for stresses above some "transition" range, the samples passed through the inflection point between secondary and tertiary creep in a relatively short time. Once in tertiary creep the strain rate accelerated until

failure **occured**. However, the length of time the sample **could** sustain a stress without passing to tertiary creep increased rapidly for stresses below the transition. This suggested the possibility that the ice might have a “fundamental” strength; that is, an upper limit of the range of stresses which the ice could sustain “indefinitely” without failing. More recently, **Jacka** (1984) showed that even at low constant stresses, the inflection point is ultimately reached, and ice passes into tertiary creep.

A knowledge of the stress range over which the transition occurs could be useful for engineering applications. It is not an indicator of a fundamental strength in the sense defined above. However, it does define a stress below which the ice can be expected to sustain a load for a relatively long time. In addition, the transition is of interest for the theory described in Section 2.3.

Data relevant to the question of transition stress are shown in Figures 2.2-9 and 10. The data in Figure **2.2-9** show the time-to-minimum strain rate and **time-to-**rupture for tests at constant stress in a relatively low temperature range. In addition, the time-to-failure for several tests at constant stress rates, and the total times of constant stress tests which did not reach the inflection point at the minimum strain rate are also shown. The data show that linear projections of curves of time-to-failure (for both the constant stress and constant stress rate tests) or **time-**to-minimum strain rate must pass through shorter times than those for which the samples were able to maintain lower stresses without reaching a minimum strain rate. Thus, the stress vs. time-to- minimum strain rate curve must flatten as indicated on the figure, defining the “transition” stress. For the data shown, the transition stress is approximately 1 MPa, and the data indicate that it is sharply defined.

A similar data set at a higher temperature range is shown in Figure 2.2-10. In this figure, the minimum strain rate was reached in even the longest tests, although

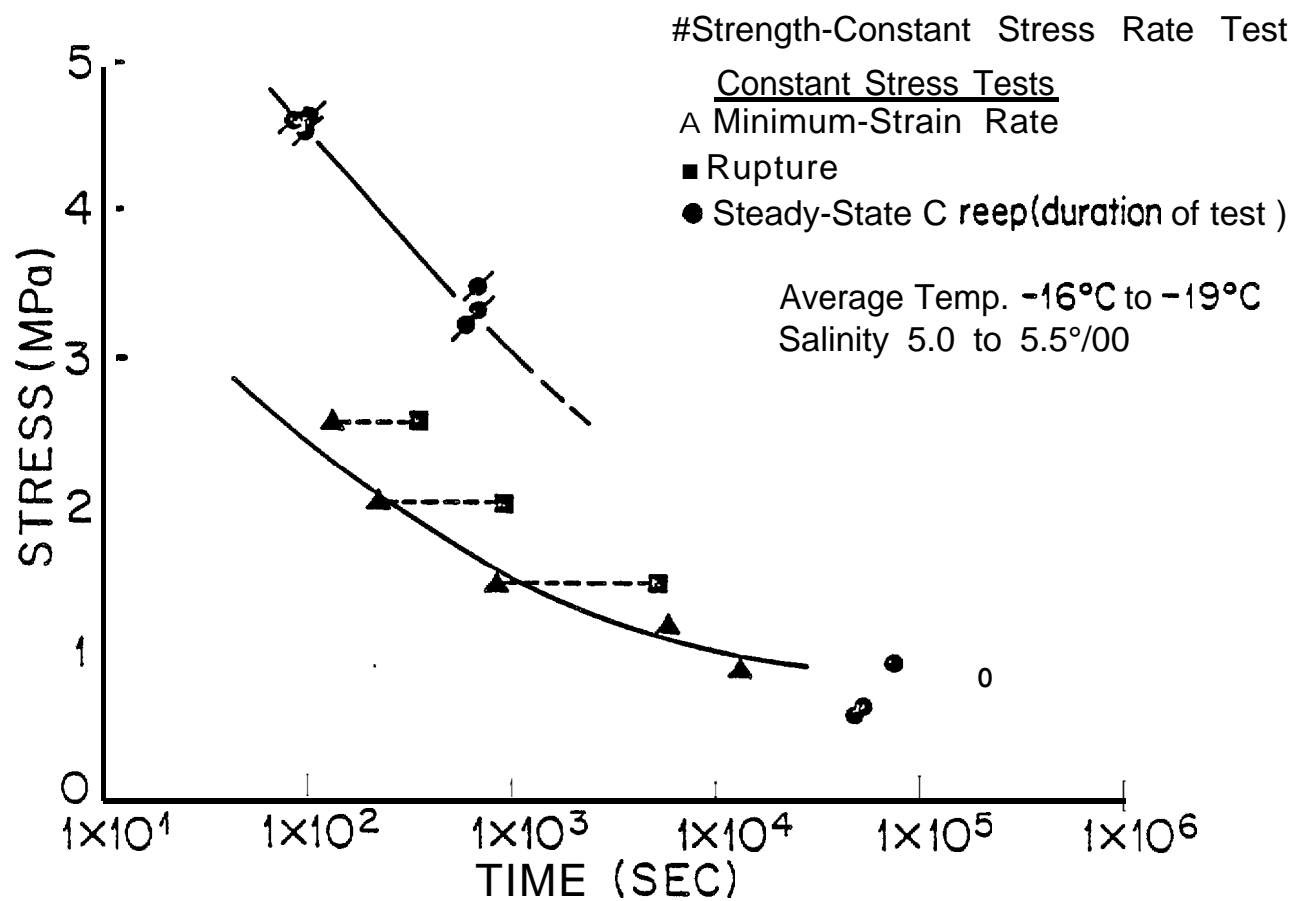


Figure 2.2-9 **Uniaxial** compressive strength vs. **time-to-failure** for constant stress rate tests and time-to-minimum strain rate and time-to-rupture at constant stress in the temperature range -10° to -19°C .

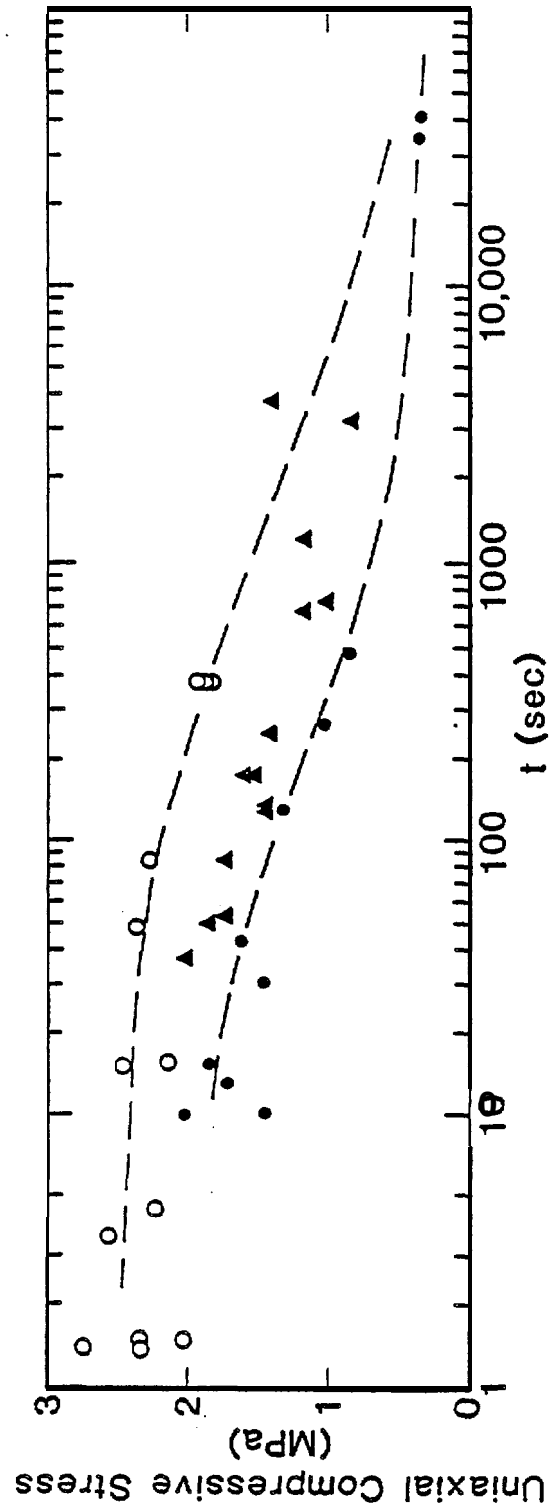


Figure 2.2-10 Uniaxial compressive strength vs. time-to-failure for constant stress rate tests (open circles), and time-to-minimum strain rate (solid circles) and time-to-rupture (solid triangles) for constant stress tests). Temperature range -5.5° to -7.5°C . Curves are estimated based on the results in Section 2.34.

it was not possible **to** hold the loads on the samples until rupture. The curves through the data points are estimates (their shapes reflect the results discussed in Section 2.34). The transition is less well-defined in this figure, because the slope of the stress vs. minimum strain rate curve is low compared to that in Figure 2.2-9. However, a value of 0.5 **MPa** might be a reasonable estimate.

In general, samples which ruptured at constant stress failed by the pervasive growth of small cracks, which gave the ice a whitish color. Few cracks were ever observed to form in samples tested at stresses below the transition stress.

It is of interest to note that for constant stress tests, the time- to-rupture is usually between a factor of 3 and 10 greater than the time-to-minimum strain rate, with a tendency to increase at lower stresses. Similar data for ice in bending would have application to the problem of the length of time for which an ice sheet can be expected to safely bear a load.

2.24.64 EFFECT OF GRAIN SIZE AND C-AXIS ORIENTATION ON STRENGTH

Peyton (1966) and Wang (1979) both demonstrated the effect of strong alignment of crystallographic c-axes of crystals in an ice sheet on the strength of the ice loaded in various orientations. In this study, similar measurements were made to include the effect of depth (and therefore increasing grain size). To accomplish this, samples were **collected** in 30 cm increments of depth down to 105 cm in the ice sheet (Figure 2.2-11). These were oriented so that loading **could** be done at 0°, 45° and 90° to the dominant c-axis direction on two samples collected for each orientation and depth interval. The study was first done in 1979 and was repeated in 1980 in an effort to collect data over a different temperature range. The results of the 1979 program are shown in Figure 2.2-12. Loading was done at a stress rate of about 52 **kPa/sec** (7.5 psi/sec) which was similar to that used by Peyton (1966) in his work on

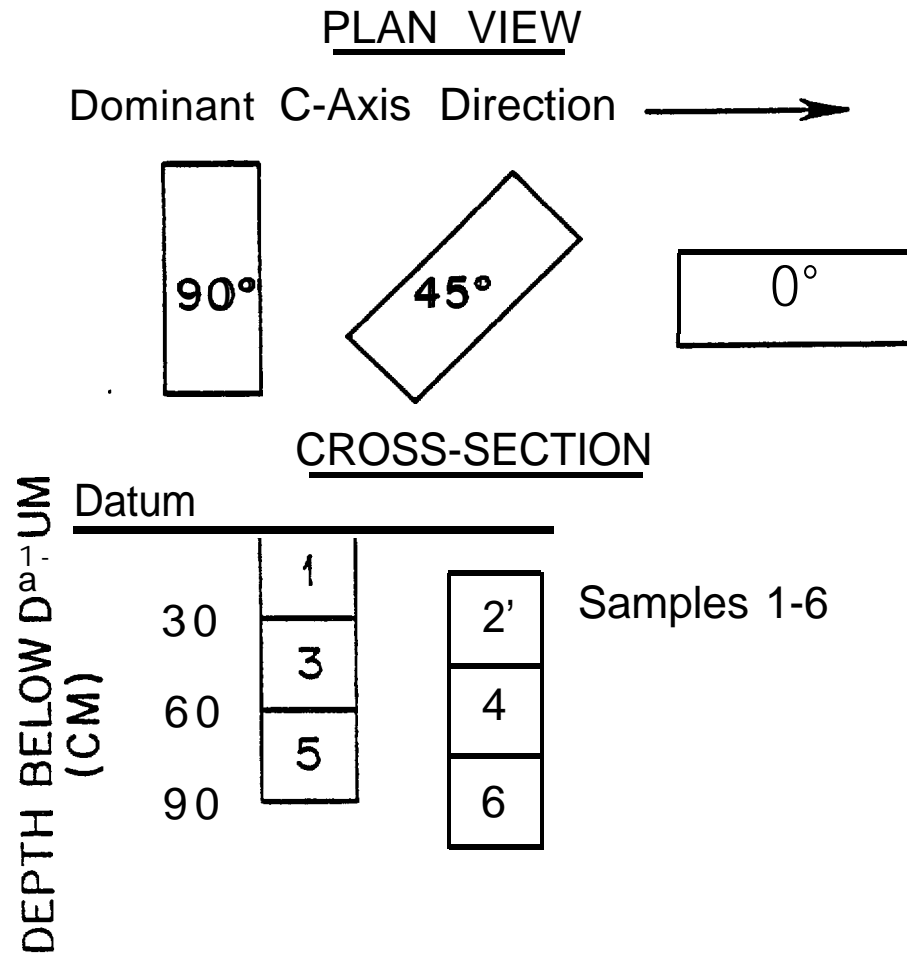


Figure 2.2-11 Arrangement of samples collected for evaluation of **uniaxial** compressive strength vs. grain **size** and **c-axis orientation**.

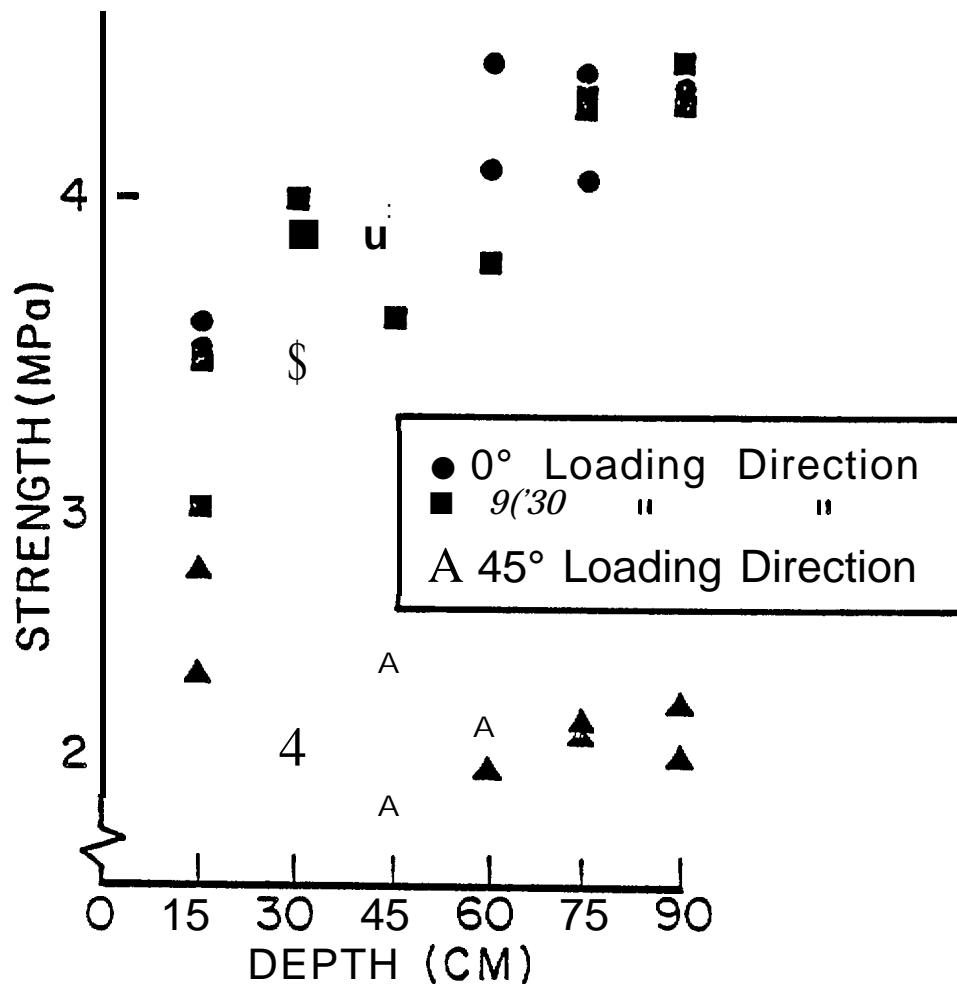


Figure 2.2-12 Results of the 1979 series of tests of uniaxial compressive strength vs. grain size and c-axis orientation.

ice strength as a function of grain size and c-axis orientation. Average sample temperatures during testing were -3°C ($\pm 0.5^{\circ}\text{C}$).

The results of the 1979 study agree with those of Wang (1979) with respect to the increase of strength with depth for the 0° and 90° orientations. However, they contrast with the results of both Wang (1979) and Peyton (1966) which show that the strength in the 0° direction is greater than that in the 90° direction. There maybe no discrepancy with respect to Wang's results because, at the loading rate used in this program, the sample strain rates would probably have been in the range of $10^{-6}/\text{sec}$ to $10^{-5}/\text{sec}$. At those rates, the difference between the strength in the 0° and 90° directions in Wang's (1979) data are small and possibly within the scatter of the results in Figure 2.2-12.

It is likely that the discrepancy is real with respect to the data in Peyton (1966) but, if so, the same discrepancy exists between Wang's and Peyton's results. In this case, the lack of agreement maybe due to the differences in the volume of the samples used in the three studies.

Peyton's tests were done on samples about 3.5 cm in diameter by 7 cm long. For depths greater than about 30 to 60 cm in an ice sheet (particularly when the c-axes are strongly oriented), samples of this size are probably closer to single crystals of ice than to polycrystalline ice. For the 90° orientation, the brine planes in the ice were aligned parallel to the sample axis. Thus, when loaded in uniaxial compression, the brine planes were properly oriented to nucleate extension fractures which, in a large sample might have been trapped at the grain boundaries and stabilized. However, for Peyton's small samples their size would have been significant compared to the length of the sample, leading to weakening and premature fracture. In contrast, the samples used by Wang (approximately, 7.5 x 15 cm) and in this study, were large enough that the grain sizes were insignificant in comparison to the sample volume.

Thus, small cracks **parallal** to the brine planes would have stabilized, increasing the stress required to cause failure.

Note that for the 45° direction the strength decreased with depth initially, and then remained constant (within the scatter) despite the increase in grain size with increasing depth. An interpretation is suggested by the observation that, with the exception of samples including the slush ice layer, failure in samples with this orientation always occurred by shear fracture at 45° to the sample axis. Thus, the fracture plane was always parallel to the orientation of the brine planes and in the plane of maximum shear stress. This implies that once the orientation was sufficiently strong for sliding to occur easily in the direction of orientation of the brine planes, further intensification of the orientation had **little** effect on the strength.

The results of the test series in 1980, in which the same test **program** was repeated at average sample temperatures of **-7** to **-9°C** are shown in Figure 2.2-13. These data indicate little or no variation in strength with depth or loading direction relative to c-axis orientation. The results of additional tests at **-3°C**, which were **run** to check the results of the first series, also indicate no difference in strength between the 45° and 90° directions (Figure 2.2-.3). The apparent reason for the absence of . any particular orientation effect in these results is that the orientation was simply not developed strongly enough. There is no question that the ice tested in 1980 should be classified as "oriented," because an average c-axis orientation could easily be identified in thin sections of the ice. However, thin section analysis showed that in **1979**, the ice at a depth of 32 cm had a maximum angular spread between c-axes of about 30°, decreasing to 15° at 1 **m**. In contrast, in 1980, the angular spread was up to 66° at a depth of 75 cm. This large variation was apparently sufficient to neutralize the effect of the average c-axis orientation, with the result that the **ice** in 1980 was essentially isotropic for loading in the horizontal plane. This result

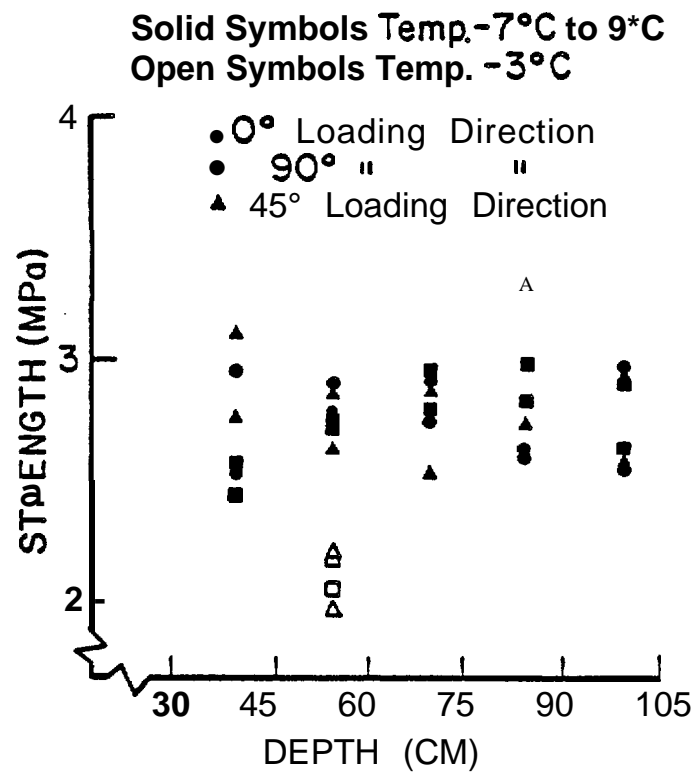


Figure 2.2-13 Results of the 1980 series of tests of **uniaxial** compressive strength vs. grain size and c-axis orientation.

indicates that there is some limit in the degree of orientation (i.e., some maximum permissible spread of c-axis orientation) which is required before the ice will exhibit mechanical anisotropy for loading in a horizontal plane. The fact that an average c-axis orientation can easily be identified in a sample does not assure that such a mechanical anisotropy exists.

2.24.65 COMPARISON OF THE STRENGTH OF FIRST YEAR AND MULTIYEAR ICE

A series of tests was run to provide a comparison between the strength of first year and **multiyear** sea ice in **uniaxial** compression at the same temperatures and loading rates. The samples of **multiyear** ice were collected from a floe frozen into the **landfast** ice sheet near the test site. Average ice temperatures ranged from -2° to -6°C during the test program. Tests at each stress rate were run consecutively, alternating between the two ice types. The results are shown in Figure **2.2-14** and indicate that there is little difference in strength between the two ice types, except possibly at the highest rate at which tests were conducted. This suggests that the strength of **multiyear** ice maybe greater than that of first year ice in the brittle range, but there is little difference over the remainder of the range of loading rates used.

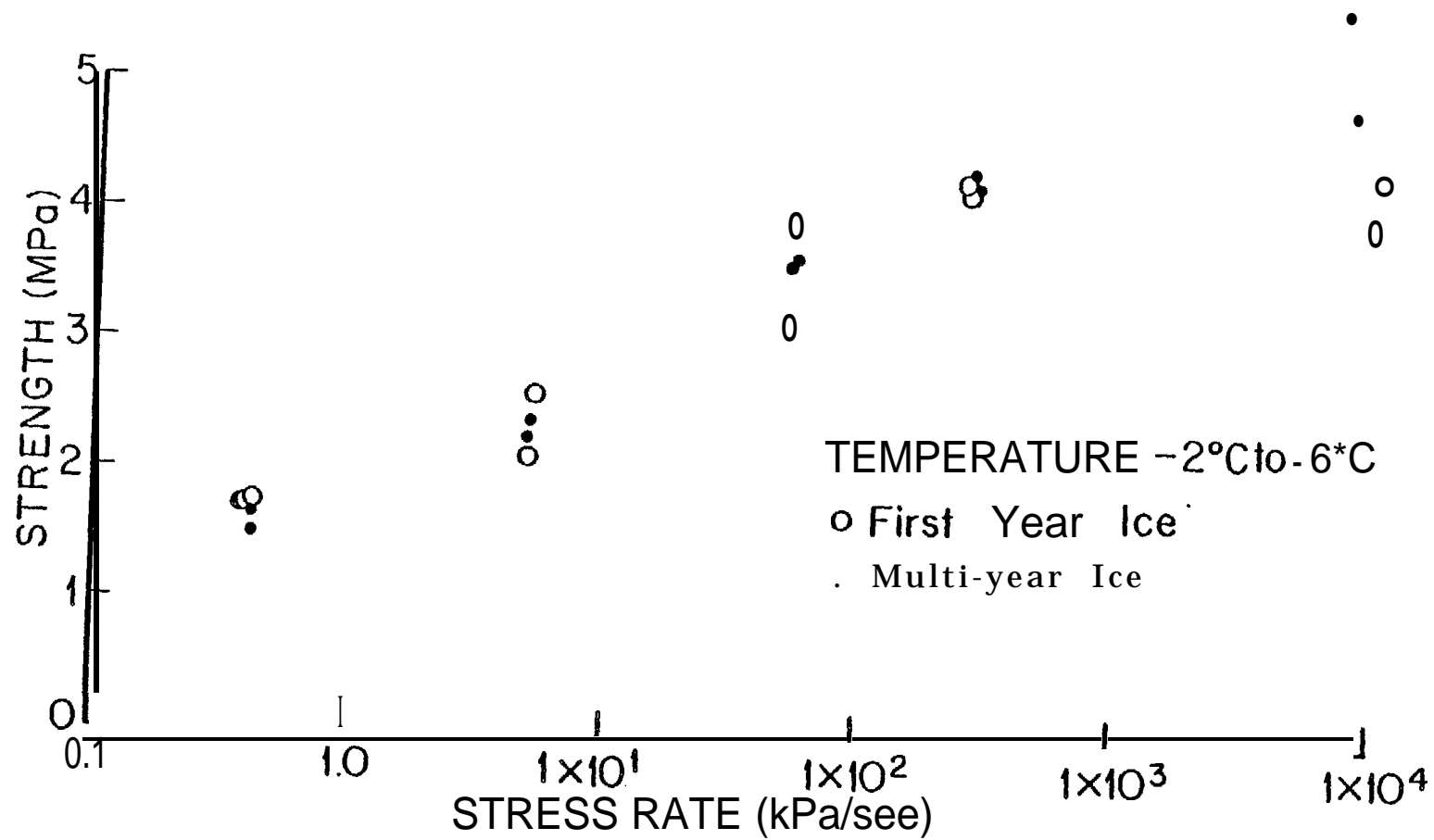


Figure 2.2-14 Uniaxial compressive strength of first year and multi-year ice vs. stress rate.

2.25 DIRECT SHEAR TESTS

A direct shear test (which is similar to a standard "shear box" test) was designed, and several preliminary experiments were run. The values are not reported here because the **flatjacks** used for loading were not calibrated. However, the test results were repeatable, and the procedure could form the basis **for a** test program to evaluate the shear strength of sea ice. Details were described in Shapiro et al. (1979) and are only summarized here.

The configuration of the test is shown in Figure 2.2-15. The sample is defined by the relief slots which are cut **to** the depth "a" with a chain saw. The test is done by loading the **flatjack** until failure occurs along the plane at the base of the block. The shear strength is then calculated assuming that the stress is uniformly distributed on the failure plane, as is done in the case with shear box experiments. Thus, if the dimensions of the **flatjacks** are a and b, and the (calibrated) **flatjack** pressure at failure is P, then the total force is **Pab**. This is assumed to be equal to τbc , where τ is " the shear strength, and b and c are the dimensions of the block in the plane of the ice sheet as outlined by the relief slots. In the tests done during the program, b and c were equal, so that $\tau = (a/c)P$. Experiments were done with the ratios **a/b** and **a/c** equal to both 1/2 and 1/3, which gave similar values of τ .

The geometry of the stress distribution in the test block was studied using a 2-dimensional plane stress, **finite** element analysis. The results were compared to similar calculations for the geometry of a punch test (Figure 2.2-16) which is often used to determine the shear strength of materials. The calculations indicate that the first crack to form in the shear test would likely be a tension crack propagating downward under the **flatjack** into the ice sheet. Subsequently, the stress configuration near the **flatjack** closely resembles that of the punch test as shown in Figure 2.2-16. The vertical crack can be simulated at the time the test is setup by deepening the chain saw cut made to receive the **flatjack** and installing a piece of

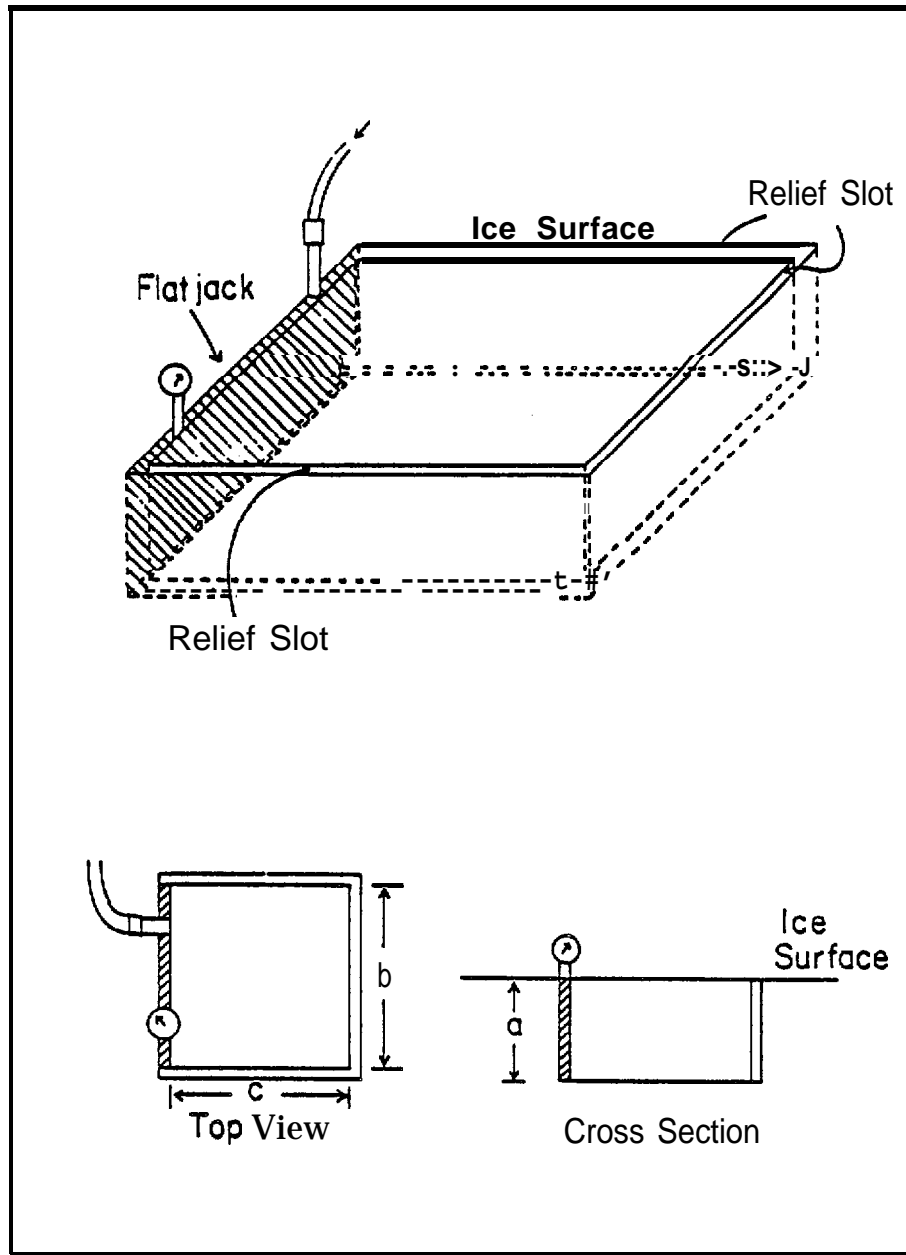


Figure 2.2-15 Set-up for direct shear test.

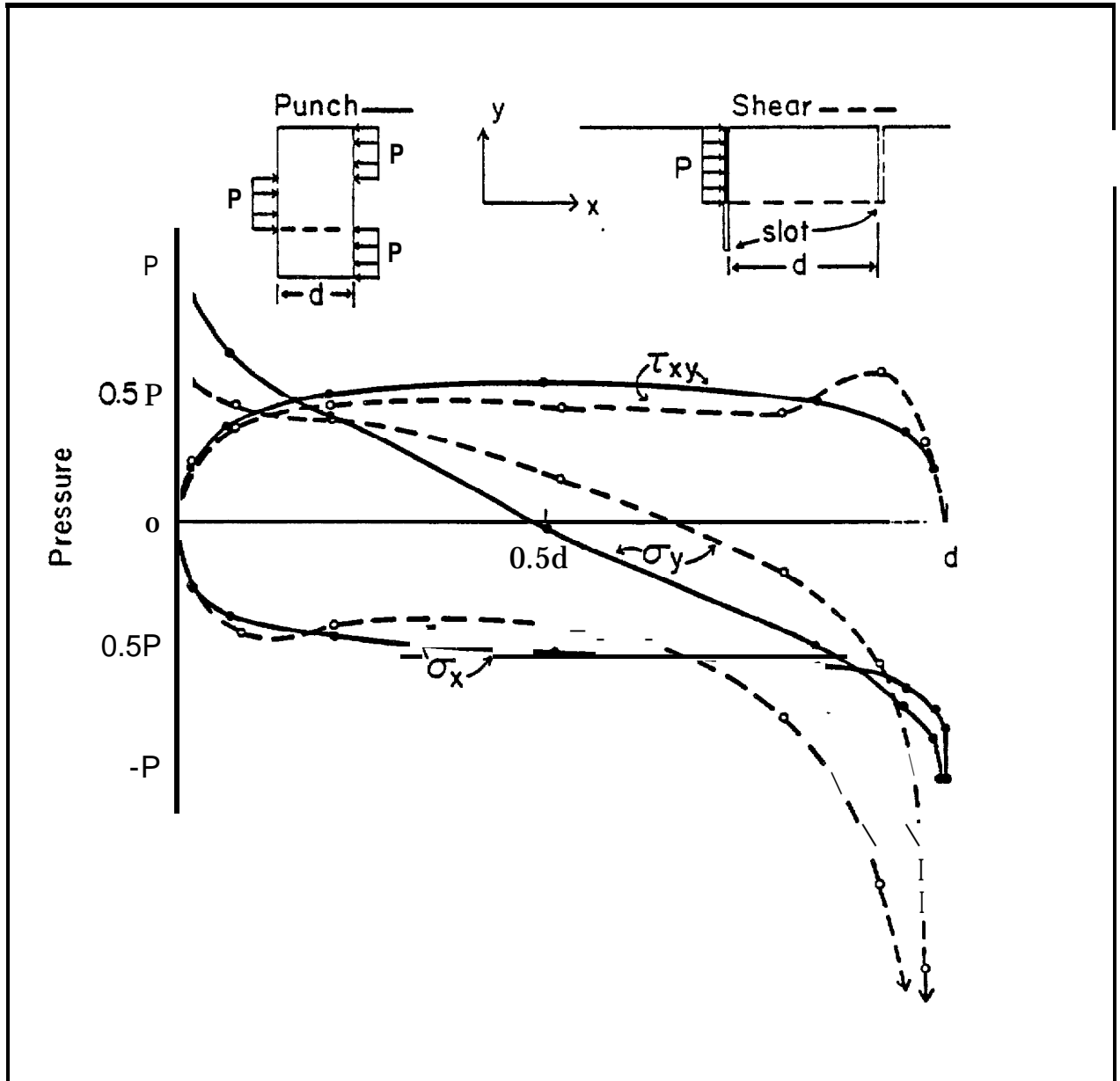


Figure 2.2-16 Results of finite element analysis of punch test (solid **line**) and direct shear test (dashed **line**). Calculations refer to a surface just below the dashed lines on the diagrams. The slot below the **flatjack** represents either the first crack or the prepared "crack" **described in the text**.

stiff cardboard wrapped in polyethylene sheeting in the slot below the **flatjack**. This would provide a low tensile strength bond, assuring that the first crack will propagate downward.

Examination of the fracture zones which formed on the shear plane as a result of the tests, shows that the zones were generally thin, involving only the lower 20% of the thickness of the blocks. Within the zone, the ice tended to shatter into flat plates about 1 cm thick, with linear dimensions of several centimeters. The failure plane, in the ice sheet typically showed irregular "step" asperities oriented transverse to the direction of motion of the failed block, with the riser of the step facing the loading direction. Flat cracks extended down into the ice from the base of each step, as evidenced by the distinct gray color of the ice in these areas. The failure mode was similar to that in the fracture zone of rocks which fail in shear by brittle fracture in **uniaxial** compression. The mechanism clearly indicates failure under the influence of a shear stress parallel to the failure plane.

It should be noted that attempts to conduct direct shear tests using square **flatjacks** and blocks with dimensions $a = b = c$ invariably resulted in tensile failure across the base of the specimen. Thus, cubical blocks simulate the bending of a thick cantilever beam under a uniformly distributed load. However, tests in which the width of the **flatjack** was at least twice the depth always failed in shear.

Finally, note that the test described above can be used to determine the shear strength of the ice in any direction. This would involve quarrying samples from the ice sheet, rotating them into the desired orientation, and then freezing them into holes prepared in the surface of the ice sheet. A sample need only be large enough that the set-up shown in Figure 2.2-15 can be made on its surface.

2.26 INDIRECT TENSION (BRAZIL) TEST

A procedure for running indirect tension tests in situ in the ice sheet was also tried (Shapiro et al., 1979). Only two tests were required to duplicate failure patterns obtained in the laboratory. In the first of these, a circle with a diameter of 59 cm was outlined on the ice surface and two 15 x 60 cm flatjacks were installed on the opposite ends of one of its diameters; the 15 cm edges of the flatjacks were at the surface of the ice sheet. A chain saw cut 75 cm deep was made along the circumference of the circle, and the flatjacks were then loaded until failure occurred. The cylinder failed with a single crack along the diameter and minor secondary cracks near the flatjacks. This is the typical mode of failure in laboratory tests of this type when the cylinders are loaded by line loads on opposite ends of a diameter.

Curved flatjacks were used in the second test, in order to provide a load over 15° arcs of the test specimen as discussed by Jaeger and Cook (1976). The purpose of loading over the arc is to eliminate the secondary cracking near the points of application of the line load, and assure that failure occurs along a single fracture which originates near the center of the sample. The sample used for this test was another cylinder of the same size as in the first test (diameter 59 cm, depth 75 cm). The flatjacks were prepared by flattening two 46 cm lengths of 7.6 cm diameter copper tubing, and then bending them to the curvature of the test specimen. The ends of the flatjacks were sealed by silver soldering, with inlets for loading installed at one end. The test was set up and run as described above, but in this case failure occurred along a single crack with no secondary cracking near the flatjacks. Further, when the sample was cut normal to the crack with a chain saw, it separated into two blocks along the crack. There was no evidence of splaying of the crack with depth in the ice sheet, which indicates that plane strain conditions were achieved over a sufficient length of the sample to provide an adequate test.

The results show that large-scale, in situ indirect tension tests are relatively easy to setup and run and failure mechanisms duplicate those which typically occur in laboratory tests. Thus, there should be no difficulty in conducting a larger program of tests of this type if the results were needed.

2.27 BIAXIAL COMPRESSION TESTS

Experiments were done to develop a biaxial compression test using rectangular prisms of sea ice of the same dimensions as those used in the **uniaxial** compression tests (Shapiro et al., 1979). The tests differ only by the addition of a confining pressure applied through 30x 60 cm **flatjacks** installed along the sides of the samples. The confining pressure was controlled by a loading system which was separate from that used to apply the loads to the ends of the sample.

The tests were done by loading both pairs of **flatjacks** simultaneously, until the selected confining pressure was reached. Then, the pressure in the confining pressure **flatjacks** was held constant, **while** the pressure in the **flatjacks** at the ends of the sample was increased at a constant rate **until** failure occurred.

The results of the experiments indicate that this test is likely to be useful only when the ice temperature is **low** and the loading rate of the axial **flatjacks** is less than 0.35 **MPa/sec** (50 psi/sec). The limitations are due to the increase in the strength of the samples with application of confining pressure. This allows the pressure in the axial **flatjacks** to become so **large** that the ice sheet (the "loading frame"), which is not under confining pressure, is not sufficiently strong to resist the expansion of the **flatjacks** under internal pressure. As a result, the axial **flatjacks** fail along the edge weld at the ice surface as the **flatjack** overexpands.

Additional work in progress when the **field** program was terminated was directed at testing the use of aluminum or steel plates installed behind the axial **flatjacks** to spread the load and reduce the stress applied to the ice sheet by the

reaction pressure. A few experiments run under these conditions suggested that the approach might lead to" an increase in the range of pressures over which tests could be done.

Since the procedure was never developed to the point of running a series of tests to obtain numerical values of the strength, the **flatjacks** used to apply the confining pressure were not calibrated. For the limited data obtained, the results suggest that the increase in peak axial stress with increase in confining pressure is strongly dependent on both the temperature and the rate of loading. In addition, it was never possible to bring a **sample** to failure by the development of through-going cracks, although a few tests were done at rates which, for **uniaxial** compression, would have caused failure by that mechanism. Instead, cracking was always pervasive, turning the sample milky-white, as occurred in **uniaxial** compression tests at low loading rates (Section 2.24.62).

The procedure as described above could be used for conducting creep tests at low **flatjack** pressures, but further development is required if the test is to be used to establish the strength at higher rates of loading and confining pressures.

2.28 SUMMARY AND DISCUSSION

The physical properties of sea ice, and its mode of occurrence in nature require that at least some determinations of the mechanical properties of the ice must be conducted in situ in order to supplement laboratory results. In situ tests involving vertical loading of an ice sheet (or of beams isolated within an ice sheet) had been done previously, but the problem of testing under in-plane loading had received little attention prior to this program. Therefore, one task was to investigate methods through which the properties of sea ice could be determined on relatively large samples under conditions of in-plane loading, and with minimal disturbance to the samples being tested.

Flatjacks proved to be ideal devices for introducing controlled stress fields into an ice sheet. They are relatively simple and inexpensive to construct in any shape, and can be adapted to a variety of test types. Loading by high pressure gas **controlled** by a pressure regulator proved to be satisfactory for tests at both constant load and constant loading rate. For the latter, rates ranging from less than 1 **kPa/sec** to greater than 104 **kPa/sec** were achieved.

Deformation measurements can be made using a variety of equipment but are limited by the fact that, in the tests described here, only the face of the sample at the ice surface can be instrumented. The result is that as the sample surface bulges upward in response to the in-plane shortening, the measured strain on the single exposed face ceases to be representative of the true shortening. The method of attaching displacement measuring devices to pegs in the ice overcomes this **difficulty** to some extent, but introduces the question of whether the pegs affect the deformation characteristics of the ice. The results presented here suggest that it is possible to determine the conditions under which this does not occur. However, it would still be desirable to verify the validity of the strain determinations by other methods.

During the program, procedures for conducting tests in **uniaxial** compression (triangular and prismatic specimens), direct shear and indirect tension were designed and tested with satisfactory results. A biaxial compression test was also tried. It is adequate for creep tests or for measurements of strength at low confining pressures (i.e., **less** than about 20% of the peak axial stress), but requires further work if it is to be extended to higher confining pressure.

The data on **uniaxial** compressive strength as a function of loading rate follows the same trend of increasing strength with increasing rate as established for constant deformation rate tests. There is no stress-strain law available with which to correlate between test types. However, estimates suggest that the data presented

here are comparable to those obtained by Wang (1979) on smaller samples, implying that there is no marked decrease in strength with increasing sample dimensions for samples in which the c-axes are not strongly oriented.

The results of tests at constant stress verify that some transition stress range exists for sea ice, below which the time that the ice can sustain a load increases rapidly. The transition is defined by plots of stress vs. time-to-minimum strain rate (the onset of the tertiary creep stage leading to rupture) for a series of tests. The data indicate that the transition is sharp at low temperatures but becomes more gradual as the temperature increases. The recognition of the transition range may have engineering applications by defining the upper limit of the stress which the ice can sustain for a relatively long time. In addition, while any sample under load must eventually fail, the data indicate that the time between the inflection point and rupture of the sample is from 3 to 10 times as great as the time-to-minimum strain rate. This may provide a basis for deriving safety factors for loads on ice sheets.

A series of determinations of sea ice strength as a function of depth in the **ice** sheet (or, alternatively, grain size) and c-axis orientation follows trends indicating strong mechanical anisotropy of the ice. The tests were done on strongly oriented ice, and the trends are similar to those derived in laboratory measurements. However, the results of a second series of tests raise the question of the intensity of **c**-axis orientation which is required in order for the **anisotropic effects** to become important. In that series, the intensity of c-axis orientation **of** the ice was weaker than that in the first series, but still strong enough to be easily recognized. The results showed that the ice was essentially mechanically isotropic for loading in the plane of the ice sheet, implying that there is a relatively sharp transition from isotropy to anisotropy as the intensity of c-axis orientation increases.

Finally, a short series of measurements was done to compare **the strengths** of first year and multi-year ice. The results showed no significant differences over the range of loading rates and temperatures used in the experiments.

/

REFERENCES CITED

- Croasdale**, K. R. (1974) Crushing strength of Arctic Ice; *in* Coast and Shelf of the **Beaufort** Sea, Proceedings of a Symposium on Beaufort Sea Coast and Shelf Research, J. C. Reed and J. E. **Slater**, eds., Arlington, Virginia, Arctic Institute of North America, PP. 377-399.
- Groasdale**, K. R., Morgenstern, N. R. and **Nuttall**, J. B. (1977) Indentation tests to investigate ice pressures on vertical piers; Jour. **Glac.**, v. 19, no. 81, pp. 301-312.
- Deklotz**, E. J. and **Boisen**, B. P. (1970) Development of Equipment for determining deformation modulus on in situ stress by means of large **flatjacks**; *in* Determination of the In Situ Modulus of Deformation of Rocks, ASTM STP 477, pp. 117-125.
- Gold, L. W. (1979) The process of failure of **columnar-grained** ice; Phil. Msg., v. 26, *no.* 2, pp. 311-328.
- Jacka**, T. H. (1984) The time and strain required for development of minimum strain rates in ice; Cold Regions Sci. and Tech. v. **8**, pp. 261-268.
- Jaeger, J. C. and Cook, N. G. W. (1976) Fundamentals of Rock Mechanics, 2nd cd., **Halsted** Press, New York, pp. 585.
- Peyton, H. R. (1966) Sea ice strength; Geophysical Inst. U. of Alaska-Fairbanks Report UAG R-182, pp. 273.
- Pratt, **H. R.**, Black, A. D., Brown, W. **S.** and Brace, **W. F.** (1974) A new technique for determining the deformation frictional characteristics of in situ rock; *in* Field Testing and Instrumentation of Rock; ASTM STP 554, pp. **3-19**.
- Shapiro, **L.H.** and Hoskins, **E. R.** (1975) The use of **flatjacks** for the in situ determination of the mechanical properties of sea ice; **Proc. 3rd Conf.** on Port and Ocean Eng. under Arctic Conditions, Fairbanks, Alaska, pp. 427-436.

- Shapiro, L. EL, Hoskins, E. R., Nelson, R. D. and **Metzner, R. C. (1979) Flatjack** methods of in situ measurement of the mechanical properties of sea ice; Trans., A.S.M.E., Jour. Energy Resources Tech., v. 101, pp. 1996-2002.
- St. Lawrence, W. F. and Cole, D. M. (1982) Acoustic emissions from **polycrystalline** ice; Cold Regions Sci. and Tech. v. 5, pp. 183-199.
- Wang, Y. S., 1979, Crystallographic studies and strength tests of field ice in the Alaskan Beaufort Sea; Proc. 5th **Conf.** on Port and Ocean Eng. under Arctic Conditions, **Trondheim**, Norway, pp. 651-655.
- Weeks, W. F. and Assur, A. (1967) The mechanical properties of sea ice; USA **CRREL** Cold Regions Science and Engineering, Part **II**, Section C, pp. 80.
- Weeks, W. F. and Gow, A. J. (1978) Preferred crystal orientations in the fast ice along the margins of the Arctic **Ocean**; USA **CRREL** Report 78-13.

2.3 A STRESS-STRAIN LAW AND FAILURE CRITERION FOR SEA ICE

by

Lewis H. Shapiro

ABSTRACT

The objective of this section is to describe **the deformational** behavior of the **spring-dashpot** model of a 4-parameter **viscoelastic** fluid constrained to fail according to the distortional strain energy density criterion. The results predict upper and lower strength limits for the model, and permit curves to be derived which show the relationships between the results of hypothetical tests on the models at different loading paths and rates. Comparison of the analytical results to experimental data for sea ice and **polycrystalline** fresh ice shows that the trends of the curves are similar and that the strength limits may correspond to transitions in deformation mechanisms. This suggests that the combination of a more realistic non-linear model with the failure criterion could provide an accurate description of the stress-strain relations and failure of ice under a range of loading conditions.

2.31 INTRODUCTION

A program of evaluation of previous work on the strength and mechanical properties of sea ice was conducted along with the experimental work described in the last section of this report. The objective was to identify and characterize the reformational behavior of sea ice, with the intent of using the results to indicate a possible form of a stress-strain law and failure criteria for sea ice. Since most of the available data are for loading in **uniaxial** compression (as are the results reported in Section 2.24.5), the law was to be restricted to deformation in that loading mode. However, examination of the published data for tests in other loading modes suggests that the results may be applicable to some of these as well.

It is well known from experimental work that, for **uniaxial** compression tests, most types of ice follow the same basic patterns of response to load. In general, the strength and rate of deformation are non-linearly **related** to the load (in constant load tests) or to the rate of loading (in constant load rate or constant deformation rate tests). This is certainly true for sea ice, as shown by the data in the last section and by the review of the literature. In addition, as has been previously noted (see, for example, **Mellor**, 1980), the stress-strain curves for ice are qualitatively similar to curves calculated for the response to load of the model of a linear 4-parameter **viscoelastic** fluid (**4-PF**). This suggested that the stress-strain law for a 4-PF with non-linear elements might provide realistic curves to match the data. Accordingly, a series of stress-strain calculations were done for such a **4-PF** model, and the work was extended to consider the case where the model is constrained to fail under the **distortional** strain energy criterion (**DSEC**). The results qualitatively predict the relationships between tests along different loading paths and also provide a basis for explaining many of the results of experimental programs. In addition, they lead to suggestions for further experimental work.

The stress-strain law for the 4-PF model with non-linear elements is cumbersome and requires numerical values of the parameters for calculation of the curves, so that it is **difficult** to generalize the results. In order to permit generalizations to be made, and to examine the details of the behavior of the combined 4-PF and DSEC model, it is preferable to use the model with linear elements for which most of the derivations can be done in closed form. The presentation and discussion of the results of that work in terms of available data is the subject of this report.

The remainder of this section is divided into five sub-sections. The characteristics and justification for the use of the 4-PF model and the DSEC are described in Sections 2.32 and 2.33 respectively. They are then combined in Section 2.34 and the conditions for **yield** of the model under different loading programs are derived without reference to experimental results. There are two reasons for this approach. First, as noted above, the stress-strain laws for the elements in the model are taken to be linear. This permits most of the derivations and proofs to be done in closed form rather than numerically, which is convenient for qualitative comparison between the deformation of the model and the available data. However, the results of this analysis cannot be applied quantitatively to the non-linear behavior of sea ice. The results of calculations based **on** the non-linear model are shown for comparison, to illustrate that the trends of the relationships are independent of the form of the laws. However, the results of this section are intended to be interpreted qualitatively.

The second reason is to emphasize the fact that the **model** is simply a mathematical device which may (or may not) represent the response to load of a real material over some range of conditions. **In** effect, it is a mathematical entity which is independent of any data set. Its utility for describing the reformational behavior of a real material depends upon the extent to which the calculated deformation of the

model and the actual data agree. There is no *a priori* reason to expect these to agree over any, or all, of the possible ranges of the variables; the degree to which they correspond is a matter to be determined from examination of the data. The model responses are discussed in terms of imaginary experiments on some ideal material which the model represents. This is done so that uncertainties which arise in experimental programs can be included in the interpretation of the calculated results.

The results of the calculations are compared to the data on different ice types in Section 2.35. This section relies heavily on the data for sea ice presented in Section 2.24.5 and 2.24.6, and on data from Hawkes and **Mellor** (1972), **Mellor** and Cole (1982) and **Jacka** (1984) on **polycrystalline** fresh ice.

The summary, conclusions and suggestions for further work are given in Section 2.36, which is followed by an appendix where the details of the derivations appear.

In the equations which follow, the symbols σ for stress and ϵ for strain are assumed to be functions of time. They are written as shown in the interest of brevity. A dot over a time-dependent variable indicates the time derivative, and a zero subscript always defines a constant value (i.e. ϵ_0 is a constant strain rate; σ_0 is a constant stress). The "constants" used in the model are constant with respect to stress and strain, but would be expected to vary with the temperature and physical properties of the medium they represent. That variability is not considered here.

2.32 DESCRIPTION OF THE 4-PARAMETER FLUID MODEL

The justification for the use of the 4-PF model follows from the assumption (commonly used in the analysis of deformation experiments on ice and other materials) that the total deformation includes elements of instantaneous elastic

response to the applied load followed by both time-dependent elastic and plastic behavior. Thus, the total strain is often represented by the equation

$$(1) \quad \epsilon_T = \epsilon_E + \epsilon_V + \epsilon_D$$

where ϵ_T , ϵ_E , ϵ_V and ϵ_D are the **total** strain, “instantaneous” elastic strain, **time-**dependent elastic strain and time-dependent plastic strain, respectively. Equation (1) represents the response to load of the spring- dashpot model of a 4-PF (shown with linear elements in Figure 2.3-1) consisting of **Voigt** and Maxwell models connected in series. This is the simplest of the **spring-dashpot** models that contains all of the elements of a creep curve. The spring of the Maxwell model gives the “instantaneous” elastic response to an applied load while the viscous creep of the **dashpot** of the Maxwell model at constant stress represents the summation of the contributions of the mechanisms which produce time-dependent permanent deformation in actual materials. The **Voigt** model provides a time-dependent elastic response which, in a creep curve, gives the decrease in strain rate with time through the primary creep stage and the time-dependent recovery of strain in the recovery stage following release of the load. Sinha (1979) suggested that grain boundary sliding is the mechanism which is responsible for this behavior. The use of the **Voigt** model here is justified by Hart et al. (1975) based upon experimental data from metals. They argued that the data require that the stress-strain relationship for delayed (time-dependent) elasticity is of the form

$$(2) \quad \dot{\epsilon} = f[\sigma - M\epsilon]$$

where $\dot{\epsilon}$ is the strain rate and σ is the applied stress. The parameter M is defined as the “saturation” modulus and is found from the equation

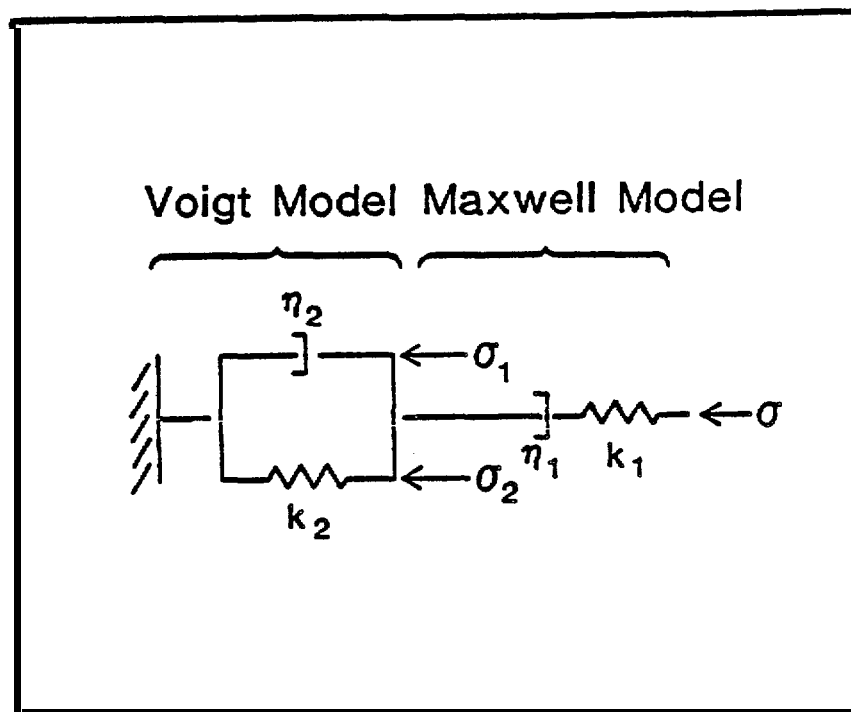


Figure 2.3-1 **Spring-dashpot** model of a 4-parameter linear **viscoelastic** fluid. k_1 and k_2 are spring constants, η_1 and η_2 are the Newtonian viscosities of the dashpots. σ_1 and σ_2 show the partitioning of the applied stress σ across the arms of the **Voigt** model, such that $\sigma = \sigma_1 + \sigma_2$ (see text).

$$M = \sigma_0 / \dot{\epsilon}_M$$

when $\dot{\epsilon}$ goes to zero and the strain reaches its maximum value ϵ_M at the transition from primary to steady state creep in a test at constant stress. Equation (2) is simply the form of the stress-strain law for a **Voigt** model (**Flugge**, 1967) in which M corresponds to the modulus of the spring k_2 in the 4-PF model (Figure 2.3-1).

Equilibrium of the stresses across the **Voigt** model (Figure 2.3-1) requires that

$$\sigma = \sigma_1 + \sigma_2$$

so that, for the linear case, the strain and strain rate are

$$\epsilon_V = \sigma_1 / k_2$$

and

$$\dot{\epsilon}_V = \sigma_1 / \eta_2,$$

where η_2 is the coefficient of Newtonian viscosity. Thus, the stresses, strain and strain rate of the **Voigt** model are related by the equilibrium condition at any stage in the loading path.

An important limitation on the ability of the 4-PF model to predict the response of actual materials follows from the form of equation (1) in which the contributions of the mechanisms which produce each of the types of response to load described above are added linearly. This is equivalent to the assumption that the elements do not influence each other in the sense that, for example, the magnitude of deformation due to time-dependent plastic flow mechanisms does not lead to changes in the values of the parameters which govern other types of deformation. It seems likely

that this assumption must fail at some point in the deformation process, but the subject has not been investigated.

The parameters of the linear form of the 4-PF model have been determined for **polycrystalline** fresh ice from creep tests in tension (**Jellenick** and **Brill**, 1956) and in **uniaxial** and biaxial compression (Lindgrin, 1970), and for young sea ice in compression and bending (**Tabata**, 1958). **Nevel** (1976) used this stress-strain law in a theory of the creep of floating ice sheets. Stress-strain laws which are similar to the 3-or 4-parameter **viscoelastic** model have been applied to ice by Maser (1972) and Sinha (1978). The general application of these types of laws to ice has been discussed by **Mellor** (1980).

Note that there is no requirement that the elements of the model in Figure 2.3-1 be **linear**; non-linear elements (both springs and dashpots) have been used by different authors to describe the deformation of different materials. Hutter (1980) pointed out that only the hyperbolic sine law for steady-state creep is based on a theory of material behavior, the rate process theory [**Glasstone et al.**, (1941); **Krausz** and Eyring, (1975)]. Commonly, the hyperbolic sine law is used for the dashpot of the Maxwell model in Figure 2.3-1, as in the non-linear stress-strain rate law for creep

$$\dot{\epsilon} = A (\sinh \phi \sigma)^n.$$

However, it has also been used for the dashpot of the Voigt model in the application of the stress-strain law of a 3-parameter viscoelastic solid to polymers, rubber and textiles (**Krausz** and Eyring, 1975, and references cited therein). The non-linear law considered earlier in this project (and described in the appendix) involved the use of the hyperbolic sine law for both dashpots. Other workers have used other

combinations of linear and non-linear elements. This is permissible, provided that the contributions of the model elements add as shown in equation (I).

For any stress-strain relations of the individual elements, the 4-PF model yields a differential equation which can be integrated for any loading path. The discussion here will be restricted to the paths commonly used in experimental programs; constant stress (**CS**), constant stress rate (**CSR**) and constant strain rate (**CDR**). The curves from the integrated equations for these paths for the linear model are shown in the appendix. They are qualitatively similar to experimental curves for ice up to the point of failure (see, for example, the discussion in **Mellor**, 1980).

The parameters of an ideal linear material represented by a 4-PF model can be determined from the results of a single creep test. More creep tests would be required in order to determine the form of the stress-strain law for the dashpot of the Maxwell model of an ideal non-linear material. Given that law, the form of the laws for the elements of the **Voigt** model can be found. However, these determinations assume that the material is in steady state creep, as required by the definition of the "saturation" modulus above. As discussed in Section 2.35.2, this condition is probably never reached in experiments on ice. Thus, there is a question as to the significance of the parameters reported in the references above. The point is discussed in Section 2.35.4.

2.33 **DESCRIPTION** OF THE DISTORTIONAL STRAIN ENERGY DENSITY YIELD CRITERION

Reiner and Weissenberg (1939) suggested the idea of applying the DSEC to spring-dashpot models, and **Reiner** (1960) demonstrated the results for the **3**-parameter linear **viscoelastic** solid. The extension to the 4-parameter model follows directly. Day (1975) has given a general proof that the application of the DSEC to models of this type is valid without restriction to elements with linear stress-strain

laws, provided that the model elements do not influence each other, in the sense described above.

The DSEC is based upon Von Mises criterion expressed in terms of the strain rather than the stress (Reiner, 1960). The work done by the applied stress in deforming the dashpots of the model is assumed to be dissipated through internal friction, while that done on the springs is stored as **distortional** elastic strain energy. Yield is assumed to occur when the stored distortional strain energy reaches the resilience, "R", the energy (per unit volume) required to deform an elastic body to its elastic limit.

Note that while the Von Mises criterion was derived to predict yield (the onset of flow) of plastic materials, it has also been used as a fracture criterion for ice, rock, and other materials as in (Section **3.1below**) For the remainder of this work, the general term "failure" is used in place of "yield" since, as shown below, the DSEC appears to apply to experimental results over the range from ductile to true brittle behavior.

Von Mises criterion is expressed by the equation

$$J_2 = K^2,$$

where J_2 is the second invariant of the stress deviator tensor and K is the shear strength of the material represented by the model. Assuming the material to be elastically isotropic, for **uniaxial** loading at a stress σ , following **Mendelson (1968)**

$$J_2 = (1/3) \sigma^2$$

and the distortional strain energy is

$$U_d = (1/6G) \sigma^2 = (1/2G) J_2$$

where G is the shear modulus. Then, from Reiner (1960) the distortional strain energy of the 4-parameter model is simply the sum of the strain energies stored in the two springs. Failure occurs when

$$(3) \quad U_d = R = k_1(\epsilon_E)^2 + k_2(\epsilon_V)^2$$

in which k_1 and k_2 are the spring constants (Figure 2.3-1).

Note that this relationship applies regardless of the functional form of the stress-strain laws of the elements of the model, or the loading path. It simply expresses the required relationship between the spring **moduli** and the stored elastic energy at the instant of failure. In this sense, the **DSEC** differs from some other failure criteria in that it is written in terms of the material parameters rather than the instantaneous state of stress, strain or strain rate, or their histories. It is this aspect of the criterion which provides flexibility in application to different loading paths and has the potential to predict the strength of the model from its properties alone, independently of the the loading paths. However, the influence of deformation history is accounted for in the calculation of the failure stress in any particular case, as shown in Section 2.34.

In using the **model** to represent a real material, the model parameters are determined from experiments in which no permanent deformation of the **sample** (i.e., fracturing or **re-crystallization**) occurs. This introduces a question as to the meaning of the term "failure" as it applies to the model. In general, failure can be viewed as a process, rather than an event, in the sense that a critical stress at which failure occurs is not reached throughout the entire test specimen at the same instant. Instead, the sample breaks down over a finite time interval as the stress is redistributed after each successive failure of a relatively small volume within which

the critical state has been reached. The time required for the process to run its course varies from almost instantaneous for the case of brittle fracture at high loading rates, to much longer times for lower loading rates or low magnitudes of constant stress. In any case, the breakdown of the sample is accompanied by changes in the material constants, such as the decrease in Young's modulus which results from an increase in the number and lengths of cracks in a sample. Similarly, re-crystallization during creep at low stresses produces an essentially new material. Now, assume that an accurate stress-strain law is written for some material based upon its properties in the initial state, and the law is used to calculate the response of the material for a particular loading path. The experimental curve for such a material loaded to "failure" along that loading path would initially follow the calculated curve. However, as the material parameters of the sample change by crack growth or **re-crystallization** as failure is approached (depending upon the loading path, as discussed below) the experimental curve would tend to deviate from the calculated curve. The separation of the two curves **would** occur when the material parameters had changed sufficiently that the material no longer followed the calculated curve. Subsequently, the test is, in effect, being conducted on a "new" material, in the sense that its properties are not the same as those at the start of the test. In an actual experiment, the identification of the point where the curves separate would depend upon the precision with which the test parameters could be monitored.

The sense in which the discussion above is meant is well illustrated by the inflection point at the minimum strain rate of a **CS** test. Since the stress (and other test conditions) are held constant through the test, the change in response of the sample to the load as it passes from the secondary to tertiary creep stages can best be explained as resulting from changes in the values of the material parameters. The

changes may occur gradually through the test, but only become apparent when they are cumulatively great enough to cause the curve to deviate from its projected path.

The suggestion is that the point of separation of the experimental and theoretical curves in CS tests is predicted by a failure criterion based upon the initial parameters. This raises the question of whether the comparable point in CSR or CDR tests is close to or at the peak stress which might ultimately be reached in the test. There is presently no firm basis for answering this question **in** the absence of experimental data. The best that can be done is to compare the theory to the data, as is done in Section 2.35.

The reader who is familiar with the literature on the deformation of ice in **uniaxial** compression will undoubtedly recognize the similarities to the behavior of the model as they arise in the following sections. However, for purposes of discussion, it is simpler to describe these relationships first in terms of the idealized model. Then, the results can be compared to the data for the real material. This approach has the added advantage of emphasizing the fact that the model is a mathematical device which may or may not represent the behavior of a real material over some range of conditions. The degree to which the response to applied load of the model and the real material correspond is a matter to be determined.

2.34 APPLICATION OF THE DSEC TO THE 4-PF MODEL

2.34.1 UPPER AND LOWER STRENGTH LIMITS

An immediate result of the application of the DSEC to the 4-PI? model is to set upper and lower bounds on the strength of the model. Further, these limits are independent of the loading path and the functional forms of the stress-strain laws **for the viscous elements of the model. The upper limit can be found in terms of the strain in the springs by rewriting equation (3) in the form of the ellipse**

$$(k_1/R)(\epsilon_E)^2 + (k_2/R)(\epsilon_V)^2 = 1$$

in which k_1/R and k_2/R are the major and minor axes respectively. Note that this assumes that $k_1 > k_2$, which seems to be justified based upon the determinations of the parameters noted above. Stable combinations of the elastic strains plot within the ellipse while failure occurs for combinations of the elastic strain of the two spring elements which plot along the ellipse. Failure at the point of intersection of the ellipse and the ϵ_E -axis corresponds to the case when all of the strain energy required to cause failure is stored in the lead spring of the model. Since the spring of the Voigt element extends as a function of time, it follows that failure under this loading condition occurs instantly on application of the load, before any strain can accumulate in the Voigt model. The stress required to cause failure under this condition is simply

$$(4) \quad \sigma_u = k_1 \epsilon_u$$

where $\epsilon_u = \epsilon_E$ when the strength $\sigma_c = \sigma_u$ as time t goes to zero in the limit.

Failure at the intersection of the ellipse and the ϵ_V -axis (i.e. $\epsilon_E = 0$) requires that the applied stress and the modulus of the spring of the Voigt model be infinitesimally **small**. This is because any applied stress of finite magnitude must cause some strain in the spring of the Maxwell model. Thus, if the spring **moduli** are finite, there must be some lower limit to the stress which can cause failure.

The stresses at both the upper and lower limits can be found by rewriting equation (3) in terms of the stresses across the springs at failure, using **Hooke's** law for each of the springs, to give

$$(5) \quad U_d = R = (l/k_1) \sigma^2 + (1/k_2)(\sigma_2)^2$$

or

$$(1/k_1 R) \sigma^2 + (1/k_2 R)(\sigma_2)^2 = 1.$$

As above this is also the equation of an ellipse with $k_1 R$ and $k_2 R$ as the major and minor axes respectively (Figure 2 3-2). Equilibrium of the stresses across the elements of the **Voigt** model requires that σ_2 be less than or equal too. Therefore, the stresses at failure must lie on the ellipse and to the right of the 45° line in Figure 2.3-2. Stable combinations of stresses plot inside the ellipse.

The intersection of the failure ellipse with the o-axis gives σ_u as defined in equation (4) or, from equation (5), with $\sigma_2 = 0$,

$$(6) \quad \sigma_u = (k_1 R)^{1/2}.$$

Note that this represents an upper limit to the strength only in the sense that **it is** the largest stress that the model can sustain for a finite length of time and can therefore be measured against the model in an experiment. Any attempt to apply a load larger than σ_u would cause the model to fail instantly as the stress passed through σ_u . The intersection of the 45° line and the ellipse gives the minimum value **of σ ($= \sigma_b$)** required to cause the **model to fail**. From the appendix, this occurs when the time t approaches infinity in the limit, so that $\sigma_2 \rightarrow \sigma$, which, from equation (5), gives

$$(7) \quad \sigma = \sigma_b = [R k_1 k_2 / (k_1 + k_2)]^{1/2}.$$

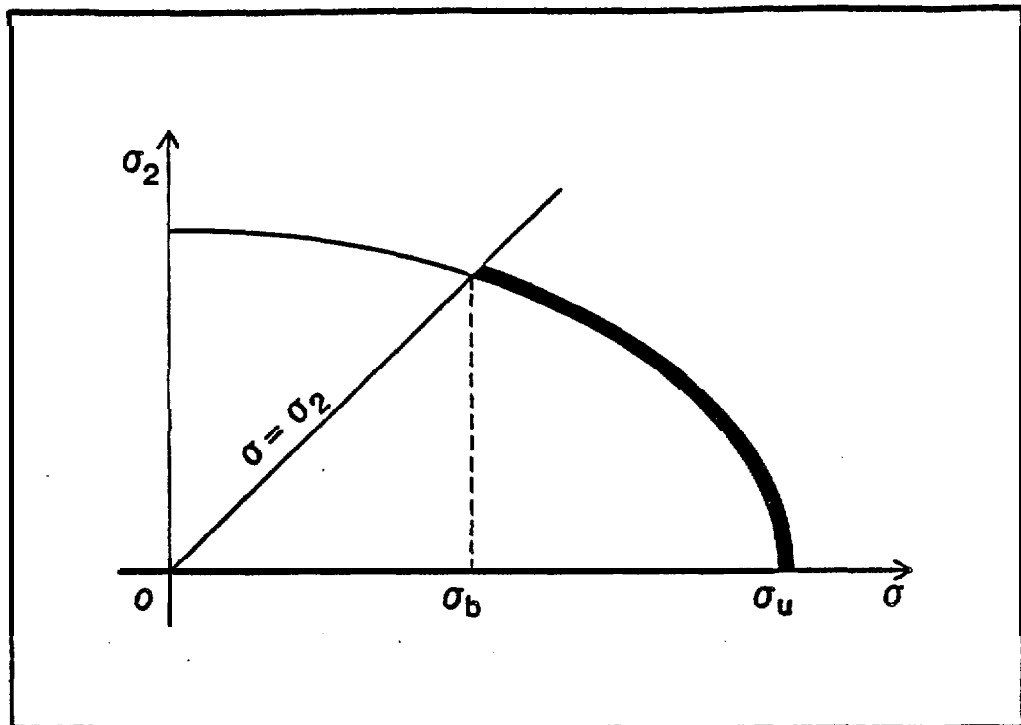


Figure 2.3-2 **Yield** envelope **in** terms of the applied stress σ and the stress across the spring of the **Voigt** model, σ_2 . Since $\sigma_2 \leq \sigma$, the state of stress must plot to the right of the line at 45° to the o-axis. σ_u and σ_b as indicated (see text for discussion).

Note that for a CS test at some $\sigma > \sigma_b$ failure depends upon the time required for the stress σ_2 to rise to the ellipse along a path normal to the o-axis. The time depends on both elements of the Voigt model through the relaxation time

$$\tau_2 = \eta_2/k_2$$

and the applied stress (see appendix). It is small when the stress is large, and approaches infinity as $\sigma \rightarrow \sigma_b$. Any $\sigma < \sigma_b$ can be sustained indefinitely by the model, because no stress path which does not intersect the ellipse to the right of the 45° line can cause failure. In the limit, a **CS** test on the model at a stress less than σ_b should reach steady state (in the ideal sense of a constant strain rate) because there will never be sufficient strain energy accumulated in the springs to cause failure. This is the condition at which the “saturation modulus” of Hart et al. (1975) referred to above can, theoretically, be determined. From **that** point, no further elastic strain occurs, and the only element of the model which is active is the dashpot of the Maxwell model. Similarly, a CDR test in which

$$\sigma = \eta_1 \dot{\epsilon}_D < \sigma_b$$

will go to a steady state stress.

The stress σ_b thus represents the “fundamental strength” of the model; it is the largest stress which the **model** can sustain indefinitely without failure. While, as noted, experimental evidence indicates that it is incorrect to suggest that there is a lower limit to the strength of ice (see Section 2.24.63), the concept has implications for theoretical and experimental work as well as potential utility in applied problems. The point is discussed further in Section 2.35.4 below.

Finally, note that, for the, case when the elastic **modulii** are constant,

the fundamental and maximum strengths of the model are related through the ratio of the spring **moduli** as [from equations (6) and (7)]

$$\sigma_u/\sigma_b = [1 + (k_1/k_2)]^{1/2}.$$

2.34.2 RELATIONSHIPS AT FAILURE

2.34.21 INTRODUCTION

The DSEC prescribes relationships at failure of the 4-PF model between stress, strain, strain rate and time which are similar to those observed from experiments on ice. This will be illustrated by considering the determination in CS, CSR and CDR tests of both the linear 4-PF model and a non-linear model in which the strain rates of the dashpots are related to the stress through the hyperbolic sine law. It will be apparent that the qualitative results (i.e. the forms of the curves) are independent of the linearity or non-linearity of the stress-strain laws of the model elements.

In developing the arguments below, the solutions for the relationships between strength, strain rate, strain and time for **CS** and CSR tests are derived in closed form for the linear model (see appendix). In both tests, the stress applied to the model is specified, so that the stress across each of the model elements connected in series is known independently of the deformation. The partitioning of the stress across the elements of the **Voigt** model can be found from the equilibrium condition above. Thus, the response of any element of the model to the applied load can be determined without reference to the state of deformation of any other element and it is not necessary to assign specific stress-strain **laws** (with numerical values of the constants) to the dashpots of the **model**. In CDR tests, this is not the case. When a constant strain rate ($\dot{\epsilon}_0$) is applied to the linear model, the strain rate is partitioned across the elements so that the equation

$$\dot{\epsilon}_0 = \dot{\epsilon}_E + \dot{\epsilon}_D + \dot{\epsilon}_V$$

is satisfied. As a result, the stress varies with the deformation according to a rather complicated algebraic expression (see appendix) which requires that a stress-strain relationship and numerical values be assigned to the dashpot of the Maxwell model if the stress is to be determined. For convenience, ~~the~~ solutions were done numerically and the results non-dimensionalized to the same parameters as were used **in** the case of the CS and **CSR** tests. The procedures are given in the appendix.

For the non-linear 4-PF model, closed form solutions were derived for the cases of **CS** and CSR tests, but a numerical solution was required for CDR tests. **In** addition, it was not practical to non-dimensionalize the parameters of the non-linear model. Instead, numerical values were used. The values were selected based on the results of experimental determinations of the parameters of the linear **model** for different ice types (see reference in section 2.32). They are clearly approximations, so that the results are not intended to represent any particular type of ice. The values used in the calculations for the non-linear model are given in the appendix.

In the discussion which follows, the term “strength” refers to the stress in a CSR or **CDR** test at the instant the failure criterion is satisfied. In **CS** tests, strength is simply the applied stress, which is assumed to be between the strength limits so that “failure” occurs as a function of time. The equations which describe the deformation of both the linear and non-linear **models** (see appendix) permit the stress, strain, stress rate, strain rate, and time at “failure” to be calculated for any test. The results of these calculations were used to prepare the curves in the following sections.

2.34.22 STRAIN AT FAILURE

Figure 2.3-3 is a chart which shows the stress-strain and stress- strain rate relationships for each of the elements of the linear model at the instant of failure under a **uniaxial** compressive stress for CS, CSR and CD tests. As illustrated in the chart, the elastic strain in the springs of the model must be partitioned in the same manner regardless of the loading path. This is because the strain of the lead spring is determined by the stress at failure (through a 1-dimensional elastic stress-strain **law** applied to the spring). This, in turn specifies a single value of the strain in the Voigt model which is required to satisfy the **DSEC**. The proof is given in the appendix for **CS** and CSR tests; calculations for CDR tests (also in the appendix) give the same result.

A plot of the elastic strain at failure vs. compressive strength (see appendix for elastic **modulii**) is shown in Figure **2.3-4** in which σ_u is the upper strength limit of the model and ϵ_u is the strain at that stress. Note that the curve shows relatively little "variation over most of the range of possible strengths. However, it passes through a maximum value of the elastic strain at failure at the "fundamental strength," (as indicated in Figure 2.3-4), which is too low to be evident at the scale of the plot.

In order to find the total strain at failure for comparison, it is necessary to include the strain **of** the dashpot of the Maxwell model. To permit this strain" component to be calculated, the **coefficient** of Newtonian viscosity (η_1) was assumed to have the value required to match the strain rate predicted by the power law at a stress of 1 **MPa** (see appendix). The curve for the total strain at failure for a CS test on a model with the same ratio of elastic **modulii** as was used to calculate the elastic strain at failure is also shown in Figure 2.3-4. The curve for the total strain at failure for CSR and **CDR** tests (with the same **modulii**) must lie between the two

| | | STRAIN AND STRAIN RATE | CONSTANT STRESS CL. $\sigma_c = \text{CONSTANT}$ | CONSTANT STRESS RATE CLR. $\sigma_c = \dot{\sigma}_0 t_f$ | CONSTANT DEFORMATION RATE CD. $\epsilon_T = \dot{\epsilon}_0 t_f$ |
|---------------|---------|-------------------------|---|--|--|
| MAXWELL MODEL | SPRING | $\epsilon_{ef} =$ | $\frac{\sigma_c}{k_1}$ | $\frac{\sigma_c}{k_1} = \frac{\dot{\sigma}_0 t_f}{k_1}$ | $\frac{\sigma_c}{k_1}$ |
| | | $\dot{\epsilon}_{ef} =$ | 0 | $\frac{\dot{\sigma}_0}{k_1}$ | $\frac{\dot{\sigma}_0}{k_1}$ |
| | DASHPOT | $\epsilon_{of} =$ | $\frac{\sigma_c t}{\eta_1}$ | $\int_0^t \frac{\dot{\sigma}_0 t}{\eta_1} dt$ | $\int_0^t \frac{\sigma}{\eta_1} dt$ |
| | | $\dot{\epsilon}_{of} =$ | $\frac{\sigma_c}{\eta_1}$ | $\frac{\dot{\sigma}_0}{\eta_1}$ | $\frac{\dot{\sigma}_0}{\eta_1}$ |
| VOIGT MODEL | | $\epsilon_{vf} =$ | $\frac{\sigma_2}{k_2}$ | $\frac{\sigma_2}{k_2}$ | $\frac{\sigma_2}{k_2}$ |
| | | $\dot{\epsilon}_{vf} =$ | $\frac{\sigma_c - \sigma_2}{\eta_2}$ | $\frac{\dot{\sigma}_c - \dot{\sigma}_2}{\eta_2}$ | $\frac{\dot{\sigma}_c - \dot{\sigma}_2}{\eta_2}$ |

Figure 2.3-3 Chart showing the relationships between the stress, strain and strain rate in each element of the linear 4-PR **model** at yield according to the DSEC for three loading paths.

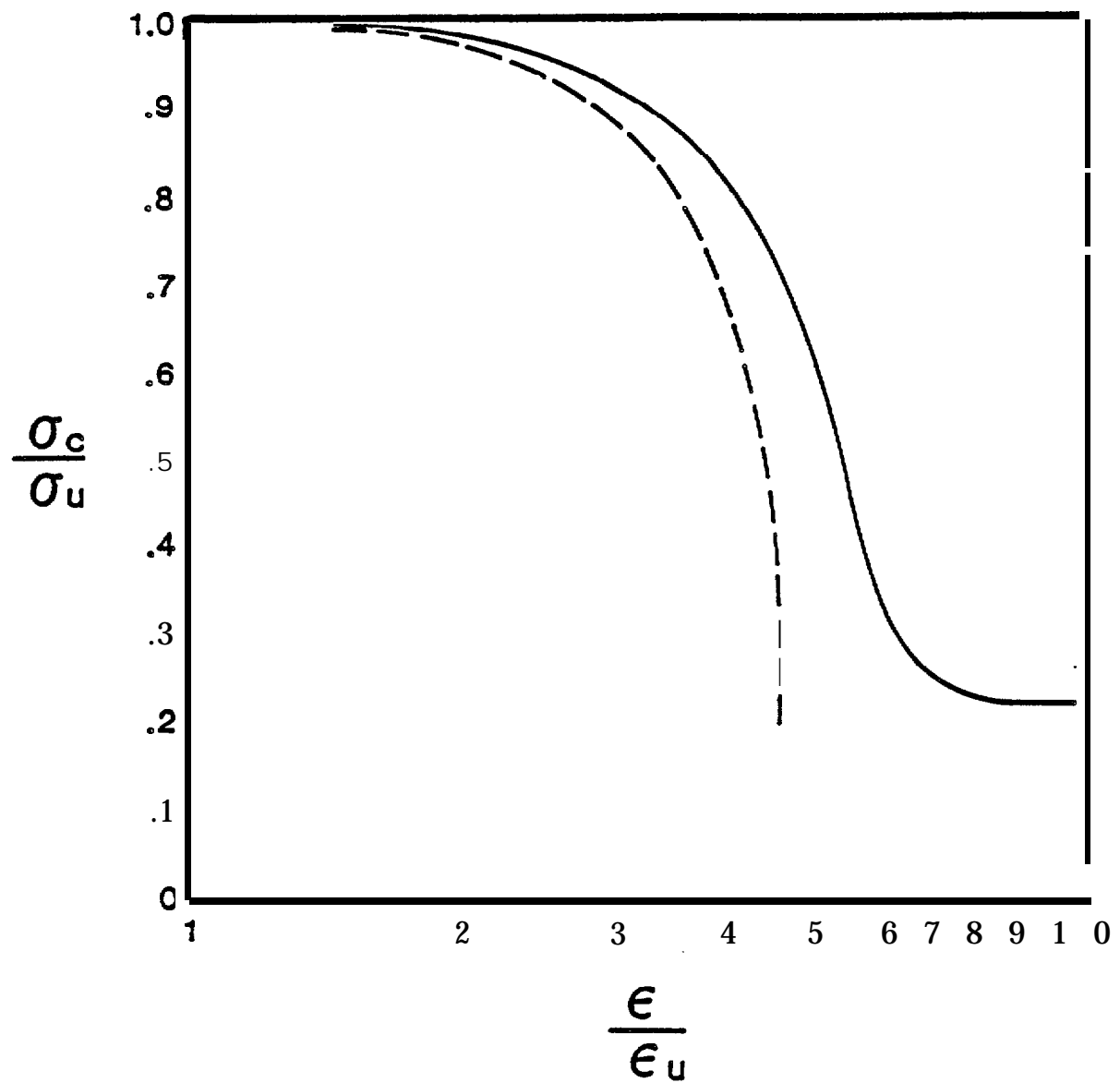


Figure 2.3-4 Stress ratio vs. strain ratio at yield for the linear model.
Dashed line is elastic strain and solid **line** is total strain (see text for discussion).

curves shown. This follows because the strain in the dashpot of the Maxwell model at failure must be greatest for CS tests since the sample is under the peak load for the duration of the test. Figure 2.3-4 shows that, as for the elastic strain, the total strain at failure is also relatively constant over most of the range of possible strengths. The increase in total strain at low strength reflects the increase in **time-to-failure** (discussed in Section 2.32.24) which permits the strain in the dashpot of the Maxwell **model** to become large.

The shape of the curve for the total strain is obviously dependent on the **stress-strain** law of the lead dashpot. For a non-linear **dashpot**, in which the strain rate increases rapidly with increasing stress, the curve for total strain might be anticipated to be straighter than that for the linear model. An example calculated from the non-linear law is shown in Figure 2.3-5. The relevant derivation is given in the appendix.

The results suggest that, over most of the range of strengths, the total strain at failure in **CS**, CSR and CDR tests should show **little** variation. Thus, in actual experiments, the normal uncertainties of strain measurement might prevent the details of the curve from being defined, so that the results would suggest that the strain at failure is independent of the strength.

2.34.23 STRAIN RATE AT FAILURE

A second point that can be deduced from the chart in Figure 2.3-3 is that the strain rates at the instant of failure should also be similar for any strength for CS, **CSR** and CDR tests. This follows because the strain rate of the lead dashpot is fixed by the stress at failure regardless of the form of its stress-strain law. Further, since the strain of the **Voigt** model must be the same at any strength for any loading path, the partitioning of stress in the Voigt **model** requires that the stress on the spring (σ_2) be the same at failure, independent of the loading path. Therefore, the stress on

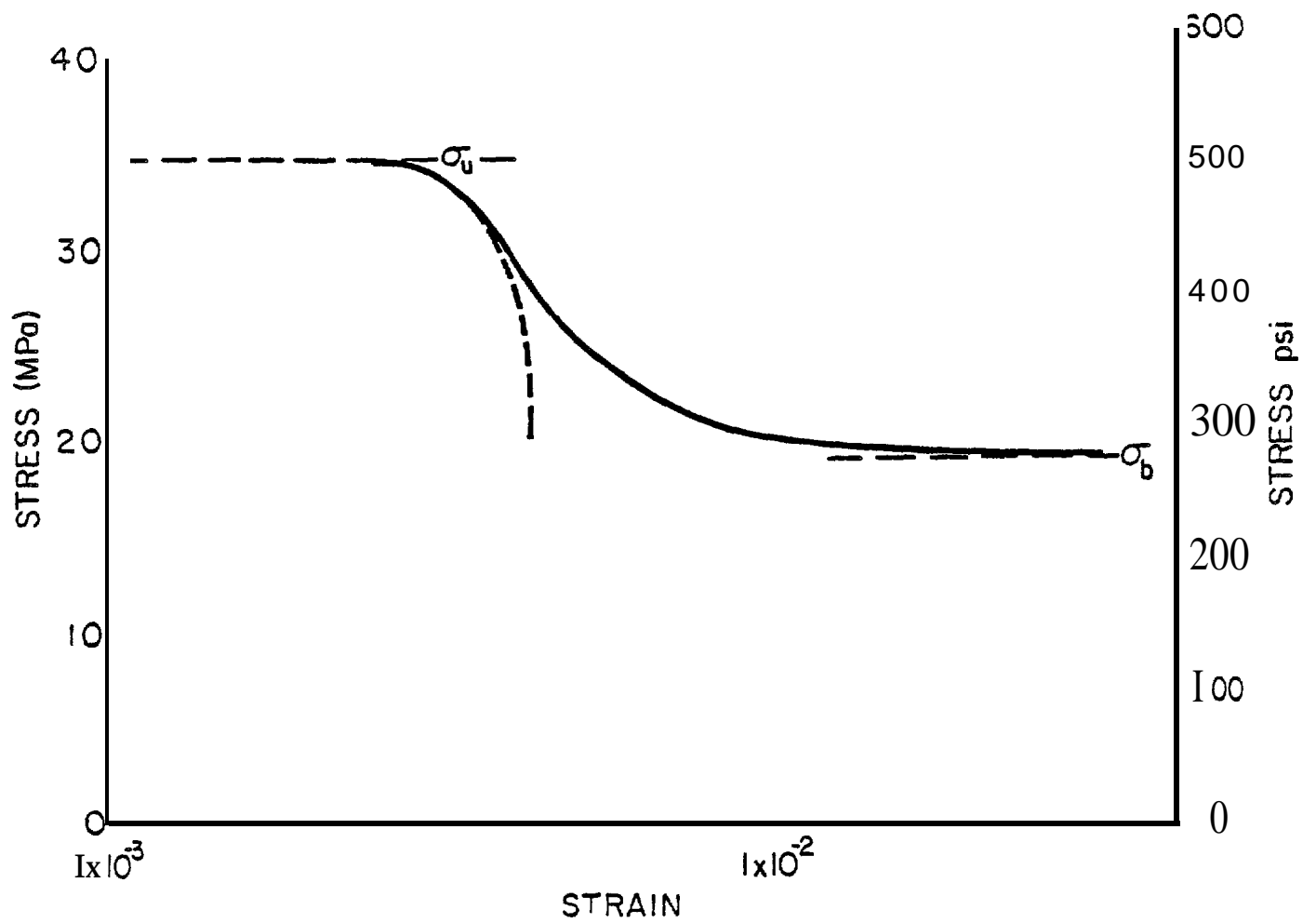


Figure 2.3-5 Stress vs. strain at yield for the non-linear 4-PI model described in the text. Dashed line is elastic strain and solid line is total strain. σ_u and σ_b are the upper and lower strength limits.

the dashpot ($\sigma - \sigma_2$) is also the same, so that the strain rate of the Voigt model is the same. Thus, the differences between strain rates at failure for different loading paths depends only on the strain rate of the lead spring. This rate, in turn, depends on the rate of change of the stress according to the equation

$$\dot{\epsilon}_E = (1/k_1)\dot{\sigma}$$

For CS tests, the applied stress is constant so that the strain rate in the lead spring is zero. For CSR and CDR tests the strain rate at failure must therefore be greater, as shown in Figure 2.3-6 for the three loading **paths**. The limits on the range of possible strengths is indicated by the asymptotes to the upper and lower limits. For stresses below the fundamental strength, the model would simply go to steady state creep and the stress-strain rate curve in that range would follow the stress-strain curve for the **lead dashpot**.

The magnitude of the difference between the curves, and the limited range of strain rates over which failure occurs, reflect the assumption of linearity of the dashpots. This can be seen by comparing Figure 2.3-6 with Figure 2.3-7 which was calculated from the non-linear model. In this example, the curves for the three loading paths could not be separated at the scale of the plot and the range of strain rates at failure is clearly increased.

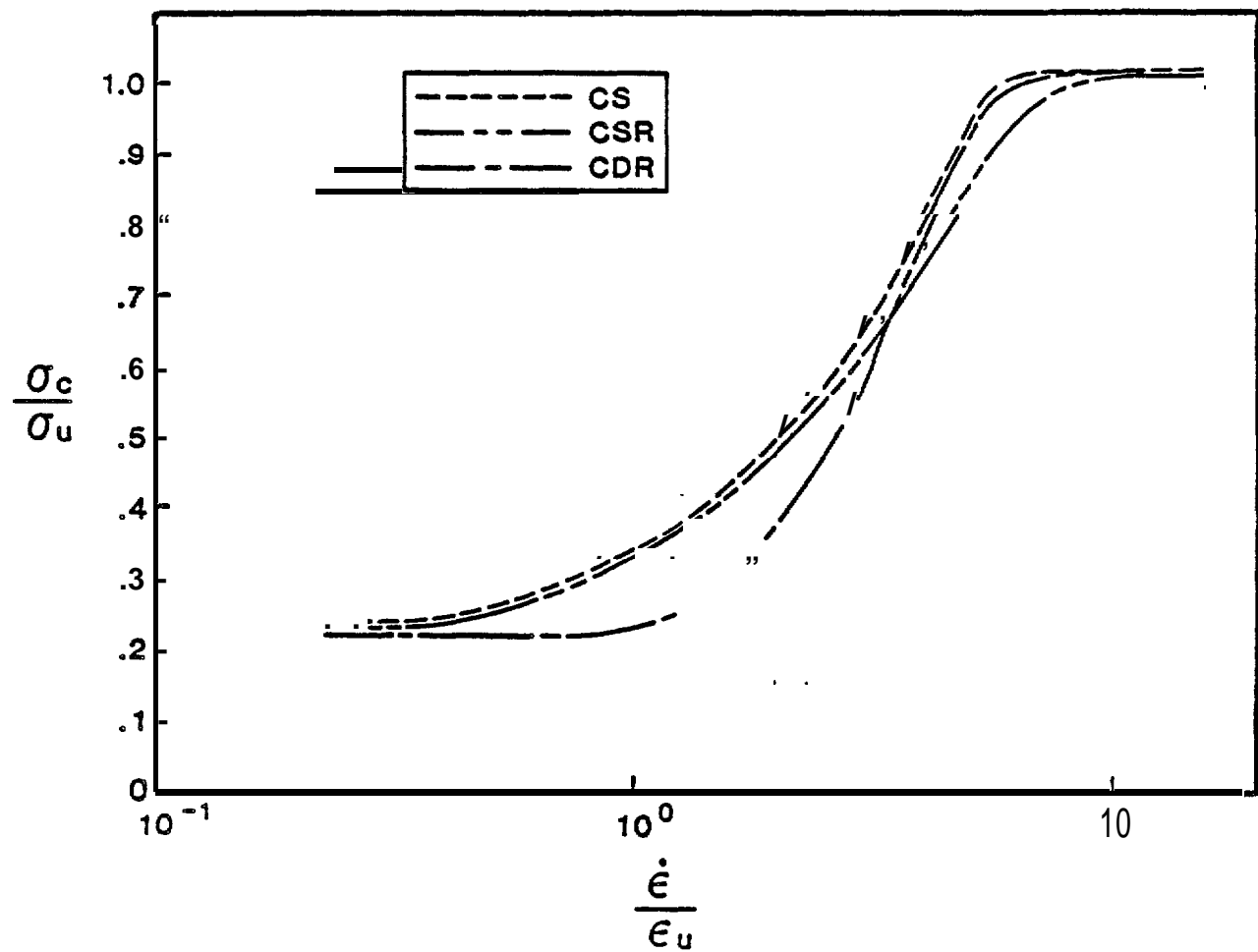


Figure 2.3-6 Stress ratio vs. strain rate ratio at yield for the linear model. Loading paths indicated in key.

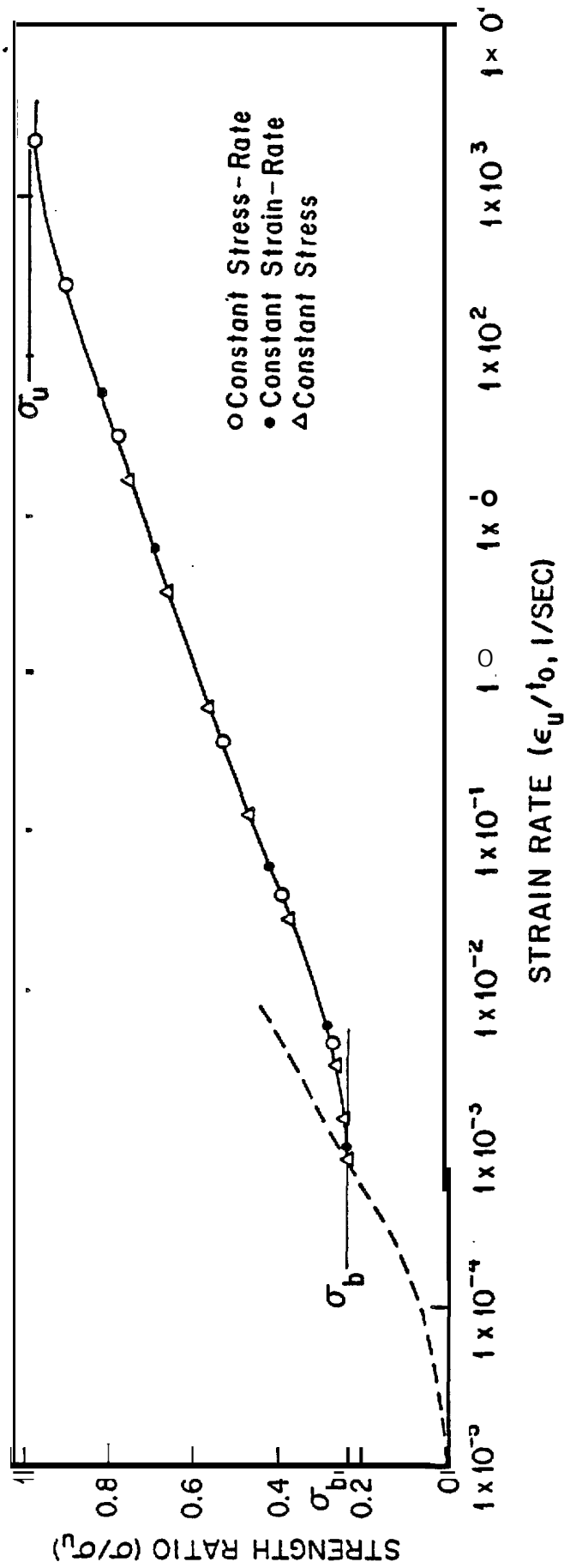


Figure 2.3-7 Stress ratio vs. strain rate at yield for the non-linear 4-PF model. Calculated points for the three loading paths define curves which are too close to draw separately at this scale. σ_u and σ_b are the upper and lower strength limits. Dashed line is the stress vs. strain rate curve for the dashpot of the Maxwell model.

2.34.24 **TIME-TO-FAILURE**

The time-to-failure as a function of strength for the three tests depends on the rate of loading and the time constants of the dashpot of the Voigt model. The curves for the linear model are shown in Figure 2.3-8 as ratios of σ_c/σ_u and time-to-failure to relaxation time of the dashpot of the Voigt model.

As might have been anticipated from consideration of the loading function, the time-to-failure at any stress is lowest for CS tests, since the **model** is under the peak stress from the instant of application of stress.

The curves reverse the pattern of the strength vs. strain rate curves and are asymptotic to both the upper and fundamental strengths. Note also that, on the semi-logarithmic plots used here, there are pronounced decreases in the slopes of the curves as the fundamental strength is approached. The rapid increase in the total strain at failure at stresses just above the lower limit (noted in Section 2.34.22) reflects the increased time-to-failure in this stress range.

For completeness, the comparable relationships for the non-linear model are shown **in** Figure 2.3-9.

2.34.3 SUMMARY OF THE MODEL

The application of the **DSEC** to the 4-PF model leads immediately to upper and lower limits to the strength of the model. The significance of the limits for studies of ice properties is discussed in the next section.

The relationships between the calculated curves for the three loading paths can be expected to vary depending upon the forms of the stress-strain laws of the individual model elements and the values of the model parameters. However, the model developed here provides the basis for interpretation of the relationships between tests to failure along different loading paths, through curves of the type in

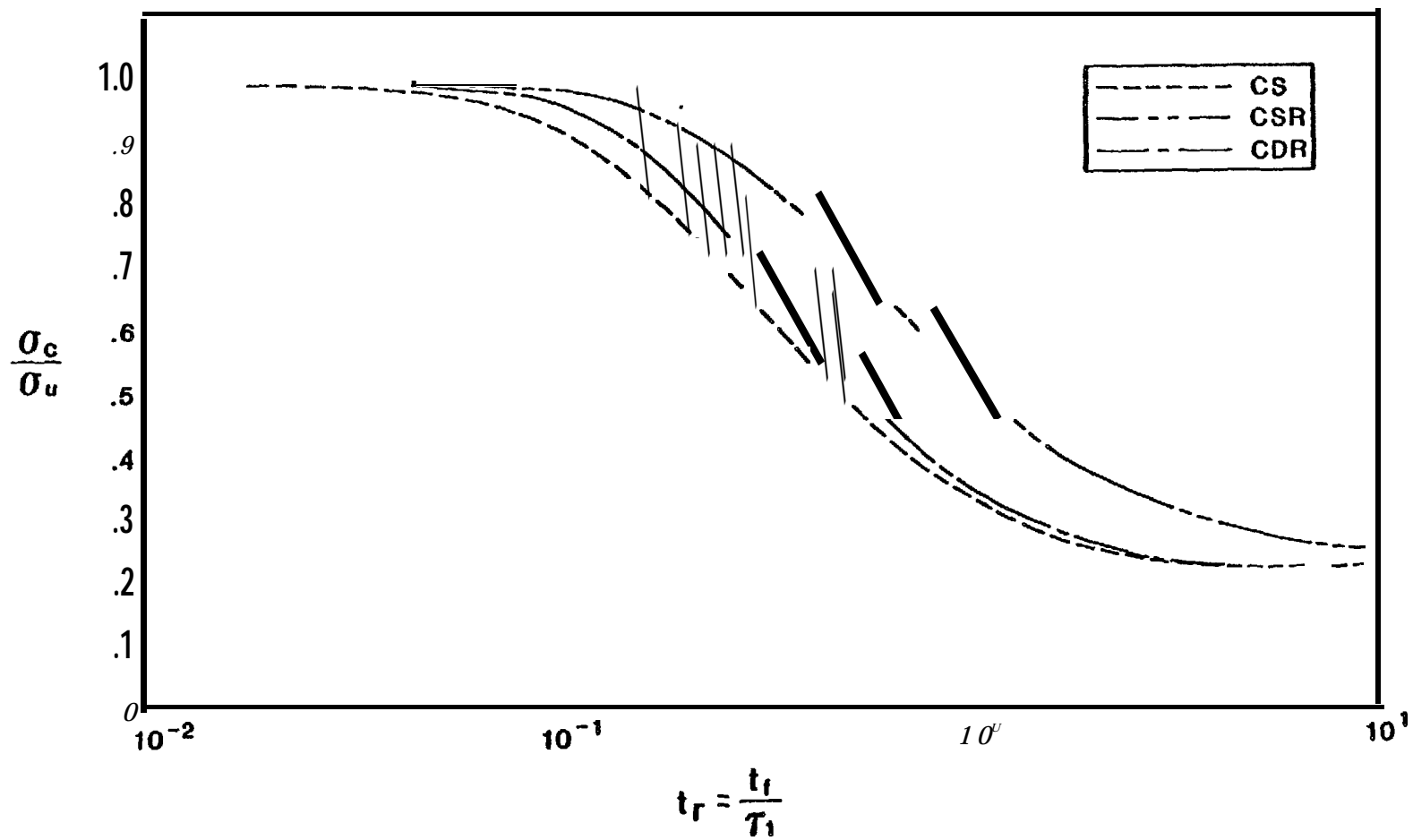


Figure 2.3-8 Stress ratio vs. time ratio at **yield** for the linear model. Loading paths as indicated in the key.

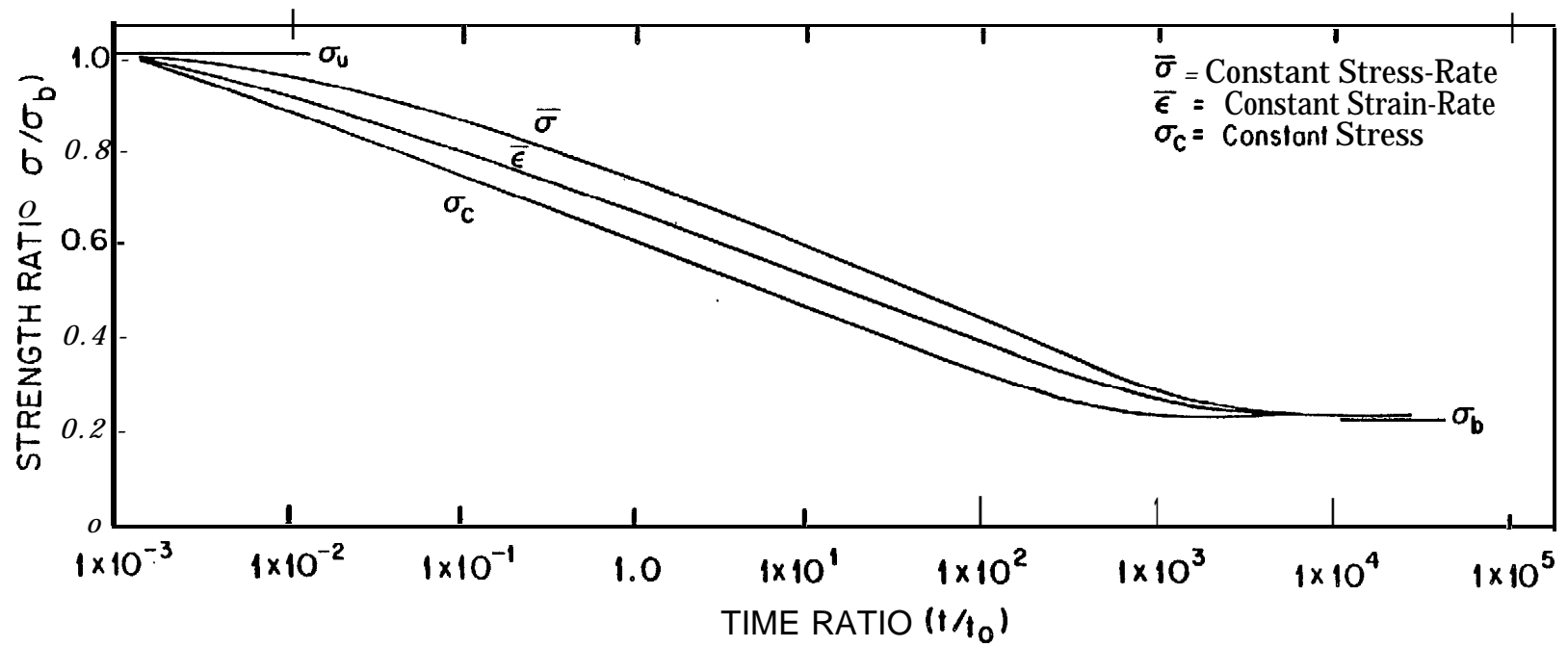


Figure 2.3-9 Strength vs. time-to-rupture for the non-linear model. Loading paths as indicated in the key.

Figures 2.3-4 to 9 (note that strength-stress rate curves could be calculated for **CSR**- and CDR tests).

For both the linear and non-linear models the elastic strain at failure is the same for the three loading paths for every strength between the limits. The total strain tends to follow the elastic strain, but becomes large near the lower limit. However, over most of the range of strengths, the strain at failure is likely to be about the same for the three loading paths considered here.

Plots of strength vs. strain rate at the instant of failure for the three loading paths show the same trend of increasing strength with rate that is known from experimental data. The transition from the lower to the upper strength limit for the linear model occurs over a change in strain rate of about one order of magnitude of the strain rate, while for the non-linear model the transition takes place over about 5 to 6 orders of **magnitude**. **This** illustrates the strong dependence of this relationship on the form of the **model**.

The strength vs. time-to-failure curves show similar forms for the two models, with (for a given strength) the time increasing from **CS** to CDR to CSR tests. In addition, the asymptotes at the upper and lower strength limits are apparent.

2.35 COMPARISON WITH DATA

2.35.1 INTRODUCTION

The calculated curves presented in the last section are qualitatively similar to experimental curves for ice in **uniaxial** compression, but, it is clear that the assumption of a linear model will not permit numerical values for the parameters to be determined from experimental data over more than a limited range of the test variables. However, it maybe possible to find reasonable parameters using **non-linear** models for the dashpots.

Perhaps the greatest use of the results above is in the possibility of establishing a framework for the interpretation of experimental data based on the theoretical upper and lower limits to the strength which result from the application of the **DSEC**. As discussed next, based on comparison with experimental data, the limits may define the boundaries of ranges of test parameters across which the deformation mechanisms change.

2.35.2 LOWER LIMIT OF STRENGTH

The experimental data indicate that there is no lower limit to the strength of ice as the theory predicts. (Section 2.34). This was shown by **Jacka** (1984) in experiments on **polycrystalline** ice, in which CS tests were conducted over time periods of up to 9×10^7 seconds at temperatures from -5° to -32.5°C and stresses in the range of 0.1 to **1.7** MPa. In all cases, the strain rate decreased with time through the experiments, so that steady state creep, in the sense of the model, was never reached. In addition, the strain rate passed through a minimum (**the** inflection point of the strain-time curve) in most of the tests, with the exception of those at the lowest temperatures and stresses. These were stopped while the strain rate was still decreasing. **Jacka's** (1984) data for stress vs. time to the minimum strain rate are plotted in Figure 2.3-10, along with similar data from **Mellor** and Cole (1982). Note

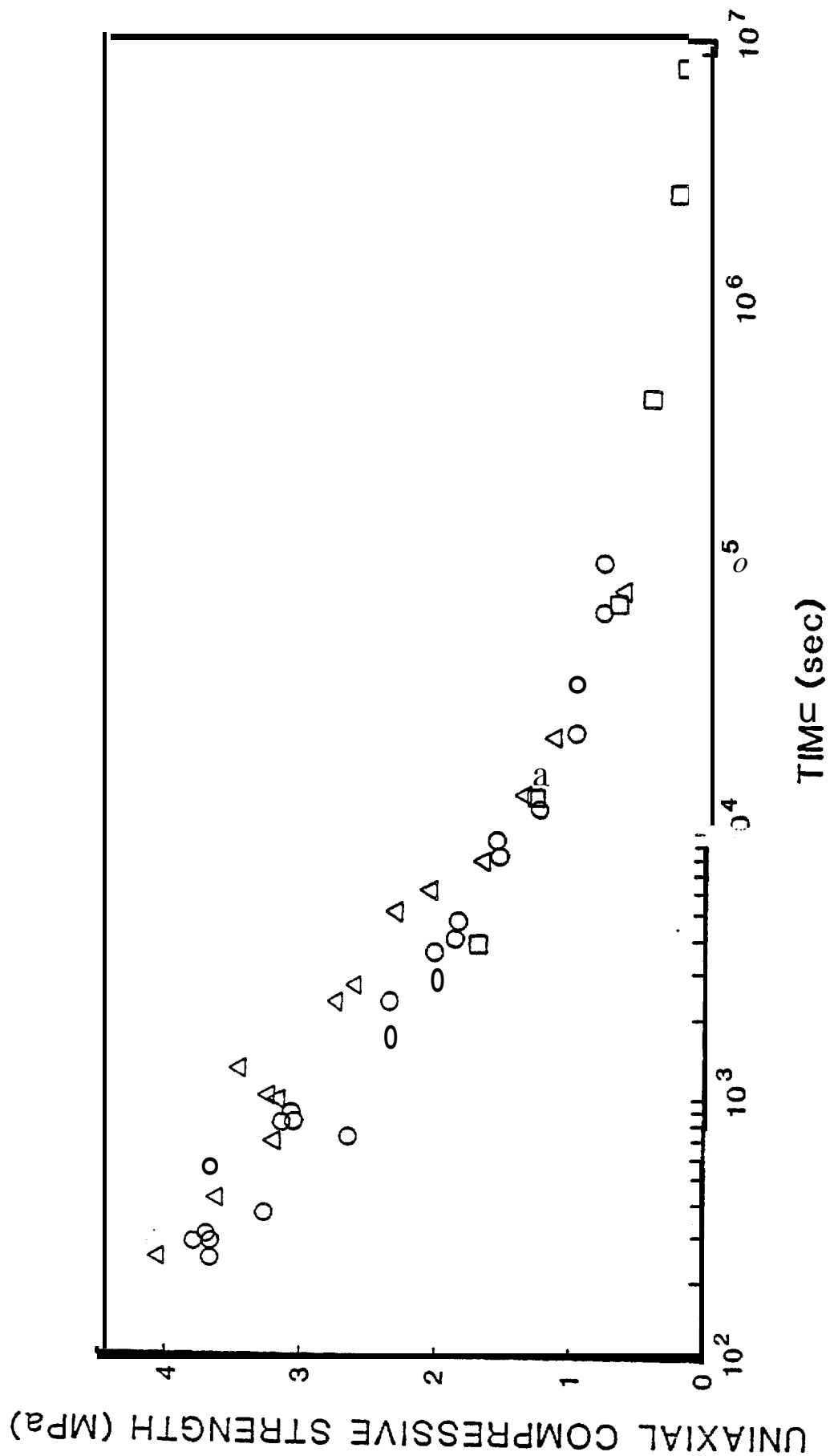


Figure 2.3-10 Uniaxial compressive strength of polycrystalline fresh ice vs. (1) time-to-minimum strain rate for CS tests [circles -- Mellor and Cole (1982); squares-Jacka (1984)], and (2) peak stress in CDR loading [triangles--Mellor and Cole (1982)]. Compared trends in data to Figures 2.3-8 and 2.3-9.

the change in slope of the curve at a stress of about 0.5 MPa. Similar data from sea ice samples, acquired during this project are shown in Figures 2.2-9 and 10, and show the same change in slope with decreasing stress.

There are numerous studies which provide data to suggest that the slope break in the stress vs. time-to-minimum strain rate curve for CS tests in **uniaxial** compression is associated with a change in deformation mechanism. St. Lawrence and Cole (1982) conducted CS tests on **polycrystalline** fresh ice during which cracking rates of the sample were monitored. The results showed that, at low stresses, the dominant deformation mechanism was by recrystallization with no cracking. However, at higher stresses the samples deformed by the growth of numerous small fractures without recrystallization. **Duval** et al. (1983) also showed that minimum strain rates occur in **CS** tests with and without cracking, depending upon the stress level. **Jacka** and **Maccagnan** (1984) examined the onset of recrystallization in **CS** tests, and demonstrated that the process is associated with the minimum strain rate. Finally, in the tests on sea ice reported in Section 2.24.63, failure in CR tests at low stresses always occurred by the progressive growth and coalescence of many small cracks, so that the ice samples turned milky white as deformation proceeded. Tests in which the minimum strain rate was not reached showed no such pervasive cracking. These studies all imply that the slope break in the stress vs. time to minimum strain rate in **CS** tests is related to the change in deformation mechanism from recrystallization to "brittle creep" (i.e., deformation by propagation of small fractures) leading to failure. A similar conclusion applies to CDR and CSR tests since all three tests types give the same break in slope (Figure 2.3-8), and results from tests at the three paths are included in Figures 2.2-10 and 2.3-10.

2.35.3 UPPER STRENGTH **LIMIT**

The existence of an upper limit to the strength of ice in **uniaxial** compression seems to be reasonable on physical grounds. As noted, it is simply the smallest stress which will cause “instantaneous” failure of the sample. An upper limit is implied by the results of experimental studies of the strength vs. strain rate relationship for ice from CDR tests either as an asymptote (**Mellor** and Hawkes, 1972) or as a peak, following which the strength decreases with increasing strain rate [see, for example, Vaudrey (1977)]. The calculated results above show that the DSEC applied to the **4-PF** model requires that the strength become asymptotic to an upper limit with increasing rate of deformation or decreasing time to failure, rather than passing through a peak (Figure 2.3-6). Further, this applies to CS and **CSR** tests as well as CDR tests.

The failure mechanism in the upper range of strengths (i.e., at, or beyond, the peak) for the sea ice tests was described (Section 2.24.62) as brittle fracture along one **(or a few)** cracks which **propagate across the sample, as opposed to the pervasive growth and coalescence of small cracks** which lead to failure at lower strengths. The transition between mechanisms is gradual; the number of cracks in the sample at failure decreases with increasing stress. Samples which fail at high stresses tend to retain their initial clarity in the ice between the major fractures, as opposed to the **milky** white appearance of those failed at lower stresses.

2.36 DISCUSSION AND CONCLUSIONS

The comparison between the theory and the data suggests the following preliminary conclusions:

(1) **With** an appropriate choice of parameters the combination of the 4-PF model and the DSEC can be made to predict the strength and **deformational** behavior of both **polycrystalline** fresh ice and sea ice over the range between the upper and

lower strength limits. Further, the limits correspond to changes in deformation mechanisms, rather than to limits on the actual strength of the ice.

(2) At stresses **below** the **lower** limit, **polycrystalline** fresh ice deforms by ductile mechanisms **of** which recrystallization is probably most important. Unfortunately, there are no data available regarding deformation mechanisms of sea ice in this range.

(3) As the upper **limit** is approached, the failure mechanism for both **polycrystalline** fresh ice and sea ice becomes true brittle fracture.

(4) Between the limits is a range of stresses in which the failure mechanism for both ice types involves the formation and coalescence of small, stable cracks. No studies have been done to examine the contribution of ductile deformation mechanisms to the total strain within this range. However, whatever the mechanisms, the process results in a response to stress which (for the bulk sample) can be described as **viscoelastic**.

Thus, in effect, the model defines the boundaries of three discrete ranges of reformational behavior of ice, each of which may require a different stress-strain law for description.

The values of the upper and lower **limits** are known approximately for a few temperature ranges. A reasonable upper limit to the **uniaxial** compressive strength of **polycrystalline** ice at -7°C is about 9 **MPa** (**Hawkes** and **Mellor**, 1972). A lower limit of about 0.5 MPa at -5°C is suggested from the data in Figure 2.3-10. For sea ice, approximate values can be inferred using the data in Sections 2.24.63 and 2.24.64; the upper limit ranges from **2.7** to 6.2 MPa and the lower limit from 0.5 to **1 MPa** as the temperature decreases from **-5° to -20°C**. It is of interest to note that most past work on the **uniaxial** compressive strength of all types of ice has been done in the **lower** half of the stress range between the limits.

As suggested in Section 2.34.25, it is questionable whether it is possible to **determine** appropriate values of **the model parameters from creep tests on ice**. This is because such determinations require that some of the measurements be made as the ice deforms in steady state creep which, as noted above, probably does not occur. However, it should be noted that all determinations of the parameters for the commonly cited one-dimensional creep laws (i.e., power, exponential or hyperbolic sine) are made based on the assumption that the ice is deforming in steady state. **It** is likely that, in future, it will be necessary for parameters to be determined by approximate methods, or by fitting assumed functions to data (i.e., **Szyszkowski and Glockner, 1985**).

The results above suggest that further experimental work could usefully be directed at studies of the transitions between mechanisms as the upper and lower limits predicted by the model are approached. In addition, the fact that a failure criterion based on strain energy appears to define that boundaries suggests that energy considerations in brittle fracture and in dynamic recrystallization might be useful in analysis of the problem.

APPENDIX

The deformation of the spring-dashpot model of the 4-parameter linear **viscoelastic** fluid in **uniaxial** compression is governed by the differential equation

$$(A-1) \quad \dot{\epsilon} + \tau_2 \ddot{\epsilon} = \frac{1}{\eta_1} \sigma + \left(\frac{1}{k_1} + \frac{\tau_2}{\eta_1} + \frac{1}{k_2} \right) \dot{\sigma} + \frac{\tau_2}{k_1} \ddot{\sigma}.$$

This equation can be integrated to give the stress-strain or strain-time curves for each of the three loading programs from which the conditions at failure can be derived, as shown below. Note that the derivations do not include the case of recovery of strain after unloading from a test which was not taken to failure.

CONSTANT STRESS (CS)

For a constant stress σ_c [Note: the **symbol- σ_c** is used here in place of σ_0 for constant stress for convenience in defining the dimensionless parameters introduced below] applied at $t = 0$, equation (A-1) can be integrated to give the strain-time relationship

$$(A-2) \quad \epsilon_T = \frac{\sigma_c}{k_1} + \frac{\sigma_c t}{\eta_1} + \frac{\sigma_c}{k_2} \left(1 - e^{-t/\tau_2} \right)$$

where the terms on the right side of the expression correspond (from left to right) to the strain in the spring (**ϵ_E**) and dashpot (**ϵ_D**) of the Maxwell model, followed by the contribution of the Voigt model (**ϵ_V**). Note that the strain in each element depends only on the applied stress and not on the parameters of other elements of the model. This follows because, as noted in the text, equilibrium requires that the stress across each element be the same, so that the applied stress is transmitted uniformly across the elements and each responds as if it were isolated from the remainder of the

model. Clearly, ϵ_E is constant through the test, ϵ_D increases linearly with time (since ϵ_D is linearly related to the applied stress), and ϵ_V goes from zero to a constant as the time goes from zero to infinity. Curves of strain vs time for different stress levels, calculated from equation (A-2), are shown in Figure 2.3-A1.

At failure, the strain energy stored in the two springs of the model must equal the resilience, or

$$(A-3) \quad R = \frac{\sigma_2^2}{k_1} + \frac{\sigma_c^2}{k_2} \left(1 - e^{-t_f/\tau_2} \right)$$

where t_f is the time to failure and τ_2 is the relaxation time of the Voigt model. For failure at the upper strength limit (σ_u), $t_f = 0$ and the strain is given by [from equation (4)]

$$\epsilon_u = \sigma_u/k_1$$

and R is

$$(A-4) \quad R = \sigma_u^2/k_1.$$

Introducing this relationship, and the dimensionless constants

$$a = \sigma_c/\sigma_u \quad (0 \leq a \leq 1),$$

$$(A-5) \quad b = k_2/k_1 \quad (0 \leq b \leq 1),$$

$$\tau_r = t_f/\tau_2$$

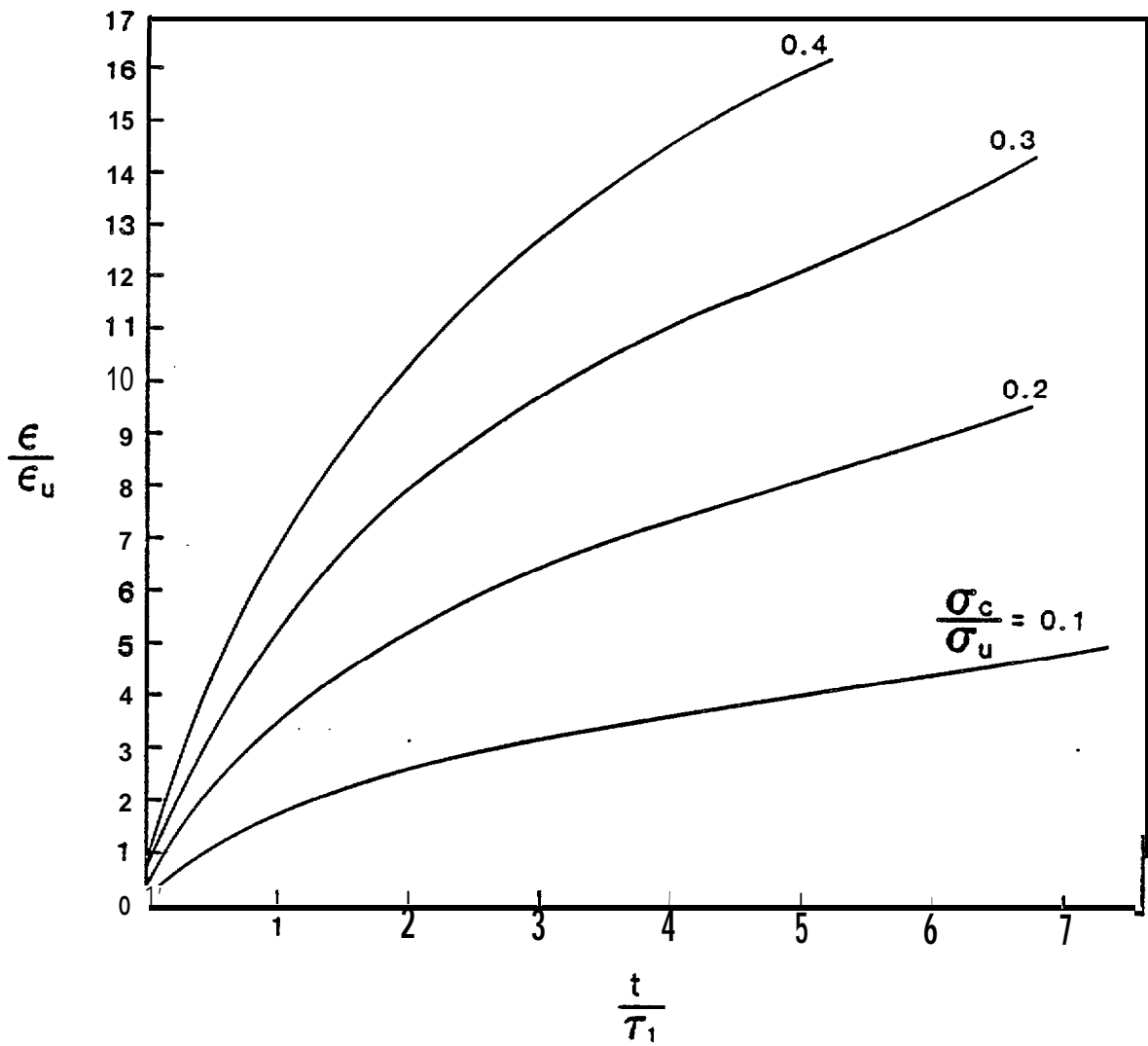


Figure 2.3-AI Strain ratio vs. time ratio for CS tests at indicated stress ratios for the linear 4-PF model. See text for discussion.

into equation (A-3) and solving for t_r gives the time-to-failure as a function of the stress and the **moduli** as

$$(A-6) \quad t_r = -\ln \left\{ 1 - \left[b \left(\frac{1}{a^2} - 1 \right) \right]^{1/2} \right\}.$$

The elastic strain at failure (ϵ_{Ef}) is the sum of the first and third expressions on the right side of equation (A-2) evaluated at t_r ;

$$(A-7) \quad \epsilon_{Ef} = \frac{a_c}{k_1} + \frac{\sigma_c}{k_2} (1 - e^{-t_r}).$$

Substituting for t_r from equation (A-6) and using equations (A-4) and (A-5) then leads to the elastic strain ratio at failure,

$$(A-8) \quad \frac{\epsilon_{Ef}}{\epsilon_u} = a + \frac{1}{b^{1/2}} (1 - a^2)^{1/2}.$$

To find the total strain at failure, the contribution of the dashpot of the Maxwell **model**

$$(A-9) \quad \epsilon_D = \frac{\sigma_c t_f}{\eta_1}$$

is added to equation (A-7). Introducing the definition

$$(A-10) \quad c = \frac{\eta_2}{\eta_1} \quad (0 \leq c \leq 1)$$

into equation (A-9), adding to equation (A-8) and using (A-5) then gives the **total strain ratio at failure** as

$$\frac{\epsilon_f}{\epsilon_u} = \frac{\epsilon_{Ef} + \epsilon_D}{\epsilon_u} = a + \frac{1}{b^{1/2}} (1 - a^2)^{1/2} + \frac{ac}{b} t_{r''}$$

Finally, the strain rate at failure is found from the derivative of equation (A-2) which, after rearrangement and substitution of (A-6) and (A-10) leads to

$$\dot{\epsilon}_f = \frac{\sigma}{\eta_1} \left\{ 1 + \frac{1}{c} \left[1 - b^{1/2} \left(\frac{1}{2} - 1 \right)^{1/2} \right] \right\}.$$

CONSTANT STRESS RATE (CSR)

For a constant stress rate σ_0 , the stress as a function of time is simply

$$\sigma = \sigma_0 t$$

The stress-strain relationship given by the integral of equation (A-1) for this condition is

$$(A-11) \quad \epsilon_T = \left\{ \frac{t}{k_1} + \frac{1}{\eta_1} \frac{t^2}{2} + \frac{1}{k_2} \left[t - \tau_2 \left(1 - e^{-t/\tau_2} \right) \right] \right\} \sigma_0$$

in which the terms in brackets correspond (from left to right) to the strain in the dashpot and spring of the Maxwell model, and the **Voigt** model. Note that, as was the case for **CS** tests, the strain in each model element depends only on the applied stress. The stress-strain curve is shown in Figure 2.3-A2.

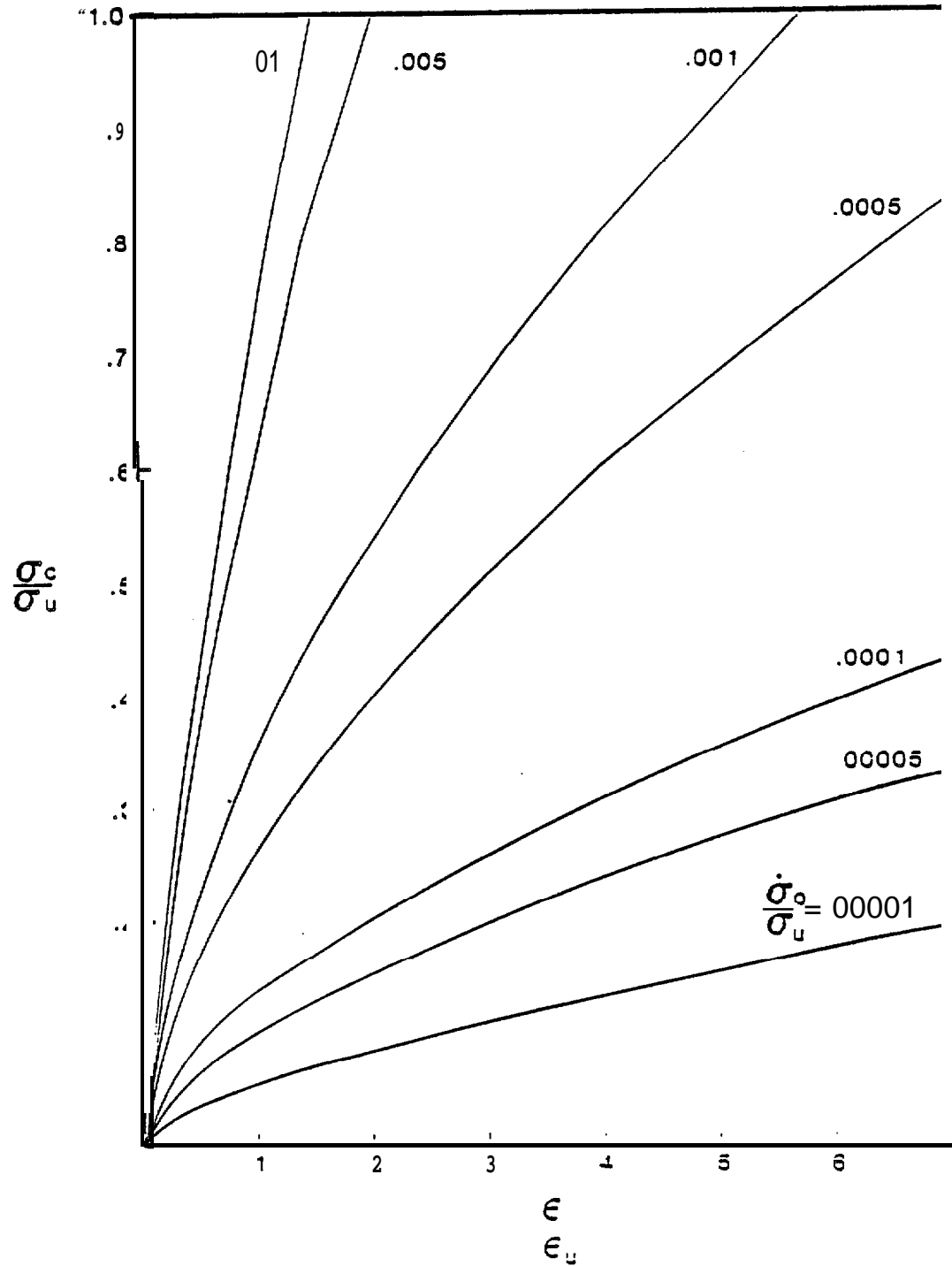


Figure 2.3-A2 Stress ratio vs. strain ratio for CSR tests at stress rates shown on curves. See text for discussion.

The elastic strain at the failure stress σ_c and $t = t_f$ is

$$(A-12) \quad \varepsilon_r = \frac{\sigma_c}{k_1} + \frac{\sigma_c}{k_2} \left[1 - \frac{t_2}{t_f} \left(1 - e^{-t_f/t_2} \right) \right]$$

and the failure criterion

$$(A-13) \quad R = \frac{\sigma_c^2}{k_1} + \frac{\sigma_c^2}{k_2} \left[1 - \frac{t_2}{t_f} \left(1 - e^{-t_f/t_2} \right) \right]^2.$$

Introducing the definitions from equations (A-4), (A-5) and (A-6) and rearranging leads to

$$(A-14) \quad 1 - \frac{1}{t_r} \left(1 - e^{-t_r} \right) = \left[\left(\frac{1}{a^2} - 1 \right) b \right]^{1/2}.$$

Substitution into equation (A-12) **and** using (A-4) then gives the elastic strain ratio at failure as

$$\frac{\varepsilon_{Ef}}{\varepsilon_u} = a + \frac{1}{b^{1/2}} (1 - a)^{1/2}$$

which is the same as that for CS tests at the constant stress [equation (A-8)1.

The strain rate at failure for **CSR** tests is found by differentiation of equation (A-n) and substitution of (A-10) and (A-14) to get

$$\dot{\varepsilon}_t = \frac{\sigma_c}{\eta_1} \left\{ 1 + \frac{1}{c} \left[1 - b^{1/2} \left(\frac{1}{a^2} - 1 \right)^{1/2} \right] \right\} + \frac{\sigma_o}{k_1}$$

which differs from the strain rate at failure for CS tests by the addition of the term for the strain rate of the spring of the Maxwell model, as noted in the text.

CONSTANT STRAIN RATE (CDR)

In the case of a constant strain rate $\dot{\epsilon}_0$ applied to the model, the strain at any time is

$$\epsilon_t = \dot{\epsilon}_0 t$$

and equation (A-1) can be integrated to

$$(A-15) \quad \sigma = c_1 e^{c_3 t} + c_2 e^{c_4 t} + \eta_1 \dot{\epsilon}_0$$

where

$$c_1 = -\frac{c_4}{c_4 - c_3} \left(\frac{k_1}{c_4} + \eta_1 \right) \dot{\epsilon}_0,$$

$$c_2 = \frac{c_4}{c_4 - c_3} \left(\frac{k_1}{c_4} + \eta_1 \right) \dot{\epsilon}_0,$$

$$c_3 = -\frac{1}{2} c_5 + c_6,$$

$$c_4 = -\frac{1}{2} c_5 - c_6,$$

$$c_5 = \frac{k_1}{\eta_2} + \frac{k_1}{\eta_1} + \frac{k_2}{\eta_2},$$

$$c_6 = \left(c_5^2 - 4 \frac{k_1}{\eta_1 \eta_2} \right)^{1/2}.$$

The form of equation (A-15) reflects the fact that in CDR tests, the stress varies so that the applied strain rate is partitioned between the model elements so that the relationship

$$\dot{\varepsilon}_o = \dot{\varepsilon}_E + \dot{\varepsilon}_D + \dot{\varepsilon}_V$$

is satisfied at all times. Thus, the stress must be a function of all of the model parameters.

The stress-strain relationships for the spring and dashpot of the Maxwell model are

$$(A-16) \quad \varepsilon_E = \frac{\sigma}{k_1}$$

and

$$(A-17) \quad \varepsilon_D = \int \frac{\sigma}{\eta_1} dt$$

respectively. The comparable equation for the Voigt model is found from the equilibrium equation

$$\sigma = \sigma_1 + \sigma_2$$

which, using the stress-strain laws of the spring and dashpot, can be written as the differential equation

$$\dot{\varepsilon}_v + \frac{1}{\tau_2} \varepsilon_v = \frac{\sigma}{\eta_2}.$$

The solution is

$$(A-18) \quad \varepsilon_v = \frac{1}{\eta_2} \left[\frac{c_1}{D_1} \left(e^{c_3 t} + e^{-t/\tau_2} \right) + \frac{c_2}{D_2} \left(e^{c_4 t} - e^{-t/\tau_2} \right) + \eta_1 \varepsilon_o \tau_2 \left(1 - e^{-t/\tau_2} \right) \right]$$

where

$$D_1 = c_3 + \frac{1}{\tau_2}; \quad D_2 = c_4 + \frac{1}{\tau_2}.$$

Equations (A-16), (A-17) and (A-18) can be **non-dimensionalized** to the same parameters as those used for CS and **CSR** tests, and the conditions at failure can then be calculated after assuming numerical values for the parameters. In this case, the value of **k₁** was taken as 9 GPa, following (**Hawkes and Mellor, 1972**). **η₁** was taken as 5 x 10⁶ to approximate the strain rate at a stress of 1 MPa as would be calculated from the power law for creep with typical parameters, (i.e., **η = 3**, A = 2 x 10⁻⁷). The values of **k₂** and **η₂** were then fixed by the choice of **the constants** b (=0.05) and c (=0.2). The choice of the upper limit of the strength is arbitrary since all of the equations are normalized to its value. The stress-strain curve from equation (A-15) using these values is shown in Figure 2.3-A3.

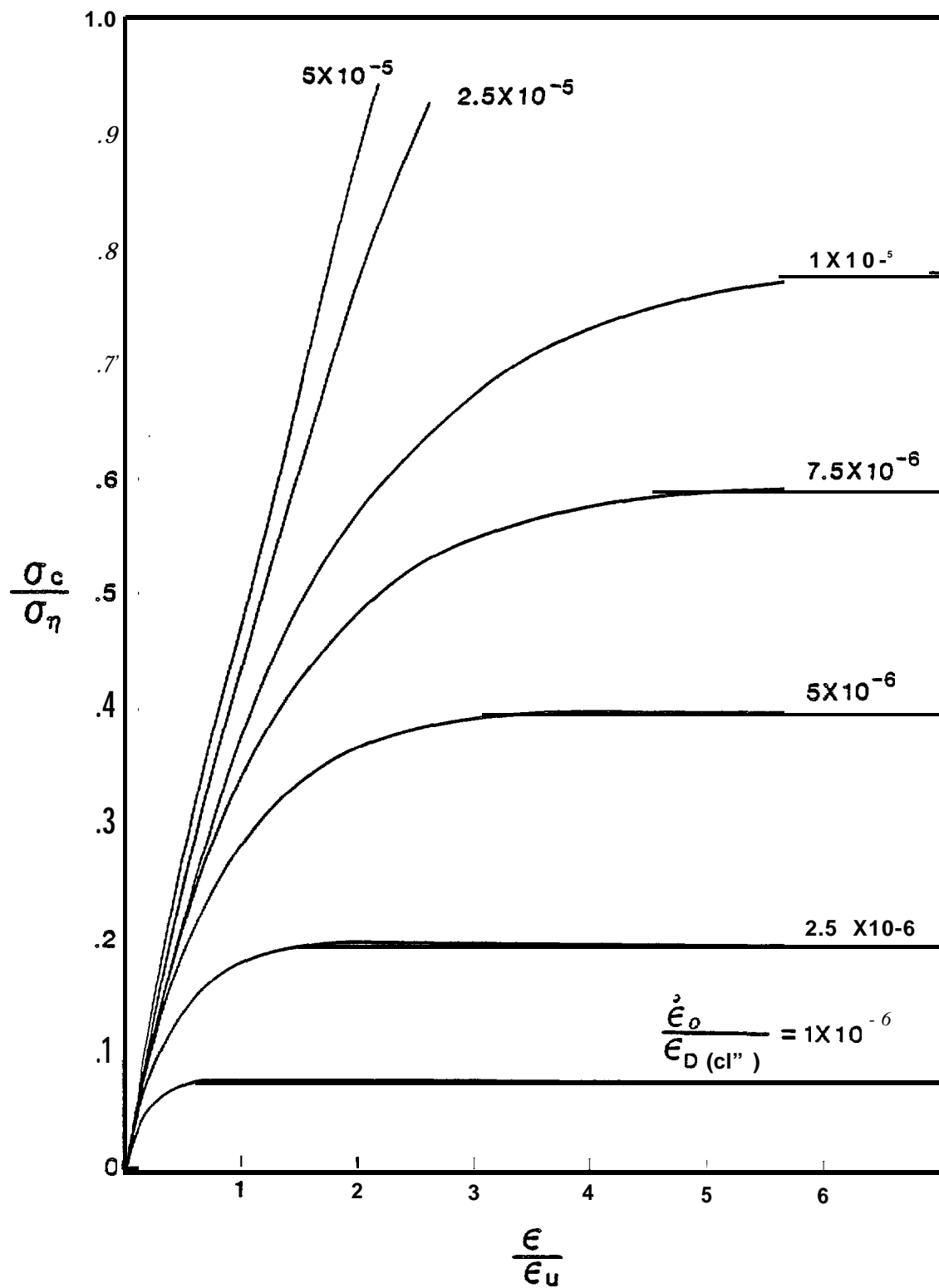


Figure 2.3-A3 Stress ratio vs. strain ratio for CDR tests at strain rates indicated on curves. See text for discussion.

HYPERBOLIC SINE MODEL,

If the strain rate of the dashpots of the Maxwell and Voigt models are represented by the equations

$$\dot{\epsilon}_D = B \sinh \theta \sigma$$

and

$$\dot{\epsilon}_V = A \sinh \phi \sigma_2$$

respectively, and k_1 and k_2 are the spring moduli, then the stress-strain law of the model is

$$\epsilon_T = \frac{\sigma}{k_1} + B \int_0^t \sinh \theta \sigma dt' + A \int_0^t \sinh \phi \left[\sigma - k_2 \epsilon_V \right] dt'$$

where the primes indicate dummy variables. This equation can be integrated directly to give the strain-time and stress-strain curves for CS and CSR tests as

$$\epsilon_T = \frac{k_1 + k_2}{k_1 k_2} \sigma_c + B t \sinh \theta \sigma_c - \frac{2}{\phi k_2} \tanh^{-1} \left(\tanh \frac{\phi \sigma_c}{2} e^{-A \phi k_2 t} \right)$$

and

$$\epsilon_T = \frac{k_1 + k_2}{k_1 k_2} \sigma_o t + \frac{B}{\theta \dot{\sigma}_o} (\cosh \theta \sigma_o t - 1) - \frac{1}{\phi k_2} \sinh^{-1} \left[\frac{a \sinh (\beta t - \delta) - 1}{a + \sinh (\beta t - \delta)} \right]$$

respectively where $\dot{\sigma}_o$ is the applied constant stress rate in CSR tests.. The constants a , β and δ in the second equation are

$$\alpha = \frac{\dot{\sigma}_o}{Ak_2},$$

$$\beta = \phi k_2 (1 + \alpha^2)^{1/2},$$

$$\delta = \sinh^{-1} 1/\alpha.$$

The stress-strain curve for **CDR** tests is found numerically from the equation

$$\sigma = \frac{1}{\theta} \sinh^{-1} \frac{f(t)}{A} + k_2 f(t)$$

where

$$f(t) = \dot{\varepsilon}_o t - \frac{\sigma}{k_1} - B \int_0^t \sinh \theta \sigma dt'.$$

The curves in Figures 2.3-5,7 and 9, were found by calculation using values of the parameters which were selected based on data from linear models for different types of ice reported in the literature. The values are given in Table 2.3-AI.

TABLE 2.3-AI

VALUES OF CONSTANTS USED IN CALCULATIONS OF THE
RESPONSE TO LOAD THE NON-LINEAR 4-PF MODEL

| <u>CONSTANT</u> | <u>VALUE</u> |
|-----------------|----------------------------|
| k_1 | 3.45 GPa |
| k_2 | 0.21 GPa |
| ϕ | 4.06 MPa ⁻¹ |
| θ | 3.09 Mpa ⁻¹ |
| A | 5 x 10 ⁻⁶ see-l |
| B | 1 x 10 ⁻⁷ see-l |
| σ_b | 0.86 MPa |

REFERENCES CITED

- Day, W. **A.** (1975). On the Reiner-Weissenberg criterion for yield; Quart. Jour. **Mech.** and **Appl.** Math., v. 28, pp. 207-221.
- Duval, P., Ashby, M. F. and Anderman, I. (1983). Rate-controlling processes in the creep of **polycrystalline** ice; J. Phys. **Chem.**, v. 87, pp. 4066-4074.
- Flugge, W. (1967). **Viscoelasticity**; Blaisdell Pub. Co., **Waltham**, Mass., pp. 12'?
- Glasstone, S., **Laidler, K.** J. and Eyring, H. (1941) The Theory of Rate Processes; McGraw-Hill, **N.Y.**
- Hart, **E. W.**, **Li**, C. Y., **Yamada**, H. and Wire, G. L. (1975). **Phenomenological** Theory: A guide to constitutive relations and fundamental deformation properties; in **A. S.** Argon, cd., **Constitutive** Equations in Plasticity, **M.I.T.** Press, Cambridge. Mass., pp. 149-197.
- Hawkes, I. and **Mellor**, M. (1972). Deformation and fracture of ice under **uniaxial** stress; Jour. **Glaciology**, v. **11**, no. **61**, pp. 103-131.
- Hutter, K.** (1980). A note on rate process theory and creep response of ice; Cold Regions Sci. and Tech., v. 3, pp. 335-336.
- Jacka**, T. H. (1984). The time and strain required for development of minimum strain rates in ice; Cold Regions Sci. and Tech., v. 8, pp. 261-268.
- Jacka, T.** H. and **Maccagnan**, M. (1984). Ice crystallographic and strain rate changes with strain in compression and extension; Cold Regions **Sci.** and Tech. v. 8, pp. 269-286.
- Jellinek**, H. H. G. and **Brill**, R. (1956). **Viscoelastic** properties of ice; Jour. **Appl.** Physics, v. 27, pp. 1198-1209.
- Krausz**, A. S. and **Eyring, H.** (1975). Deformation **Kinetics**; John **Wiley** and Sons, New York, pp. 398.

- Lindgren, S.(1970). Thermal **ice pressure**; **IAHR Symposium, Ice and its** Action on Hydraulic Structures, **Reykjavik**, Iceland.
- Maser, K. R. (1972). An analysis of the small-scale strength testing of ice; **M.I.T.** Sea Grant **Office**, Rept. No. **MITSG** 72-6, pp. 137.
- Mellor, M.** (1980). Mechanical properties of **polycrystalline** ice; in P. Tryde, cd., Physics and Mechanics of Ice; **IUTAM** Symposium, Copenhagen, 1979, pp. 217-245.
- Mellor, M.** and Cole, **D. M.** (1982). Deformation and failure of ice under constant stress or constant strain-rate; Cold Regions Sci. and Tech., **v.** 5, pp. 201-219.
- Mendelson, A.** (1968). Plasticity: Theory and Applications; Macmillan Co., New York, pp. 353.
- Nevel, D. E.** (1976). Creep theory for a floating ice sheet; USA CRREL SR 76-4, pp. 98.
- Peyton, H. R.** (1966) Sea Ice Strength; Geophysical Inst., **U.** of Alaska, Report UAG R-182, pp. 273.
- Reiner, M.** (1960). Plastic yielding in inelasticity; J. **Mech. Phys.** Solids, v. 8, **pp.** 255-261.
- Reiner, M. and Weissenberg, K. (1939). **Rheol.** Leaflet v. 10, p. 12.
- Sinha, N. K.** (1978). Rheology of **columnar-grained** ice: Experimental Mechanics, **v. 18, pp. 464-470.**
- Sinha, N. K. (1979.) Grain boundary sliding in **polycrystalline** materials; Phil. Msg. A, **v. 40, pp. 825-842.**
- St. Lawrence, W. F.** and Cole, D. M. (1982). Acoustic emissions from **polyrystalline**; Cold Regions Sci. and Tech., v. 5, pp. 183-199.
- Szyszkowski, W.** and **Glockner, P. G.** (1985). **Modelling** the time-dependent behavior of ice; Cold Regions **Sci.** and Tech., v. 11, pp. 3-21.

- Tabata, T. (1958).** Studies on the viscoelastic properties of sea ice; in **Arctic Sea Ice, U.S. Natl. Acad. Sciences-Natl. Res. Council, Pub. 598,** pp. 139-147.
- Vaudrey, K. D. (1977). Ice engineering study of related properties of floating ice sheets and summary of elastic and **viscoelastic** analyses; Naval Civil Eng. Lab., Tech. Rpt. R-860, pp. 79.

2.4 FRACTURE TOUGHNESS OF SEA ICE

by

Lewis H. Shapiro, Ronald C. Metzner and Jerome B. Johnson

2.41 .INTRODUCTION

A short series of fracture toughness tests was run in the laboratory using small beams of natural sea ice. The purpose was to obtain a set of data for comparison with the fracture toughness measurement made by Vaudrey (1977) on laboratory-grown saline ice.

2.42 SAMPLE DESCRIPTION AND TESTING

Beams used in the study were cut from slabs of sea ice collected from the landfast ice offshore from Barrow, Alaska. The slabs represented a profile of the ice sheet from the surface to a depth of 76 cm. After collection they were packed in insulated boxes, shipped to Fairbanks and stored until sample preparation and testing. The samples were subjected to a limited range of temperature changes during this process (-11° to -16°C) and were tested at -14°C.

The sample beams were 5 x 5 cm in cross section and about 40 cm long. The slit which provided the stress concentration was 1.3 cm deep, and a scalpel was run along the base of the slit to nucleate small cracks from which the main crack could propagate. A total of 30 beams were tested. Loading was done in 4-point bending through a spherical seat (Figure 2.4-I).

The sample beams cut from the uppermost 25 cm of the ice sheet were composed of **fine-grained** (maximum diameter of a few mm) randomly oriented crystals. The ice over the next 20 cm of depth had a similar appearance in thin section, but contained dispersed sediment and macroscopic inhomogeneities in the form of networks of whitish-colored ice lenses. These were apparently areas of closely

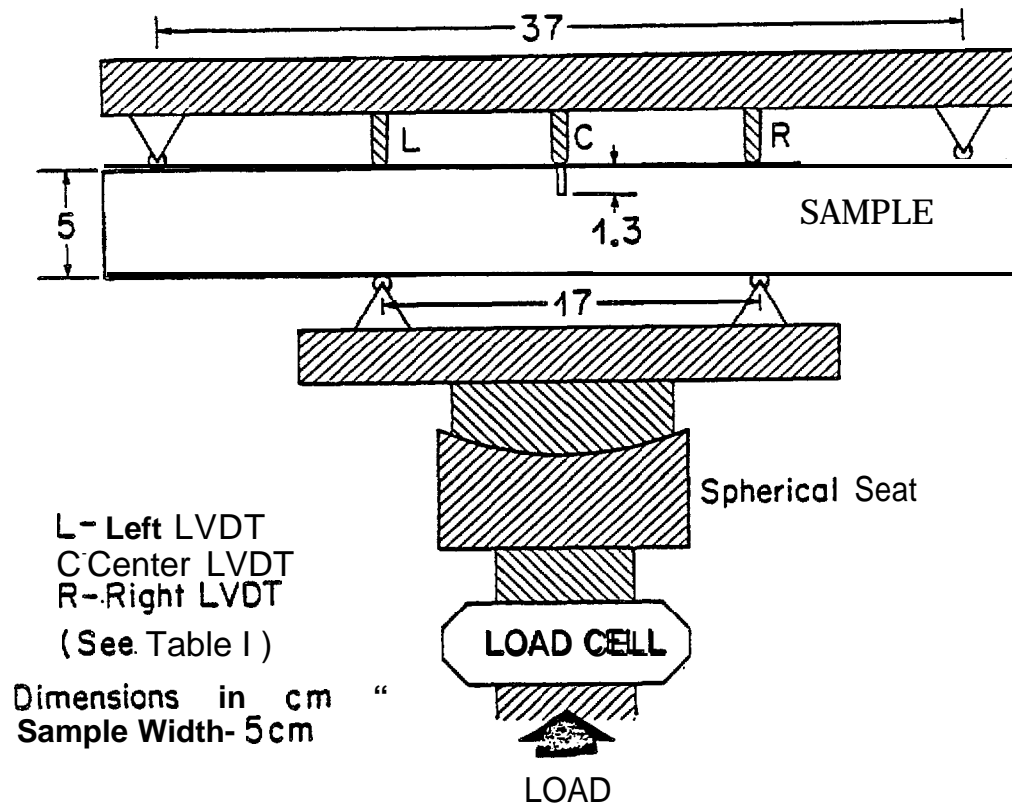


Figure 2.4-1 Schematic diagram of the four-point bending apparatus and sample geometry.

spaced brine channels or large, irregular pockets of trapped brine. . The remainder of the samples were composed of elongate crystals from the columnar zone which ranged in size from 0.6 x 1.3 to 2.5 cm at 45 cm depth to 1.3 x 2.5 to 4 cm at 75 cm depth. The c-axes of the crystals showed a weak orientation, and the beams were cut normal to this direction. Thus, the average direction of the long dimension of the grains was aligned parallel to the axis of the sample beams.

The load was applied by a hand operated hydraulic pump and was measured by a load cell below the spherical seat (Figure 2.4-1). The samples always failed within a small fraction of the possible travel during one stroke of the pump, so that smooth loading curves with respect to time were obtained. Loading rates varied from 550 to 690 **kPa/sec**. Data were recorded on a chart recorder and scaled by hand.

Beam displacements were measured by **LVDT's** positioned as shown in Figure 2.4-1. However, there were discrepancies in the displacement measurements which were determined to be due **to** slight rotations of the samples as the spherical seat aligned them during the initial loading phase. It would have been possible to correct the data **to** compensate for the errors if the data had been in digital form. However, the need to scale the data by hand from the charts made it impractical to attempt to do **SO**.

Calculation of the fracture toughness (**K_{IC}**)**was** done using the procedures in Vaudry (1977); that is,

$$K_{IC} = 3Pb^{1/2} (L_1 - L_2) \beta (2wd^2)^{-1}$$

where P is the load, b is the slot depth, L₁ and L₂ are the spacings between load points, w is the sample width, d is the thickness and β is given by

$$\beta = 1.99 - 2.47 (b/d) + 12.97 (b/d)^2 - 23.17 (b/d)^3 + 24.80 (b/d)^4$$

For $b/d = 0.25$,

$$\beta \approx 1.918$$

so that

$$K_{IC} = 1.97P$$

2.43 RESULTS AND CONCLUSIONS

The data are given in Table 2.4-1. Fracture toughness is plotted against brine volume in Figure 2.4-2. The values are comparable to those reported by Vaudry (1977) although, as expected, the scatter in the data points is large.

Four of the 30 samples broke along surfaces away from the slit. The load at failure was low, and these values are not included in the plots. These samples were from the interval which contained the dispersed sediments and lenses of whitish ice described above, and their salinities were abnormally high (Table 2.4-1). Apparently the samples contained large inhomogenities which limited their strength.

The remaining samples broke cleanly along a single crack, with no visible internal cracking in the sample.

Vaudry (1977) determined a least square straight line fit to his **results** for fracture toughness vs. brine volume for the laboratory **grown** saline ice tested in his study. That line is shown in Figure 2.4-2 along with a similar line determined from the data of this study. The two lines do not differ significantly. This suggests that the calculated values for fracture energy ($y_c \approx 3 \times 10^{-3}$ **kPa-m**) and critical crack length ($c \approx 0.6$ cm) should be the **same** for both test series. However, the variation of grain size and fabric in the samples used in this study, coupled with the fact that no independent measurements were made of the bending strength or Young's modulus, suggests **that such a comparison should be treated with caution**. In addition, the

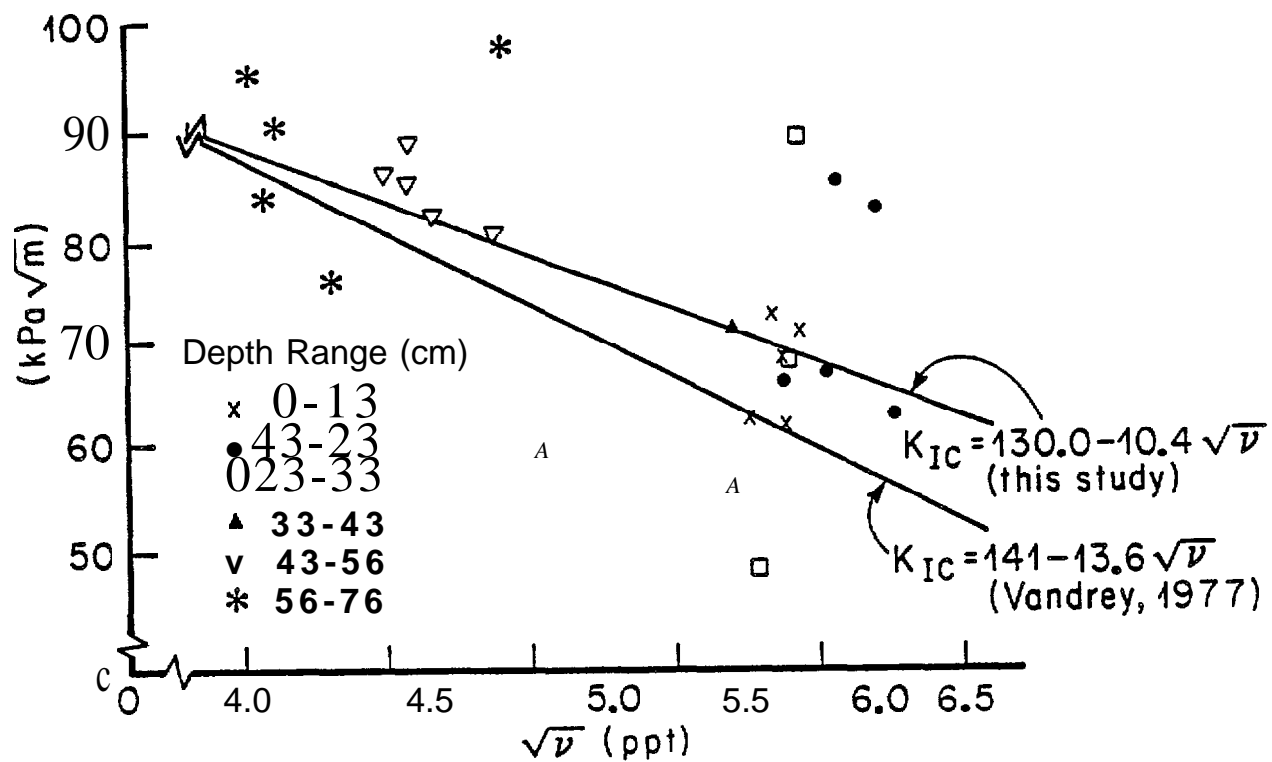


Figure 2.4-2 Fracture toughness vs. square root of brine volume.

similarity of the results of this study and those of **Vaudry** (1977) and **Urabe** et al., (1980) implies that there is little to be gained by additional fracture toughness testing of sea ice which is not directed to investigating the influence of specific variables.

TABLE 2.4-1
RESULTS OF FRACTURE TOUGHNESS TESTS

| Sample No.** | Displacement (cm x 10 ²) | | | Load (kPa) | K _{IC} *** (kPa√m) | Salinity (ppt) | √v ppt |
|----------------|---|-------------|-------------|---------------|--------------------------------|-------------------|-------------|
| | L | C | R | | | | |
| 0-5-1 | 3.18 | 4.47 | 4.17 | 199 | 62.3 | 8.2 | 5.76 |
| 0-5-2 | 3.07 | 3.43 | 4.27 | 229 | 71*9 | 8.4 | 5.83 |
| 0-5-3 | 3.18 | 3.71 | 4.24 | 217 | 67.9 | 8.6 | 5.89 |
| 0-5-4 | 2.51 | 2.77 | 2.77 | 226 | 70.8 | 8.7 | 5.93 |
| 0-5-5 | 2.06 | 3.33 | 3.53 | 195 | 61.2 | 8.6 | 5.89 |
| 5-9-1 | 2.54 | 3.05 | 3.35 | 210 | 65.8 | 8.5 | 5.86 |
| 5-9-2 | 6*86 | | ... | 262 | 82.3 | 9.5 | 6.20 |
| 5-9-3 | 5.46 | 4.27 | 4.24 | 270 | 84.5 | 9.1 | 6.06 |
| 5-9-4 | 5.46 | 4.27 | 4.24 | 270 | 84.5 | 9.1 | 6.06 |
| 5-9-5 | 5.03 | 5.51 | 3.10 | 211 | 66.3 | 9.0 | 6.03 |
| 9-13-1 | 3.63 | 6.15 | | 152 | 47.8 | 8.3 | 5.79 |
| 9-13-2 | 2.16 | 2.79 | 3.28 | 283 | 89.0 | 8.7 | 5.93 |
| 9-13-3 | 5.84 | - | - | 78 | 24.5 | 9.1 | 6.06 |
| 9-13-4 | 2.82 | 2.49 | 2.46 | 215 | 67.6 | 8.6 | 5.89 |
| 9-13-5 | 0.711 | 6.30 | 0.813 | 117 | 36.8 | 9.3 | 6.13 |
| 13-17-1 | 1.40 | 1.30 | 1.45 | 148 | 46.5 | 6.3 | 5.05 |
| 13-17-2 | 1.88 | 2.46 | | 187 | 58.7 | 6.6 | 5.16 |
| 13-17-3 | 2.59 | 2.92 | 3.05 | 226 | 71.0 | 7.9 | 5.65 |
| 13-17-4 | 5.84 | 8.33 | 4.09 | 177 | 55.6 | 7.9 | 5.65 |
| 13-17-5 | 2.18 | 3.00 | 3.07 | 131 | 41.2 | | |
| 17-22-1 | 2.21 | 3.33 | 2.92 | 281 | 88.1 | 5.2 | 4.58 |
| 17-22-2 | 1.88 | 1.73 | 1.65 | 268 | 84.2 | 5.3 | 4.58 |
| 17-22-3 | 1.09 | 1.30 | 1.42 | 260 | 81.5 | 5.4 | 4.67 |
| 17-22-4 | 2.79 | 2.34 | 2.11 | 272 | 85.5 | 5.0 | 4.49 |
| 17-22-5 | 4.06 | 4.45 | 3.89 | 254 | 79.9 | 5.9 | 4.88 |
| 22-30-1 | | - | 5.26 | 241 | 75.6 | 4.6 | 4.31 |
| 22-30-2 | 2.06 | 2.57 | 3.25 | 312 | 97.9 | 4.9 | 4.45 |
| 22-30-3 | 3.96 | 4.50 | 4.65 | 265 | 83.1 | 4.1 | 4.07 |
| 22-30-4 | 2.69 | 3.53 | 3.15 | 304 | 95.4 | 4.0 | 4.02 |
| 22-30-5 | 3.58 | 4.85 | 5.13 | 286 | 89.9 | 4.2 | 4.12 |

*Failed away from the slit.

**The first two numbers of the sample designation refer to the depth range in inches.

***Multiply by 0.910 to convert to psi √in.

REFERENCES CITED

- Urabe N. .Iwaski T. and Yoshitake A. (1980).** Fracture toughness of sea ice; Cold Reg. Sci. and Tech., v. 3, pp. 29-37.
- Vaudrey, K. D. (1977). Ice engineering study of related properties of floating ice sheets and summary of elastic and **viscoelastic** analyses; Naval Civil Eng. Lab., Tech. Rpt. R-860,79 pp.

2.5 AN INEXPENSIVE STRAIN TRANSDUCER FOR LABORATORY EXPERIMENTS

by

Lewis H. Shapiro, Ronald C. **Metzner** and Jerome B. Johnson

2.51 INTRODUCTION

At the time the experimental phase of the program was terminated, it was intended that a series of small-scale **uniaxial** compression tests on sea ice be conducted in the field in conjunction with the larger-scale experiments described in Section 2.24. This would have involved testing samples to failure in compression at high rates of loading, which often results in explosive failure of the samples. Because of the inherent difficulty in attaching resistance wire strain gauges to the surface of ice samples, it would have been necessary to use an extensometer to measure strain during the tests. These are relatively fragile instruments which are also quite expensive. Rather than subject them to possible damage during the testing program we searched for an inexpensive substitute. We found no suitable equipment available commercially and, as a result, undertook the task of designing one. The result was a clip gage in the form of a semi-circular arch (Figure 2.5-1) which can be fabricated for about 1/20 the cost of a commercial extensometer. The characteristics of the gage are described in the following sections.

2.52 CLIP-TYPE STRAIN GAGES

Clip gages (Perry and **Lissner**, 1962) operate on the principle that the true strain of the sample is sensed as the strain across the tips of the gage (**er**), which are attached to the sample. This strain is transformed **into** bending strain which is

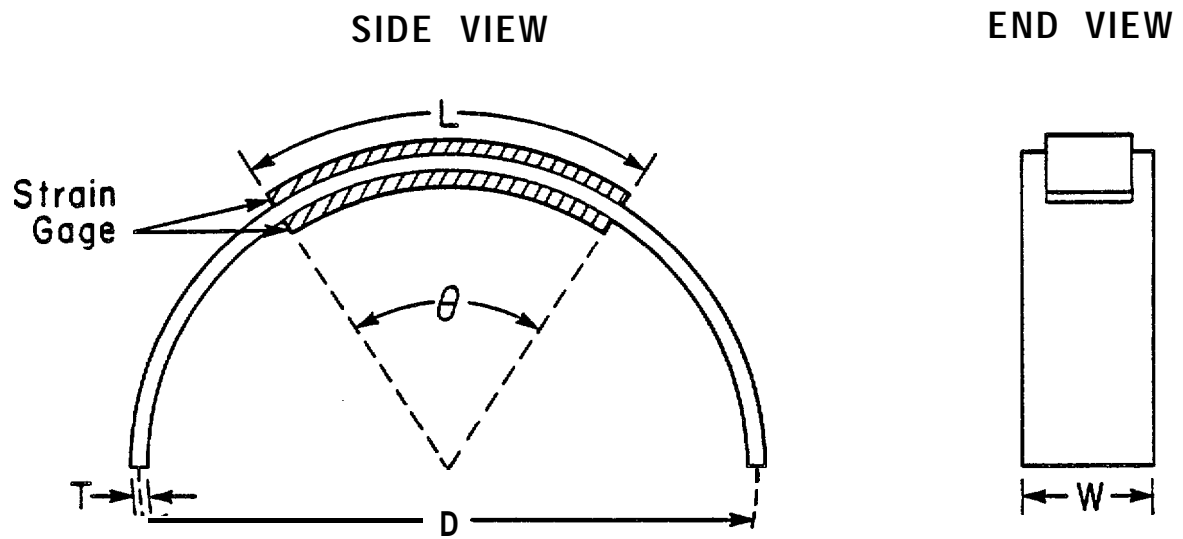


Figure 2.5-1 Schematic diagram of a clip gage in the form of a semi-circular arch. The ends of the arch are attached to the sample so that the sample strain (ϵ_f) is shown as an apparent change in the arch diameter D .

measured by wire strain gages mounted on the clip gage. The measured strain (ϵ_b) is then used to determine the true strain (ϵ_f) through a calibration curve. Typically, clip gages are made of spring steel or similar material, bent into a channel shape (Figure 2.5-2). In this form they are much less sensitive to the strain in the sample than resistance wire gages attached directly to the sample. Thus, clip gages are normally used in applications in which it is anticipated that the strain will exceed the limits of resistance wire gages. However, for the application we anticipated, it was necessary that the clip gages be capable of monitoring strains in the same range as wire gages. Therefore, we sought alternatives to conventional clip gages, which led to the recognition that the circular arch design might be sufficiently sensitive to strain to serve the desired purpose. To investigate this, we did a series of calculations using a simple finite element model of a circular arch, and fabricated several arches for experimental study. The characteristics of the arches are given in Table 2.5-1.

2.53 CALCULATION OF ARCH-GAGE PROPERTIES

The finite element model consisted of a 180° arch represented by 40 connected linear elements. The boundary conditions required the tips of the arch to remain in the plane of the base diameter during deformation. The strain which **would** be sensed by resistance strain gages fixed to the arch and covering different arc lengths L [= $(li/2)$] was determined by **summing** the strain in the individual elements of the model over the desired length. Calculations were done for arches of various dimensions and material properties for several values of ϵ_f and L . The results indicated that (1) small wire gages over the crest of the arch provided the greatest sensitivity, and (2) the sensitivity of the arch gages is linearly related to the ratio of the gage thickness to the diameter (T/D) and independent of the properties of the material from which the arch is constructed.

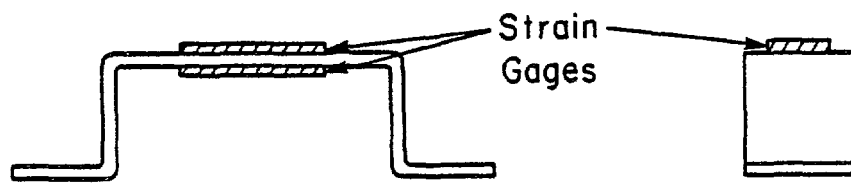


Figure 2.5-2 Schematic diagram of a typical channel-type clip gage.

TABLE 2.5-1 CHARACTERISTICS OF FABRICATED ARCH-TYPE CLIP GAGES

| Arch Number | Material | Diameter (D cm) | Thickness (T cm) | Width (W cm) | θ (Deg) | Resistance Gages |
|-------------|-------------------|-----------------|------------------|--------------|----------------|--------------------------|
| 1. | Steel (AISI 1020) | 2.54 | 0.0178 | 0.953 | 121.8 | 1/2 bridge, 120 ω |
| 2. | Steel (AISI 1020) | 2.54 | 0.0305 | 0.953 | 121.8 | 1/2 bridge, 120 ω |
| 2a. | Steel (AISI 1020) | 2.54 | 0.0394 | 0.953 | 64.5 | 1/2 bridge, 350 ω |
| 3. | Steel, stainless | 5.24 | 0.0838 | 1.270 | 56.4 | full bridge, 350 G.) |
| 4. | Steel, stainless | 5.24 | 0.0838 | 1.270 | 56.4 | 1/2 bridge 350 ω |
| 5. | Acrylic Plastic | 15.24 | 0.3175 | 2.54 | 20.3 | full bridge 120 ω |
| 6. | Acrylic Plastic | 5.4 | 0.3175 | 1.270 | 56.4 | full bridge 350 ω |

**Arch 2a* is Arch 2 with a second set of strain gages fixed on top of the first set to increase the thickness, T.

The calculated effective modulus (M_e) of an arch followed a relationship of the form

$$M_e = AE (wD^3)^{-1}$$

where A is a constant (3.48×10^2 in SI units for the values used in the calculations), w is the width of the gage, and E is Young's modulus of the material. The form of the equation is similar to that determined from the solution to a similar (though not identical) problem by Timoshenko and Goodier (1951).

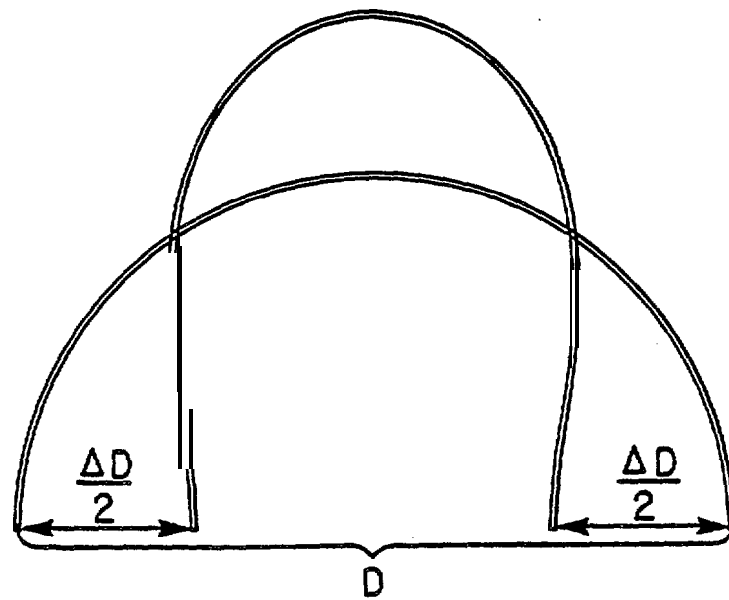
Based on the calculations from the finite element model, it was assumed that the true strain (e_f) and the strain sensed by the gage (e_b) would be related by an expression of the form

$$e_f = f(\theta) g(T/D) e_b$$

in which $g(T/D)$ is a linear function of the ratio T/D and $f(\theta)$ is a correction factor involving the function $\cos(\theta/2)$ which is required to account for the irregular shape to which the gage bends (Figure 2.5-3).

2.54 MEASUREMENT OF GAGE RESPONSE

All of the gages listed in Table 2.5-1 were deformed on a traveling stage micrometer which could be advanced in precise increments of 0.001 mm. A standard strain increment and excitation voltage were used for all tests to facilitate comparison of the results. Each arch was mounted on the micrometer and stepped through several increments of a standard strain and the results were averaged to determine the voltage output per unit strain. The degree of linearity was determined by recording the voltage output vs. accumulated strain in tension or compression. Because only a few gages were constructed, the results should be



ARCH STRAIN TRANSDUCER

Figure 2.5-3 Bending of an arch clip gage as a result of shortening of the diameter D .

regarded as preliminary, pending additional experiments. However, as described below, the results suggest that the model predictions are, at least, approximately correct.

The results of the experiments showed that all of the gages were linear for strains (ϵ_f) up to at least 2% in both tension and compression (linearity ranged up to 8% in compression for the steel gages). In addition, the sensitivity of the gages was linearly related to the ratio T/D (Figure 2.5-4) and independent of the material used in construction, as predicted by the calculations. Finally, the results of an experiment in which an arch gage was used to track the strain sensed by a resistance strain gage attached to a small beam are shown in Figure 2.5-5. In the experiment, the beam was forced to bend slightly out of plane to simulate the “barreling” of a test specimen. The linearity of the relationship is apparent.

2.55 DISCUSSION AND CONCLUSIONS

We believe that the use of arch clip gages is practical now, provided that the calibrations are established for the exact conditions under which they are to be used (i.e. method of attachment to the samples, temperature, etc.). However, additional work is needed in several areas to define the general properties of the gages. These include (1) the range of T/D ratios for different materials for which the calculations are valid, (2) the detailed form of the correction factor $f(\theta)$, and (3) the variations in response of the gages for different methods of attachment to the sample.

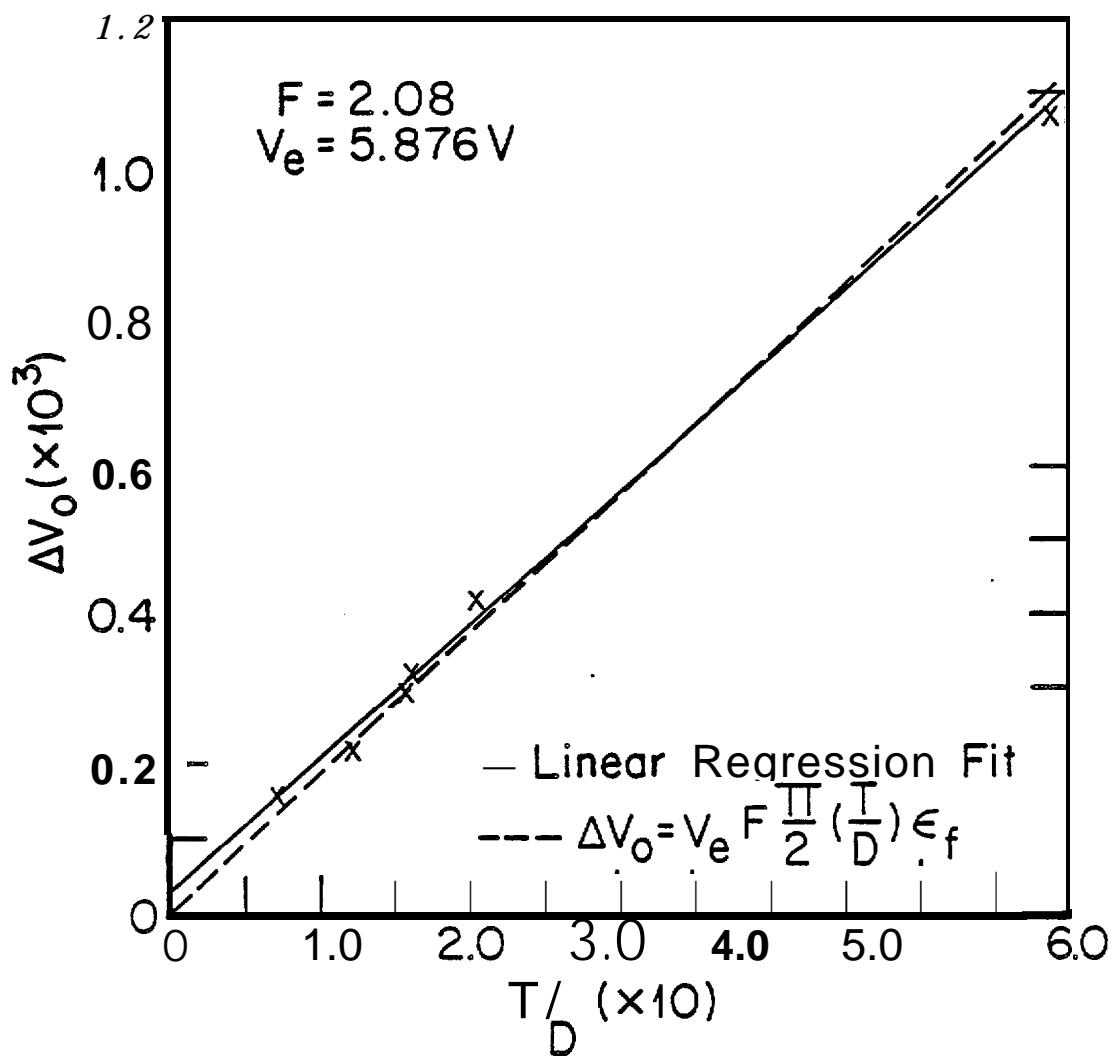


Figure 2.5-4 Voltage output per unit strain vs. thickness to diameter ratio for the six arch gages listed in Table 2.5-1.

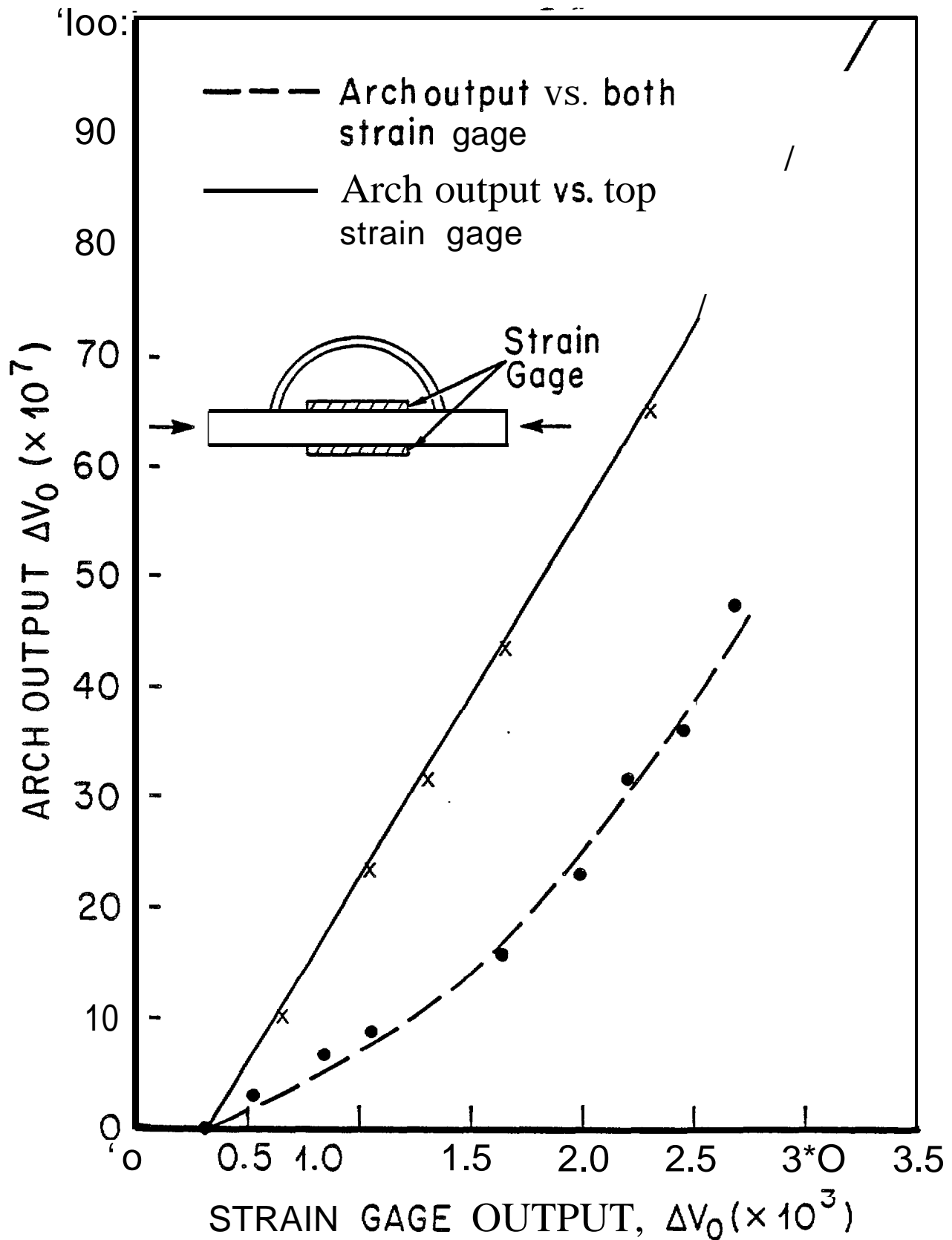


Figure 2.5-5 Plot of arch clip gage output vs. resistance gage output for the bending beam experiment. The arch gage accurately tracked the resistance gage over which it was mounted. The curve for the combined output of both resistance gages reflects the bending of the beam.

REFERENCES CITED

- Perry, **C.C.**, and Lissner, **H.R.** (1962) The Strain Gauge Primer, McGraw-Hill, New York, 2nd ed., pp. 332.
- Timoshenko, S., and Goodier, J. N., 1951, Theory of Elasticity, McGraw-Hill, New York, 2nd ed., **pp.506.**

3.0 DEFORMATION OF SEA ICE IN THE NEAR-SHORE ZONE

3.1 FAST ICE SHEET DEFORMATION DURING ICE PUSH AND SHORE ICE RIDE-UP

by

Lewis H. Shapiro, Ronald **C. Metzner**

and Arnold Hanson* and Jerome B. Johnson

3.11 INTRODUCTION

During the course of this project, we had the opportunity to study several **ice-**push events in the Barrow area. The events occurred over the three year period between **1975** and 1978 and were described and analyzed in Shapiro et al. (1984). This section is a summary of the results presented in that paper.

The study is an extension of the general problem of determining the forces associated with the formation of shore ice pile-ups and grounded pressure ridges. The basic approach used in these studies follows that of Parmenter and Coon (**1972**) for free-floating pressure ridges, in which the force is calculated from the work required to store the potential energy in the ridge and overcome friction (see for example, **Kovacs** and Sodhi, 1979; **Vivatrat** and Kreider, 1981). Other possible energy sinks in the process (i.e., ice fracture, gouging of the sea floor, etc.) are not accounted for. The contributions from these sources are not considered to be **large**, but neglecting them emphasizes that the forces calculated represent lower limits to the possible forces acting at the ridge site or along the beach. Calculated stresses range up to 3.5×10^5 Pa (**Kovacs** and Sodhi, 1979) and are thus higher than the estimated maximum stress which can be transmitted through pack ice (approximately 10^5 Pa; Pritchard, 1977). This suggests that shore ice pile-up and ride-up require some mechanism for stress concentration, through which stresses transmitted through the pack ice are amplified at the point of ridging or ice pile-up.

The mechanism might involve a variety of factors including **(1)** the initial distribution of stress along the pack **ice-landfast** ice boundary at the start of the event, **(2)** the changes in the stress field internal to the landfast ice sheet due to deformation and fracture as the motion proceeds and, **(3)** the shape of the shoreline and the nature of the bonding between the ice and the shore.

The results of this study provide a description of some of the processes which operate during ice push events, and lead to the suggestion of a model through which numerical studies could be done.

The events which were studied are listed in Table 3.1-1 along with their key characteristics.

3.12 SUMMARY OF DATA AND OBSERVATIONS

We can make six generalizations from the observational **data**:

(1) In ice ride-up events, the length of beach affected is probably significantly shorter than the length of the edge of the fast ice along which the driving forces are applied.

(2) The pack ice through which the driving force is transmitted is likely to be compact, indicating that ridging of thin, weak ice has **already** occurred at the time of an ice push event. Thus, the stresses transmitted to the fast ice edge and on toward the beach may be greater than those in normal pack ice where thin ice is present. This also implies that ice push or ride-up events are driven by wind stress imparted to the ice over large areas, and that local winds are not alone responsible.

(3) During the spring events the ice sheet was initially driven toward the beach as a unit, closing the shore lead. Then, fractures formed parallel to the direction of the motion (usually at high angles to the shore). During small advances the cracks did not propagate far offshore, but during large advances some of the fractures crossed the entire width of the fast ice sheet. This indicates that the length

TABLE 3.1-1 Ice Pile-up and Ride-Up Events in the Point Barrow
Area, 1975-1978

| Location | Date | Major Features |
|-----------------------------------|-----------------------|---|
| Along beach at NARL | July 4-6, 1975 | Offshore boundary of fast ice sheet moved shoreward about 250 m. Extensive ice pile-up and ride-up along about 2.5 km of beach. |
| Along beach at NARL | June 30, 1976 | Fast ice sheet moved 15-25 m shoreward. Ice pile-up, ride-up and over-thrusting along the same area as 1975 event. |
| City of Barrow | Dec. 30, 1977 | Ice advanced up the beach on a 725 m front; maximum advance of 35 m. Ice pile-up along the entire front. |
| Point Barrow | Dec. 30, 1977(?) | Small ice pile-up on Chukchi Sea side of Point Barrow. |
| Tapkaluk Island | Late January 1978 | Ice advanced along a 900 m front and overrode the island in several locations. |
| Martin Island | Late January 1978 | Ice advanced onto island about 55 m along a 215 m front. |
| Igalik Island | Late January 1978 | Ice advanced 105 m and overrode the island along a 400 m wide front. |

of the cracks depends upon the extent of the advance. In addition, the longer fractures separated the ice sheet into segments, each of which advanced through a different distance.

(4) The three winter events at Barrow, **Tapkaluk** Island and Martin Island show a similar pattern of fractures bounding the segment of the fast ice sheet which advanced. The pattern consists of two **fractures**; one is approximately perpendicular to the beach and may show evidence of active compressive and/or shear stresses in the adjacent ice sheet. The second fracture extends from a point at or near the intersection between the first fracture and the beach. At its origin, it is approximately tangent to the beach but it curves offshore with increasing distance. No movement of the ice sheet occurs until these fractures form.

(5) The **Igalik Island** event, which occurred in winter, was like the spring events **at** Barrow in that fractures bounding the thrust sheet were at a high angle to the shore and the thrust sheet moved as a plug with little internal fracturing.

(6) The spring events caused extensive bulldozing of the beach gravel into **ice**-push ridges as much as **1** m high which enhanced the probability of formation of ice pile-ups. In contrast, bulldozing of the beach during the winter events was minor.

3.13 DISCUSSION

The cracks bounding the winter thrust sheets at Barrow, **Tapkaluk** Island, and Martin Island share a geometric configuration which has an analogy in the theory of plasticity. The pattern of two cracks meeting at a right angle **at** the boundary of a field of deforming material, one curving and tangent to the boundary and the other normal, occurs frequently in slip-line field theory (see for example, **Prager** and Hedge, 1951). An example is shown in Figure 3.1-1, which is part of the solution to **Prandtl's** problem for the flow field of a perfectly plastic material squeezed in plane strain between two rigid plates with rough (no-slip) surfaces. The lines indicate the

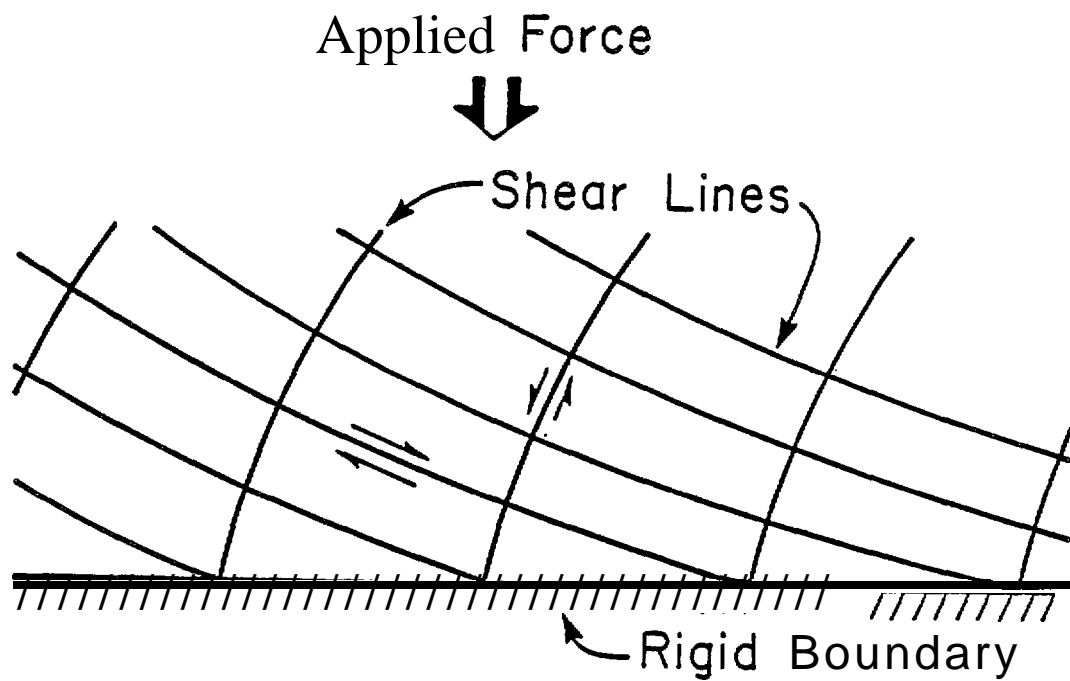


Figure 3.1-1 Example of the relationships between shear lines and a rigid boundary from prandtl's solution for an infinite **slab** of a perfectly plastic material compressed between rough, rigid plates (from Prager and Hedge, 1951).

trajectories of the maximum shear stresses and, according to von **Mises'** criterion, can be viewed as lines along which failure in shear can occur. This interpretation has been used to explain fracture patterns observed in rocks (Varnes, 1962; Cummings, 1976).

If we assume the analogy to apply at least qualitatively to the plane stress problem for an ice sheet in winter, an immediate implication is that the ice was firmly frozen to the beach when the cracks were initiated, in accordance with the requirement that the boundary be rough. There is also the suggestion that the direction of loading was normal to the beach. However, this does not require that the force arising from the interaction between the pack ice and the fast ice be directed normal to the shore. Some deviation can occur, depending upon the value of the effective coefficient of friction at the boundary. Clearly, if this is low, then the normal component of the applied force will be preferentially transmitted.

As noted, in the two spring events at Barrow the edge of the ice sheet was melted back from the shore when the **first** motion occurred. Thus, movement through several meters was possible before the ice contacted the beach. Subsequently, the advance was irregular with some sections of the leading edge stopped while others continued to move. A similar pattern of displacement apparently developed in the **Tapkaluk** Island event. Possible patterns of stresses and displacements in the fast ice sheet resulting from movements of this type were examined using finite-element methods.

The SAP **IV** structural analysis finite-element program (Bathe et **al.**, 1973) was used to model a fast ice sheet in irregular contact with the shore under a distributed load along its offshore boundary. A two-dimensional array of linearly elastic membrane elements was used to form a 300-element rectangular mesh to represent an ice sheet adjacent to a beach. The state of the ice sheet-beach interface was specified by the boundary conditions along one of the long edges of the rectangle.

These determined **the lengths of reaches** of the boundary along which **the ice edge** was fixed or free to move in response to the applied loads. The configuration used in most of the calculations consisted of a fixed boundary with central free segments of various lengths.

A uniformly distributed load was applied on the seaward boundary of the ice sheet (the grid boundary opposite the ice-beach interface) for each calculation run. The loading direction was varied to simulate normal loading (load directed normal to the beach), simple shear loading (load directed parallel to the beach) and combined shear and normal loading (load directed at 45° to the beach). /

The calculations did not include a mechanism by which fixed node points along the beach could be released and moved according to some criterion in the program. Further, the SAP IV program has no provision for the use of stress-strain laws other than linear elasticity. Therefore, the results of the computations can only be used as indicators of the geometries of the stress and displacement fields at the instant the **load** is applied. These fields were interpreted on the assumption that stress concentration points and zones of high stress or displacement gradients indicated the points of origin and directions of propagation of fractures in the ice sheet. While a more flexible model would have been useful, the results are adequate for our qualitative interpretations.

The most important results of the calculations are that, for cases of normal loading and combined normal and shear loading, the highest stress concentrations occur (as expected) at the points of transition from the fixed- to **free-**boundary condition along the ice-beach interface. In addition, the zones of high displacement gradient which trend offshore from these points suggest the formation of shear zones oriented approximately parallel to the line of action of the boundary stresses. Thus, if only part of the ice-beach boundary is free to be displaced, the ice sheet within this segment will tend to advance up the beach as a plug, as would be

anticipated for a punch test. The same displacement pattern would also **result** if the ice sheet was in motion and then stopped along sections of its leading edge due to interaction with the beach or other obstacles. In that case, a crack at a high angle to shore and parallel to the direction of motion would be expected to form.

Examples of this pattern were noted in the 1975 and 1976 events at Barrow and within the thrust sheet at **Tapkaluk** Island. **In** these cases, the fractures separated the segments of the ice sheet that moved through different distances.

3.14 PROPOSED MODEL

The results of the observations and analysis can be combined to suggest a model for the fracture and displacement of a fast ice sheet during a typical winter ice-push or ice ride-up event (Figure 3.1-2). The ice is assumed to be initially fixed to the beach, and the possible effects of grounded features **are** ignored. Figure 3.1-2A shows the geometry of the initial cracks which form according to von **Mises'** criterion. Sonic minor landward movement **all** along the front can occur at this time. In the second stage (Figure **3.1-2B**), the thrust sheet is pushed up the beach with a tendency to rotate along the curving crack as indicated by the arrows. This results in the formation of compressive features along the high-angle crack. In addition, the normal force transmitted across the curving crack causes onshore movement of the wedge of ice between that crack and the shore. Figure **3.1-2C** shows the final form of the process if there is little or no differential motion at the leading edge of the thrust sheet as it moves up the beach, or if the total displacement is small. The alternative of segmentation of the thrust sheet as occurred at **Tapkaluk** Island is shown in Figure **3.1-2D**. In this case, compressive features at either side of the diagram may not be present **if,there** is little resistance to movement along the leading edge of the thrust sheet. Instead, plug geometry (as described above) develops rapidly, and motion occurs along the high-angle cracks that bound the

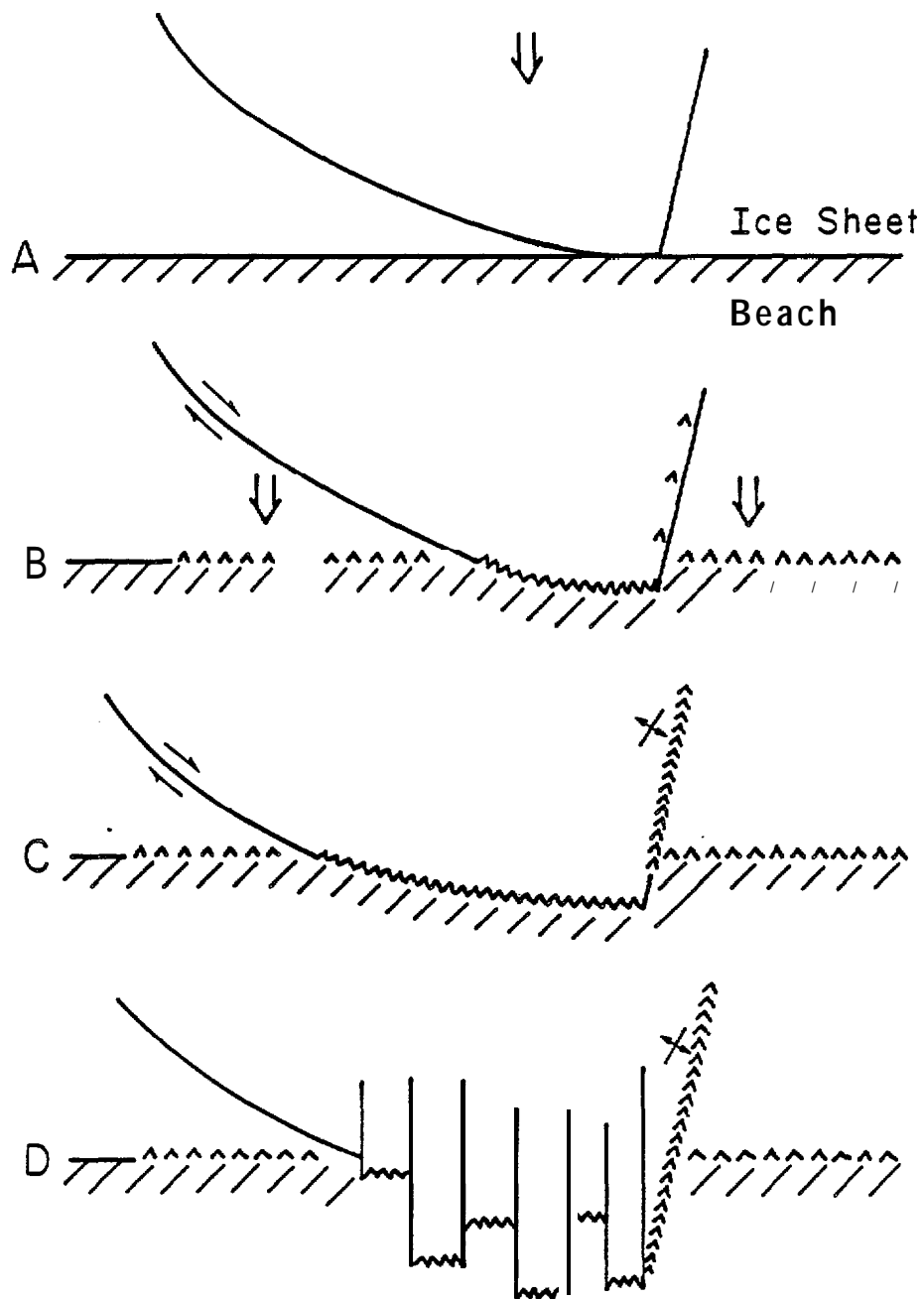


Figure 3.1-2 Proposed model **for the fracture and displacement of a fast ice** sheet during an ice-push event. See text for discussion.

plugs. Additional cracks with similar orientation then develop as the movement progresses.

For an ice-push event during break-up, melting along the shore weakens the bond between the ice sheet and the beach. Thus, the first three steps in Figure 3.1-2 do not apply. Instead, cracks at a high angle to the beach form in the early stages of the process and govern subsequent displacement of the ice sheet. A similar process might also be expected to occur for an event during freeze-up, when the ice sheet is not firmly bonded to the beach.

The geometry of the initial stress field at the time when the fractures of Figure 3.1-2A are formed can be assumed to be similar to **Prandtl's** solution, modified to reflect the distribution of grounded features, the shape of the shoreline and of the pack **ice-landfast** ice boundary, and the distribution of forces along the latter. The fractures begin at some local stress concentration along the shoreline. If no suitable stress concentration exists, then the stresses are relieved by ridging at the edge of the fast ice, or elsewhere in the fast ice sheet, and no ice advance will occur. After the fractures form or the movement of the thrust sheet begins, the stress distribution will vary in accordance with changes in the boundary conditions and the distribution of new fractures within the thrust sheet. The final form of the thrust sheet (including ice pile-up and ride-up at the beach) will depend upon the sequence of changes and the magnitudes of the stress variations which occur throughout the process. As a result, the extent to which the **local** stresses (deduced ex post facto) are representative, of the far-field stresses at the start will vary from event to event.

This model assembles the available information into a pattern; clearly the interpretation will require modification as more data become available. However, even a preliminary model can serve to emphasize questions that can usefully be raised regarding the processes of ice push and ice ride-up. Before proceeding to these, however, we should note that the January 1978 event at **Igalik** Island does not

fit the model because its crack pattern is more similar to a spring event. There are several possible explanations, but none are supported by data. It is possible that the open lead was closer to (or at) the beach here than at other localities along the barrier islands. The resolution of the satellite imagery does not permit this to be evaluated. Alternatively, it is possible that the bonding between the ice sheet and the beach was uniformly weak; thus motion occurred all along the beach when the load was applied, as is postulated during spring events. Subsequently, the low, uniform slope of the island did not resist the motion enough to break the ice sheet up into smaller segments.

3.15 CONCLUSIONS

The suggestion that ice pile-up and ride-up represent the **result** of a stress concentration mechanism is supported by three points: **(1)** The length of these features along the beach is generally less than that along which pack ice-fast ice interaction occurs; (2) For the case of winter events, the fractures bounding the thrust sheets tend to make the dimensions of the thrust sheet wider at the offshore edge than at the beach, and (3) For an ice sheet advancing as a series of discrete segments, the resistance to the motion (and thus the force) can vary between segments, depending upon local conditions. This emphasizes the need for care in deducing far-field stresses from those required to form local features. It is likely that such values will be conservative in the sense that they will overestimate the far-field stresses, but the extent **to** which this is true depends on the contribution of other energy sinks that may not be accounted for in the calculations.

The discussion above addresses a possible sequence of events for breakup of an ice sheet during an ice-push event. Other aspects **which** require study include (1) possible seasonal variation in the efficiency of grounded features in anchoring the ice sheet and thus affecting shoreward ice movement, (2) the influence of the nature of

the boundary between the fast ice and the beach, and (3) the nature of the interactions between pack ice and fast ice.

REFERENCES CITED

- Cummings, D., 1976. Bull. Geol. Soc. Amer., 88,720.
- Kovacs**, A., Sodhi, D. S., and Cox, G.F.N., 1982. **CRREL** Report 82-31. U.S. Army Cold Reg. Res. and Eng. Lab., Hanover, NH.
- Parmerter, R. R. and Coon, M. D., 1972. J. Geophys. Res., 77,6565.
- Prager, W. and Hodge, **P. G.**, Jr., **1951**. "Theory of Perfectly Plastic Solids." **Wiley**, New **York**.
- Pritchard, R. **S.**, **1977**. In: "**Proceedings, POAC "77"**", Vol. 1, p. 494, Memorial Univ. of Newfoundland, St. John's.
- Shapiro, **L. H.**, **Metzner**, R. C., Hanson, A. and Johnson, J. B., 1984. In: "The Alaskan Beaufort Sea: Ecosystems and Environments", P. W. Barnes, **D. M. Schell**, and E. Reimnitz, eds., Academic Press, New York, **p.** 137.
- Varnes, D. J., 1962. U.S. **Geol.** Survey Prof. Paper 378-B, **B-1**.
- Vivatrat, V. and Kreider, J. R., 1981. In: "Proceedings of the Offshore Technology Conference", p. 471, Houston, TX.

3.2 HISTORICAL REFERENCES TO ICE CONDITIONS ALONG THE BEAUFORT SEA COAST OF ALASKA

by

Lewis **H.** Shapiro and Ronald C. **Metzner**

3.21 INTRODUCTION

The existing data base regarding the average and extreme ice conditions along the northern coast of Alaska comes primarily from observations made since the discovery of oil at Prudhoe Bay. This followed from the increase in interest in the area, and the recognition that the adjacent continental shelf would be the subject of further exploration. In this context, the frequency of occurrence of unusual or extreme events involving the ice cover in near shore areas is of interest. It maybe true that the most severe conditions likely to be encountered have occurred since observations have increased. However, this cannot be known until the data base of observations is extended in time.

The purpose of this project was to attempt to extend the data base backward in time through interviews with local residents of the North **Slope** who had lived in coastal areas in past years. Many of these people were engaged in traditional hunting and trapping activities along the coast, and had both the opportunity and the incentive to carefully observe ice conditions in the area.

3.22 PROCEDURES

A pilot program of interviews was conducted involving eight individuals ranging from **55** to 85 years of age. All had **lived** in different coastal areas in the past, and had long experience traveling offshore along the North Slope over the ice during winter, or in small boats during the **summer**. In four cases the individual was interviewed (by Mr. **K.** Toovak of Barrow who collaborated with us on the program)

and responded to questions posed. In the others, the person was supplied with a tape recorder and a list of questions and simply asked to provide background and to respond to the questions. The interviews and commentary were all done in the **Inupiaq** language. They were translated by Mr. Toovak speaking into a tape recorder while listening to the interview being played on a second recorder and later transcribed. A second series of interviews produced a wealth of historical information, but did not add anything of interest to the objectives of the program. Thus, they were not transcribed, but copies of the tapes (as well as those from the first series of interviews) were given to the **Alaska** Native Language Center Of the University of Alaska for use in the compilation of a dictionary of the **Inupiaq** language. Copies were also archived with the oral history program at **Rasmuson** Library at the University.

3.23 SUMMARY AND DISCUSSION

A detailed description of the project, including the results and an evaluation of the methodology, was given in Shapiro and Metzner (1979). The major observations were (1) descriptions of ice-push events in the Barrow area during winter, (2) the first report of a major ice movement in Harrison Bay during winter (the formation in February of a 1 mile wide lead, probably along the trend of the 10 m depth contour, and extending from near Cape **Halkett** toward Thetis Island), and (3) the first report of a major breakup ice-push event near Cape **Halkett** (in **July**). **Negative** information was also useful. As an example, none of the people questioned reported any instances of winter ice-push events driving the ice over the barrier islands along the North Slope. However, an event of this type occurred during the 1977-78 winter along the north side of **Elson** Lagoon east of Point Barrow (Section 3.1). Thus, the lack of previous observations suggests that this is a rare event.

As anticipated, there was little reference to synoptic relationships between ice motion and weather systems. However, the point was noted that westerly winds in winter form a lead which extends from Cross Island, along the north side of the barrier islands and across Camden Bay. This is apparently a rapid event, because we have two stories of hunting parties trapped on the offshore side of the lead.

Numerous descriptions were given of summer ice conditions, particularly with regard to small boat travel. These included some general rules-of-thumb regarding relationships between wind directions and changes in position of the pack ice edge, and the drift of heavy ice near shore.

Finally, there were a few references to the relationship between marine mammals and summer ice conditions, and to bowhead whale migration and capture in the **Prudhoe** Bay area.

REFERENCE CITED

Shapiro, L. **H.** and **Metzner**, R. **C.** (1979) Historical references to ice conditions along the Beaufort Sea coast of Alaska; Geophysical Institute Report UAG R-268, pp. 62.

3.3 VIBRATION OF SEA ICE SHEETS

by

Lewis H. Shapiro and Howard F. Bates

3.31 INTRODUCTION

This study began as the result of several incidental observations which indicated that long-period (i.e. 6 to 10 minutes) vibrations of an ice sheet maybe associated with increasing stress in the ice in near shore areas. Further, in many cases, the vibrations began on the order of several hours before the effect of the increasing stress was shown by motion of the ice sheet, suggesting that long-period vibrations might be precursors to episodes of ice motion. If so, monitoring ice sheet vibration through a tide gauge under the ice in shallow water (or by tiltmeters on the surface of the ice sheet in deeper water) might provide the basis for a system to warn of impending ice motion, thus enhancing safety in offshore operations.

To investigate the association, we undertook a theoretical study of the process **of** wave propagation in an ice-covered sea. The purpose was to determine the conditions under which waves of the period observed would propagate, and the possible effect of ice stress on the wave periods. The results were published in three papers (Bates and Shapiro, 1980a, **1981a,b**). In addition, the theory was applied to the problem of breaking floating ice sheets by traveling vehicles in Bates and Shapiro (**1980b**).

3.32 BACKGROUND

Observations of ice motion or rising stress levels associated with long-period vibrations came from the following sources:

(1) On two occasions, waves with amplitudes of a few centimeters and periods on the order of 600 seconds were recorded by a tide gauge under the fast ice sheet near Point Barrow. During one of these events, several stress transducers, which

had been implanted in the fast ice sheet for other purposes, recorded a continuously increasing compressive stress with superimposed sinusoidal stress variations in phase with the waves. In addition, sinusoidal patterns of strain variation were also recorded by strain gauges in the ice sheet. The sinusoidal variations apparently resulted from flexing of the ice sheet in response to the waves propagating through the water. The stress levels were below the calibrated range of the transducers (suggesting that the stress reached a maximum of a few **kPa**) but the pattern was **clear**. In the other event, no stress transducers were installed in the ice. However, compressive stresses are indicated because the ice sheet advanced about 10 m onto the beach as the waves reached their maximum amplitude about 12 hours after they were first observed.

(2) Sinusoidal stress variations (with time) had previously been observed on stress transducer data (R. D. Nelson, **unpub.**), but no supporting tide gauge records were available with which to associate the stress variations.

(3) Hunkins (**1962**) reported that long-period waves with amplitudes inversely proportional to frequency **accompanied winds** exceeding 5 **m/sec** (10 kn) over relatively continuous floating sea ice.

(4) As discussed in Section 3.53.3, the University of Alaska sea ice radar system often recorded examples of “flickering” of reflectors on the ice surface for periods of up to several hours prior to movement of the ice sheet. The flickering is interpreted as resulting from vibration of the ice sheet, although the nature of the data do not permit the period or amplitude of the vibration to be determined. As noted in Section 3.53.3, not all episodes of ice motion were preceded by flickering, but all episodes of flickering were followed by *ice* motion.

These observations were interpreted to imply an association between **long-**period waves in the ice covered sea and rising stress levels in the ice sheet. This, in turn, implies that a means must exist by which substantial energy is coupled from the wind through the ice sheet to the water as it produces the stress in the ice. We

hypothesized that the energy might be introduced into the ice-covered sea by the impulsive breaking of ice during the production of pressure ridges. During the breaking of the ice in the ridging process, blocks of ice are abruptly displaced upward and downward, with the energy necessary for this motion supplied by the impulsive release of stored elastic energy. To maintain hydrostatic equilibrium, approximately 8 times the volume of the ice that is displaced upward must be displaced downward. The pumping action represented by the abrupt vertical motion of a substantial volume of ice would then transform a fraction of the released energy into wave motion in the ice-covered sea. Ridging involves the breaking of progressively thicker, stronger ice (i.e., the thinnest, weakest ice breaks and ridges first), so that the process tends to "harden" the pack ice. This increases the stress level in the ice sheet and permits stresses to be transmitted further.

The hypothesis accounts for the observations by providing an energy source for the waves and a mechanism for associating the waves with rising stress levels.

3.33 WAVE-PROPAGATION IN AN ICE-COVERED SEA

The basic solution to this problem was first done by **Greenhill** (1887). He solved the problem for a floating ice sheet modeled as an elastic plate **floating on a liquid, for the case of a sinusoidal displacement as a forced response. Later workers who used this formulation were Ewing and Crary (1934), Hunkins (1962) and Wadhams (1973). Nevel (1970a,b) obtained two-dimensional rectangular and cylindrical wave solutions directly from the differential equations of the system.**

In our work, we extended the solution to the case where the elastic plate is under in-plane compressive stress and found a general solution for any arbitrary boundary and initial conditions (Bates and Shapiro, 1980a). The basic approach was to model the ice sheet-ocean system as a wave guide. The wave equation was solved in the liquid **layer** subject to the boundary conditions of a rigid sea floor and **the** equation of motion of a stressed, floating, linearly elastic plate at the upper surface.

The results show that two bands of gravity waves propagate in the system in response to a plane-wave impulse. The shorter period set are **flexural** gravity waves, which depend on the elastic properties of the plate. In the longer period waves, to first order, the plate acts as a non-elastic membrane with mass. The two bands join at a critical period which depends upon the elastic modulus of the ice and the magnitude of the compressive stress in the ice sheet. For the values chosen in the calculation (Young's modulus from 6×10^8 to $6 \times 10^9 \text{ N/m}^2$ and stresses from 0 to 70 **kPa**), the critical period ranges from 11.2 to 23.9 sec; it increases with increasing Young's modulus and decreases with increasing stress. In addition, for the impulsive source, the amplitude of the long-period waves varies inversely with frequency, which agrees with Hunkins (1962) observations noted above.

The results of this work were applied to the problem of breaking floating ice sheets by traveling vehicles (Bates and Shapiro, **1980b**). That work suggests optimum speeds for safe travel (or, conversely, for breaking ice) as functions of ice thickness, water depth and compressive stress.

In the solution for the elastic plate, the stress at the critical period is unbounded, suggesting that the problem be reformulated to consider a plate with **viscoelastic** rather than elastic properties. This was done (with additional support from the National Science Foundation) through the application of the correspondence principle to the elastic solution, and the results were published in Bates and Shapiro [1981a]. These showed that the assumption that the plate was **viscoelastic** forced the stress to remain bounded at the critical period, but did not change other aspects of the elastic solution. In a later paper (Bates and Shapiro, **1981b**) the results were shown to be in reasonable agreement with the available experimental data regarding ice sheet deflection under moving loads.

3.34 SUMMARY

The results of this study provide a theoretical framework for the observations described above. They verify that long-period waves in the range of observed periods can be excited by impulsive forces, such as might be caused by ridging. The observed rise in stress level is attributed to the increased capacity of the ice to transmit stress as the weaker parts of the ice sheet are absorbed in pressure ridges.

REFERENCES CITED

- Bates, **H.F.** and Shapiro, **L.H.** (1980a). Long period gravity waves in ice covered seas; J. **Geophys. Res.** v. 85, p.1095.
- _____(1980b). Breaking ice with gravity waves; J. Energy Res. Tech., V. 102, p.148.
- _____(1981a). Plane waves in a viscoelastic floating ice sheet; J. Geophys. Res. v. 86, p. 4269.
- _____(1981b). Stress amplification under a moving load on a floating ice sheet; J. **Geophys. Res.** v. 86, p. 6638.
- Ewing, M. and **Crary, A.P.** (1934). Propagation of elastic waves in ice, 2; Physics, v. 5, p. 181.
- Greenhill, **A.G.** (1887). Wave motion in hydrodynamics; **Amer. J. Math.**, v. 9, p. 62.
- Hunkins, K. (1962). Water waves in the Arctic Ocean; J. **Geophys. Res.**, v. 67, p. 2477.
- Nevel, D.E.** (1972). Vibration of a floating ice sheet; Res. Rep. RR 281, U.S. Army Cold Reg. Res. and Eng. Lab., Hanover, **N.H.**
- Wadhams, P. (1973). Attenuation of swell by sea ice; J. Geophys. Res., V. 78, p. 3552.

3.4 COEFFICIENTS OF FRICTION OF SEA ICE ON BEACH GRAVEL

by

Lewis H. Shapiro and Ronald C. **Metzner**

ABSTRACT

The **coefficients** of static and kinetic friction of sea ice on unfrozen beach gravel were calculated from measurements made while dragging two large blocks of sea ice [approximate weights 23,300 and 26,400 lbs (10,600 and 12,000 kg)] in short increments up a sloping beach surface. The results of 36 separate experiments yielded values of the **coefficients** of static and kinetic friction of $\mu_s = 0.50$ and $\mu_k = 0.39$ respectively. These values should be applicable to calculations of the forces required to drive an ice sheet on shore during an ice push event.

3.41 INTRODUCTION

The purpose of this note is to present the results of a series of determinations of the coefficients of static and kinetic friction between sea ice and unfrozen beach gravel. The measurements were made by repeatedly dragging large blocks of sea ice along a beach with a bulldozer. The data should be useful for calculations of the forces involved in driving ice sheets on shore during ice-push events.

The work was done at the Naval Arctic Research Laboratory at Barrow, Alaska in late-June. At the time of the experiments, the beach surface was thawed, and the **landfast** ice had melted back leaving a shore **lead** about 6 ft (2 m) wide. The shoreward edge of the ice was resting on a **low** berm on the offshore side of the lead and the thickness of the ice was about 4 ft (1.3 m). The extent of melting which had occurred by the time of the experiments [from an initial thickness approaching 6 ft (2 m)] suggested that the temperature of the ice was at the melting point through its entire thickness, although this was not verified by direct measurement.

3.42 PROCEDURE

A chain saw was used to cut two blocks from the leading edge of the ice (dimensions are shown schematically in Figure 3.4-1). Note from the figure, that the leading edge of Block #1 was naturally sloped, while that of Block #2 was nearly vertical.

The arrangement of the experiments is illustrated in Figure 3.4-2. A horizontal hole was drilled through the center of each block with a hand auger. A cable was then passed through the hole, and attached to a short length of timber which served to anchor it. The cable extended about 15 meters from the leading edge of the block to a dial dynamometer [Dillon Mfg. Co., 20,000 **lbf** (44,080 N) x 100 **lbf** (220.4 N) divisions, **10 inches (0.254 m)** diameter dial face, $\pm 1/2\%$ @ full scale]; a second cable attached the dynamometer to a bulldozer which was used to drag the block.

The experiments were done during a two day period. On the first day the blocks were dragged up the sloping beach from the water line to the beach crest in a series of **start-stop** movements. The dynamometer was monitored visually as the blocks were dragged; forces were estimated to the nearest 100 **lbf** (220.4 N). The peak force reached as the block was put in motion after each stop was used to calculate the coefficient of static friction. The motion was then continued through a short distance [maximum about 6 **ft** (2 m)] at an average velocity of about 1 **ft/sec** (0.3 m/sec). During the movement, the dynamometer reading fluctuated as the force required to keep the block in motion changed. The mid-point of the range of fluctuation was estimated and used in the calculation of the **coefficient** of kinetic friction. During the traverses up the beach slope, a total of **15** determinations of the coefficients of friction were made on Block #1 and **21** on Block #2. These experiments were done over the part of the beach which an ice sheet must traverse

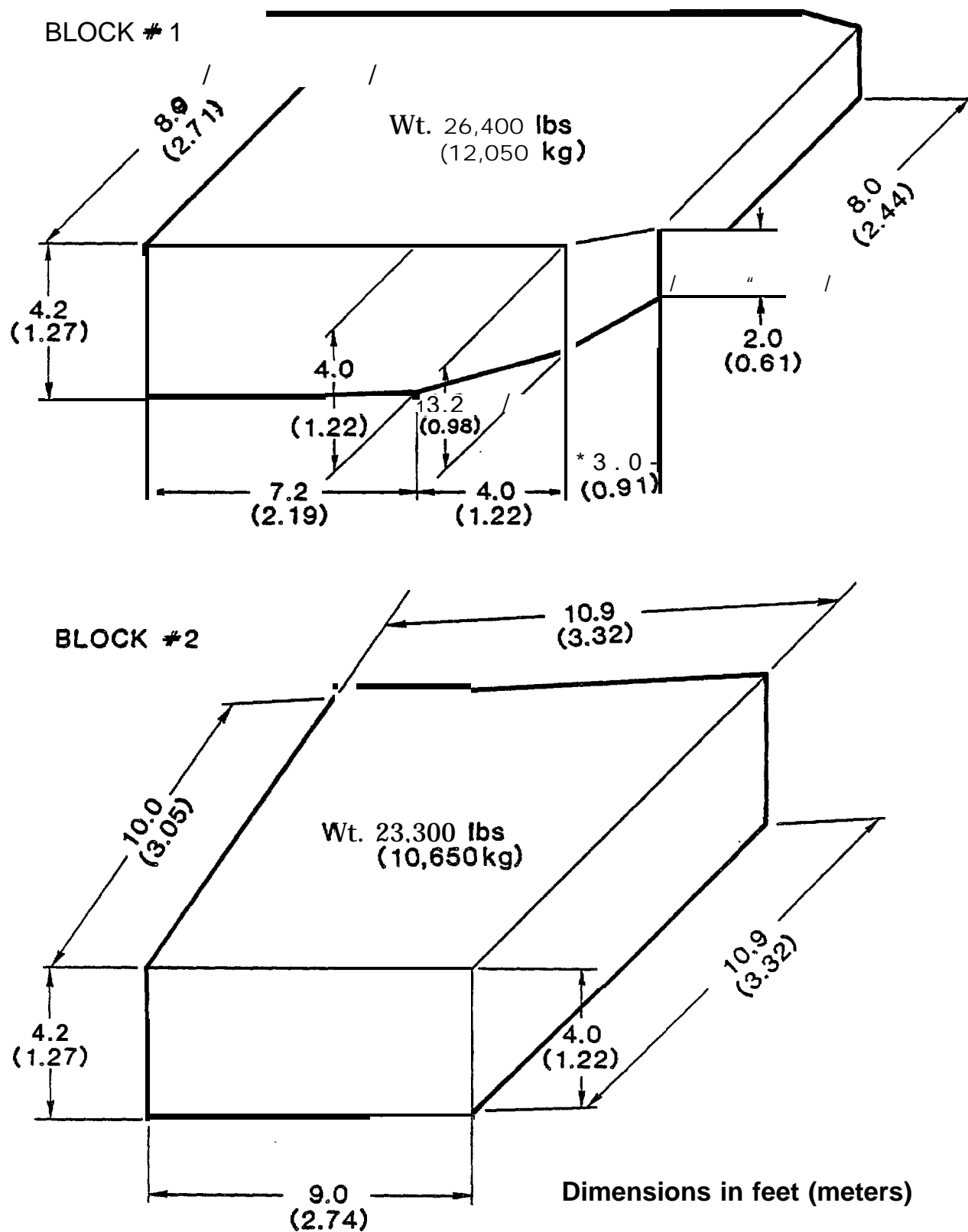


Figure 3.4-1 Geometry and weights of test blocks. The leading face of the blocks is to the right in both cases; note the sloping face of block #1 and the vertical face of block #2. Dimensions in feet (meters)

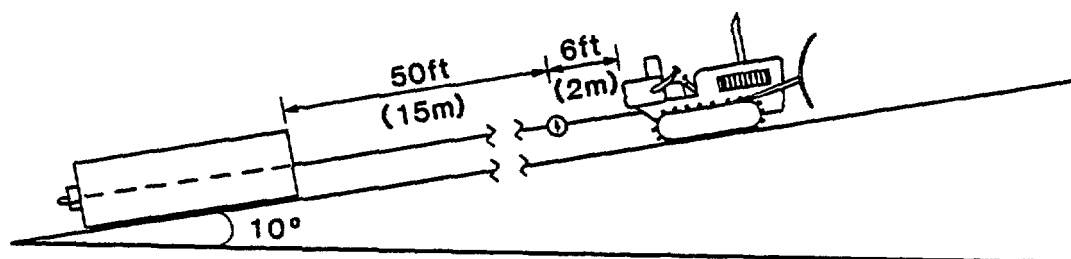


Figure 3.4-2 Schematic of the experimental setup. Dimension in feet (meters).

during an ice-push event. An additional 15 experiments were done on the second day by dragging Block #2 parallel to the shoreline along the crest of the beach.

To determine the weights of the test blocks, their volumes were calculated from the dimensions and forms shown in Figure 3.4-1. Density measurements were made on samples taken near the top, mid-height and bottom of the blocks, and from a zone of gravel-rich ice which was present in the upper parts of the blocks. Each density measurement was assumed to be representative of a fraction of the block volume, from which an average density was calculated. The result was 58.3 lbs/ft³ (936 kg/m³); the high value reflects the approximately 15% of the blocks which were gravel-rich ice. The calculated block weights are shown on Figure 3.4-1. Note that the gravel-rich ice was restricted to the upper parts of the blocks. The basal areas of both blocks were generally free of gravel, so that the experimental results can be taken as representing the coefficients of friction for "clean" ice over unfrozen beach gravel.

The pebble surface of the beach slope was relatively smooth and densely packed on its lower reaches where most of the experiments were done on the first day. However, the surface was rougher and less compact toward the crest of the slope and in the area where the experiments were done on the second day. This is reflected in the results, as discussed in the next section.

The slope of the beach was determined by placing a board about 6 ft (2m) long on the surface and measuring its inclination with a clinometer. Several measurements were made along the slope on which the experiments were done and indicated a uniform inclination of 10°. The slope of the path parallel to the beach, along which Block #2 was dragged on the second day, was assumed to be zero and was not measured.

3.43 RESULTS AND DISCUSSION

The values of the coefficients of static and kinetic friction determined from the test results are shown in Figure 3.4-3. These were calculated from the relationship

$$\mu_{s,k} = (\bar{F} - \bar{W} \sin \beta) / \bar{W} \cos \beta$$

where μ is the coefficient of static (μ_s) or kinetic (μ_k) friction, \bar{F} is the corresponding force, \bar{W} is the block weight and β is the slope angle of the beach. The mean values and standard deviations of the data in Figure 3.4-3 are given in Table 3.4-1. Note that the standard deviations indicate that the data points spread over approximately the same percentage range of the means for the three data sets.

The use of the equation above implies the assumption that the force \bar{F} was applied parallel to the beach slope and along the center lines of the blocks, so that it acted through the centers of gravity of the blocks. **If** this were true, then no vertical force components were introduced as the blocks were pulled. Deviations from the "ideal would enter as the sine of the **angle** between the force vector and the center line of the block. Calculations indicate that for small angles the resulting percent errors would be of the same order as the angular deviation (i.e., a variance of 5 degrees would result in a **5% error** in the calculated coefficients of friction).

Other sources of error arise from possible misreading of the dynamometer dial and from the estimates and approximations used in the calculation of the weights of the blocks. The former are **likely to** be small (i.e., for the magnitudes of the forces involved, the calculated coefficients of friction vary by less than **1%** per scale division on the dynamometer dial) and randomly distributed through the data, **along** with the effects of variations in roughness and texture of the beach surface. Errors in determining the weights of the blocks are linearly related to the calculated coefficients of friction. Calculations assuming "worst case" estimates suggest a maximum possible error of less than 10% in the block weights.

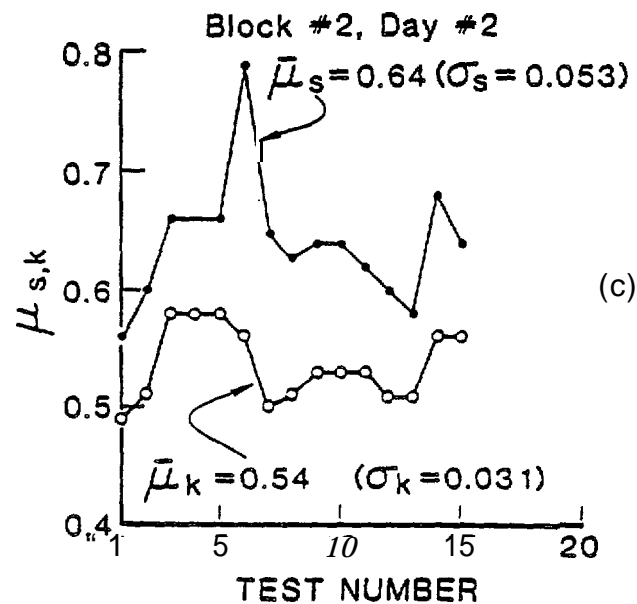
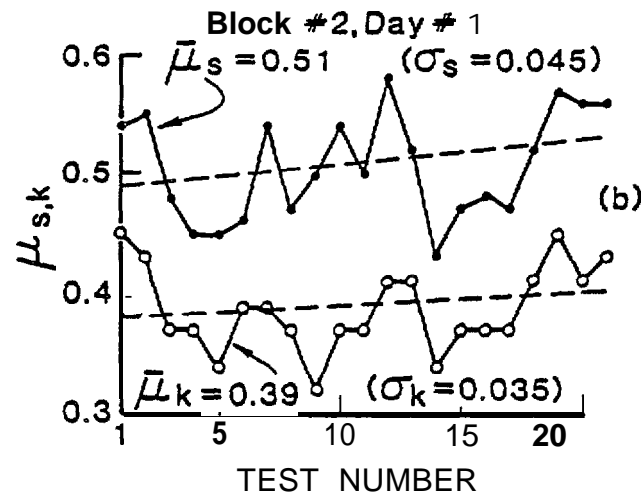
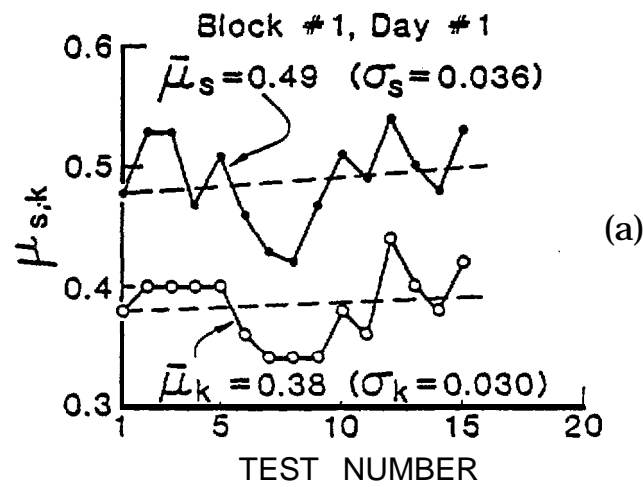


Figure 3.4-3 Plots of $\mu_{s,k}$ vs. test number for the three test series. Dashed lines in (a) and (b) are the results of linear regression calculations. Values of μ_s , μ_k , σ_k from Table 3.4-1 for each data set are indicated in the figure.

The similarity of the coefficients determined from the experiments on the two blocks on the first day suggests that the difference in the shapes of **the** leading edges of the blocks was not important. This is probably due to the fact that the shear strength of the unconfined, unfrozen gravel at the surface of the beach was negligible, so that little energy was required to plow the beach and scrape the shallow grooves which were left on the surface behind the blocks.

It might have been anticipated that, with increasing numbers of tests (and the resulting increase in the distance which the blocks had traversed), the coefficients of friction **would** decrease as the lower surfaces of the blocks were worn smooth by abrasion. Conversely, the increase in surface roughness and the decrease in packing density of the beach surface with increasing elevation above the water line would be expected to result in an increase in the coefficients. Linear regression of the four data sets from the experiments on the first day (Figure 3.4-3) shows a small increase in the magnitudes **of** the coefficients with increasing numbers of tests. However, the difference between the largest and smallest values of the **coefficients**, as calculated from the regression equations, is within the range of scatter of the data. Thus, if changes in test conditions occurred during the experiments on the first day, they were compensating or of little importance.

Note that the coefficients determined for the experiments on Block #2 on the second day are higher than those for both blocks on the first day. We can identify two factors which might be responsible for the discrepancy. First, the increase in roughness and decrease in packing density of the surface of the upper part of the beach (in comparison to the sloping surface where the experiments were done on the first day) would tend to increase the drag on the **block**. Second, it is possible that the slope was not zero as it was estimated to be (note that an upward slope of as little as 4° **would** decrease the calculated **values** of the coefficients of friction by 0.07).

Because of these uncertainties, we consider the results of the experiments on the

second day to be less reliable than those from the first day. In addition, the values of $\mu_s = 0.50$ and $\mu_k = 0.39$ reflect the interaction of the ice with the lower slope of the beach, and are thus more applicable to the problem of calculating the forces involved in ice-push events.

TABLE 3.4-1

Values of Coefficients of Friction and Standard Deviations

| | μ_s | σ | μ_k | σ |
|----------------------------|---------|----------|---------|----------|
| Block #1 (Day 1) . | 0.49 | 0.036 | 0.38 | 0.030 |
| Block #2 (Day 1) | 0.51 | 0.045 | 0.39 | 0.035 |
| All Tests (Day 1) | 0.50 | 0.041 | 0.39 | 0.032 |
| Block #2 (Day 2) | 0.64 | 0.053 | 0.54 | 0.031 |

3.5 NEARSHORE ICE CONDITIONS FROM RADAR DATA, POINT BARROW AREA, ALASKA

by

Lewis H. Shapiro and Ronald C. **Metzner**

ABSTRACT

From June, 1973 to May, 1979, the University of Alaska maintained a small radar system to monitor near shore ice motion and conditions at the Naval Arctic Research Laboratory near Point Barrow, Alaska. The purpose was to support research projects which required that information. In this report, the data acquired are compiled to describe the annual cycle of the ice year in the area. A short open water season can be defined as extending from late-July to late-September. This is followed by freeze-up, which is characterized by a decreasing frequency of occurrence of drifting pack ice **in** the area between October and January. The winter season extends from January through May. It **is marked** by generally stable or **slow-**drifting pack ice, or by the absence of pack ice offshore from the edge of the fast ice. The onset of breakup in June is characterized by the increasing occurrence of drifting pack ice again. Comparison of the ice cycle with **climatologic** data indicates no strong correlations with variables other than (possibly) air temperature. As expected, ice activity is greatest during freeze-up and breakup, with rapid changes in the directions and velocity of ice motion. Similar movement patterns occur in winter, but the ice velocities are slower. Data of the type generated by the radar system would be useful for any area in which development of offshore installations is planned. Clearly, a knowledge of the range of possible ice motion patterns and events can provide the basis for improving the design of such installations.

3.51 INTRODUCTION

From June, 1973 to May, 1979, the University of Alaska operated a radar system along the **Chukchi** Sea Coast at the Naval Arctic Research Laboratory (NARL) approximately 5 km north of Barrow, Alaska (Figure 3.5-1). Support for the installation and operation of the system over this time came from both the University of Alaska Sea Grant program and **NOAA/BLM OCSEAP**. During its operation the radar was primarily intended to support research projects in the area by monitoring local ice conditions and events. However, efforts were made to operate the system all through the year so that during the period which it was in place, a significant record of local ice conditions and events was obtained. The purpose of this report is to present a synthesis of these observations in the form of a generalized annual ice cycle at Barrow, along with brief descriptions of events and processes to which the radar observations contributed information. Although the data are limited to this particular area, the results may serve as a model for the range of ice conditions which might be encountered elsewhere, particularly along the **Chukchi** Sea coast of Alaska. In any case, they emphasize the utility of data from monitoring of ice conditions in any area prior to the planning and development of offshore installations. Clearly, a knowledge of the range of possible ice motion patterns and events can provide the basis for improving the design of such installations.

3.52 **EQUIPMENT** AND METHODS

3.52.1 RADAR SYSTEM AND DATA RECORDING

The radar system used was a 3 cm X-band standard ships radar of a the type which would normally be installed on a small fishing vessel (**Sackinger** and Rogers, 1974). It was mounted on a tower on the beach at an elevation of about 12 m, which should give a maximum range of about 15-17 km (8-9 NM, based on the **rule-of-thumb** that the range of the radar in miles is approximately equal to the square root

of twice the height of the antenna in feet). However, the radar was usually operated at a range of 5.6 km (3 NM) (Figure 3.5-1) because no man-made reflectors were deployed on the ice, and this distance proved to be nearly the maximum range from which energy was returned from a sufficient number of natural reflectors for the ice motion to be monitored by tracking "blips" on the radar screen. A discussion of the nature of the reflectors is given in Section 3.52.3 below.

The radar data were displayed on a screen which was photographed (usually at 2.5 minute intervals) as time-lapse motion pictures using a 35 mm camera driven by a timing mechanism. A clock face was included in the picture to give the date and time of the image (Figure 3.5-2). At 2.5 minute intervals between pictures, a standard roll of **film** lasted approximately 4 days. Generally, film was developed and examined within 2-3 weeks following exposure so that it was possible (in some cases) to "ground truth" the imagery.

The choice of a 35 mm camera for recording the data **was** dictated by budget considerations; a 35 mm camera was available and the cost of acquiring similar 16 **mm** equipment (with the time-lapse capability) was too great for available funds. This was unfortunate because, while the 35 mm camera provided data of excellent quality, there was no commercially available equipment (such as analyzer projectors, which were available in 16 mm) with which to analyze 35 mm film. Accordingly, a viewing system was constructed with which the **35 mm film** could be scanned so that ice conditions and motion could be characterized qualitatively. However, the resolution of the system was poor and the images did not register repeatedly on the viewing screen. This prevented the equipment from being used for detailed work, such as measuring the displacement and velocity vectors of the ice cover (**by** tracking the positions of identifiable reflectors on successive frames, as described below) or providing details of the sequence of events in development of the ice cover. For these studies, rolls of film in which events or sequences of interest

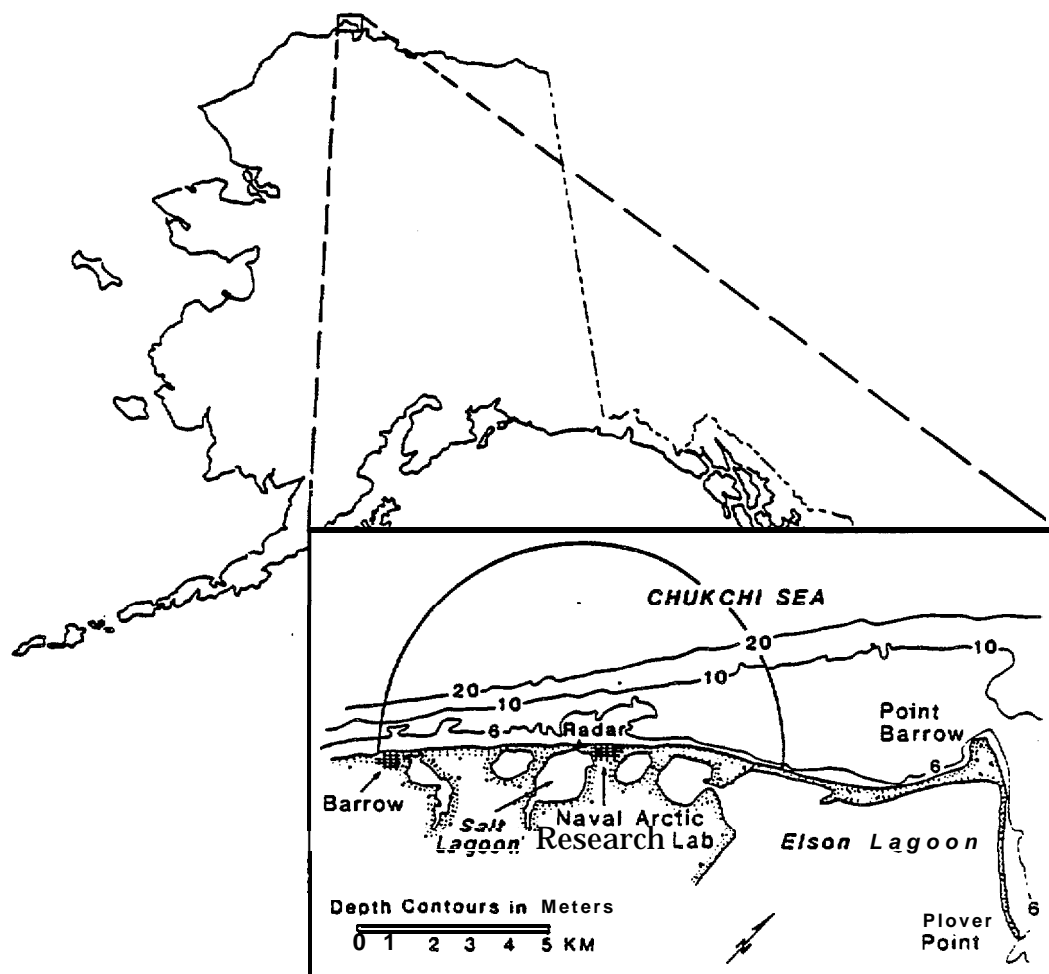
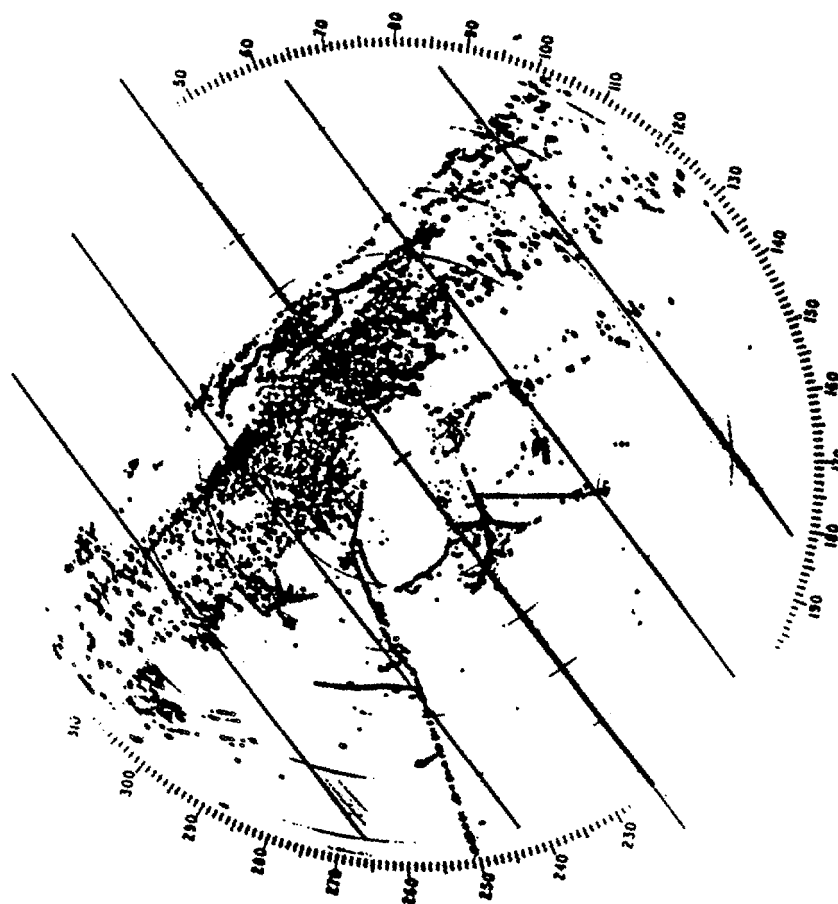


Figure 3.5-1 Map of the **Point** Barrow area showing the location of the radar site. The arc indicates the field-of-view of the radar when operated at a range of 5.5 km (3 NM).



BARROW
MARCH 75



Figure 3.5-2 Typical from ranging circles 0.93 km (0.5 NM) spacing
between concentric lines are 1.05 & (1 NM) apart.
Parallel transverse

appeared were reproduced on 16 mm **film**, for which **an** analyzer projector was available. Most of the analysis was done using this equipment. If detailed information was required from a short sequence of frames, the **35** mm data were enlarged to 70 mm and studied on a color additive viewer with **which accurate** registration could be done. However, the cost in time for this procedure was prohibitive, and it was not used as often as would have been desirable.

3.52.2 DATA ANALYSIS

A total **of 387** films were obtained, representing 1550 days, or 71% of the total days that the radar was in place. Table 3.5-1 shows the percentage of possible days of each month for which data were obtained. These range from a low of 38% of all possible days for January to a high of **75%** of possible days for May. Unfortunately, the sample is weakest for the late-Summer and Fall, so that relatively little imagery was obtained during the critical freeze-up period. Still, the data range over the entire year and provide the basis for a preliminary characterization of the variation **in** ice conditions in the area through a calendar year, as described below.

The individual film rolls cover periods **of** from 2 to 8 days, averaging 3 to 4 days per roll. For convenience, the data characterization was done by film roll, rather than time interval. Each film was scanned and ice conditions and direction of motion (if any) were noted. Unusual events, such as pack ice being driven into contact with, or drawing offshore from, the fast ice were also noted. The results are summarized in Table 3.5-2. In general, there was little variability in the direction of ice motion within any roll of **film**. As an example, of the 387 film rolls, only 25 examples were found in which the drift direction reversed (i.e., the direction of drift changed from, say, northeast to southwest along the coast) within the time covered by a film roll. Seventeen of the reversals occurred during breakup or freeze-up.

TABLE 3.5-1

TOTAL DAYS OF RADAR COVERAGE BY MONTH AND YEAR

| Month | 1973 | 1974 | 1975 | 1976 | 1977 | 1978 | 1979 | days | % |
|-------|------|------|------|------|------|------|------|------|----|
| Jan | -- | 31 | 0 | 12 | 16 | 9 | 23 | 91 | 49 |
| Feb | -- | 29 | 0 | 24 | 27 | 29 | 6 | 115 | 68 |
| Mar | -- | 31 | 26 | 23 | 26 | 30 | 12 | 150 | 81 |
| Apr | -- | 30 | 22 | 30 | 28 | 30 | 30 | 171 | 95 |
| May | -- | 31 | 31 | 31 | 31 | 25 | 26 | 175 | 94 |
| Jun | 27 | 30 | 24 | 30 | 26 | 12 | -- | 149 | 83 |
| Jul | 31 | 30 | 31 | 28 | 13 | 31 | -- | 164 | 88 |
| Aug | 23 | 30 | 29 | 30 | 0 | 1 | -- | 113 | 61 |
| Sep | 22 | 21 | 30 | 21 | 0 | 0 | -- | 94 | 52 |
| Ott | 0 | 21 | 27 | 31 | 7 | 10 | -- | 96 | 52 |
| Nov | 2 | 10 | 30 | 30 | 22 | 26 | -- | 120 | 67 |
| Dec | 24 | 0 | 28 | 20 | 31 | 2 | -- | 105 | 56 |

3.52.3 REFLECTORS

The number of reflectors visible on the radar screen was always **sufficient** to permit the distribution and motion of the ice to be determined **in** the entire **field-of-view** when the radar system was operated at a range of 5.6 km (3 NM) or less. **In** addition, linear alignments of reflectors representing shear ridges within the fast ice were usually easy to identify. Once in place following freeze-up, the features of the fast ice remained stationary until breakup. Thus, it was always possible to separate fast ice and pack ice on the imagery, because the distribution of reflectors on the fast **ice** did not change through the winter.

In general the intensity of the **energy** return from reflectors on the ice surface decreased with increasing distance from the radar. Thus, low ridges, hummocks or discrete floes of **multiyear** ice at short ranges gave strong reflections, while similar or larger features at a distance gave weaker returns. Exceptions did occur which were probably due to variations in the orientation of reflecting surfaces on the features.

Attempts to determine the nature of the actual reflecting surfaces and their relationship to the intensity of energy return (as shown by the diameter of **the** blip produced on the radar screen) were unsuccessful. It was not possible to identify particular reflecting surfaces. However, it was often (but not always) possible to identify a specific **floe** or ridge as the source of energy for a particular blip shown **on** the imagery. In this context, it should be noted that the fact that a feature was prominent did not ensure that it would return sufficient energy to produce a prominent signature on the radar screen. **As** an example, in one instance, a **large** grounded ridge (sail height in excess of 10 m) located **1.5** km offshore from the

TABLE 3.5-2
ICE DRIFT DIRECTIONS BY **MONTH**

| Month | Total Films | Drift Direction | | | | |
|------------|----------------|-----------------|-----------|----------|----------|----------|
| | | Northeast | Southwest | In* | Out* | Reversal |
| Jan | 23 | 5 | 9 | 4 | 4 | 2 |
| Feb | 29 | 4 | 3 | 0 | 2 | 0 |
| Mar | 38 | 7 | 6 | 4 | 2 | 2 |
| Apr | 43 | 3 | 7 | 6 | 5 | 2 |
| May | 44 | 7 | 6 | 3 | 3 | 2 |
| Jun | 37 | 14 | 3 | 8 | 5 | 0 |
| Jul | 41 | 19 | 12 | 10 | 13 | 4 |
| Aug | 28 | 16 | 5 | 6 | 8 | 4 |
| Sep | 24 | 11 | 5 | 2 | 3 | 4 |
| Ott | <i>24</i> | 10 | 12 | 4 | 3 | 1 |
| Nov | 30 | 11 | 10 | 8 | 8 | 4 |
| Dec | 26 | 3 | 6 | 8 | 8 | 0 |

(#) Numbers in each **category give the** number of films **on** which pack **ice** displacement occurred in the direction indicated. Totals maybe greater than the number of **films** since drift **in** more than **one** direction occurred **on some films**.

(*) Headings "In" and "**Out**" refer to onshore and offshore(respectively) displacements of pack ice normal to the coast or edge of the fast ice

radar site was invisible to the radar, although a smaller ridge about 100 m to the southwest gave a strong reflection. Apparently, there was no surface on the larger ridge which was suitably oriented to reflect energy back to the radar antenna. In contrast, features which were much smaller were often observed at greater distances from the radar. For example, reflectors defining the outlines of individual floes of thin ice in early-Fall could often be identified at the limit of the field-of-view of the radar. These reflectors were probably from low (less than 1 m high) ridges or hummocks formed during impacts between floes. Thus, there is no basis for associating the intensity of a reflector with the size of the feature which produced it.

The smallest blips which could be discriminated on the data [at 5.6 km (3 NM) scan] had diameters of about 40 m at the scale of the imagery. Clearly, the actual sizes of the reflectors on the ice surface were smaller; the enlarged scale of the blips results from the dispersion of the returned radar energy. The effect of the sizes of the blips on the lower limit of the ice displacement which could be detected is discussed in section 3.52.4.

It would have been desirable to determine the effect of changes in snow cover on the character of the reflectors through the winter. However, this was not possible because of the need to adjust the gain on the radar system periodically, which had the effect of changing the intensity of the reflectors.

3.52.4 MEASUREMENT OF ICE MOTION

Ice velocity measurements were made by tracking individual reflectors on sequential frames of the film. The scale of the imagery was provided by the range lines (Figure 3.5-2) and the time by the clock (or by simply counting frames of film since the time interval between exposures was known). In making velocity measurements it was always possible to track the motion of reflectors over at least 1.5-2 km. At the velocities measured, this took sufficient time that the

measurements are believed to be accurate to within 0.1 km/hr, so that velocities reported below are given to this precision.

Ridging events were shown by the formation of lines of reflectors. It was usually possible to identify the exact frame on which a particular reflector on a ridge line appeared, so that the time required for development of a ridge could be determined. An example of the use of this type of data in describing the process of development of the fast ice cover is given in Shapiro (1975a).

It was simple to detect pack ice motion when the data were viewed as time-lapse motion pictures because, even when the movements were slow, the displacements eventually became large enough to be obvious. Smaller displacements of the fast ice were also easy to detect if they occurred rapidly; the apparent "jump" of all of the reflectors in the fast ice was obvious. However, small displacements of the fast ice at low rates were never observed on the radar data although, as described in Section 3.54.4, at least two examples of such movements did occur during the time the radar system was operating. There is no quantitative basis for defining a lower limit of the magnitude of displacement of the ice which could be detected. However, experience suggests that displacement of a blip by about one-half its diameter (i.e., 20 m for the smallest detectable blip) should be apparent. Thus, this is assumed to be the approximate lower limit of detectable displacement within the fast ice.

As noted above, a color additive viewer was also used in the interpretation of the data. An example of the results of this type of analysis is given in Section 3.64.1 (Figure 3.6-11) which shows the displacement vectors of the fast ice during the ice push event of July, 1975 superimposed on a map of ice gouges in the sea floor.

3.53 CHARACTERISTIC ICE MOVEMENT PATTERNS

3.53.1 INTRODUCTION

No weather or current monitoring equipment was deployed as part of this project at any time during the operation of the radar system. Local weather data were acquired from the NWS station at Barrow and from the NOAA air monitoring station northeast of NARL for use in interpreting the motion during some events which were observed in the field (i.e., ice push events, lead formation, etc.). In addition, satellite imagery of the area and regional weather charts were examined regularly. As a result, various qualitative “rules-of-thumb” were developed for interpreting the local patterns of ice distribution and motion. The rules are based primarily on the assumption that pack ice tends to drift at about 30° to the right of the wind direction under “average” conditions (Whitman and McDowell, 1964). However, the actual movement patterns also reflect the shape of the coastline in the area, the topography of the sea floor (which controls the positions of grounded ice ridges within the fast ice), and the local tides and ocean currents. These factors introduce enough variation and complication into the patterns that it was never feasible to try to develop quantitative models relating ice motion to driving forces.

3.53.2 GENERALIZED DRIFT PATTERNS

The relationship between the orientation of the coastline and wind and ice drift directions (based on the rule-of-thumb given above) are shown in Figure 3.5-3. Details are discussed in Section 3.54.6. The purpose here is to describe, in general, the basic movement patterns which have been observed.

The orientation of the coastline requires that most of the observed ice motion in the area (in terms of the duration of observations) be to the northeast or southwest, since these provide the longest path lengths within the radar field-of-view. Clearly, ice drifting at a high-angle to the coast will be in view for only limited times before it

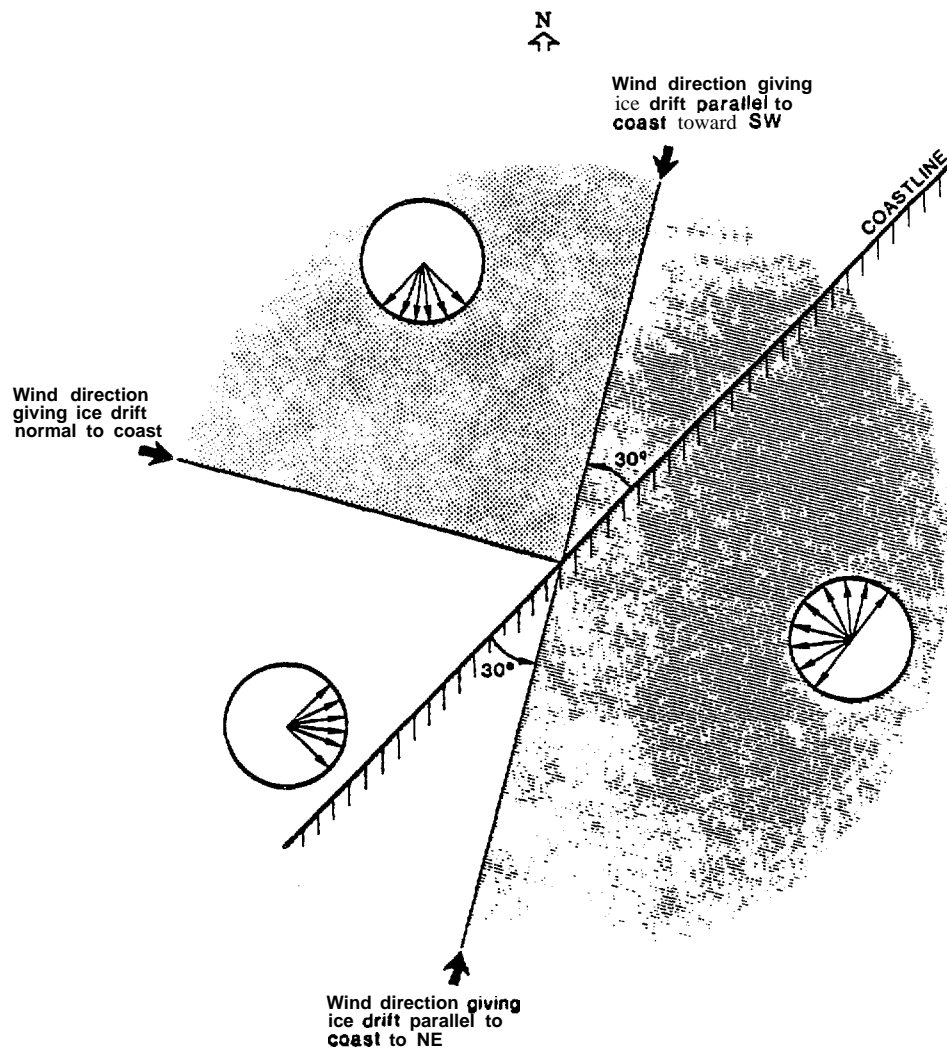


Figure 3.5-3

Schematic diagram illustrating the possible senses of ice motion within the field-of-view of the radar for wind from different directions, assuming that the ice drifts at 30° to the right of the wind direction. Arrows in circles show the range of possible ice movement directions for winds originating in each patterned sector.

either **leaves** the field-of-view of the **radar or impacts the edge of the fast ice and stops**. However, ice could drift through the area on tracks parallel to the coast for long periods of time. Ice drift along the coast to the northeast is caused by winds from the south to southwest which, in turn, occur when a low pressure system is located over the central **Chukchi** Sea. With this configuration, the winds tend to drive the pack ice close to shore so that, in general, pack ice drifting to the northeast was close to, or against, the edge of the fast ice. In addition, ice push events observed in the Barrow area always followed the northward movement of a low pressure system through the **Chukchi** Sea (Shapiro et al., 1984); the winds from such a system tend to compress the pack ice cover against the coast, so that the stress can be transmitted to the fast ice.

The prevailing winds from the east to northeast (as well as the less common winds from the southeast) tend to move the pack ice offshore opening a wide **flaw lead**. New ice was usually forming in the lead, but it was always smooth, with **relatively few reflectors, so that it was usually invisible to the radar**.

Northerly to northwesterly winds would push the ice toward the southwest, along the coast. However, this part of the coast is in the lee of Point Barrow with respect to ice drift from the north and northeast (see Figure 3.5-1). Thus, when pack ice as loose floes was observed drifting from the northeast to the southwest, it was often near the limit of the field-of-view of the radar system. Occasionally, floes were found to be drifting to the southwest when the winds were from the northeast. Examination of satellite images suggest that this occurred when pack ice drifted southwestward around Point Barrow and diverged into the nearshore area (from which pack ice had earlier been driven by the offshore sense of the wind) under the influence of internal stresses. Southwesterly movement of a continuous ice sheet was usually observed only when the ice sheet separated from the edge of the fast ice opening a lead. Once the ice sheet drifted out of view, it was usually followed by

loose floes drifting along a southwesterly track near the limit of the field-of-view of the radar, as described above.

Drag effects were commonly observed when the pack ice was driven against the edge of the fast ice at a low angle. In these case, forces resulting from the interaction of the pack ice with the edge of the fast ice served to slow the pack ice near the boundary. This produced a velocity gradient so that the pack ice velocity increased with distance from shore. In general, the effect was observable for about 1 km seaward of the fast ice edge. The best example was presented in Shapiro (1975b). More specific descriptions of patterns of ice motion and distribution through a typical year are given in Section 3.54.

3.53.3 FLICKERING OF REFLECTORS

One particularly interesting and important phenomena shown on the radar data is the flickering of reflectors on the pack ice surface prior to motion, when the data are viewed as time-lapse motion pictures. The flickering occurs for periods of up to several hours prior to movement, and is a reliable precursor. Not all movements were preceded **by** flickering, but flickering episodes were always followed by movement; the pack ice always moved offshore or compressed against the edge of the fast ice following a period of flickering.

The flickering is caused by the repeated disappearance and reappearance of individual reflectors on sequential frames of the data, with no change in their positions. We interpret this as indicating that the reflectors are vibrating, which rotates the surfaces so that energy is not returned to the radar system continuously. The vibration, in turn, is attributed to the passage of waves through the water which cause the ice sheet to **flex** to conform to the shape of the water surface. Unfortunately, the nature of the radar data does not permit the period of the waves to be determined.

The observation of flickering was one of the factors **which** led to the study of ice sheet vibration described in Section 3.3 of this report.

3.54 ANNUAL CYCLE

3.54.1 INTRODUCTION

Based upon the radar data, the ice year can be subdivided into four phases which grade gradually into each other. These phases do not coincide with the four seasons of the year, so that it is proper to assign names **to** them. Accordingly, we refer to the seasons of open water, freeze-up, winter and breakup. In addition, since the timing of the transition between these seasons probably varies along the coast, we recognize that the data apply only to the area within, or close to, the field-of-view of the radar system. However, we anticipate that similar terminology would apply elsewhere along the coast.

In the following sections, the changes in the ice cover during each season are described, and examples of particular (not necessarily "typical") events from each season are given. Then, the changes in the ice season are discussed briefly in relation to the **climatological** data for Barrow as summarized in Brewer et **al.**, (1977).

3.54.2 OPEN WATER SEASON

The term "open water" is defined here as the complete absence of ice within the field-of-view of the radar. The only months in which this condition was met for any complete roll of film were July, August and September (on 5%, **14%** and **21%** of the available data for each of these months, respectively). Note that the unusual summer ice conditions of **1975**, in which part of the fast ice remained in place all summer so that the condition of no visible ice was never met, were included in the data set. The radar was also operated through the entire summer in that year, so that the data are likely to be biased toward the presence of ice.

-

The term “open water season” itself is something of a misnomer, because it is not continuous. Ice drifted through the radar field-of-view in every month, appearing and disappearing throughout the season. If the term is defined more loosely as indicating the time when there is no “fast ice” within the field-of-view of the radar, then the season probably extends from late-July to late-September.

Note that these results give little information about **trafficability**. Minor quantities of ice grounded in shallow water would negate the classification as “open water” and, clearly, vessels can navigate through the area when drifting ice is present. However, the term is useful as an indicator of local conditions in the sense that it indicates the advance of the seasons.

3.54.3 FREEZE-UP

The results of our observations suggest that the term freeze-up is a misnomer when applied to the formation of the fast ice near Barrow; freezing is a secondary process in this area. Our observations suggest that a significant percentage of the fast ice consists of floes which drift into the area after forming elsewhere. The percentage of the fast ice cover which formed by freezing was variable from **year-to-year**, but even where ice did freeze in place, it did so because it was protected by ridges or grounded hummock fields formed from floes which drifted into the area. Observations in other areas suggest that this is a general rule along the coast.

The character of the fast ice varied depending upon the direction from which the ice came, reflecting the nature of the ice itself, and the configuration of the coastline (Figure 3.5- 1). When the ice came from the south, it consisted primarily of thin (less than 0.5 m thick) floes of first-year ice as pans which drifted northeastward along the coast. The pattern of movement during this stage suggests that the floes were stopped by a barrier to the north, out of the radar field-of-view, and gradually filled in the **nearshore** area from north to south. We suggest that the barrier is Point

Barrow, and that the process occurs when the bight south of the Point is filled with floes. Subsequently, floes passing through the field-of-view of the radar gradually slow and stop as they encounter the ice "downstream." Some pressure ridging **can** occur along the floe boundaries during this process as the ice compacts northward. Simultaneously, the streamlines of the pack ice further offshore are deflected to the north, on a trajectory which carries the ice around Point Barrow. This produces the pattern of ridges (as illustrated in Figure 3.5-4) which are aligned along that trajectory. The ridges are dominantly shear ridges and reflect the drag of the drifting pack ice against the ice inshore, which is stationary and continuous with the shore.

The process described above repeats with the addition of new ice, until the fast ice extends out to (approximately) the 20 m depth contour; each ridge in Figure 3.5-4 represents an intermediate stage in the process. Stages may last from minutes to days, but for some time, each ridge is at the offshore boundary of the fast ice.

It is not uncommon during freeze-up for the entire fast ice sheet, in some stage of development, to detach from the shore and move offshore leaving open water to the beach. The latest time at which this occurred in any year was December 31 (of 1973), during a major storm [the subsequent process of rebuilding the fast ice sheet during the storm was described by Shapiro (1975 **a,b**)] although, in general, these events were more common earlier in the season. Note that when an event of this type occurred during freeze-up, the "fast ice" sheet always moved off to the north or northeast. Attempts to associate the start of movement of the ice sheet with local winds showed no apparent relationship, suggesting that ocean currents or tides were responsible.

In the 1974-75 winter, the fast ice near Barrow contained an unusually large percentage of **multiyear** ice floes which dominated the form **of** the fast ice sheet through that winter. When these floes first entered the field-of-view of the radar

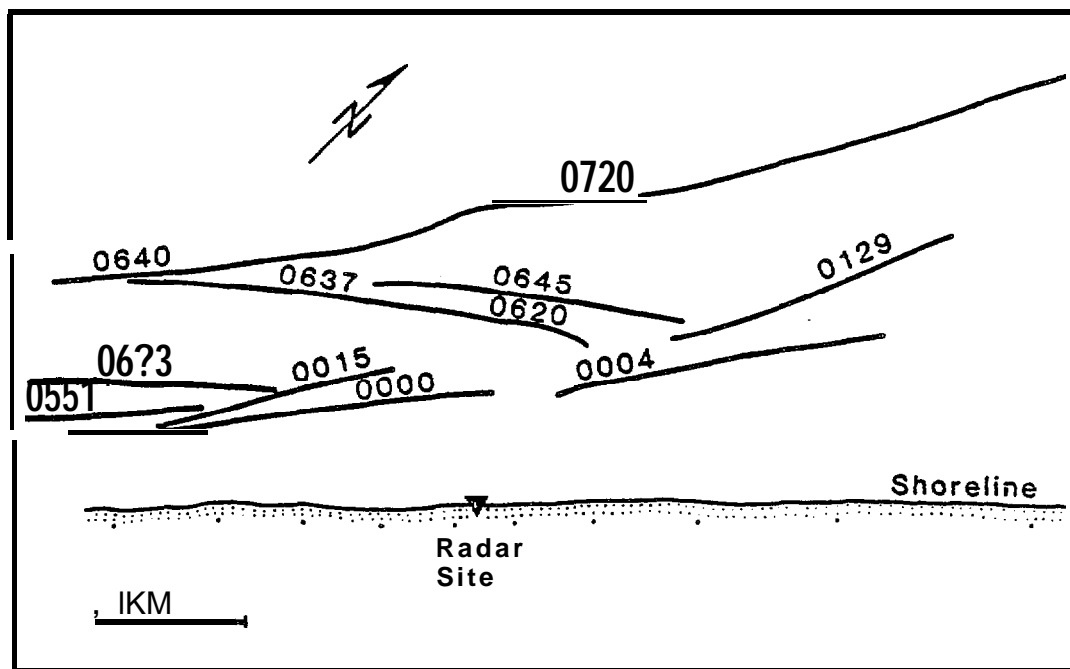


Figure 3.5-4 Pattern of shear ridges in the fast ice which formed during a storm on January 1, 1974 when ice motion was from the southwest, parallel to the coast. Numbers indicate time (hours:min) when ridge formed, starting from an arbitrary time (00:00). Similar patterns developed over the entire freeze-up period of other years when ice motion was primarily from the southwest.

system during freeze-up they were moving southeastward from the north-northwest quadrant toward the coast. Many of the floes became grounded (some had sails as high as 3 m in 5 m water depth), although the maximum depth of grounding was not determined. However, **multiyear** ice floes were common in the fast ice at least to a distance of about 2 km from shore, corresponding to a water depth of 15-20 m. Inshore, the first-year ice of the fast ice was formed by freezing in place between the **multiyear** ice floes.

The source of the **multiyear** floes was clearly either the northern **Chukchi** Sea or the Beaufort Sea, and this was verified by examination of NOAA satellite imagery. The imagery shows that the floes which drifted into the fast ice zone came into the area from the edge of the pack ice north of Point Barrow. The motion could not be tracked in detail from the satellite imagery, but it appears that the floes drifted southwest from north of Point Barrow in diffuse swirls, and then turned back toward the coast along a more southeasterly track as if caught in an eddy.

It is not possible to define the beginning and end of the freeze-up season with any precision. The earliest that fast ice was recorded by the radar (except for 1975 when the fast ice remained in place all summer) was late-September. The data on the frequency of observation of ice motion (Figure 3.5-5) indicate a **gradual** decrease in ice activity throughout the season from a peak in October to a significantly lower level in February. Note that the rise in the curve for January may reflect a bias in the data, since there are fewer observations for January than for any other month (see **Table 3.5-1**). However, the available data suggest that most of the movement episodes observed during January occurred early in the month. In addition, the latest ice events which caused movement of the fast ice occurred in late-December and early-January. This suggests that the end of the freeze-up period could be taken as, say, mid-January, with the implication that the fast ice is relatively stable from that time until breakup.

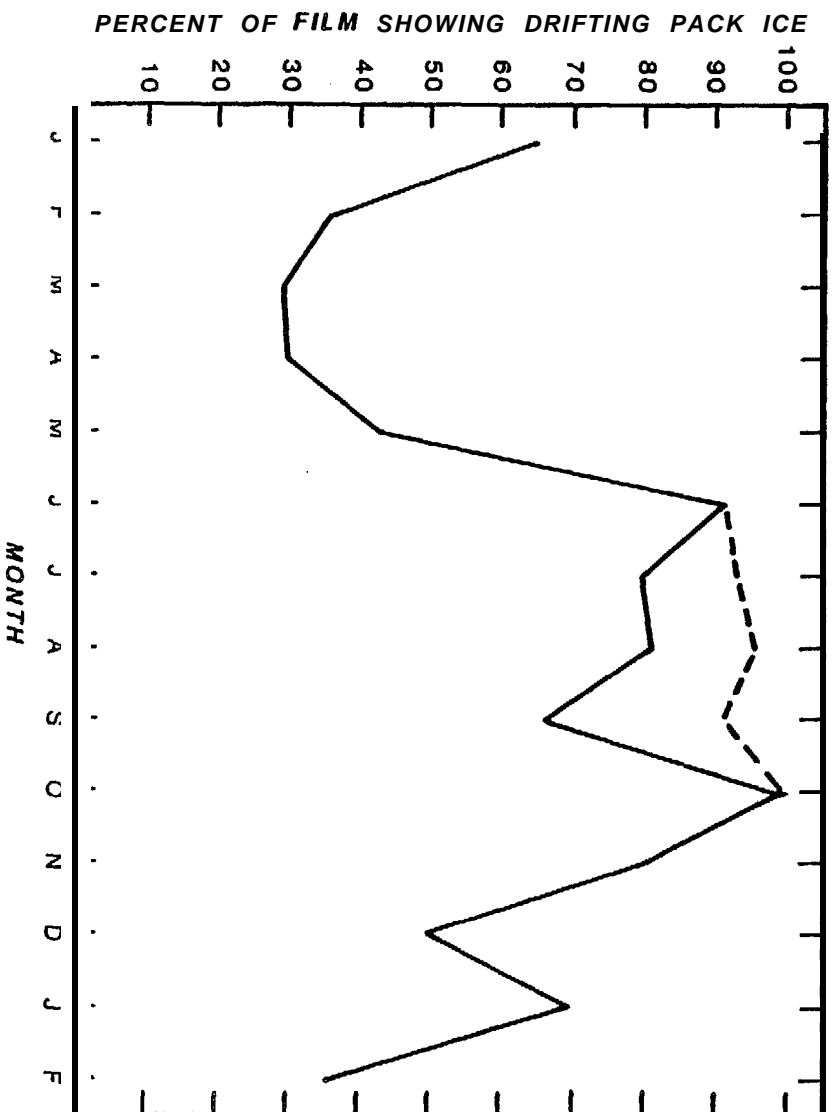


Figure 3.5-5 Percent of films of radar data showing drifting pack ice, plotted by month. Dashed line indicates curve if films with only open water for July, August and September are included. See text for discussion.

3.54.4 WINTER

The winter season, as shown by the frequency of ice motion (Figure 3.5-5) and the pattern of distribution of the ice, extends from January to May. Its start is defined by the decrease in pack ice motion and the beginning of the season of relative stability of the fast ice sheet. We identify the end of the season with the marked increase in the occurrence of drifting ice offshore between May and June (Figure 3.5-5). The onset of melting and instability of the fast ice follow in June.

The pattern of ice distribution within the field-of-view of the radar system during winter always included stationary fast ice. Offshore from the fast ice, the most common condition was for the pack ice to be either present but stationary, or absent. By month, between January and May, one of these was the only pattern shown by the data for (respectively) 57%, 75%, 63%, 58% and 75% of the films (Table 3.5-2). During March, April and May of 1976, 1977 and 1978, they were the only patterns recorded; no drifting ice was observed. On the remainder of the films, the pack ice was in motion for at least part of the time covered by the film. When ice drift was parallel to the edge of the fast ice, the direction was to the northwest or southeast with about equal frequency. Occasionally the pack ice was driven into the edge of the fast ice at a high angle (such impacts occurred on about 10% of the films for this time of year). A spectacular shear ridge formed in March 1974 from such an event (see description below in this section). However, the effects of the impact events were usually confined to the edge of the fast ice. The single exception which occurred during the time the radar operated had minor effects, as described near the end of this section.

The absence of pack ice offshore from the fast ice indicated that the ice was drifting slowly away from the coast under the influence of the prevailing northeast to east winds, leaving a lead in which new ice was forming. Since the ice in the lead

was young and thin with no sizable ridges or hummocks it was invisible to the radar. However, in one event (the 1974 ridging event described below) the radar data show the pack ice to advance directly against the edge of the fast ice after a period of more than one day when it was outside of the field-of-view of the radar. At that time, new reflectors appeared on the radar screen near the edge of the fast ice while the edge of the pack ice was still about 2 km away and advancing shoreward. This shows that thin ice was present in the lead; the appearance of the reflectors indicates that ridging was occurring as this ice was brought into contact with the edge of the fast ice.

The pattern in which stationary pack ice was located offshore from (but in contact with) the fast ice often indicated the presence of a stable extension to the fast ice (Stringer, 1974) rather than continuous pack ice cover. Stable extensions are probably ungrounded masses of pack ice which attach to the fast ice and extend offshore. They are common features in the local area and, since they often extended beyond the limits of the field-of-view of the radar, it was not possible to distinguish them from continuous pack ice cover unless they were observed during flights in the area. It is likely that stable extensions of the fast ice originate as part of the pack ice sheet, but are left behind against the fast ice when the pack ice moves offshore.

As noted, a major impact and ridging event occurred in March, 1974, which formed the highest ridge in the radar field-of-view for the entire 6 years that the system was operated; brash ice was piled to an elevation of about 13 m in water depth of 20 m. The event is described here in some detail as an illustration of the scope of possible movements in the near shore area during the winter season.

The event occurred as part of an (at least) 11-day period of pack ice activity; this was the largest number of days of nearly continuous activity recorded by the radar system during the winter season (as defined above). The movements were generally slow (ice velocities ranged from about 0.1 km/hr to less than 0.5 km/hr),

with interspersed periods of quiescence. However, even when the ice was not in motion, the reflectors on the surface flickered often, indicating that the ice sheet was vibrating and unstable (see discussion in Section 3.53.3). Figure 3.5-6 shows the displacement path of the pack ice in the field-of-view of the radar during the 1 l-day period. Each leg of the diagram represents the path of the ice during the time indicated on the figure, as calculated by multiplying the average velocity of the ice over the period of movement by the time over which the movement occurred. Thus, ideally the plot would represent the displacement path of some point on the surface of the ice sheet for the time covered by the diagram.

At the start of the event, the ice sheet had been stable for a period of about one month. The first movement was the slow opening of a lead along the edge of the fast ice. The lead widened from the south end of the radar field-of-view toward the north and reached a width of about 0.6 km before the first movement to the northeast (shown in Figure 3.5-6) occurred. The first impact of the pack ice with the edge of the fast ice, leading to the formation of the shear ridge, occurred 10 hrs after the movement began, and continued until the ice stopped moving 37 hours later (at 47:00 in Figure 3.5-6). The fact that the ridge was developing over this entire time is shown by the nearly continuous appearance of new reflectors along the line of the ridge. In addition, the ridge created a “shadow zone” for the energy from the radar, so that reflectors on the pack ice disappeared as they drifted behind the ridge.

After the movement stopped, the reflectors on the ice surface continued to flicker intermittently until the ice began moving again, but to the southwest, at 63:15 hrs, as shown in Figure 3.5-6. Movement in this direction continued for about 36 hrs, after which the pack ice stopped for about 24 hours. It then flickered for about 5 hours, and then moved off to the northwest at about 0.2 km/hr until the ice edge was out of the field-of-view of the radar, leaving a flaw lead. The pack ice remained out of view for about 28 hours, and then reappeared moving normal to the

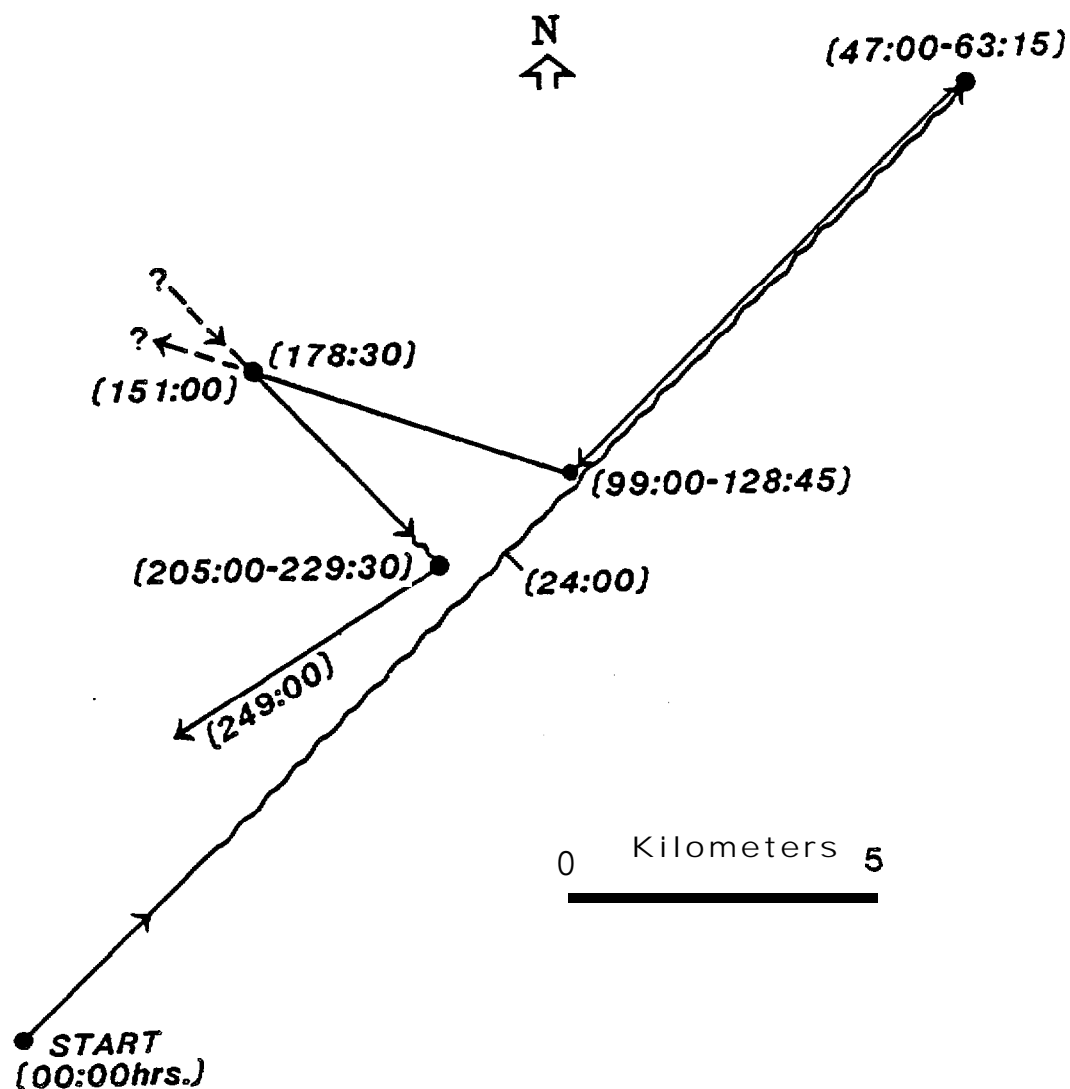


Figure 3.5-6 Displacement path of a hypothetical point on the pack ice surface during the movement episode of March, 1974. Distances calculated from ice velocity and time measurements. Arrowheads show the movement direction and numbers in parentheses are cumulative times as hours;minutes. Wavy line segment indicates duration of impact with the fast ice edge. Dashed lines show the path of ice leaving and entering the radar field-of-view.

fast ice edge at about the same velocity at which it departed. During this advance, new reflectors appeared offshore from, but close to, the fast ice boundary, while the pack ice edge was still about 2 km seaward. This is interpreted as showing that the lead was covered by thin ice (as discussed above) which, though less than 24 hours old, was capable of transmitting stress over that distance.

The pack ice advanced until it impacted the fast ice edge. It then continued to compress against the fast ice for several hours, as shown by flickering and slight shoreward motion of reflectors in the pack ice. However, there were no new ridges formed along the edge of the fast ice, and no motion was detected by the radar system within the fast ice during and after the impact. In addition, during the year in which this event occurred, precise surveys were being conducted within the radar field-of-view, in order to monitor slight movements of the fast ice during the winter. The survey data verify that no movement occurred as a result of the impact. However, it should be noted that in the Spring of 1974, numerous grounded ice ridges were distributed throughout the fast ice, so that it might have been more stable than in typical years.

Subsequently, the ice remained stationary for about 18 hours. A lead about 0.1 km wide then opened, separating the pack ice from the fast ice, and the pack ice proceeded to drift to the west-southwest (beginning at 229:30) at about 0.5 km/hr, eventually leaving the field of view. When the sequence of film terminated other floes were drifting at the same velocity to the southwest, parallel to the coast and about 2 km from the edge of the fast ice.

The total displacement of a hypothetical point on the ice surface, as represented by the vector plot in Figure 3.5-6, is more than 35 km in the 11 days represented by the data (not including the motion during the 28 hours that the ice was out of view). In addition, the direction of motion changed 4 times during the event. The

implications of movements of this type on possible offshore operations are discussed in Section 3.55.

Only two episodes of movement of the fast ice during the winter season were observed during the time the radar system was in operation. In neither case were the displacements large enough to be detected by the radar; they were noted only because observers were present in the area at the time of the events. It is reasonable to assume that other events of this type occurred but were simply not observed.

The first event occurred in March, 1976. Strong east to northeast winds forced the pack ice to drift away from the fast ice opening a lead, and also caused tension fractures up to a meter wide to form within the fast ice. This was unexpected, because the width of the fast ice in the Barrow area is too narrow for the wind fetch over the ice to generate stresses high enough to cause fracture. It is possible that the drag effect of ice ridges within the fast ice increased the wind stress sufficiently for tensile fracture to occur.

The second example of fast ice motion during winter occurred in April, 1977 when the pack ice was being compressed against the edge of the fast ice under the influence of southwest winds. Observations were made only near the shoreline, where the effects consisted of audible cracking of the ice and a slight (about 15 cm) rise of the ice sheet where it was driven up along the tide crack.

The fact that no large-scale movements of the fast ice occurred in winter while this program was operating clearly does not mean that such events cannot happen. In fact, there is anecdotal evidence that major ice push events have occurred during the winter months (Shapiro and Metzner, 1979; J. Kelley, pers. comm., 1986), although there is no indication that larger motions of the fast ice in an offshore direction have occurred. At best, the data indicate that these events are simply less likely to take place in winter. The point is discussed further in Section 3.55.

3.54.5 BREAKUP

As might be anticipated, breakup is the time of year when the ice cover is most active. As noted above, the start of the breakup process seems to be indicated by the increased occurrence of drifting ice offshore (Figure 3.4-5) and the rapid drop of the frequency of the pattern of no pack ice offshore from the fast ice in June (Table 3.5-2). The frequency of this pattern drops from 75% in May to 32% in June, and then to about 8% in July. The frequency of ice drift from the south also increases in those months, from 15% in May to 38% in June and to 51% in July. Interestingly, the frequency of winds which would tend to give these conditions does not change as much as the drift pattern (see discussion in Section 3.54.6).

The fast ice never moved out as a unit during breakup. Instead, by a combination of melting and fracture during movements it was simply reduced to small, individual floes which drifted off in streams. In general, the lines of reflectors representing grounded ice ridge lines, were the last features to disappear. Eventually, they lose sufficient mass through melting that they float up and drift offshore.

The effects of the impact of the pack ice on the edge of the fast ice are more noticeable during breakup than at other times of year. These effects generally took the form of a pervasive tightening shoreward through both the pack ice and fast ice, following an impact. However, ice push events, in which the fast ice was pushed up the beach, occurred **only early** in breakup, while the fast ice sheet was continuous, and never after the fast ice had begun to disaggregate. This may reflect the looseness of the ice within the fast ice zone, which might enhance the possibility for piling along the ridge lines, rather than transmission of stress through a continuous ice sheet to the ice along the beach. However, we have no field observations of the process to verify this.

Patterns of ice motion within the radar field of view during breakup were variable, particularly when the pack ice had been reduced to discrete floes. As a result, the patterns are difficult to describe in general. The following discussion and examples illustrate the point.

It was not uncommon for floes inshore from a line of remnants of ice ridges to be moving parallel to the coast, but in the opposite direction from that of the floes offshore from the ridge line. Examples of such patterns were observed in which the motion was in both senses (i.e., inshore floes drifting northeast and offshore floes drifting southwest, and vice-versa). This may reflect the influence of near-shore currents carrying the ice on one side of the ridge in one direction, while the wind pushed the ice on the other side in the opposite direction.

Rapid reversals of direction of ice motion (say, from southwest to northeast) were also common when the pack ice was composed of discrete floes. In some cases, the reversals occurred as part of a continuous movement, in contrast to reversals during winter, in which the pack ice always came to a halt before changing its direction of motion. When the movements were continuous, they occurred over periods of a few hours. In addition, the floes were often observed to move in patterns of whirls or eddies during these events.

The motion of a continuous pack ice sheet, and its interaction with the fast ice over a 6-day period in late-June, 1974 are illustrated in the displacement vector diagram in Figure 3.5-7. This figure was prepared using the same procedures as Figure 3.5-6. The sequence of movements began with the pack ice moving northeast along the coast at a velocity of 2.2 km/hr for about 4.5 hours. It then stopped for about 8 hours, and then moved northeast, but dragging along the edge of the fast ice as indicated by a velocity gradient in the ice which varied from 0.6 km/hr at the edge of the fast ice to 1.2 km/hr about 1 km further offshore. Drift in this direction continued for about 16 hours. Then, over the next 16 hours, the drift direction

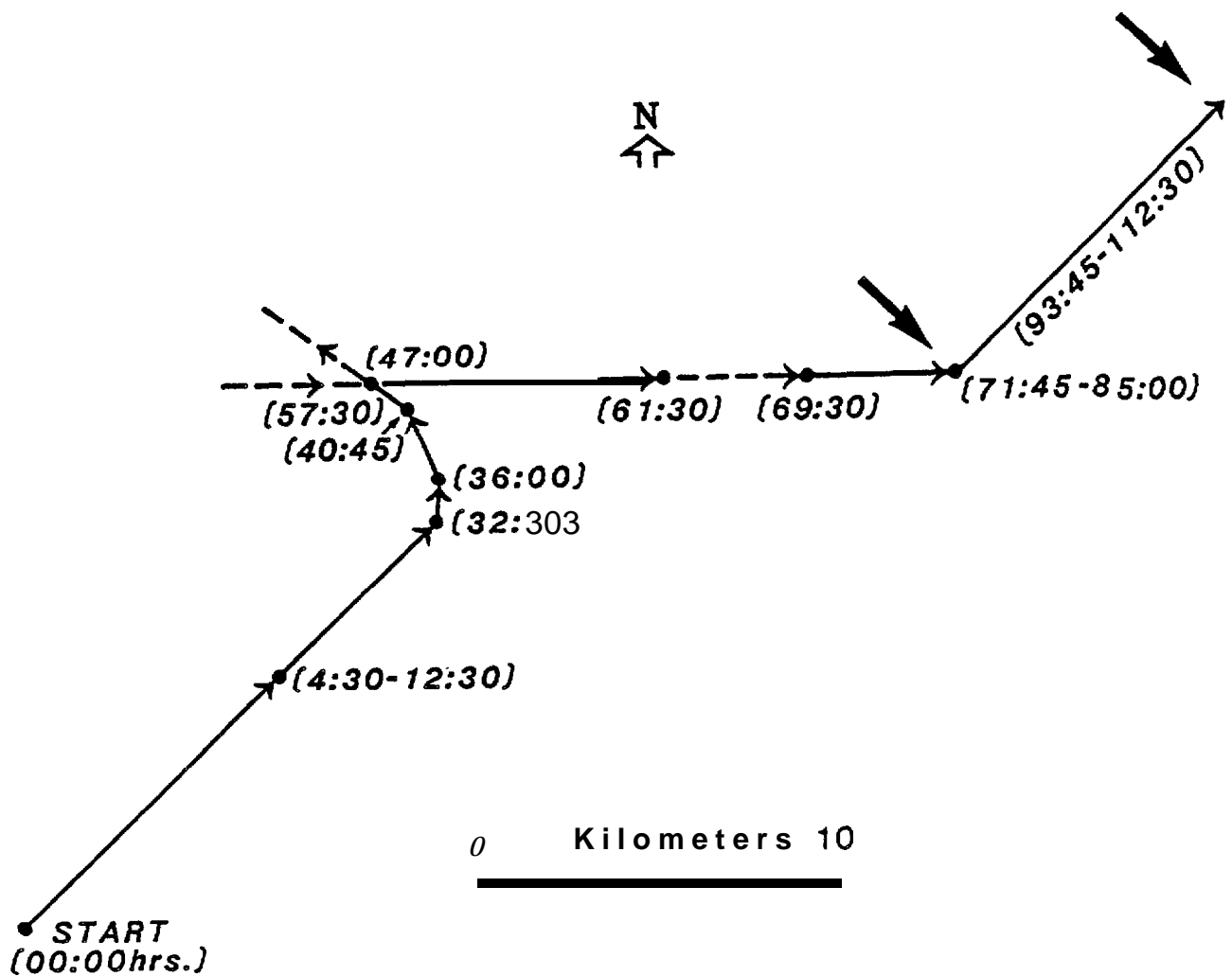


Figure 3.5-7

Displacement path of a hypothetical point on the pack ice surface during the movement episode of June, 1974. Distances calculated from ice velocity and time measurements. Arrowheads show the movement direction and numbers in parentheses are cumulative times as hours:minutes. Dashed lines show the path leaving and entering the radar field-of-view. Bold arrows indicate impact with the fast ice edge followed by compressive pulses or flickering during the times indicates.

turned from northeast to north, then to north-northwest, and finally to the northwest. During this time the ice velocity slowed gradually to 0.2 km/hr, and the ice drifted out of the field-of-view of the radar to the northwest. It remained out of view for almost 24 hours, with the exception of a 4-hour period (from 57:30 to 61:30, about midway through the 24 hour period) when floes were visible drifting northeast at 0.5 km/hr at the limit of the field of view. When the pack ice next appeared on the radar screen it was drifting eastward at 2 km/hr on a path which led to impact with the edge of the fast ice (at 71:45). For 12 hours following the impact the pack ice continued to tighten against the edge of the fast ice. Numerous compressive pulses occurred, each of which resulted in a slight shoreward displacement of the reflectors in the pack ice. Subsequently, no movement occurred for about 4 hours, when the reflectors on the pack ice began to flicker. The flickering continued for about 3 hours after which the pack ice began to move northeastward, parallel to the coast at a velocity of 1.2 km/hr. The movement continued for about 9 hours, when the pack ice stopped and compressed against the coast again. It then remained in place for about 18 hours with no further movement when the film sequence was terminated.

The most unusual movement pattern observed during the breakup season is illustrated schematically in Figure 3.5-8. The figure shows three different velocities and two different directions of ice motion occurring in the small area of the field-of-view of the radar at the same time. Inshore of a line of ice grounded ridges, small, loose floes were drifting northeast along the coast at a velocity of 0.8 km/hr. Offshore from the ridge line, larger floes were drifting northeast at 4.1 km/hr. Then, the edge of the pack ice entered the field-of-view of the radar moving almost due east toward the coast at 0.5 km/hr, crossing the path of the drifting floes. Ultimately the pack ice impacted the line of grounded ridges and compressed against it.

The examples above illustrate the difficulty of characterizing “typical” ice movements or conditions during the breakup season. It is sufficient to conclude that

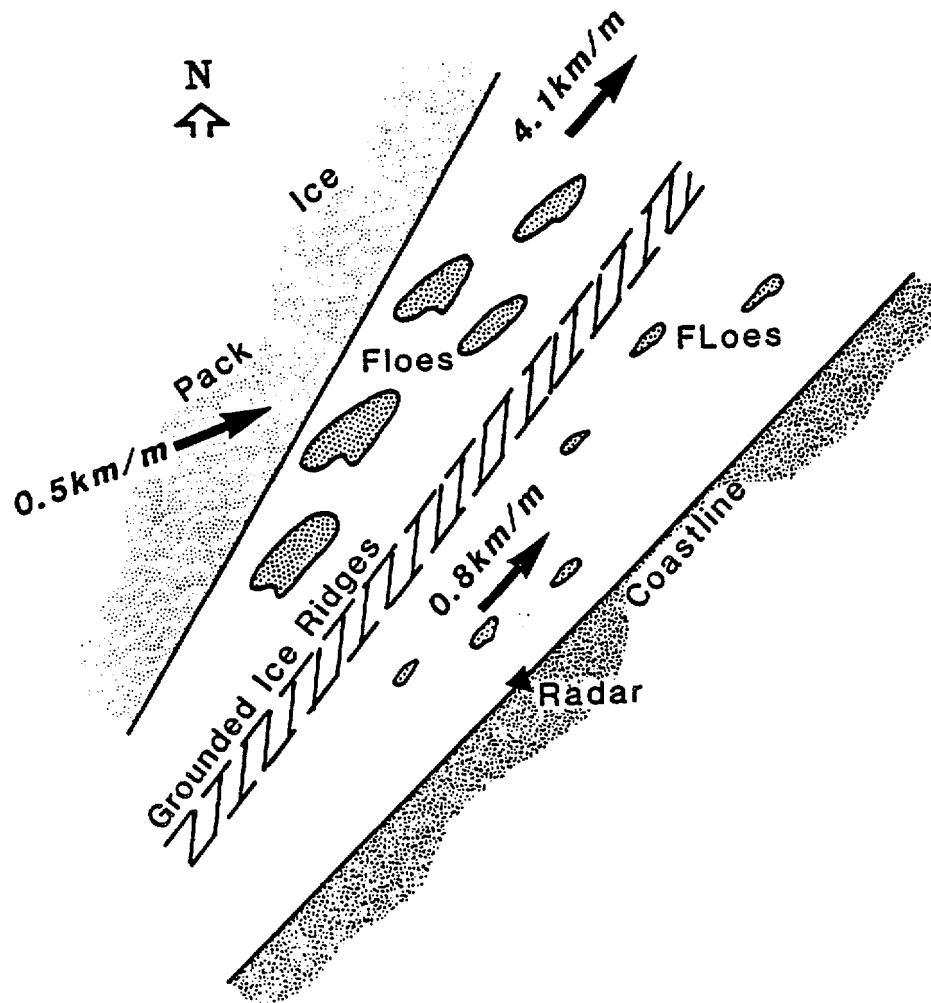


Figure 3.5-8

Schematic diagram of unusual ice movement pattern during breakup. Pack ice moving eastward at 0.5 km/hr as large floes offshore from the line of grounded ice ridges (about 1 km from shore) are moving at about 4.1 km/hr. The velocity of the small floes inshore from the ridges is about 0.8 km/hr. The pack ice ultimately impacted the line of grounded ridges and compressed against it.

breakup is a time of almost continuous ice activity leading to the disintegration of fast ice.

3.54.6 RELATIONSHIP OF THE ANNUAL CYCLE TO CLIMATIC DATA

The weather data for the Barrow area, summarized by Brewer et al. (1977), were examined for correlation with the seasons of the ice year defined above. As noted earlier, the data sets for the weather and the radar system do not overlap in time. Brewer et al. used climatic data for the period from January, 1966 to December 1974 in their compilation, while the radar system was operated from June, 1973 to May, 1979. It is assumed here that both data sets cover sufficient time to be considered as representative. However, the correlations between the climate data and the ice seasons are weak at best; they are discussed here only for the sake of completeness.

Variations in wind direction, storm tracks in the Chukchi Sea and air temperature were considered most likely to be associated with changes in the ice season. The relationship to wind direction is clear from the discussion above regarding the variation of ice drift direction parallel to the coast with the seasons. Storm tracks through the Chukchi Sea generate southerly winds which drive the ice northward and, in addition, they trigger ice push events. Temperature is simply the most reliable , indicator of seasonal change.

All the northerly moving storm tracks in the central Chukchi Sea, recorded in Brower et al. (1977) are listed in Table 3.5-3 as the number of storms per month. There are too few events to justify a statistical analysis of the data. However, it appears that storms are least common in the winter months (February, March and April), but are not noticeably more likely to occur consistently at other times of year. Clearly, there are no major “spikes” in the data which coincide with the changes in season of the ice year.

The data on wind directions are listed in Table 3.5-3 which shows the percentage of time that the wind was from the quadrants indicated in Figure 3.5-3, corresponding to the directions of pack ice motion indicated in the figure. The only suggestive points in the data are for the month of July, in which the frequency of winds from the northeast, east and southeast decreases in favor of winds from the south, southwest and west. This appears to coincide with the increased frequency of ice motion from the southwest noted above. However, it should be noted that a similar relationship occurs in January and February, so that it is difficult to draw conclusions from the data.

The monthly mean temperatures at Barrow are listed in Table 3.5-3. These indicate some correlation with the ice seasons, in that two of the ice seasons (winter and breakup) begin about 1 month following a sharp change in the mean temperature. In addition, as might be anticipated the open water season occurs during the two warmest months and the month which follows them.

It would be possible to extend the study to attempt to interpret the changes of the ice seasons in terms of the extent and nature of the ice cover (i.e., continuous pack ice cover vs. discrete, drifting floes) which clearly reflect the air temperature. However, that would require extensive examination of satellite imagery, which was beyond the scope of this project.

TABLE 3.5-3

CLIMATE DATA BY MONTH (1966-1974) FROM BROWER ET AL. (1977)

| | TOTAL NUMBER OF NORTHERLY STORMS | MEAN AIR TEMPERATURE (C) | WIND DIRECTION (%) (*) | | | |
|-----|---|--------------------------------|------------------------|------|----|-----------|
| | | | NE-E-SE | S-SW | W | N-NW |
| JAN | 6 | -26 | 52 | 20 | 12 | 18 |
| FEB | 1 | -29 | 53 | 15 | 13 | 18 |
| MAR | 2 | -27 | 58 | 15 | 10 | 17 |
| APR | 0 | -19 | 62 | 15 | 6 | 15 |
| MAY | 6 | -7 | 67 | 15 | 6 | 12 |
| JUN | 2 | 0 | 60 | 12 | 10 | 17 |
| JUL | 5 | +3 | 48 | 18 | 15 | 17 |
| AUG | 4 | +3 | 54 | 15 | 12 | 18 |
| SEP | 2 | -1 | 58 | 15 | 8 | 17 |
| OCT | 5 | -9 | 62 | 20 | 5 | 12 |
| NOV | 4 | -25 | 64 | 16 | 7 | 12 |
| DEC | 3 | -25 | 56 | 18 | 11 | 12 |

(*) NOTE: Percent of time that weather is calm brings the total of these four columns to 100910.

3.55 SUMMARY AND DISCUSSION

The descriptions above can be summarized into the following generalizations regarding the seasons of the ice year:

1. The open water season, defined as those months in which no ice was visible in the field-of-view of the radar system for the time represented by at least one roll of film, ranges from late-July to late-September. However, drifting pack ice or remnants of the fast ice were often visible during these months, so that the radar field-of-view was never totally free of ice for more than a few weeks.

2. The process of freeze-up (in particular, the formation of the fast ice) begins in late-September and can extend to about mid-January. The definition of the duration of the season is based upon (1) the observation of the earliest occurrence of fast ice in the area (neglecting the single year when the fast ice remained in place through the entire summer) and (2) the last observed offshore movement of fast ice and the frequency of observation of drifting pack ice in the field-of-view of the radar.

In the Barrow area, a significant portion of the fast ice is composed of floes which drift into the area. First-year ice which freezes within the fast ice zone forms primarily in sheltered areas between floes or inshore from grounded ice ridges. In three of the years in which our observations were made, the pack ice came from the southwest in the form of floes of first-year ice up to 0.5 m thick. In one year, it originated ice remained in place through the following summer, so that no new floes were introduced during the subsequent freeze-up.

When the fast ice formed from floes drifting into the area from the southwest, it commonly developed in segments which became attached to the offshore boundary of ice already in place. Segments frequently broke loose and drifted off, to be replaced by other floes until the fast ice was built seaward to (approximately) the 20 m depth contour. The offshore edge of each segment was usually marked by a shear ridge which, at some stage, had represented the fast ice-pack ice boundary.

The highest ice velocity measured during the years the radar system operated was 8 km/hr, which occurred during a storm late in the freeze-up season.

3. The winter season extends from mid-January through May. During this time, the pack ice is most commonly either out of the field-of-view of the radar system (i.e., greater than about 5.5 km from shore) or adjacent to the fast ice but stationary. Note that the latter condition may be due to the presence of a local floating extension of the fast ice which could not be distinguished from pack ice without independent observations.

Incursions of pack ice against the fast ice are not uncommon during the winter season and can lead to the formation of ice ridges along the edge of the fast ice. During the course of the project there were no cases of large-scale motion of the fast ice as a result of impacts. However, there is anecdotal evidence that such movements, in the form of ice-push events, have occurred in the past, but there are no reports of the fast ice sheet floating offshore during the winter season.

There was no preferred direction for pack ice motion observed by the radar during the winter, and ice velocities were generally low.

4. The start of the breakup season is indicated by the increase in the occurrence of drifting ice in the field-of-view of the radar in June. Ice motion is dominantly to the north during this season and, as the fast ice deteriorates (primarily through melting) it tends to break into small floes which drift off in that direction. However, examples of a wide range of movement patterns and directions were observed during the course of the project. In addition, in 1975, the fast ice remained in place through the entire summer. In that year, pack ice drift from the north was common through July, August and September. This does not presuppose a cause and effect relationship between the pattern of ice drift from the north and the absence of a true breakup that year. Rather, it suggests that both resulted from an unusual distribution pattern of weather systems during the summer of 1975.

The changes in the ice cover with the seasons, as defined above, maybe related to variations in air temperature through the year. However, they cannot be correlated to changes in prevailing wind directions or the passage of storm systems, the only other climate variables examined.

The patterns of ice distribution and motion in the field-of-view of the radar can be interpreted as being driven primarily by the regional wind field, but strongly influenced by the local regime of tide and currents, sea floor topography and the configuration of the coastline. It seems probable that similar influences would operate elsewhere along the coast, reflecting local conditions. Quantitative modeling of ice motion under these conditions would be difficult, because of the number of variables and the range of possible interactions between them. Thus, rules-of-thumb developed from repeated observations may be necessary if local ice conditions are to be predicted. This, in turn, requires a period of monitoring of local patterns of ice movement and distributions, such as was done for the Barrow area on this project.

Many of the problems of operating a program such as this have been negated by technological advances in recent years. Smaller, portable radar systems are available, and the availability of low-light video equipment for recording images of the radar screen would eliminate many of the difficulties we faced in attempting to interpret the data. In addition, it would make the data available quickly and facilitate ground truth studies.

The range of changes in ice movement direction described in the winter and breakup movement episodes (Figures 3.5-6 and 7) indicates some of the problems which might be encountered in developing offshore installations in exposed coastal areas. An example is provided by suggestions for the design of a tanker terminal for the Chukchi Sea coast of Alaska, using a single-point mooring system mounted on a monopod. The idea is that a ship at the terminal could be positioned so that it was

always on the lee side of the structure with respect to moving pack ice. However, the data raise the question of whether a vessel could maneuver near the **monopod**, given the rate of ice motion and associated problems of clearing ice from around the structure. This is not to suggest that the design is not feasible; instead, it is emphasize the point that knowledge of the pattern of ice motion in the area should be available for consideration during the design stage.

REFERENCES CITED

- Sackinger, W. M. and J. C. Rogers, 1974, Dynamics of breakup in shorefast ice; in J. C. Reed and J. E. Sater, eds., *The Coast and Shelf of the Beaufort Sea*; Arctic Inst. of North America, pp. 367-376.
- Shapiro, L. H., 1975a, A preliminary study of the formation of landfast ice at Barrow, Alaska, winter, 1973-1974; U. of Alaska Gee. Inst. Rpt. UAG R-235, 44 pp.
- Shapiro, L. H., 1975b, A preliminary study of ridging in landfast ice at Barrow, Alaska, using radar data; *Proc. 3rd Int. Conf. on Port and Ocean Eng. under Arctic Conditions (POAC)*, Fairbanks, Alaska; pp. 417-426.
- Shapiro, L. H. and Metzner, R. C., 1979, Historical references to ice conditions along the Beaufort Sea Coast of Alaska; U. of Alaska Gee. Inst. Rpt. UAG R-268, 11 pp. + App.
- Shapiro L. H., R. C. Metzner, A. Hanson and J. B. Johnson, 1984, Fast ice sheet deformation during ice-push and shore ice ride-up; in P. W. Barnes, D. M. Schell and E. Reimnitz, eds., *The Alaskan Beaufort Sea, Ecosystems and Environments*, Academic Press, New York, pp. 137-158.
- Stringer, W. J., 1974, Morphology of the Beaufort Sea shorefast ice; in J. C. Reed and J. E. Sater, eds., *The Coast and Shelf of the Beaufort Sea*; Arctic Inst. of North America, pp. 165-172
- Wittman, W. I. and G. P. MacDowell, 1964, Manual of short-term sea ice forecasting Spec. Pub. 82, U.S. Navy Oceanographic Office, Wash. D. C., 142 pp.

3.6 CORRELATION OF NEARSHORE ICE MOVEMENT WITH SEA-BED ICE GOUGES

by

Lewis H. Shapiro, Peter W. Barnes* and Ronald C. Metzner

ABSTRACT

Side-scan sonar surveys of the seafloor were made in consecutive summers (1977 and 1978) in an area within the field-of-view of the University of Alaska sea ice radar system near Barrow, Alaska. The purpose was to interpret changes in ice gouge characteristics in terms of the history of the ice cover in the time before and between the surveys, as recorded by the radar. The survey showed that the principal direction of the gouges in the area is at a high angle to the coast (and to both the isobaths and the predominant direction of ice drift, which are parallel to the coast). We interpret the principal ice gouge orientation as primarily due to the drag of keels of multiyear floes during ice-push events. The gouge density is greatest in the area in which most ice ridges occur, which may reflect the incision of keels into the sea floor during ridging. Changes in gouge density between the surveys are interpreted as due to sediment movements during a period of storms following the 1977 survey.

3.61 INTRODUCTION

The interaction between ice movement and ridge growth and ice gouging of the sea floor has received little attention because of the difficulty of obtaining data on both the nature of the ice cover and the sea floor for the same area and time frame. The sea floor preserves gouges beyond the ice event(s) which cause them, recording

*U. S.-Geological Survey, Branch of Marine Geology, 3435 Deer Creek Rd., Palo Alto, CA 94304

evidence of ice motion which can be studied when the ice melts or moves away. Thus, knowledge of both the history of the ice cover and the evolution of ice gouges from year-to-year at the same location should provide insight into the relationships between ice canopy processes and the resulting disruption of the sea floor, as well as the seasonal timing of gouging events. The opportunity for such a study was presented by the presence of the University of Alaska sea ice radar system at Barrow. The radar monitored ice conditions relatively continuously and the results could be coupled with the results of summer studies of ice gouging within the radar field-of-view.

A bathymetric survey of the area within the the field-of-view of the University of Alaska sea ice radar system at NARL (Figure 3.6-1) had been conducted by two of the authors (L.H.S. and R. C.M.) in September, 1976. The purpose was to supply bathymetric data to aid in the interpretation of ice motion and ridging patterns in the area. Data were acquired by a continuous recording fathometer installed on a 14-foot Boston Whaler; the position of the vessel was monitored by the radar system as the survey was made. The records were examined by E. Riemnitz of the U.S.G.S. who pointed out that numerous ice gouges were visible on the data, although the records were too coarse for accurate gouge depths to be measured. In addition, since the fathometer only measured the depth below the boat, the area sampled was small and the orientation of the gouges could not be determined. However, a preliminary analysis of the distribution of ice gouges-with-depth was made from the data, and the systematic aspect of the pattern suggested that further work in the area might be useful,

Subsequently, more detailed ice gouge surveys were conducted during the summers of 1977 and 1978 using a precision fathometer and a side-scan sonar

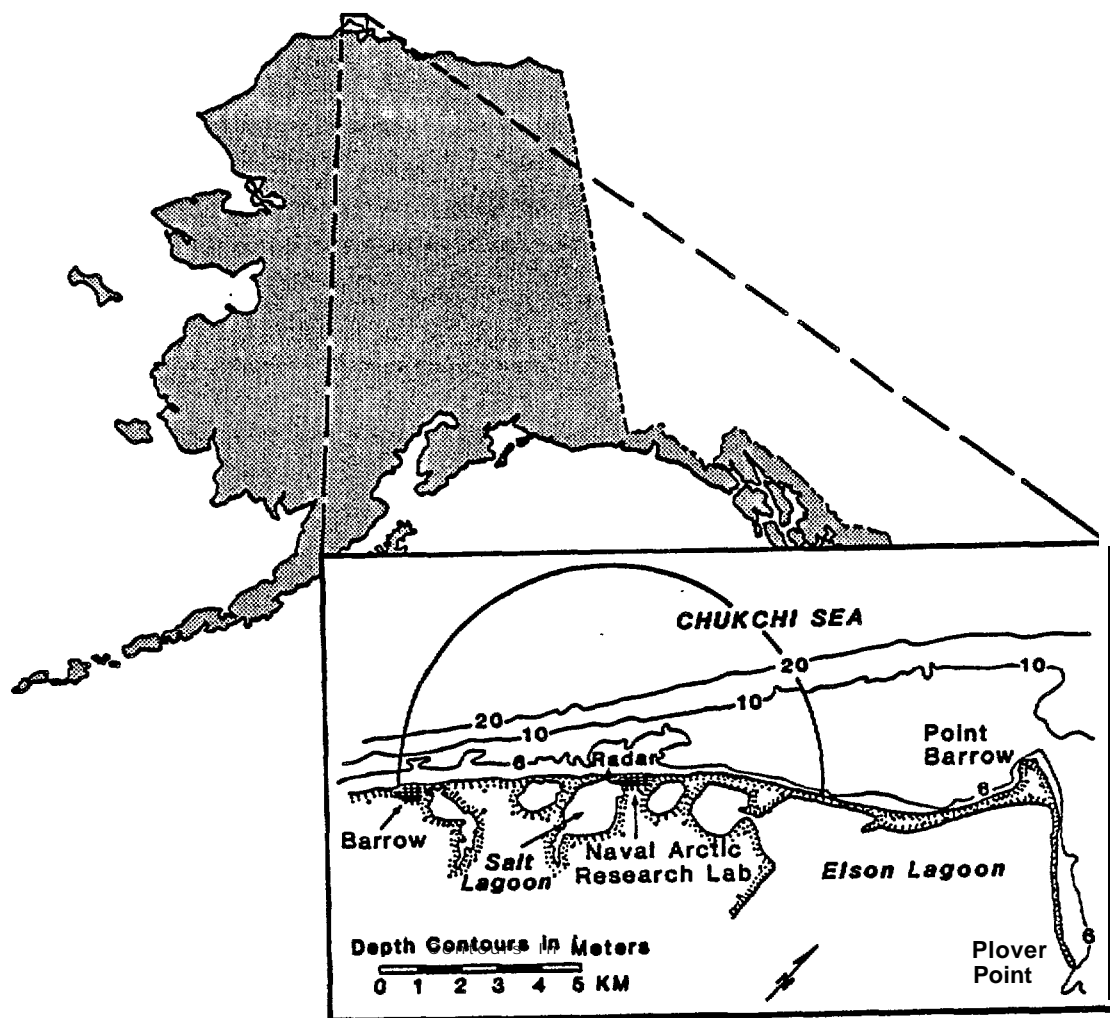


Figure 3.6-1 Map of the location of the survey area showing the field-of-view of the University of Alaska sea ice radar system and the boundaries of the survey area.

The data from these surveys, along with the results of the study of local ice motion using the radar data (Section 3.5) form the basis for this report.

3.62 METHODS AND EQUIPMENT

The first survey using this instrumentation was conducted in September 1977; the second was done in August, 1978. The surveys covered about 6 sq km within the field-of-view of the radar (Figures 3.6-2 and 3) with overlapping side-scan sonar data.

The vessel used in the 1977 survey was a 16-foot skiff with the side-scan sonar tow fish suspended from the bow and the fathometer on an outrigger along the side. The tracklines were navigated by installing range markers at 200 m intervals along the beach on a nominal heading of 310° T. Due to strong coastal currents, problems were encountered on the vessel in maintaining the alignment of the markers at distances of more than 1.5 km from shore. However, a radar reflector was mounted on the vessel and the radar screen was photographed at 1.5 minute intervals, providing a time-lapse motion picture of the path of the vessel. The positioning data from the range markers were probably more accurate within 1 km of shore, while the radar data were more accurate seaward. Positions along the tracklines were determined from the radar data with the radar clock synchronized with the clock used to mark the records of the survey vessel. The 1977 survey speeds generally ranged between 5 and 6 kts.

The 1978 survey was run at a speed of about 5 knots using a 42-foot vessel with a narrow beam fathometer and towing a side-scan sonar fish. The tracklines were navigated with a precision range system which gave position accuracies within 10 m, although range markers were again set up at 200 m intervals along the beach for close inshore navigation. The ranges were maintained using equi-distant baselines for the two range stations set upon the beach along a known baseline.

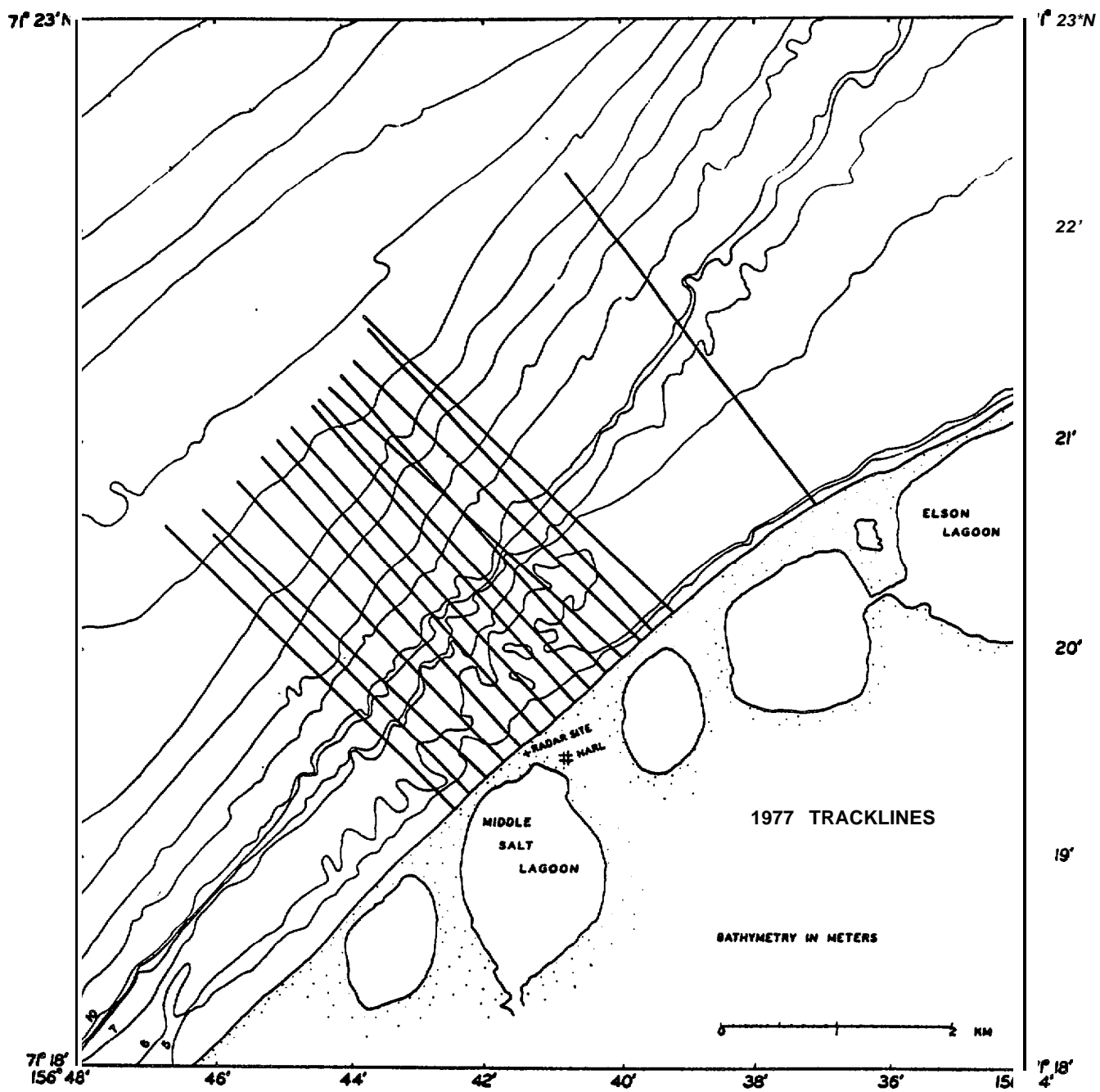


Figure 3.6-2 Tracklines of the 1977 side-scan sonar survey.

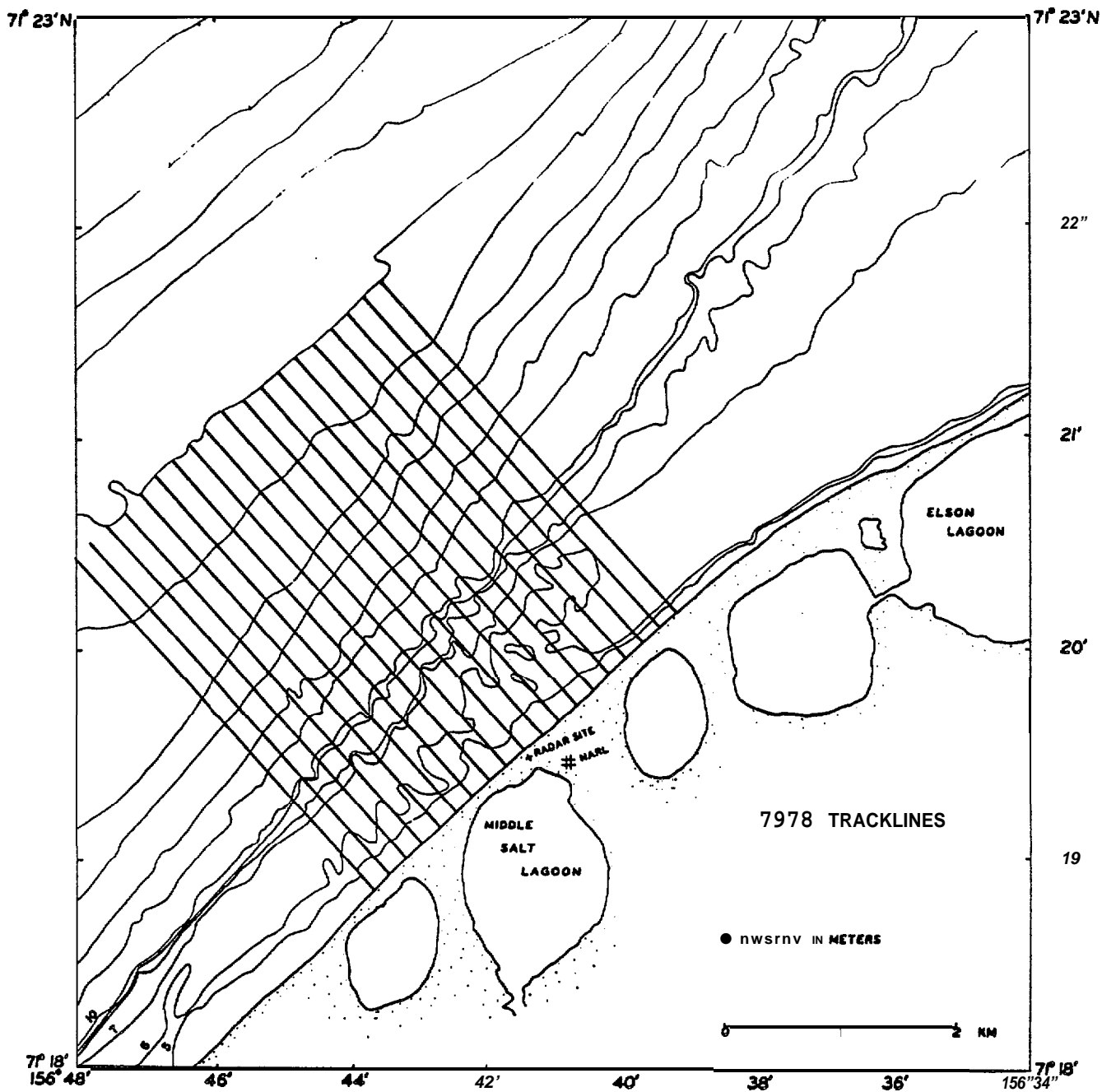


Figure 3.6-3 Tracklines of the 1978 side-scan sonar survey.

The fathometer used in both years recorded at a scale of 1 cm equals 1 m. At this scale, depth differences of greater than 10 cm were usually resolvable. No corrections to depth were made to the fathogram records for tides or changes in the velocity of sound with depth, although the transducer depth (25 cm) was compensated for. Thus, the absolute depths observed in the surveys might be subject to sea level correction although the comparative gouge depth observations are quite accurate.

Monographs were obtained on a wet paper, dual helix recorder which scanned the sea floor for approximately 125 m on either side of the vessel. System vagaries and problems associated with record interpretation have been dealt with at length (Belderson, 1973; Toimil, 1978; Barnes and others, 1984). With the 250 m swath width of the monographs and the 200 m spacing of tracklines used in the survey, the nominal overlap of monographs should have been 25 m, so that a mosaic of the monographs of the survey area could be constructed. However, in the 1977 survey speed variations along the trackline, variation in record quality due to sea state and tow depth limitations, and problems encountered in compensating for the surface current all interacted to hinder the creation of the hoped for mosaic.

In the 1978 survey, the navigation was improved and the vessel was larger, which allowed for more even coverage of the survey area. However, the record quality was poor and it was not possible to correlate the results with the 1977 survey in detail.

3.63 OBSERVATIONS

The number of linear traces made by ice gouging the sea floor was counted on the monographs for each 0.5 km segment of trackline. The resulting value, corrected for orientation and scale problems (Barnes and McDowell, 1978), was used to describe

the density (in terms of number of gouges per 0.5 km of trackline) in the survey area. The gouge densities for the two survey years are shown in Figures 3.6-4 and 5.

Gouge densities were generally higher in 1977 than in 1978 in all water depths within the survey area. However, the distribution pattern was similar in both years; the maximum gouge densities were found in a narrow band between 5 m and 20 m water depths, with the highest densities at about 7 m to 8 m depths. This agrees with the observations of Toimil (1978) in the Barrow area. Note that the highest gouge densities were found within the area of highest density of prominent lines of grounded ice ridges as mapped from the radar imagery of the area for the years from 1973 to 1978 (Figure 3.6-6).

The maximum depth of ice gouge incision below the sea floor was determined from the fathograms for each of the 0.5 km segments in each year (Figures 3.6-7 and 8). The maximum gouge depths inshore of the 10 m isobath and seaward of the 30 m isobath are generally less than 1 m. Peak values exceeding 2 m occur in the vicinity of the 20 m isobath. It is interesting to note that the most numerous gorges occur inshore of the zone of deepest gouge incision. Comparison of figures 3.6-7 and 8 shows that, with the exception of a small area centered 2 km west of the radar site, the depth of gouge incision decreased between 1977 and 1978.

The principal orientation of ice gouges in each of the 0.5 km segments was also determined using the techniques outlined in Barnes and others (1978) and Barnes and others (1984). The results are shown in Figures 3.6-9 and 10. It is apparent that the principal gouge orientation was at a high-angle to the coastline and to the isobaths over the entire survey area in both years. This is in marked contrast to the results of other surveys along the northern coast of Alaska, where the principle trends tend to be parallel to the coastline and the isobaths (Toimil, 1978; Barnes and others, 1984).

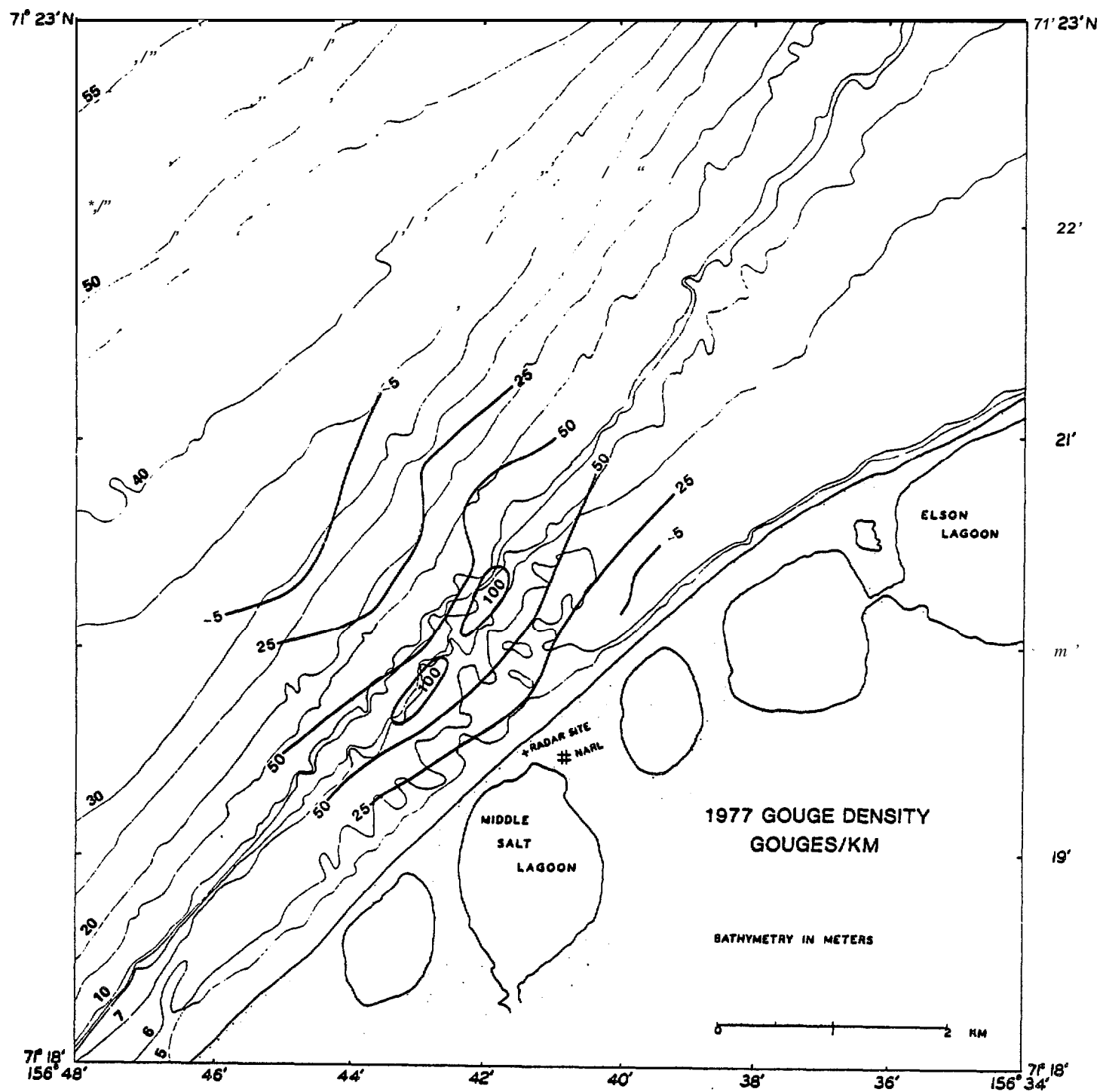


Figure 3.6-4 Density of ice gouges in 1977.

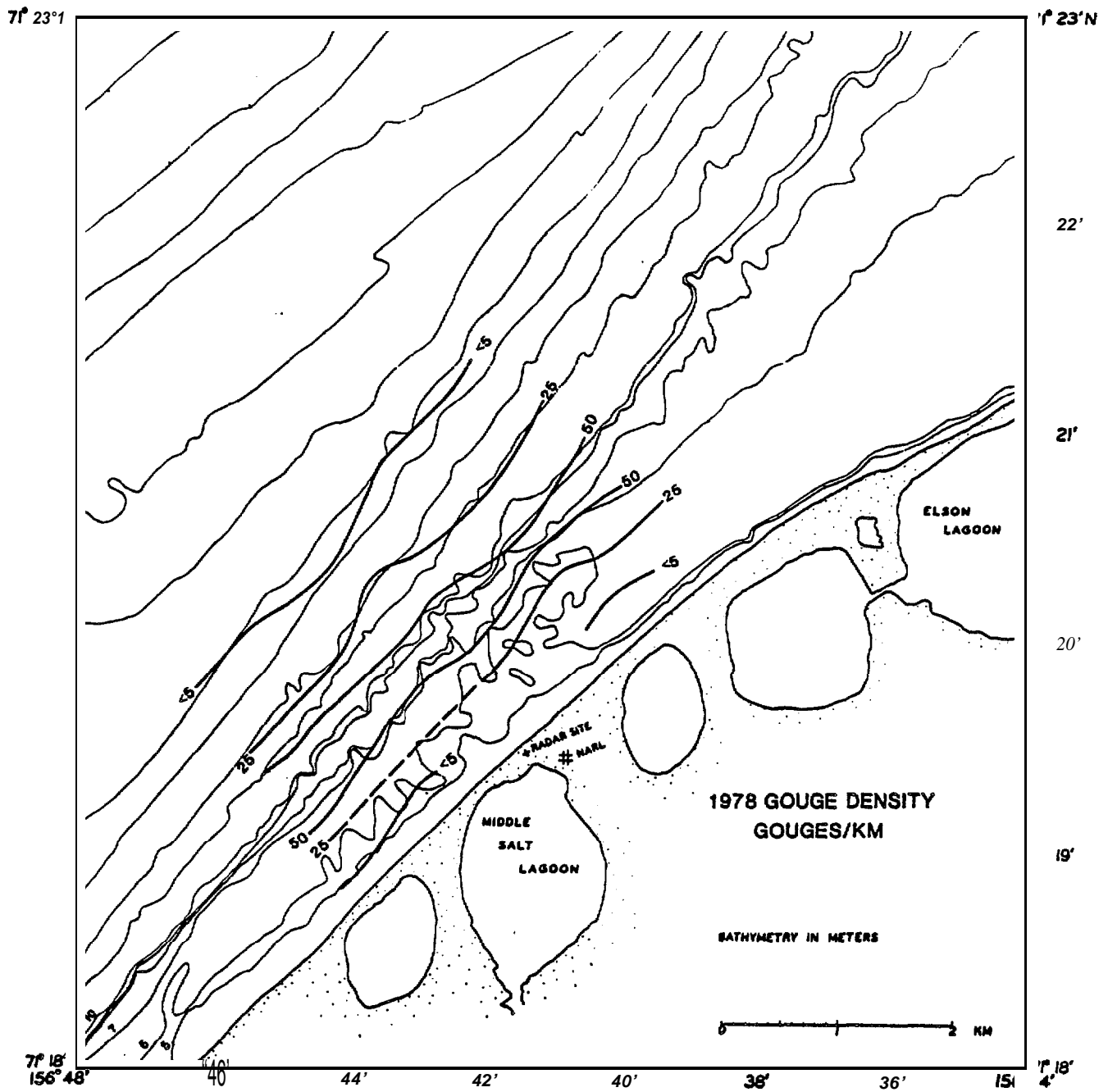


Figure 3.6-5 Density of ice gouges in 1978.

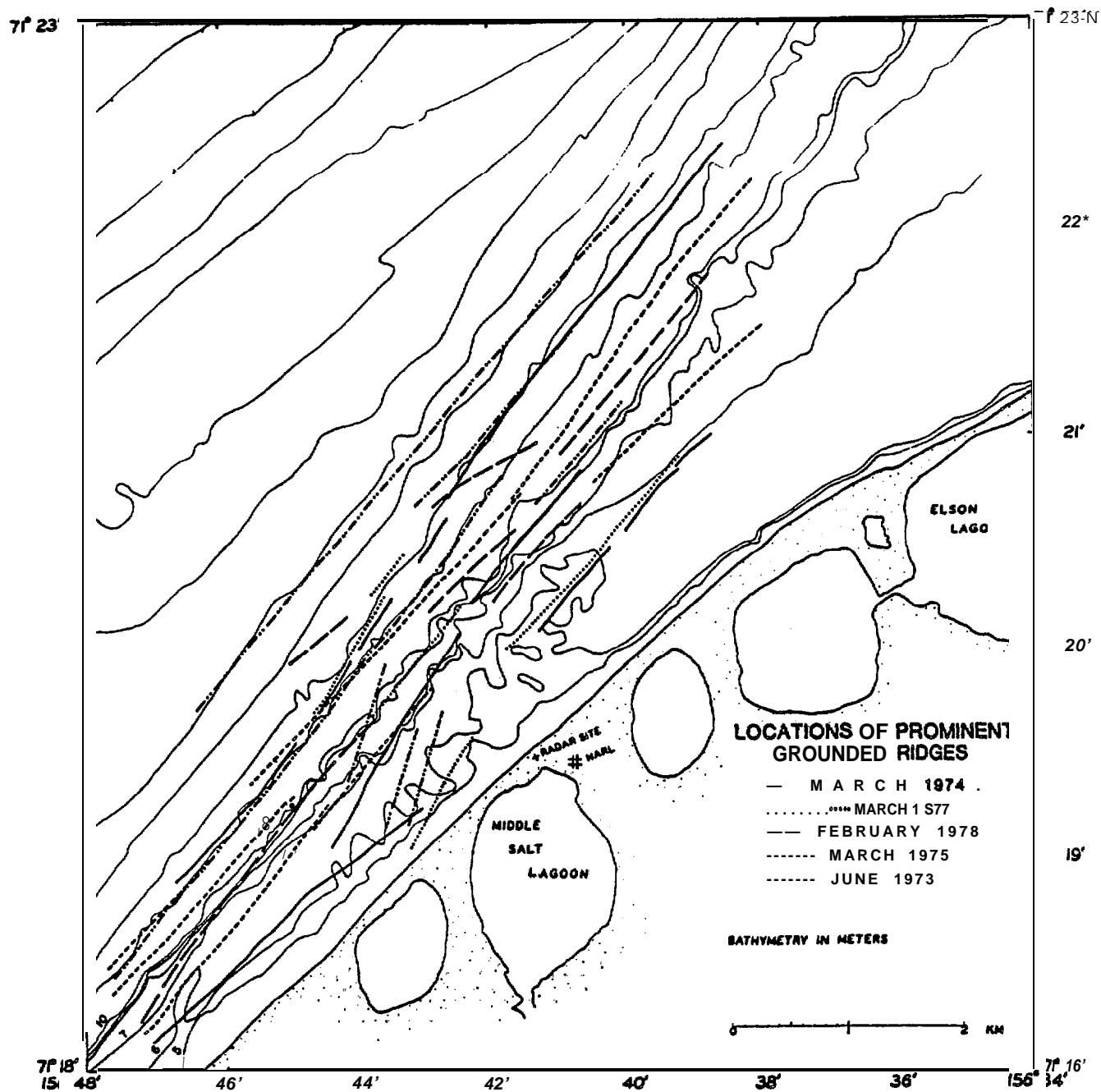


Figure 3.6-6 Locations of prominent grounded ice ridges in the field-of-view of the radar system.

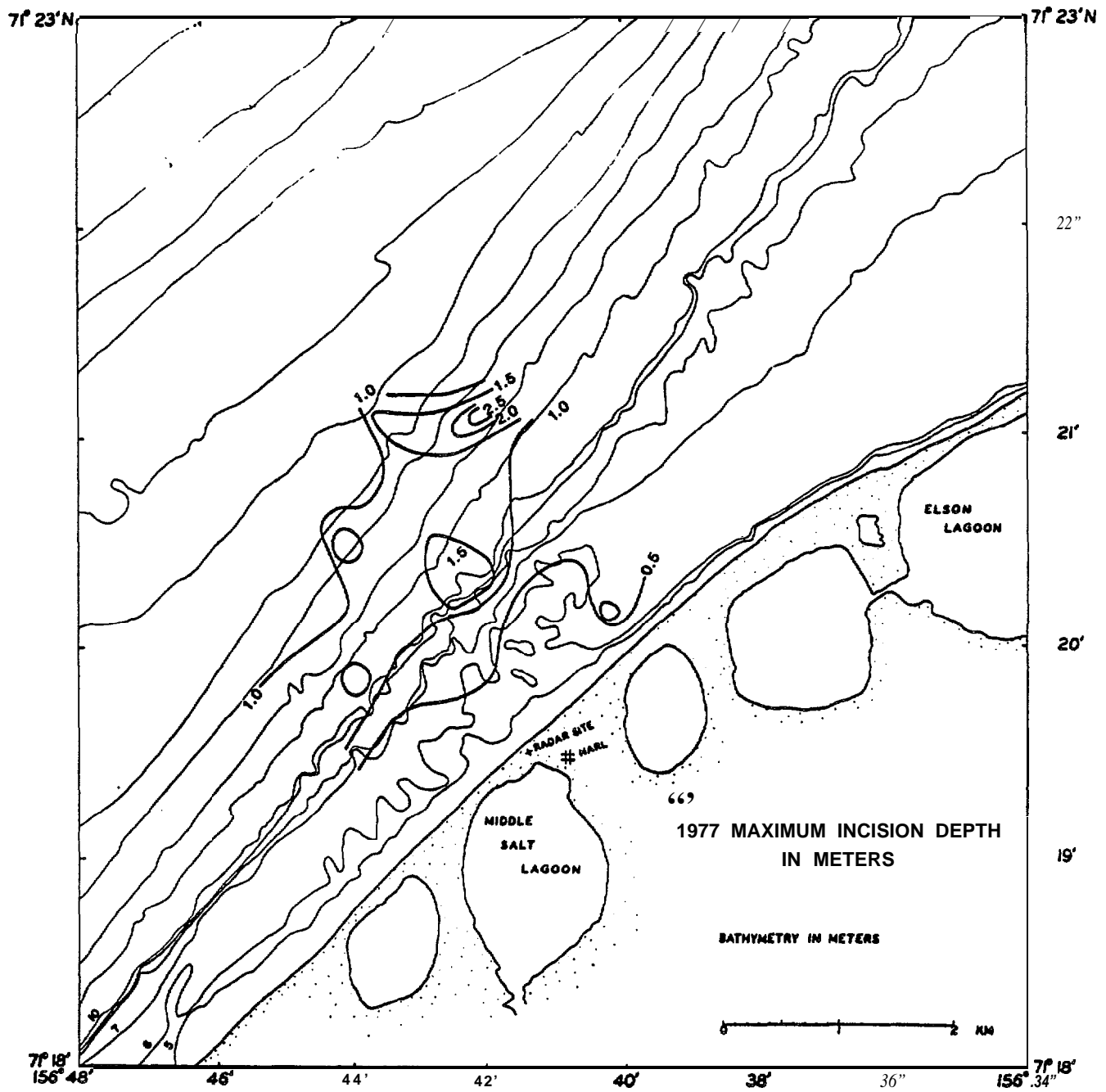


Figure 3.6-7 Maximum ice gouge incision depth, 1977.

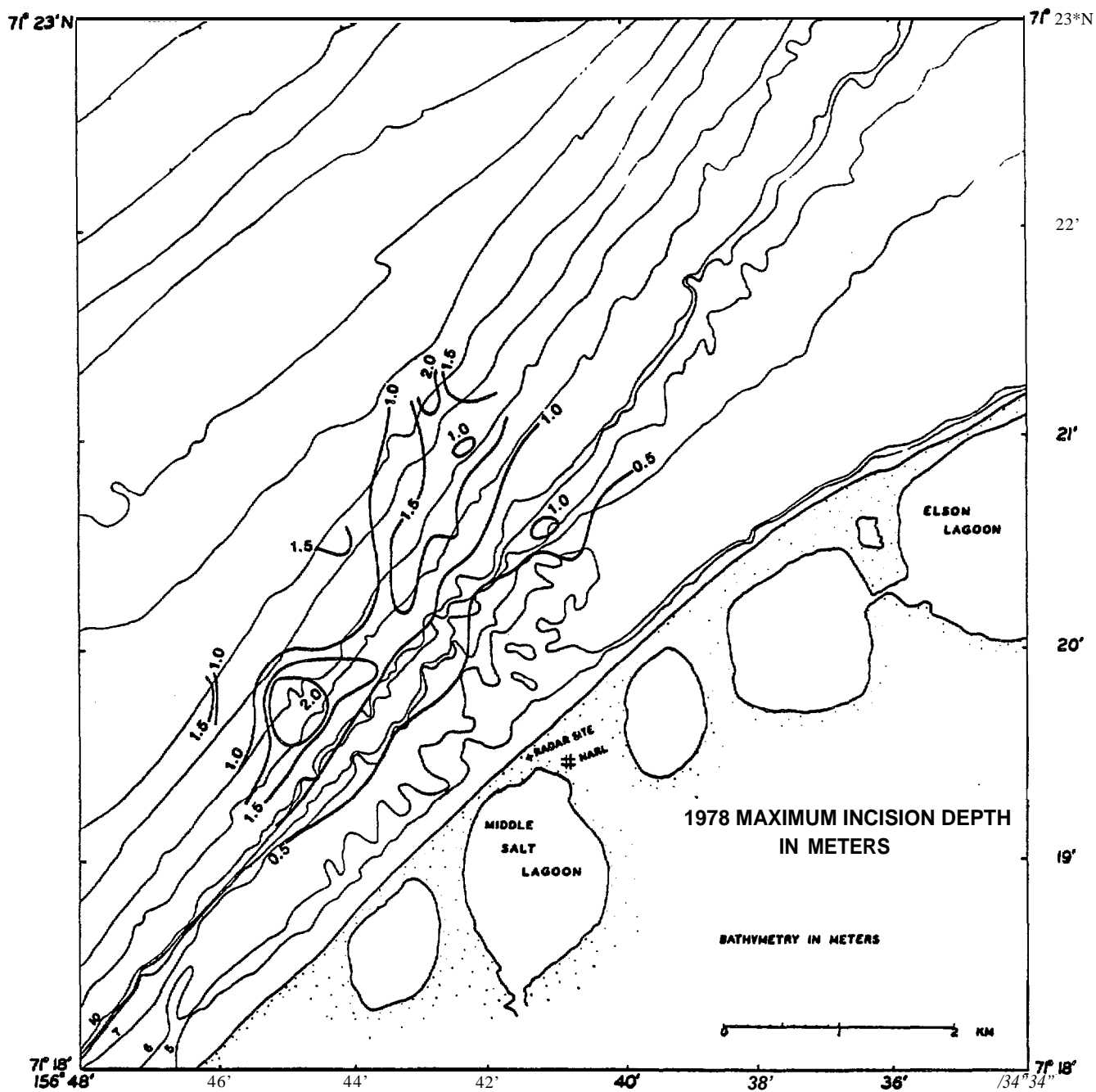


Figure 3.6-8 Maximum ice gouge incision depth, 1978.

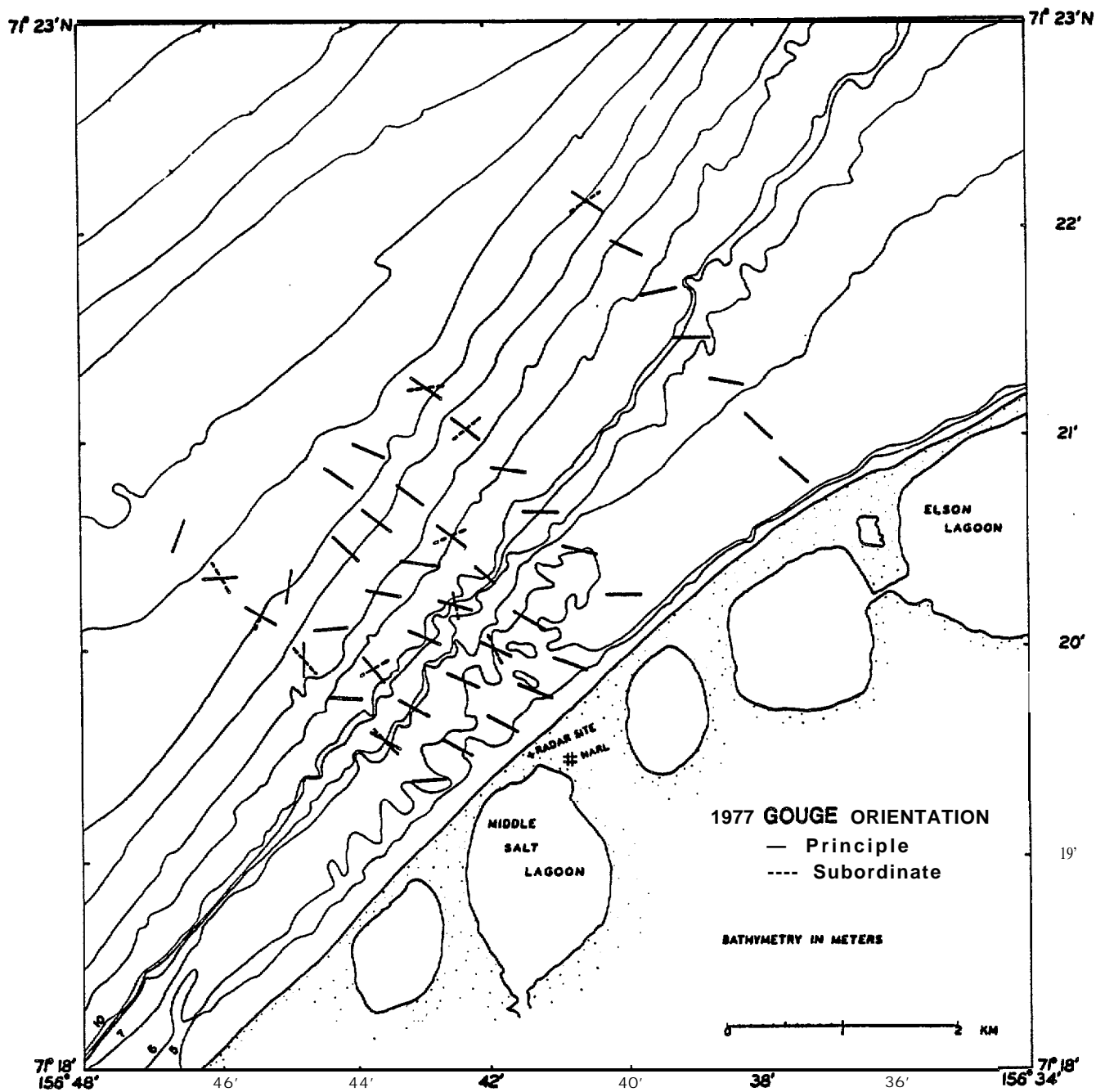


Figure 3.6-9 Principal orientation of icegouges, 1977.

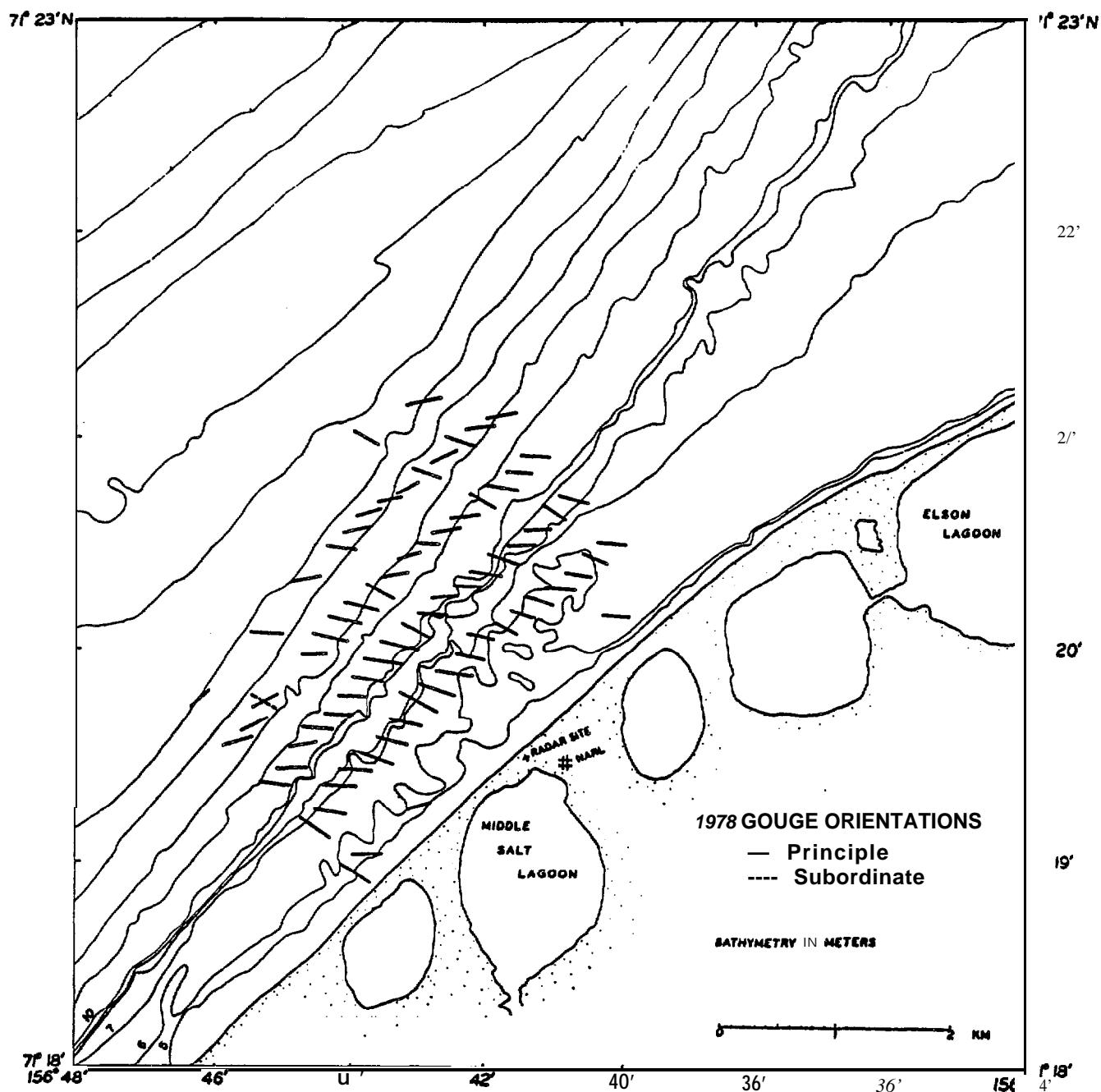


Figure 3.6-10 Principal orientation of ice gouges, 1978.

3.64 DISCUSSION

3.64.1 ICE GOUGE ORIENTATION AND ICE MOTION

Ice gouges record the ice motion direction during gouging events and may not reflect the general pattern of ice drift in an area. This is true particularly if, in general, the ice does not have sufficient draft to reach the sea floor. Gouges inshore from the (approximately) 20 m isobath probably form mainly during freeze up (October-November) and breakup (July). During the winter the fast ice is generally (but not always) stationary and the motion needed to generate gouges is absent. This suggests that the ice gouge density, depth and orientation in the study area should primarily reflect the patterns of ice motion during freeze up and breakup. However, as described below (and in Section 3.54), the dominant drift directions of the ice in the area are parallel to the coast during both freeze up and breakup. Thus, assuming that the gouges reflect the drag of deep keels in the ice cover, the principal gouge orientations would be expected to also be aligned parallel to the coast. The fact that the principle gouge orientations are at a high-angle to both the coast and the isobaths suggests that they reflect “unusual” movements of the ice cover. Two possible patterns of movement which could be responsible for the observed gouge pattern are developed in the following discussion.

As noted in Section 3.54.3 the term “freeze up” is something of a misnomer for the mechanism by which the fast ice in the study area develops, because it suggests general freezing of the ice sheet in place. In fact, in most years the fast ice sheet probably consists of pack ice which drifts into the area from the southwest, having formed further south in the Chukchi Sea. Freezing in place occurs only in the spaces between floes. The pack ice from the southwest generally includes only floes of thin (i.e., less than 0.5 m thick), young *ice*, and ridges formed from them are not likely to have the deep keels required for gouging of the sea floor, other than in shallow water near the beach or possibly during grounding on shoals. In addition, minor ice-push

events frequently occur during freeze up. In these events, the pack ice is driven into the edge of the developing fast ice sheet at a high-angle, pushing it shoreward. The shoreward movement of first-year ridge keels incorporated in the fast ice could result in additional gouging but, in general, it does not seem probable that first year ice alone was responsible for the extent and depth of gouging in the area. Instead, the most prominent gouge orientations shown in Figures 3.6-9 and 10 were probably created by the keels of **multiyear** floes, as described next.

In 1974, the pack ice which drifted into the area during freeze up consisted primarily of **multiyear** ice floes which, from study of satellite imagery, can be shown to have originated in the Beaufort Sea, and drifted southwestward around Point Barrow. Some of the floes then turned and drifted into the field-of-view of the radar at a high-angle to the beach. Ultimately, the floes grounded, possibly producing gouges as they slowed after contacting the sea floor. In addition, they may have subsequently been driven further shoreward by floes arriving behind them, extending the gouges. Field studies showed that the freeboards of some of the floes were up to 3 m in water depths as shallow as 5 m, indicating that they were grounded. Once in place, the floes sheltered the inshore area, permitting first year ice to freeze in the interstices, thereby solidifying the fast ice sheet.

The drift of thick **multiyear** ice floes along the track described above (which, of course, may also occur at other times of year than freeze up) clearly provides one mechanism for producing gouges at a high-angle to the coast. It maybe particularly important in water depths greater than those usually covered by fast ice, because it is not likely that first year ice ridge keels could form gouges in deep water.

There are few data available on the frequency with which the source of floes for the fast ice varies from northeast or southwest. For the five freeze up seasons through which the radar system operated, the floes came from the southwest during three years, from the northwest in one year, and in one season (Summer, 1975) most

of the fast ice stayed in place through the summer. However, these few years are probably not representative of the actual frequencies, and the few air photos we have seen of the fast ice in the study area for other years indicate that a southwesterly source for the fast ice is more common. No studies have been done to determine how often multi year ice enters the area from north of Point Barrow at other times of year, although satellite imagery might provide information to examine this question.

Ice-push events provide a second possible mechanism for producing gouges at a high-angle to the shoreline. As noted in Shapiro et al. (1984) and in Section 3.1 above, the passage of a storm northward through the central Chukchi Sea generates southwesterly winds which tighten the pack ice against the fast ice along the coast of Alaska, forcing the latter toward the shore. If an ice-push event results, grounded first year and multiyear ice keels within the fast ice can be dragged over the sea floor creating or lengthening gouges. The magnitude of the displacement in any ice-push event probably varies with the time of year, the state of the ice, and the duration of the driving force. However, the typical displacement direction of the ice (as shown by the radar data) is similar to the principle gouge orientation directions shown in Figures 3.6-9 and 10.

A major ice-push event occurred in July, 1975 as the result of the passage of such a storm system [the details are given in Shapiro et al. (1984)]. The fast ice sheet was still intact at the time, although surface melting had reduced its thickness by about 50% to 1 m. The pattern of motion of the fast ice during the 1975 event is illustrated in Figure 3.6-11 which shows displacement vectors of prominent reflectors in the fast ice sheet (as mapped from the radar data) superimposed on the map of ice gouge orientations from the 1977 survey. The similarity between the orientation of the displacement vectors and the principle gouge orientation is apparent from the figure. As noted above, the fast ice sheet in 1975 included numerous grounded multiyear floes which would have been dragged across the sea floor during the event. In

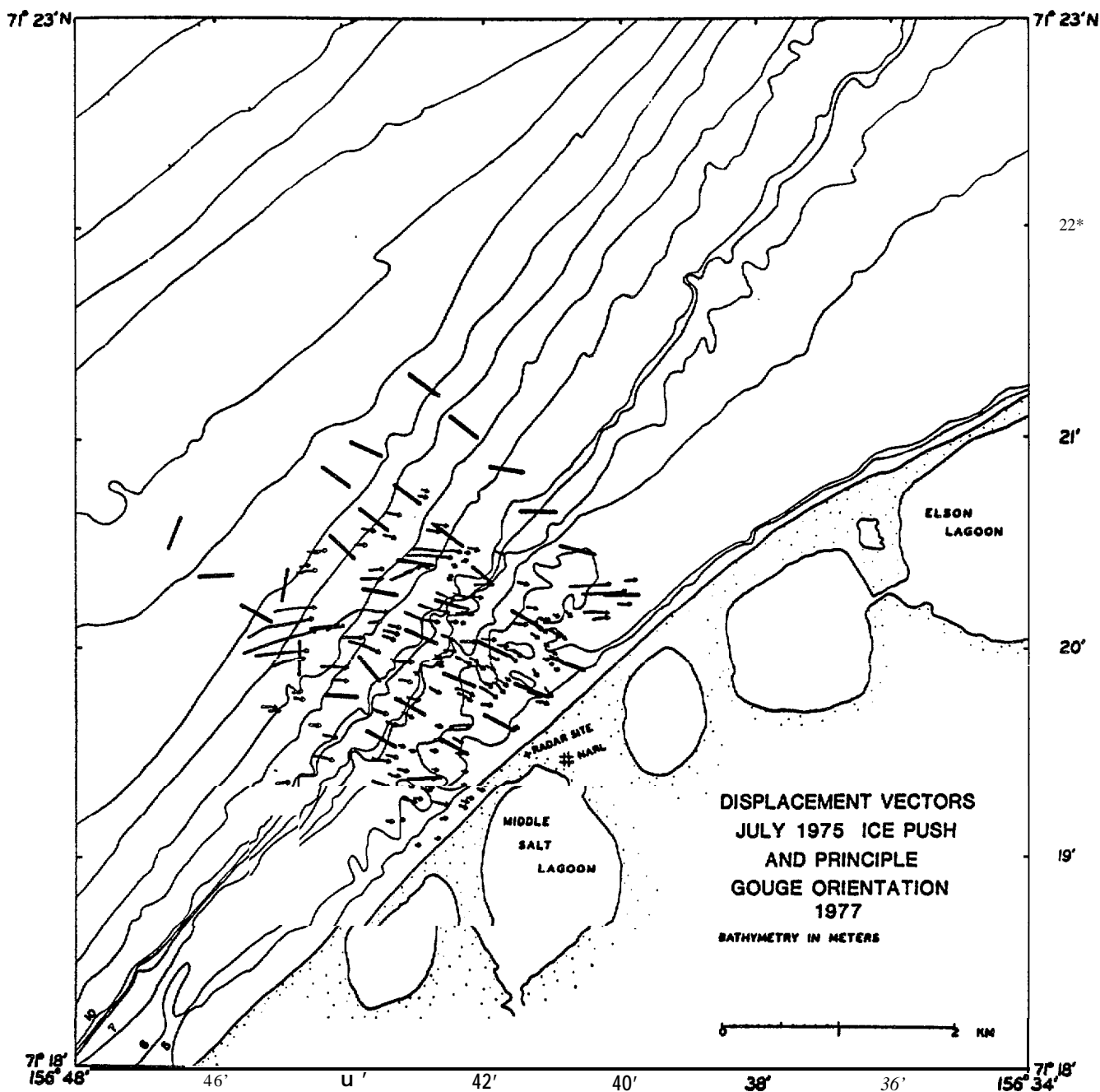


Figure 3.6-11 Displacement vectors from the 1975 ice-push event (small arrows) superimposed on principal ice gouge orientations mapped in the 1977 survey (from Figure 3.6-9).

3.64.2 DENSITY AND DEPTH OF ICE GOUGES

The maximum gouge densities in both surveys occur within the zone of most intense ridging activity (Figures 3.6-4, 5 and 6), implying that most of the gouges are due to the incision of keels during ridging events. In addition, the low density of grooves in the area inshore from about 5 m water depth in either year (Figures 3.6-4 and 5) emphasizes the vigorous wave and current reworking of the sea floor in these depths which obliterates the gouges.

Gouge densities were higher in the 1977 survey than in the 1978 survey, particularly in the inshore segments of the survey area (Figures 3.6-4 and 5). In 1977, densities of from 50 to in excess of 100 gouges per 0.5 km of trackline were common in water depths from 8 to 15 meters. In contrast, densities observed in the 1978 survey were generally less than 50 gouges per 0.5 km of trackline. In particular, there was a marked decrease in gouge density in the area of the survey inshore from about 8 m (Figures 3.6-4 and 5). We suggest that the difference in the gouge densities between the two surveys reflects the timing of the surveys and the nature of the ice and storm events between the surveys.

Freeze up following the September, 1977 survey was late and followed more than a month of stormy weather which, based upon the records from the NWS station at Barrow, began shortly after the survey. During this period, waves and coastal currents probably reworked the sea floor, infilling and eroding the ice gouge morphology (Barnes and Reimnitz, 1979). The radar data show that the first emplacement of fast ice which remained through the winter was in late October. Subsequently, there were five separate pack ice incursions into the near shore zone which produced minor ice-push events. However, the floes which formed the fast ice were all first year ice from the southwest. Thus, it is probable that gouging due to ice-push was relatively minor and new gouges formed during freeze up were

restricted to incision of keels during ridging. The fast ice was stable through the winter, no ice-push events occurred during breakup in 1978, and the fast ice was gone by mid-July, shortly before the survey in early August. As a result, during the time between the surveys there was ample opportunity for gouges in the sea floor to be reworked by nearshore waves and currents while few new gouges would have been formed. The gouges formed during the ice-push event of July, 1975 and in the winter of 1975-76 would still have been prominent features at the time of the 1978 survey, although somewhat subdued by reworking during the storms in the fall of 1977.

3.65 CONCLUSIONS

The principle direction of the ice gouges in the area of the side-scan sonar surveys along the Chukchi Sea coast near Pt. Barrow is at a high angle to the beach and isobaths, and to the dominant direction of ice drift in the area as shown by radar data. The principle gouge orientations can be interpreted to have been caused primarily by two processes. The first is the repeated occurrence of ice-push events in which the fast ice is pushed toward the shore by impact of the pack ice. Ice-push occurs during both freeze up and breakup, but is more common in the latter. During these events, keels of multiyear floes or, possibly, grounded first-year ice ridges are dragged over the sea floor creating the gouges.

The second process is probably responsible for the gouges at a high angle to the beach in water depths greater than those normally covered by fast ice, as well as some of the gouges in shallower water. It occurs when multiyear ice drifts southwestward toward the coast during freeze up. The source of the floes is either the Beaufort or northern Chukchi Sea.

The gouge density is greatest in the area in which most ice ridges occur. It may be related to the incision of keels into the sea floor during ridging as well as to drag

during ice-push events. We attribute the change in gouge density between the two surveys to reworking of the bottom sediments by waves and currents during the storms which followed the 1977 survey.

The maximum gouge incisions are located in a zone just offshore from the zone of maximum gouge density. This probably reflects the drift of larger, heavier floes into the near shore area, which are stopped as they reach shallow water.

The pervasive onshore ice push and ice gouge events documented here suggest that this process may be important in bringing material to the beach, as first suggested by Hurne and Schalk (1976). However, the supply of material from ice-push events may be inconsequential when compared to the volume removed during reworking by waves and currents, or by man.

REFERENCES CITED

- Barnes P. W. and Reimnitz E. 1979, Ice gouge obliteration and sediment redistribution event: 1977-1978, Beaufort Sea, Alaska; U. S. Geol.Survey, Open-File Report, 79-848, 22p.
- Barnes, P.W., McDowell, D.M., and Reimnitz, E., 1978, Ice gouging characteristics: their changing patterns from 1975-1977, Beaufort Sea, Alaska: U.S. Geological Survey Open-File Report 78-730, 42p.
- Barnes, P.W., Rearic, D.M. and Reimnitz, E., 1984, Ice gouge characteristics and their relation to ice gouging and ice dynamics; in O.W. Barnes, D.M. Schell and E. Reimnitz (eds.), The Alaskan Beaufort Sea-Ecosystems and Environment: Academic Press, San Francisco, California, p.85-212.
- Hume, J.D., and Schalk, M., 1976, The effects of ice on the beach and nearshore, Point Barrow, Arctic Alaska, Review Geography deMontreal, v. 30, p. 105-114.
- Shapiro, L. H., Metzner, R. C., Hanson, A., and Johnson, J. B. (1984) Fast ice sheet deformation during ice-push and shore ice ride-up; in Barnes, P. W., Schell, D. M. and Reimnitz, E., The Alaskan Beaufort Sea, Ecosystems and Environments, Academic Press Inc., New York, pp.137-157.
- Toimil, L.J., 1978, Ice gouge microrelief on the floor of the eastern Chukchi Sea, Alaska: a reconnaissance survey; U.S. Geological Survey Open-File Report, 78-693, 94p.